Coupled Large Eddy Simulations of combustion chamber-turbine interactions

Dimitrios Papadogiannis

THÈSE

En vue de l'obtention du

DOCTORAT DE L'UNIVERSITÉ DE TOULOUSE

Délivré par :

Institut National Polytechnique de Toulouse (INP Toulouse)

Discipline ou spécialité :

Dynamique des fluides

Présentée et soutenue par :

M. DIMITRIOS PAPADOGIANNIS

le mercredi 6 mai 2015

Titre :

COUPLED LARGE EDDY SIMULATIONS OF COMBUSTION CHAMBER-TURBINE INTERACTIONS

Ecole doctorale :

Mécanique, Energétique, Génie civil, Procédés (MEGeP)

Unité de recherche :

CERFACS (CERFACS)

Directeur(s) de Thèse :

M. LAURENT GICQUEL

M. FREDERIC SICOT

Rapporteurs :

M. EDWIN VAN DER WEIDE, UNIV. TWENTE ENSCHEDE PAYS-BAS

M. PAUL TUCKER, UNIVERSITE DE CAMBRIDGE

Membre(s) du jury :

M. PASCAL FERRAND, ECOLE CENTRALE DE LYON, Président

M. FLORENT DUCHAINE, CERFACS, Membre

M. LAURENT GICQUEL, CERFACS, Membre

M. STÉPHANE MOREAU, UNIVERSITE DE SHERBROOKE QUEBEC, Membre

M. VINCENT BRUNET, GROUPE SAFRAN, Membre

Acknowledgements

Firstly, I would like to thank all the members of the jury for accepting to evaluate the work presented in this dissertation and taking the time to review it thoroughly. Their very interesting comments and discussions present an excellent basis for further improvements in the future.

I would also like to thank my supervisors, Laurent, Frédéric and Florent. Not only they believed in me from my first day in Cerfacs and encouraged me but they have also always managed to find time to answer my questions and provide ideas and perspectives when they were needed the most. It is through their guidance that the completion of this PhD was made feasible.

Of course, I am also grateful to Gaofeng. His idea to use overset grids for the coupling of different AVBP's has been behind all these developments on LES of turbomachinery. He was also patient and willing to transfer me part of his expertise on several areas (for example his excellent meshing tricks for Centaur that I hope I have since managed to pass on others at Cerfacs). I am sure he is currently doing an equally great work teaching young engineers in China!

My PhD experience would not be the same without Stéphane. I would like to thank him for his comments throughout this PhD and for the opportunity to work together at the summer program in Stanford. It was a great experience (as well as a showcase of the capacities of TurboAVBP) and I had the chance to try the famous swimming pool that many other PhD's had been talking about! Of course, I would also like to thank Thierry for the opportunity and the incredible house next to the university (everyone at CTR, including professors who go there frequently, still wonder how he finds these places).

Completing successfully a PhD thesis does not only demand hard work but also being between people with who you can have constructive discussions, share and sometimes relax. And everyone at Cerfacs is very good at that! From all the seniors, Benedicte, Eleonore, Olivier, Jérome, Gabriel to the PhD's and PostDoc's: Michaël (with whom I also had the luck to share my office), Anthony, Damien, Corentin, Raphael, Luis, Lucas, Jérome, Thomas, Sandrine, Majd, Romain, Elena, Manqi, Pierre and so many others. Their contribution in creating a pleasant, motivating environment and their support was essential to the completion of this PhD. Not only one can have fruitful discussions on technical/scientific issues with them but also spend a little time of relaxation (i really enjoyed the barbecues!).

During my PhD I had also the chance to spend 3 months at Turbomeca. I would particularly like to thank Lorenzo Pons, for welcoming me warmly into his team as well as Guillaume Bonneau for following all parts of my work with great interest. The

varied discussions on different aspects of my simulations with many interesting people I encountered at Turbomeca, Jean-Loup Bourguignon, Gilles Leroy, Christophe Favre, Nicolas Chauvet, Mickaël Philit, Etienne Tang, were an additional factor contributing to the outcome of my passage there. The time I spent at Bordes allowed me to learn how to work with a different, more applied, perspective and reflect on how the things I was doing at Cerfacs can function in a more industrial environment.

Finally, I wish to express my gratitude to my family. They have been a constant source of encouragement in all my endeavors and have never stopped supporting me, despite the distance and the long periods between visits. My friends from Greece, George, Panos and Stelios have also been an invaluable additional support.

The final words have to be dedicated to Adéle for the wonderful time we have spent together and the boundless understanding during the last three years (although she is well aware of the difficulties having been through the same process). I cannot thank you enough for your support and I cannot wait for our future trips together!

To my family and Adèle

Contents

1 General Introduction **1**
1.1 Gas Turbines 1
1.2 The combustion chamber 3
1.3 The high-pressure turbine 4
1.4 Combustor-turbine interactions 5
1.5 Objectives of the PhD 8

I Flow modeling of turbomachinery stages **13**

2 Flow modeling in turbine stages **15**
2.1 CFD of turbulent flows 15
2.2 Near-wall treatment 18
2.3 Modeling of the rotor/stator interface 19

3 An overset-grid method for the treatment of rotor/stator interactions **25**
3.1 Numerical schemes for the solution of the Navier-Stokes equations 26
3.1.1 Domain Decomposition for standard simulations 27
3.2 Principle of the overset method for rotor/stator interactions 27
3.3 Validation test cases 31
3.3.1 Acoustic waves traveling in a static coupled simulation 32
3.3.2 Convection of a 2D isentropic vortex 34
3.3.3 Turbulent pipe flow 41
3.4 Conclusions 45

4 Large-Eddy Simulation of a transonic, high-pressure turbine stage **49**
4.1 Applications of LES in turbomachines 50
4.2 High-pressure turbine flow characteristics 52
4.3 MT1 Turbine Stage 58
4.4 Simulation set-up 58
4.5 Global characteristics 65
4.6 Basic flow topology 66
4.7 Low resolution results 70
4.8 High resolution results 78

4.9 Conclusions 88

II LES of combustor-turbine interactions 89

5 Indirect combustion noise generation in a high-pressure turbine 91
5.1 Motivation 92
5.2 Indirect combustion noise state-of-the-art 93
5.3 DMD test case: 2D entropy spot propagation in a periodic channel . . . 95
5.4 Turbine stage simulation set-up 99
5.4.1 Mesh 100
5.4.2 Numerical schemes 100
5.4.3 Boundary Conditions 101
5.5 Numerical Results 105
5.5.1 Overall flow topology 105
5.5.2 Dynamic Mode Decomposition of the LES flow field 107
5.5.3 Quantifying the indirect noise and comparisons with the compact theory 117
5.6 Conclusions 119

6 LES of an industrial combustion chamber-turbine system 121
6.1 Multicomponent simulations of gas turbines 122
6.2 Hot-streak migration across turbines 125
6.2.1 Segregation effect 125
6.2.2 Other parameters influencing the hot-streak migration 126
6.3 LES of an industrial high-pressure turbine stage 129
6.3.1 Standalone turbine geometry 129
6.3.2 Mesh 130
6.3.3 Boundary conditions 132
6.3.4 Numerical setup and initialization 133
6.3.5 Results 133
6.4 Fully coupled combustion chamber-turbine simulation 141
6.4.1 Geometry 141
6.4.2 Mesh 142
6.4.3 Combustion modelling 142
6.4.4 Initialization and numerical set-up 144
6.4.5 Results 146
6.5 Conclusions 152

General conclusions and perspectives **155**

III Appendices **159**

A Equations of fluid motion **161**
A.1 Navier-Stokes equations 161
A.2 Filtered Navier-Stokes equations 163
A.2.1 LES modeling 164

B Combustion modeling **169**

C Theory of Dynamic Mode Decomposition **171**

D MISCOG method - Journal of Computational Physics **175**

List of Figures

1.1 Ideal thermodynamic cycle of a gas turbine. 2

1.2 A basic jet engine highlighting the position of the different components and the corresponding processes of the Brayton thermodynamic cycle. After the 3 main processes of the cycle propulsion/work is extracted either through a nozzle or an additional power turbine. 2

1.3 A sector of a modern annular combustion chamber of Snecma [1]. 3

1.4 Photo of an experimental high-pressure turbine [2]. 4

1.5 Combustor-turbine interaction paths - (a) Turbine inflow non-uniformities created in the combustion chamber [3, 4] and (b) Interaction mechanisms due to combustion noise. 6

2.1 Typical energy spectrum of a homogeneous isotropic turbulent flow. The different levels of modeling in the principal methods for simulating turbulent flows are depicted [5]. 16

2.2 Necessary mesh points for the resolution of a turbulent boundary layer as a function of the Reynolds number [6]. 17

2.3 Number of mesh points needed for wall resolved and wall modeled LES as a function of the Reynolds number using Choi and Moin's estimates [7]. . 19

2.4 Chorocronic boundaries in a model turbine: the neighboring blade passages see the same flow with a time shift [5]. 21

3.1 (a) DDM for cell-vertex schemes used in parallel computations and (b) the proposed method for rotor/stator interface. $\mathbf{L_{1,2,3,4}}$ (composed of: solid lines - edges and filled symbols for the vertices) and $\mathbf{R_{1,2,3}}$ (composed of: dashed lines - edges and open symbols for vertices) denote the cells on the left and right sides of a partitioned domain, respectively. In the case of a moving fluid boundary, points $\mathbf{a}$ of domain $\mathbf{L}$ and points $\mathbf{b}, \mathbf{c}$ of domain $\mathbf{R}$ are the vertices to be coupled at the interface. Points $\mathbf{p_{1,2,3}}$ and $\mathbf{L_{3,4}}$ are additional vertices involved in the coupling when the overlapping method is introduced. 28

3.2 Linear (a) and quadratic (b) triangular elements. 29

3.3 Communication framework of coupling rotor/stator interface. 30

3.4 $1D$ acoustic wave propagation simulated by two approaches: (a) the stand-alone solver and (b) the equivalent coupled approach. The total length of the computational domain is L and the cell size is Δ_x. 31

3.5 Inlet wave signal (P0) and signals at the downstream probe for the standard simulation (P1) and the coupled simulation (P2) as a function of time t normalized by the period T (mesh resolution of $\Delta x/\lambda = 0.125$ and LW scheme). Definitions of the gain factor F and phase-shift τ. 32

3.6 The gain factor F (a) and phase-shift τ (b) errors for both standard and coupled simulations. 1P indicates one overlapping cell, 4P four and 5P five overlapping cells each side of the interface. 33

3.7 Schematic of standard and coupled simulations of vortex traveling: (a) Standard case; (b) Static coupled case (c) Moving coupled case: similar mesh sizes as the previous coupled case, except that mesh B is translating at speed of u_{trans}=100, 200 or 300 m/s. The mesh size is $\Delta_x = R_c/4$ with $N_x = 80$ and $N_o = 4$ (only one-fourth of grid points are shown). The inviscid vortex (with radius R_c), shown by isolines of lateral velocity, is initialized at time $t = 0$ and is traveling from left to right and passing through the interface ($t = 0.5$). Time t is normalized by the vortex convection time over travel distance, $20R_c/U_0$. 35

3.8 The quadratic mean errors of instantaneous pressure fields $L_2(P)$ versus mesh resolution N_x for different cases using the LW or TTG4A schemes. The pressure profiles are compared with the analytic profiles when the vortex reaches upstream of the interface ($t = 0.25$), the interface ($t = 0.5$) and the downstream of the interface ($t = 1$). The computations are using two sets of time steps with CFL= 0.07 (top) and CFL= 0.7 (bottom). The translation speeds for the translating coupled cases is $U_{trans} = 200$ m/s. 37

3.9 The maximum errors of instantaneous pressure fields $L_\infty(P)$ versus mesh resolution N_x for different cases using the LW or TTG4A schemes. The pressure profiles are compared with the analytic profiles when the vortex reaches upstream of the interface ($t = 0.25$), the interface ($t = 0.5$) and the downstream of the interface ($t = 1$). The computations are using two sets of time steps with CFL= 0.07 (top) and CFL= 0.7 (bottom). The translation speeds for the translating coupled cases is $U_{trans} = 200$ m/s. 38

3.10 Temporal evolutions of pressure signals at the central position (0,0) of interface for different vortex intensities (top: $\Gamma = 0.5$ m^2/s; bottom: $\Gamma = 0.036$ m^2/s) in standard, static coupled and translating ($U_{trans} = 200$ m/s) coupled cases. Time traces (a) and spectra (b)-(c) for CFL=0.07. (d) Spectra for CFL=0.7. 39

3.11 Spectra of pressure signals at the central position (0,0) of interface in translating coupled cases (CFL= 0.07; vortex intensity $\Gamma = 0.5$): (a) with different translating speeds, $U_{trans} = 100,\ 200$ and 300 m/s and mesh size $\Delta x = R_c/4$; (b) with different mesh sizes, $\Delta x = R_c/4$, $R_c/6$ and $R_c/8$ for a translating speed $U_{trans} = 200$ m/s; (c) at different monitoring positions for a translating speed $U_{trans} = 200$ m/s; (d) using different time ratios $\alpha_t = 38.9$, 19.45, 7.78 and 3.89. 41
3.12 The quadratic mean errors of instantaneous pressure fields $L_2(P)$ versus mesh resolution N_x for different cases using the LW or TTG4A schemes using 3rd-order interpolation. The pressure profiles are compared with the analytic profiles when the vortex reaches upstream of the interface ($t = 0.25$), the interface ($t = 0.5$) and the downstream of the interface ($t = 1$). The computations are using two sets of time steps with CFL= 0.07 (top) and CFL= 0.7 (bottom). The translation speeds for the translating coupled cases is $U_{trans} = 200$ m/s. 42
3.13 The maximum errors of instantaneous pressure fields $L_\infty(P)$ versus mesh resolution N_x for different cases using the LW or TTG4A schemes using 3rd-order interpolation. The pressure profiles are compared with the analytic profiles when the vortex reaches upstream of the interface ($t = 0.25$), the interface ($t = 0.5$) and the downstream of the interface ($t = 1$). The computations are using two sets of time steps with CFL= 0.07 (top) and CFL= 0.7 (bottom). The translation speeds for the translating coupled cases is $U_{trans} = 200$ m/s. 43
3.14 Numerical set-up of the pipe test case. 44
3.15 Velocity magnitude across the pipe of an instantaneous solution - Standalone AVBP (top), coupled simulation with MISCOG (bottom). 46
3.16 X-normal plane of the velocity magnitude at the interface for the coupled case - AVBP01 (left) and AVBP02 (right). 47
3.17 Mean axial velocity (left) and turbulent kinetic energy k (right) profiles as a function of the radius for the standard and coupled simulations at the interface. 47

4.1 View of the experimental high-pressure turbine MT1 [2]. 50
4.2 Number of published ASME papers on LES of turbomachinery and power of the Top 500 supercomputers for the last 20 years [8]. 51
4.3 Typical velocity triangles across a turbine stage. Absolute velocity is V, relative velocity is W and U is the velocity due to the blade rotation. . . 53
4.4 Topology of the different transition regimes as a function of the flow acceleration level and turbulence intensity [9]. 54
4.5 Secondary flow field in a cascade according to Sharma and Butler [10] (top) and according to Wang *et al.* [11] (bottom). 56
4.6 Smoke visualization of tip leakage in a turbine blade [12] (left) and schematic of the formation of the tip leakage flow on a thin blade [13] (right). . . . 57
4.7 Schematic of the TTF facility. 59

4.8 A view of the MT1 domain highlighting the decomposition of the turbine stage to the corresponding AVBP instances and the overlap between them for application of the MISCOG method. 60
4.9 Cylindrical and x-plane cuts of MESH1. 61
4.10 y^+ values for the two meshes across the stator (left) and rotor blades (right) at mid-span. 62
4.11 Practical LES hierarchy [14]. 63
4.12 Mass (left) and energy (right) conservation at the rotor/stator interface. . 64
4.13 Operating point of the different cases analyzed. The target mass flow is shown with the vertical line. 66
4.14 Isosurfaces of the Q criterion across the turbine stage. 67
4.15 Q criterion of a time-averaged solution across the stator blade (a) and flow visualization of the secondary flows across the blade from experiments [15] (b). 68
4.16 Q criterion of a time-averaged solution across the rotor blades (a) and tip clearance flow topology of a cascade from the LES of You *et al.* [13] (b) and from the experiments of McCarter *et al.* [16] (c). 69
4.17 Helicity of a time-averaged relative velocity flow field. 70
4.18 Time-averaged axial velocity at a probe in the rotor wake as a function of the averaging time. 70
4.19 Isentropic mach number across the stator at 10% (a), 50% (b) and 90% span. 71
4.20 Static pressure across the rotor blade at mid-span. 71
4.21 Radial profiles for **Cases 1**, **2**, **3** at the rotor exit (a) near field (b) far field. 72
4.22 Vorticity of the mean velocity field at the rotor exit for **Case 1** (a), **Case 2** (b) and **Case 3** (c). 73
4.23 Total pressure of the mean velocity field at the rotor exit for **Case 1** (a), **Case 2** (b) and **Case 3** (c). 73
4.24 Instantaneous views of $\frac{||\nabla\rho||}{\rho}$ at mid-span (a)-(c) and FFT's of the pressure signal for the identified probe (d)-(f) for **Case 1** (a) & (d), **Case 2** (b) & (e) and **Case 3** (c) & (f). 74
4.25 Deterministic oscillation (solid line) and deterministic oscillation with random fluctuations (dotted line). 75
4.26 Radial profiles of the unsteady activity obtained at the rotor / stator interface for all three LES and based on a triple decomposition using (a) the rotor BPF (9.5 kHz) and (b) the stator BPF (4.75 kHz). 76
4.27 Radial profiles of the unsteady activity obtained at the exit of the rotor (near field plane of Fig. 4.21) for all three LES and based on a triple decomposition using (a) the rotor BPF (9.5 kHz) and (b) the stator BPF (4.75 kHz). 77
4.28 Isentropic mach number across stator blade at 10% span (a), 50% span (b), 90% span (c) and normalised pressure across the rotor blade at 50% span (d) for the cases employing MESH2. 78

4.29 Rotor exit profiles in near (a) and far (b) field for the cases employing MESH2. 79
4.30 Vorticity magnitude comparisons at the rotor exit all cases grouped according to the SGS model employed. 80
4.31 Azimuthally averaged loss coefficient as a function of the normalized radius for the six cases. 81
4.32 Instantaneous views of $\frac{||\nabla\rho||}{\rho}$ at mid-span for Cases 4 (a), 5 (b) and 6 (c). 82
4.33 Power Spectral Density of the axial velocity signal recorded at a probe in the stator wake. 83
4.34 Shear stress across the stator blades for the two mesh resolutions. With the smagorinsky model (a),(b) - WALE model (c),(d) and σ model (e),(f). 84
4.35 Positions across the suction side of the stator blade where the boundary layer profiles are plotted. 85
4.36 Wall tangential velocity across the boundary layer at 4 different suction side positions. The red line corresponds to zero velocity. 86
4.37 Turbulent kinetic energy across the boundary layer at 4 different suction side positions. 87

5.1 Noise emissions and directivity of gas turbine components - Typical 1960's turbojet engine (left) and a recent 1990's turbofan design (right) [17]. . . 93
5.2 Estimation of the ratio η between indirect and direct noise by an analytic approach. The ratio η is plotted here as a function of the Mach number $\overline{M}_1$ representing the Mach number in the combustion chamber and at the nozzle inlet, and of the Mach number $\overline{M}_2$ representing the outlet nozzle Mach number - Typical combustor operating point indicated with a red point [18]. 94
5.3 Schematic of the 2D test case and boundary conditions employed. 96
5.4 Instantaneous temperature flow field of the 2D test case. 96
5.5 Maximum and minimum temperature (a) and pressure (b) across the domain as a function of time. Entropy forcing of amplitude 20 K is active. . 97
5.6 DMD temperature spectrum of the 2D test case and FFT of the temperature signal captured at a probe in the center of the channel. 98
5.7 DMD 4 kHz mode - Temperature modulus (top) and phase (bottom). . 99
5.8 DMD temperature spectrum of the 2D test case for different sampling frequencies. Duration of the signal 4T. 100
5.9 DMD temperature spectrum of the 2D test case for different runtimes. Sampling frequency 10 kHz. 101
5.10 mesh view of the stator at mid-span (a) of the rotor at mid-span (b) and at the rotor tip (c) 102
5.11 Characteristic waves crossing an inlet and outlet 103
5.12 Time-averaged mid-span profiles of the isentropic Mach number across the stator blade (a) and of the static pressure across the rotor blades (b). . . 105

5.13 Contours $\frac{|\nabla\rho|}{\rho}$ of an instantaneous solution at mid-span for the steady inflow (a) and pulsed cases (b). Contours of the same variable and at an x-normal plane near the rotor exit for the steady inflow case (c). 106
5.14 Q-criterion of an instantaneous solution across the turbine stage. 107
5.15 DMD temperature spectrums of the stator (left) and rotor domain (right) at mid-span - Steady inflow case. 108
5.16 DMD pressure spectrums of the stator (left) and rotor domain (right) at mid-span - Steady inflow case. 109
5.17 DMD BPF mode at mid-span - Modulus and phase of the temperature (a and b) and pressure (c and d) respectively. 110
5.18 DMD 57 kHz mode at mid-span - Modulus and phase of the temperature (a and b) and pressure (c and d) respectively. 111
5.19 DMD temperature spectra of the stator (left) and rotor domain (right) at mid-span - Steady inflow case (∘) and pulsed case (×). 112
5.20 DMD pressure spectra of the stator (left) and rotor domain (right) at mid-span - Steady inflow case (∘) and pulsed case (×). 112
5.21 DMD 2 kHz mode at mid-span - Modulus and phase of the temperature (a and b) and pressure (c and d) respectively 114
5.22 DMD temperature spectrums of the pulsed case with different number for different runtimes - stator (left) and rotor domain (right) at mid-span. . . 115
5.23 DMD pressure spectrums of the pulsed case with different number different runtimes - stator (left) and rotor domain (right) at mid-span. 115
5.24 Sparsity-Promoting DMD at the stator inlet (left) and rotor outlet (right) - Original DMD modes (∘) and SPDMD selected modes (×). 117
5.25 Transmission coefficients - a) Ra b) Tr and c) Ts - Compact theory (solid line), 2D simulations (+ and •) and LES (•) 120

6.1 Full GE90 simulation comparison to engine cycle data. Percent difference in total pressure (P), total temperature (T) and flow rate (W) from experimentally measured values [19]. 123
6.2 LES/RANS interface at the compressor exit with turbulent fluctuations superimposed at the time averaged RANS solution [20]. 123
6.3 View of the high-pressure flow field from the full engine simulation (top) and radial pressure profiles at two different engine positions (bottom)[21]. 124
6.4 Typical combustor outlet temperature profile [22]. 125
6.5 Schematic showing the segregation effect. 126
6.6 Effect of clocking on the NGV heat load [15]. 127
6.7 Heat transfer coefficient across a high-pressure NGV under the influence of free-stream turbulence [23]. The turbulence alters the thermal flow field, forms elongated structures and enhances the heat transfer. 129
6.8 Rotor geometry with squealer. 130
6.9 Views of the mesh at mid-span (left) and at the rotor tip (right). 131
6.10 Distribution of y^+ across the stator (a) and rotor (b) blades at mid-span. 131

6.11 Non-dimensional total temperature (top) and pressure (bottom) profiles imposed at the turbine inlet. 132
6.12 Isosurfaces of the Q-criterion across the NGV (a) and the rotor blade (b) calculated based on a mean flow and colored by the temperature. 135
6.13 Temperature across the NGV passage - Turbine inlet (a), 10% of the chord (b), 60% (c) and at the NGV exit (d). 137
6.14 Temperature across the rotor passage - Rotor inlet (a), 10% of the chord (b),50% (c) and at the rotor exit (d). 138
6.15 Azimuthally averaged temperature profiles at three different axial positions as a function of the height. 140
6.16 Blade wall temperature of the stator (a) and rotor (b) blades - Blade surface is opened around the Leading Edge (LE) for clarity. 140
6.17 View of the combustion chamber-turbine geometry with important technological aspects highlighted. 141
6.18 View of the combustion chamber mesh with the different refinement zones. 142
6.19 Instantaneous flow field of the coupled combustor-turbine simulation. The central image depicts temperature isosurfaces and the blade surface temperature. The top images present the heat release and temperature around the flame front (zoomed) and at the bottom the $\frac{|\nabla\rho|}{\rho}$ and temperature at mid-span across the turbine are depicted. 145
6.20 Static temperature at the turbine inlet - HPT LES (a) and combustor/HPT LES (b). 147
6.21 Turbine inlet profiles of the coupled combustor/HPT and HPT simulations - Temperature (a), temperature fluctuations (b) and turbulence intensity (c). 148
6.22 Temperature across the NGV passage for the coupled simulation - Turbine inlet (a), 10% of the chord (b), 60% (c) and at the NGV exit (d) 149
6.23 Temperature across the rotor passage for the coupled simulation - Rotor inlet (a), 10% of the chord (b), 50% (c) and at the rotor exit (d). 150
6.24 Azimuthally averaged temperature profiles at the stator/rotor interface at the the turbine exit as a function of the height. 151
6.25 Blade wall temperature of the stator (a) and rotor (b) blades for the coupled cases - Blade surface is opened around the Leading Edge (LE) for clarity 152

A.1 The LES concept: large turbulent scales can be resolved by the mesh while the smaller ones have to be modeled 165

B.1 Direct Numerical Simulation of flame/turbulence interactions by Angelberger *et al.* [24] and Poinsot and Veynante [25]. (a) non-thickened flame and, (b) thickened flame ($\mathcal{F} = 5$) 169

Nomenclature

A	Pre-exponential constant.
C_p	Specific heat capacity at constant pressure (kJ/(kg.K)).
$D^k_{\Omega_j}$	Distribution Matrix.
E	Total energy (kJ).
F	Gain factor.
H	Total enthalpy (kJ/kg).
K	Von Karman constant.
K_p	Relaxation coefficient on static pressure.
K_{pt}	Relaxation coefficient on total pressure.
K_{tt}	Relaxation coefficient on total temperature.
L	Length (m).
M_{is}	Isentropic Mach number.
N	Number of blades.
Pt	Total pressure (Pa).
R	Radius (m).
R_c	Vortex radius (m).
R_d	Degree of reaction.
Re	Reynolds number.
S	Scaling ratio.
S^0_L	Laminar flame speed (m/s).
T	Temperature (K).
Tt	Total temperature (K).
Tu	Turbulence Intensity.
U^*	Friction velocity (m/s).
V_{Ω_j}	Cell volume.
Δ	Filter width.
Δ_x	Cell length in x direction (m).
Ψ	Streamfunction.
δ^0_L	Laminar flame thickness (m).
$\dot{m}$	Mass flow (kg/sec).
η_{is}	Isentropic efficiency.
γ	Heat capacity ratio.
λ	Wavelength (m).
λ_t	Thermal diffusivity (W/(m.K)).

$\mathbb{R}_{\Omega_j}$	Cell-based residual.
$\mathbf{W}$	Conservative variables vector.
σ	Singular values of velocity gradient tensor.
$\mathcal{E}$	Flame efficiency function.
$\mathcal{F}$	Flame thickening factor.
$\mathfrak{L}f$	Lagrange Interpolators.
ν	Kinematic viscosity (m^2/s).
ν_τ	Turbulent viscosity (m^2/s).
ω	Angular velocity (rad/s).
ϕ_i	Shape functions.
π_t	Turbine total pressure ratio.
ρ	Density (kg/m^3).
τ	Time delay (sec).
τ_w	Wall shear stress (Pa).
θ	Azimuthal angle (deg).
$\tilde{\mathbf{S}}$	Resolved rate-of-strain tensor.
$\tilde{\mathbf{g}}$	Resolved velocity gradient tensor.
$\vec{\mathcal{F}}^C$	Convective fluxes.
$\vec{\mathcal{F}}^V$	Viscous fluxes.
ζ	Aerodynamic loss coefficient.
f	Frequency (Hz).
k	Turbulent kinetic energy (J).
p	Pressure (Pa).
r	Mixture gas constant (J/(kg.K)).
s	Specific entropy (J/(kg.K)).
t	Time (sec).
w^+	Downstream propagating acoustic wave.
w^-	Upstream propagating acoustic wave.
w^s	Entropy wave.
x^+	Non-dimensional streamwise distance.
y^+	Non-dimensional wall-normal distance.
z^+	Non-dimensional spanwise distance.

Abbreviations

(U)RANS	(Unsteady) Reynolds Averaged Navier-Stokes.
ACARE	Advisory Council for Aeronautics Research in Europe.
BPF	Blade Passing Frequency.
CFD	Computational Fluid Dynamics.
CFL	Courant-Friedrichs-Lewy number.
DDM	Domain Decomposition Methods.
DMD	Dynamic Mode Decomposition.
DNS	Direct Numerical Simulations.
DTF	Dynamic Thickened Flame.
EWF	Entropy Wave Frequency.
FAR	Fuel-to-Air Ratio.
FFT	Fast Fourier Transform.
GT	Gas Turbines.
HPT	High-Pressure Turbine.
LES	Large Eddy Simulation.
LODI	Linear One-Dimensional Inviscid.
LW	Lax-Wendroff scheme.
MISCOG	Multi Instance Solvers Coupled via Overlapping Grids.
MPI	Message Passing Interface.
NGV	Nozzle Guide Vane.
NSCBC	Navier-Stokes Characteristic Boundary Conditions.
PSD	Power Spectral Density.

RMS	Root Mean Square.
RQL	Rich-Quench-Lean.
SGS	Sub-Grid Scale.
SPDMD	Sparsity-Promoting DMD.
TFLES	Thickened Flame LES.
TTG	Two-step Taylor Galerkin.

Chapter 1

General Introduction

Contents

1.1 Gas Turbines 1

1.2 The combustion chamber 3

1.3 The high-pressure turbine 4

1.4 Combustor-turbine interactions 5

1.5 Objectives of the PhD 8

1.1 Gas Turbines

The general field of this thesis is Gas Turbines (GT). Since their conception in the 1930's by Sir Frank Whittle, GT have evolved to dominate the air transport industry with large commercial and military aircraft relying solely on turbofan gas turbines for their propulsion. Smaller regional/private aircraft and helicopters make extensive use of the turboprop and turboshaft variants respectively. GT also hold an important share in land-based power generation units and have found other applications, such as in oil and gas rigs and ground transportation. The main advantages of GT, compared to piston engines, are the significantly higher power-to-weight ratio and increased reliability as well as easier maintenance due to the fewer moving parts present in the engine.

The operation of the GT is based on the Brayton thermodynamic cycle, shown in Fig. 1.1 in a temperature-entropy plot. The cycle consists of four processes: compression of air ($1 \Rightarrow 2$), isobaric addition of heat (through mixing with fuel and ignition of the mixture under constant pressure, $2 \Rightarrow 3$), expansion ($3 \Rightarrow 4$), cooling and return to the initial state ($4 \Rightarrow 1$). In the ideal cycle, the compression and expansion are performed isentropically, which is practically not possible as these are physically irreversible processes and losses occur in real engines. The components that perform these processes are the compressor (typically a multistage compressor for large engines) for the compression phase, the combustion chamber for the heat addition and the turbine for the expansion

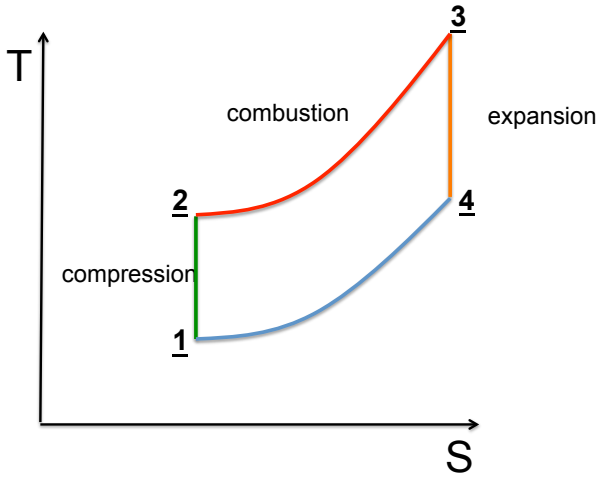

Figure 1.1: Ideal thermodynamic cycle of a gas turbine.

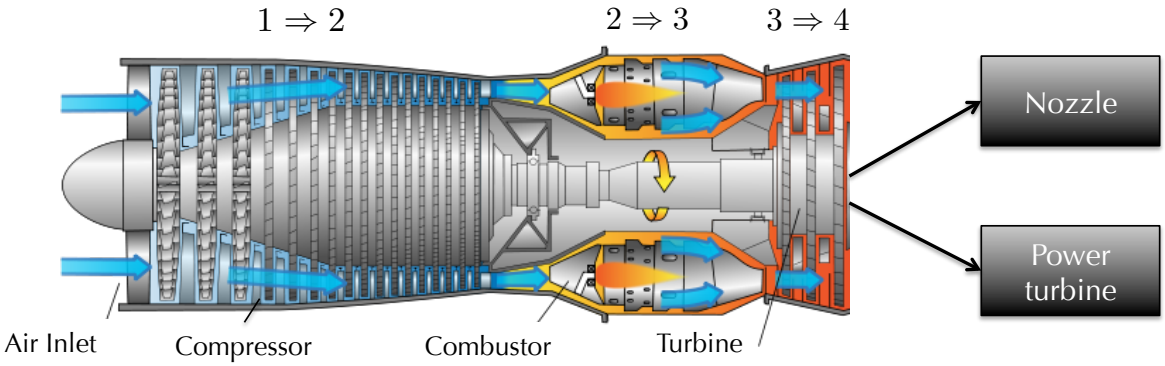

Figure 1.2: A basic jet engine highlighting the position of the different components and the corresponding processes of the Brayton thermodynamic cycle. After the 3 main processes of the cycle propulsion/work is extracted either through a nozzle or an additional power turbine.

(also called the High-Pressure Turbine (HPT) as it is behind the combustion chamber and functions at the peak pressure of the cycle.

These three basic components are present in all types of GT, irrespective of their application. Figure 1.2 provides a view of a typical jet engine illustrating the basic GT structure and placement of the components. After performing the 3 main processes of compression, combustion and expansion the necessary propulsion/work is extracted from the flow exiting the HPT either through a nozzle that accelerates the flow (configuration employed in large aircraft) or through an additional turbine, called power turbine. This is, for example, the case in helicopter engines (turboshaft), where work recovering from the engine is needed to drive the main rotors of the aircraft.

Modern GT have remarkable capabilities compared to the earlier designs: higher power output and power-to-weight ratios, reduced fuel consumption, reduced pollutant emissions and limited noise signature. One of the driving factors behind many of these

improvements has been the rising temperature at the inlet of the HPT. Indeed, from Fig. 1.1 it can be easily deduced that increasing the temperature of point 3, for example by increasing the compression ratio, increases the work available by the cycle. There has been, therefore, a constant effort the last decade to develop improved rotating machinery that can handle these processes. The HPT, in particular, requires considerable attention due to the aggressive, unsteady and high-temperature environment in which it has to operate (point 3 in the thermodynamic cycle, after the combustion chamber). However, as of today and despite continuous research on the topic, the predictions of the complex aerothermal flow inside the HPT and its interactions with the combustor are still lacking. One objective of this work is to contribute to today's CFD capabilities in predicting these flows thereby opening new possibilities in improving further the understanding of the physical processes occurring in the HPT. There are two issues that will be of specific interest to this dissertation: *a*) The development and validation of a high-fidelity numerical simulation tool applicable to this context and *b*) address with such tools the combustion chamber/turbine flow interactions.

Before going more into details on specific issues, some basic notions on the operation of the two components of interest for this thesis are provided.

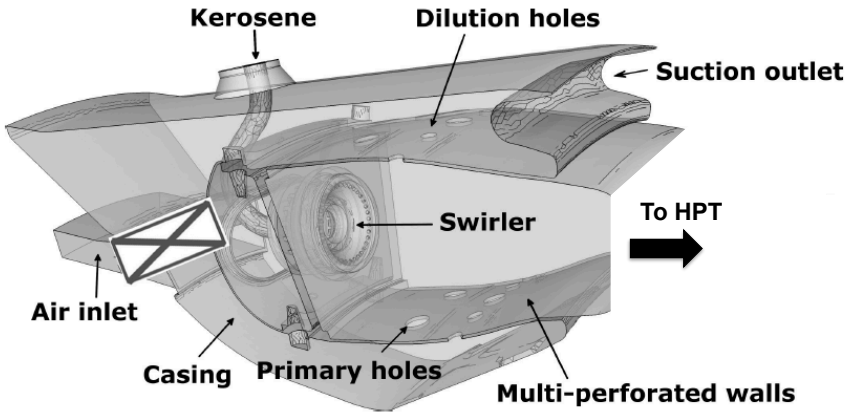

Figure 1.3: A sector of a modern annular combustion chamber of Snecma [1].

1.2 The combustion chamber

The combustion chamber is responsible for the heat addition to the flow. In typical designs, the flow arriving from the compressor goes through a swirler before entering the main chamber. The swirling flow then undergoes vortex breakdown to create a central recirculation zone in the chamber. At the same time, the fuel injectors release fuel that atomizes, evaporates and mixes with the air, with the mixture undergoing combustion at the flame front. The central recirculation zone serves to stabilize the flame and reduce its length, compared to a non-swirled jet flame for example.

Most modern combustors are designed with a Rich-Quench-Lean approach, where close to the fuel injector the Fuel-to-Air Ratio (FAR) corresponds to rich combustion, followed by a large amount of air injected by primary and dilution holes that quench the flame and mix with the hot products before reaching the combustor outlet. The designs typically also include multiperforated plates and/or film cooling to protect the liners from the extreme temperatures of the hot gases. These cooling flows also serve to reduce the overall temperature of the flow to temperatures that can be handled by the turbine blade materials. A typical example of such a combustor design is the Snecma combustor of Fig. 1.3.

1.3 The high-pressure turbine

The HPT is the component located after the combustion chamber. It is placed on the same axis as the high-pressure compressor and its purpose is to extract the necessary energy from the hot and high-energy gases to drive the compressor. Every turbine stage is comprised of two blade rows: the stator, often called the Nozzle Guide Vane (NGV), and the rotor. The purpose of the stator is to accelerate and turn the flow to the correct angle for the proceeding rotating blades where work extraction takes place. Figure 1.4 depicts an experimental high-pressure turbine from the Oxford Turbine Research Facility [2]. The first blade row contains the stator (only 4 blades are placed for the experiments in Fig. 1.4) that orients the flow for the rotors, which are placed on a rotating disc linked to the high-pressure shaft.

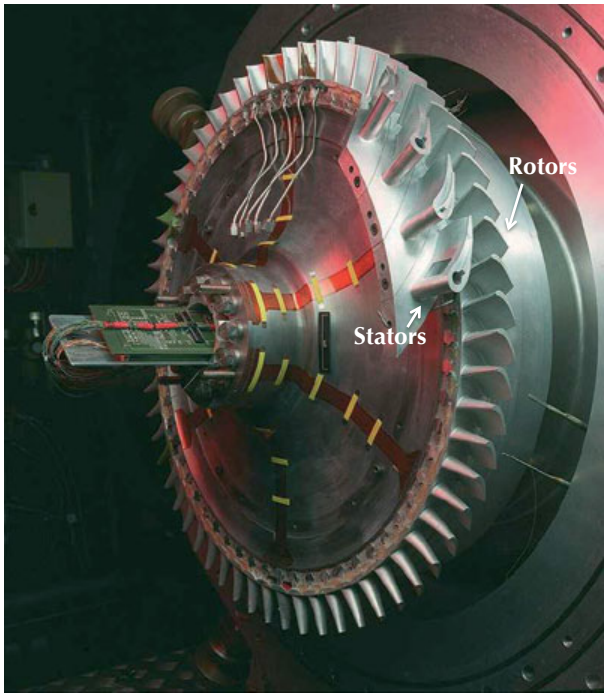

Figure 1.4: Photo of an experimental high-pressure turbine [2].

The HPT works with a favorable pressure gradient, i.e. the total pressure decreases as the flow goes through the blades. As a result and contrary to compressors, they are less prone to flow separation and a significant amount of work can be extracted from a single stage. The Rolls-Royce Trent 900 that powers the Airbus A380, for example, has a single-stage axial high-pressure turbine driving a six-stage axial compressor. However, the HPT design still remains a particularly critical exercise. As it is placed behind the combustor, it operates under extreme temperatures and is subject to a non-uniform and unsteady flow generated in the chamber. These heterogeneities, as they propagate across the HPT, can alter considerably the thermal load, reduce the life expectancy of the blades and may also impact the aerodynamic performance of the turbine. Note also that, to complicate things further, the HPT can also influence the combustor flow field.

1.4 Combustor-turbine interactions

One of the principal objectives of the new designs of aeronautical GT is the minimization of weight which translates directly into reduced operating costs. To this end, modern designs are characterized by tight spacing between components, rendering the identification of their interfaces more and more difficult and intensifying the interactions between the components. Due to this close proximity, the combustor and HPT will interact which can potentially result in an engine operating mode that is inefficient or dangerous for the device. Two paths of interaction are specifically identified for this work: Inflow non-uniformities that will migrate in the turbine stage, Fig. 1.5(a), and combustion noise, Fig. 1.5(b).

1. **Inflow non-uniformities**

Figure 1.5(a) highlights the first form of these interactions. In a combustion chamber, the finite number of fuel injectors and the protective cooling systems (to shield the combustor liners from the hot gases) create temperature non-uniformities. These features, combined with with the reduced length of modern combustors, imply that flow does not have the time to mix sufficiently which results in highly non-uniform temperature profiles at the chamber exit. These non-uniformities, frequently called hot-streaks, can be seen by the time-averaged flow and induce important temperature gradients both in the azimuthal and radial direction. Note that non-uniformities can also occur in time due to the unsteady combustion and the high levels of free-stream turbulence generated in the combustor that will then propagate towards the turbine. Finally, residual swirl issued at the fuel injector to improve the combustion process will propagate and arrive at the turbine inlet altering further the inflow. This highly complex inflow can have a significant impact on the heat loads across the turbine.

To understand and control these issues, a significant amount of research has been performed. Typically, a large number of experimental and numerical studies focused on evaluating the migration of hot streaks as a function of their azimuthal placement with respect to the stator leading edge [15, 26, 27]. The radial placement and migration have also been studied [28, 29, 30] to evaluate the effect of hot streaks on the endwalls, where

strong secondary flows[1] will interact with the non-uniformities. The impact of the inflow turbulence levels at the inlet of turbines has also been confirmed, along with its critical role in the laminar-to-turbulent transition [23, 31] that impacts both the thermal and the aerodynamic flow field. Turbulence-hot streak interaction has also been investigated [32]. Finally, recent works showed that the swirl propagated from the combustor to the turbine inlet impacts both the aerodynamic and thermal flow field by altering the effective flow angles while also modifying the hot-streak migration [33, 4].

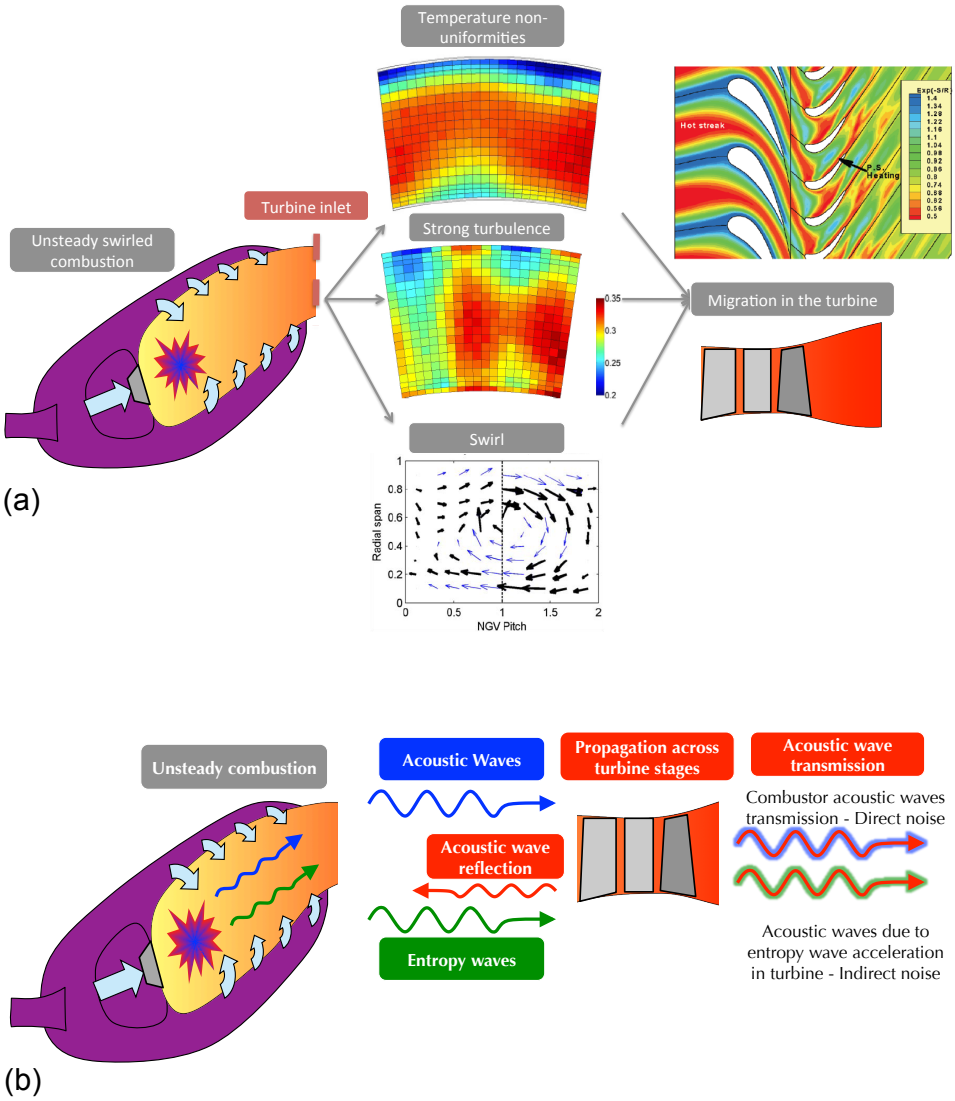

Figure 1.5: Combustor-turbine interaction paths - (a) Turbine inflow non-uniformities created in the combustion chamber [3, 4] and (b) Interaction mechanisms due to combustion noise.

All these findings highlight the importance of a realistic inflow in HPT simulations. Such an inflow, with all the inherent heterogeneities found in the real engines, is however

[1] see Chapter 4 for more details

the result of the combustor and can therefore only be available if a coupled combustor-HPT simulation is produced.

2. **Combustion noise**

The second form of interactions is related to combustion noise and is depicted in Fig. 1.5(b). It can be separated in two distinct types:

- Direct noise

Direct combustion noise emanates from the acoustic waves created at the unsteady, turbulent flame front. These waves then propagate with the speed of sound combined with the local flow velocity towards the turbine stages, from which they are partly reflected and transmitted to the engine outlet.

- Indirect noise

The second form of combustion noise is less intuitive but equally important [18]. It arises from the unsteady temperature profile generated within the combustion chamber. As mentioned in the previous sections, the unsteady heat release gives rise to low-frequency temperature fluctuations, also called entropy waves. These are then convected by the flow to the turbine where they are accelerated and distorted due to the presence of the blades. This process generates acoustic waves that propagate both back to the combustion chamber and downstream [34, 18]. This specific mechanism of entropy wave generated noise inside the HPT is usually referred to as indirect combustion noise. Its implications are not only important for the overall noise signature of an engine but also for the combustor design. Indeed, the biggest challenge of combustion chamber designs is the prediction and control of their thermoacoustic stability which involves the coupling between acoustic waves and unsteady heat release in this enclosed domain. Indirect combustion noise generated in the turbine can propagate back to the flame and contribute to the formation of a closed loop and coupling with the unsteady heat release [25]. As a result, a two-way interaction between the combustor and the HPT can appear under this form. Indeed, entropy-induced combustion instabilities have been reported in the literature [1, 35].

Several theoretical studies have been performed to better understand the indirect noise generation mechanism, using simplified turbine-like geometries such as quasi 1D nozzles [36, 37] and 2D turbine blades [38]. They have been complemented by experimental data [39, 40] and numerical simulations [41, 42] of similar configurations. It is nonetheless evident that considering the full 3D turbine is important if we take into account the highly complex flow and the strong endwall effects. These effects are potentially important in the generation of indirect noise as they alter considerably the flow field. To evaluate them and quantify their effect, the indirect combustion noise generated across a 3D turbine stage is examined later in this work.

1.5 Objectives of the PhD

One of the purposes of this thesis is to try to bridge the gap between numerical simulations of combustion chambers and high-pressure turbines. Current industrial state-of-the-art treats the HPT and combustion in a decoupled way. The communication between the combustor and the turbine design teams is usually made by exchanging steady-state homogeneous (0D or 1D) boundary conditions for the respective computations. However, the large amount of unsteady interactions between the two components indicates that treating the problem in a coupled, unsteady fashion is essential to improve the predictive capabilities of real engine flows with numerical tools. Addressing this coupling issue and then using the developed methodologies to study the combustor-turbine interactions the main objective of this thesis. The high-fidelity Large Eddy Simulation (LES)[2] formalism is chosen for both components. While it is still computationally intensive for regular use in the design phase today, the rapid growth of available computational power [43] will make such computations more accessible in the future. It is also commonly identified as a very promising approach to provide turbulent flow predictions with a clear gain in accuracy [14, 44, 45]. It is furthermore currently used in the design phase of real combustors [46].

To achieve this objective several intermediate steps are necessary. Indeed, with LES of rotating machinery only recently emerging as a potential candidate to further our understanding of the flow physics in gas turbines, a significant amount of work is necessary to adapt and validate the approach in turbine configurations. To adequately address such issues the following steps are taken:

- Chapter 2 provides an overview of different modeling techniques for turbulent fluid motion, near-wall flows and for the rotor/stator interactions as well as the challenges created by the LES formalism.

- Chapter 3 proposes an overset grid method that couples different instances of the LES solver AVBP for the treatment of rotor/stator interactions. A significant challenge in performing LES of a turbomachinery stage is the treatment of the rotor/stator interface. High-fidelity LES require minimal dispersion and dissipation of the turbulent structures or waves and the treatment of the rotor/stator interface should not impose additional errors. Several test cases are performed to evaluate the conformity of the method with such LES requirements.

- Chapter 4 contains an extensive validation of the method, as well as a sensitivity analysis, on a realistic rotor/stator configuration: an experimental 3D high-pressure turbine stage. These steps allow to establish best practices, advantages and limitations of the overset grid method as well as necessary post-processing techniques.

After validating the selected approach and solver in academic test cases and realistic turbine configurations (Part I), two applications of the developed techniques for the predictions of combustor/turbine interactions are investigated in Part II:

[2] more details on flow modeling are provided in Chapter 2

- Chapter 5 focuses on the generation of indirect combustion noise in a realistic 3D high-pressure turbine, in an effort to explore in more depth this path of combustor-turbine interactions and complement/validate the analytical approaches and low fidelity simulations.

- Chapter 6 demonstrates a fully coupled combustion chamber-HPT simulation of a helicopter engine. The discussion is split in two parts: *a*) The aerothermal predictions and hot-streak migration are examined first in the HPT stage alone and *b*) the turbine is then attached to the combustion chamber of the engine and a fully coupled reactive simulation is performed and compared to the previous results.

The work presented during this thesis was performed in close collaboration with the University of Sherbrooke and more specifically with Dr. Gaofeng Wang and Prof. Stéphane Moreau. This thesis was funded by the European Commission as part of the Marie Curie Initial Training Network project COPA-GT. During this dissertation, a number of conference and journal publications was produced. A list of these publications is presented in the next section.

List of publications produced during this thesis

D. Papadogiannis, G. Wang, S. Moreau, F. Duchaine, and L.Y.M Gicquel. Effects of sgs modeling on the deterministic and stochastic turbulent energetic distribution in les of a high-pressure turbine stage. *submitted in Journal of Turbomachinery*.

G. Wang, S. Moreau, M. Sanjose, D. Papadogiannis, F. Duchaine, and L.Y.M Gicquel. Noise mechanisms in a transonic high-pressure turbine stage. *in press International Journal of Aeroacoustics*, 2015.

D. Papadogiannis, G. Wang, S. Moreau, F. Duchaine, L.Y.M Gicquel, and F. Nicoud. Assessment of the indirect combustion noise generated across a high-pressure turbine. In *Proc. of the Summer Program* . Center for Turbulence Research, 2014.

D. Papadogiannis, G. Wang, S. Moreau, F. Duchaine, L.Y.M Gicquel, and F. Nicoud. Assessment of the indirect combustion noise generated across a high-pressure turbine. In *Proc. of the ASME Turbo Expo 2015*, number GT2015-42399 and accepted for publication in Journal of Turbomachinery, 2015.

G. Wang, F. Duchaine, D. Papadogiannis, I. Duran, S. Moreau, and L.Y.M Gicquel. An overset grid method for large eddy simulation of turbomachinery stages. *J. Comput. Phys.* , 274:333–355, 2014.

G. Wang, D. Papadogiannis, F. Duchaine, N. Gourdain, and L.Y.M Gicquel. Towards massively parallel large eddy simulation of turbine stages. In *Proc. ASME Turbo Expo 2013*, number GT2013-64852, 2013.

D. Papadogiannis, G. Wang, S. Moreau, F. Duchaine, F. Sicot, and L.Y.M Gicquel. Large eddy simulation of a high-pressure turbine stage: Effects of sub-grid scale modeling and mesh resolution. In *Proc. of the ASME Turbo Expo 2014*, number GT2014-25876, 2014.

Part I

Flow modeling of turbomachinery stages

Chapter 2

Flow modeling in turbine stages

Contents

2.1 CFD of turbulent flows 15
2.2 Near-wall treatment 18
2.3 Modeling of the rotor/stator interface 19

2.1 CFD of turbulent flows

Performing numerical simulations of high-speed flows around complex geometries, such as the combustion chamber and the HPT, is not an easy task. The physics of these flows are governed by the non-linear Navier-Stokes equations (more details on the formulation of the equations and fluid properties are provided in Appendix A) and is characterized by the Reynolds numbers (Re), a non-dimensional number that is a function of a characteristic length of the flow, the velocity and the fluid properties (viscosity). Most industrial flows are high-Reynolds number flows, where non-linearities are dominant and are typically qualified as turbulent. Turbulence is a three dimensional unsteady phenomenon that can be viewed as an ensemble of flow eddies with varying length scales. In turbulent flows, energy is extracted from the mean flow by the larger eddies and then cascades down to the smaller ones, where it is dissipated into heat by viscosity [47, 48]. Figure 2.1 depicts the repartition of energy among the different scales of a typical turbulence spectrum of a homogeneous flow. The broadband nature of turbulence and its interactions with other flow phenomena are very challenging to simulate numerically although it seems to be the only approach feasible today. There are three popular numerical techniques for computing such flows:

- Direct Numerical Simulations (DNS)

Resolving numerically the flow with all the turbulent length scales is possible by performing Direct Numerical Simulations (DNS) of the Navier-Stokes equations. DNS provide highly accurate depictions of the flow field. However, they require a mesh capable

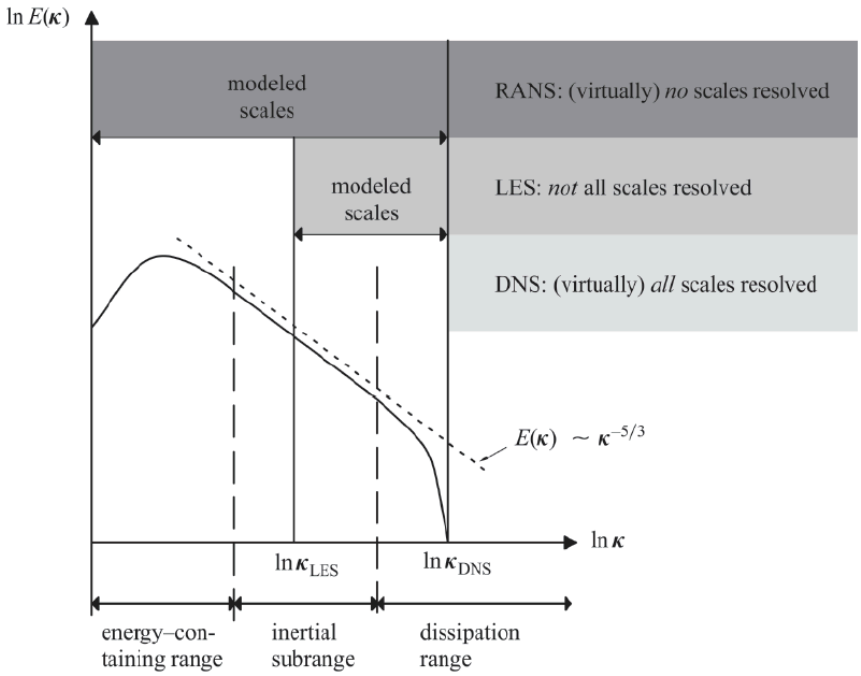

Figure 2.1: Typical energy spectrum of a homogeneous isotropic turbulent flow. The different levels of modeling in the principal methods for simulating turbulent flows are depicted [5].

of resolving from the large and most energetic scales up to the smallest scales of turbulence (Kolmogorov length scales), where the energy dissipation takes place. This implies a cost for the computation which increases as $Re^{9/4}$ for a free flow [47]. To complicate things further, for high Reynolds wall-bounded flows the length scales of turbulence are rapidly decreasing as the wall is approached and an extremely fine mesh is required for the near-wall region [47]. Figure 2.2 shows an estimate of the necessary mesh points to fully resolve the different regions of wall-bounded flows as a function of the Reynolds number [6]. Clearly after a certain limit, the mesh requirements of the inner boundary layer are far superior to those of the outer layer and most of the computational resources will be spent to resolve that region. Turbine flows of interest to this thesis are wall-bounded flows characterized by Reynolds numbers of the order $10^5 - 10^6$, rendering the cost of DNS prohibitive. This approach is indeed still dedicated to the study of academic cases, such as turbulent channels [49] and low-Reynolds, low-pressure turbine cascades [50, 51]. For engineering applications, the development of alternative solutions with some level of turbulence modeling is necessary and gave rise to the following approaches.

- Reynolds Averaged Navier-Stokes (RANS) simulations

The most popular method for computing turbulent flows is to solve the RANS equations combined with a turbulence model for closure of the system of equations [47]. In this approach a Reynolds decomposition of the flow variables is performed to split the averaged and fluctuating components. The resulting system is however unclosed and a

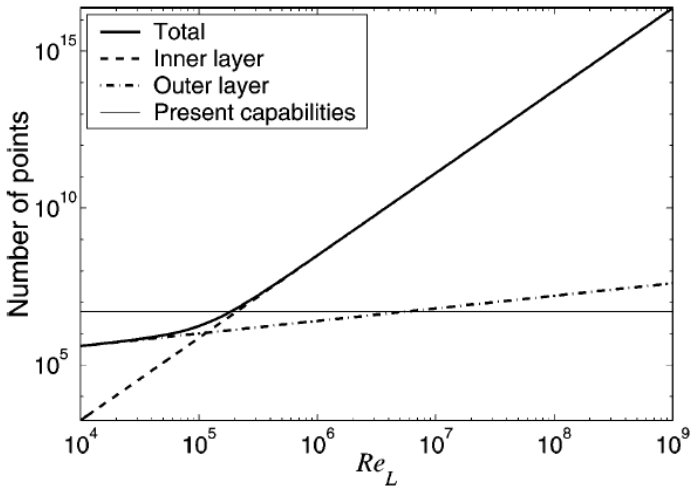

Figure 2.2: Necessary mesh points for the resolution of a turbulent boundary layer as a function of the Reynolds number [6].

turbulence model is employed. This technique is a low-cost, robust solution and is well integrated in the design process of the gas turbine industry. However, the approach requires modeling the entire turbulence spectrum and introduces known weaknesses, such as the validity of the turbulence models in certain flow regimes, which can impact the quality of the predictions [47].

- Large Eddy Simulations (LES)

In LES a spatial filtering of the Navier-Stokes is performed (Appendix A contains more details on the filtering and the resulting equations). As a result, the larger scales of turbulence are explicitly resolved while the smallest ones, that the mesh is not capable of resolving (sub-grid scales), are modeled [52]. The cut-off length of the filter is usually placed in the inertial range of the turbulent spectrum (where the energy spectrum has a constant slope equal to $-5/3$ [47]). This formulation is unsteady and no additional modeling is formally applied for capturing phenomena such as the laminar-to-turbulent transition if a proper grid resolution is guaranteed. These characteristics make LES a very attractive approach for simulating turbulent flows as it can capture more accurately large scale unsteady features, provide access to the turbulence characteristics and alleviate the modeling requirements. The disadvantage of the method lies in its computational cost, much higher than for steady RANS computations [23]. The increasing computational resources however make them more accessible even for relatively high Reynolds number flows. Note nonetheless that LES of wall-bounded flows is not trivial and the formalism is frequently employed with some form of near-wall treatment as detailed below.

2.2 Near-wall treatment

The near-wall flows and boundary layers pose considerable challenges for CFD simulations regardless of the modeling techniques. In the cheaper RANS formalism, typical issues that can be encountered include unphysical near-wall behavior of turbulence models or incompatibility when they are used in conjunction with wall functions. [53].

In LES, where the large turbulent length scales and 80-90% of the turbulent kinetic energy needs to be resolved [54], the changes that turbulence undergoes as the wall is approached create additional difficulties. As mentioned in section 2.1, the turbulent energy-containing length scales decrease rapidly in near wall regions, demanding a significant decrease of the mesh cell size for reliable LES predictions that comply to the requirements [55]. As a result, two different approaches are employed when simulating boundary layers with LES:*a*) wall-resolved and *b*) wall-modelled approaches. [7, 6]

a) In the wall-resolved approach, one attempts to resolve all the scales of the boundary layer and most of the turbulence produced. This implies a mesh resolution where the maximum non-dimensional wall normal distance of the first node off the wall is $y^+ < 1$ [56]. It offers very high accuracy, does not require any further modeling but demands extreme computational resources. Choi and Moin [7] evaluated the cost to scale with $Re^{13/7}$, placing it not far from DNS requirements. Note also that the influence of the SGS model is critical in such simulations, as it needs to be capable to correctly model the near wall turbulence behavior and damping near the walls [57]. Appendix A details the formulation and the properties of some of the most common SGS models.

b) The wall-modeled approach avoids resolving the tiny length scales in the inner boundary layer and the flow gradients at the viscous sublayer. Instead, it models their contribution while resolving only the outer boundary layer, whose length scales are larger. In this case, the first node off the wall is placed in the logarithmic region of the turbulent boundary layer, i.e $y^+ \approx 50 - 100$. There are several ways to model the inner layer (Piomelli and Balaras [6] provide a thorough review of different wall modeling techniques). The most popular is for the wall model to compute the wall shear stress (using flow variables from the LES flow field and a law-of-the-wall, frequently analytical) and pass it to the LES solver. During this work, this is the approach selected to alleviate the computational cost. The problem is locally reformulated into finding the wall friction velocity as:

$$\frac{U}{U^*} = (1/K)ln(E\frac{U^*y}{\nu}). \tag{2.1}$$

In Eq. (2.1), U^* is the wall friction velocity, $K = 0.41$, $E = 9.2$, y is the distance to the nearest wall and ν is the kinematic viscosity of the fluid. The above equation is solved using a simple iterative method and used to express the wall shear stress τ_w using

$$\tau_w = \rho U^{*2}. \tag{2.2}$$

The cost of the wall-modeled approach was calculated in [7] to scale only with Re, highlighting the significant gains compared to the wall-resolved approach (other more

elaborate approaches such as the non-equilibrium model of Park and Moin [58] increase the cost somewhat). Figure 2.3 depicts an estimate of the number of mesh points needed for wall resolved and wall modeled LES as a function of the Reynolds number using Choi and Moin's estimates [7].

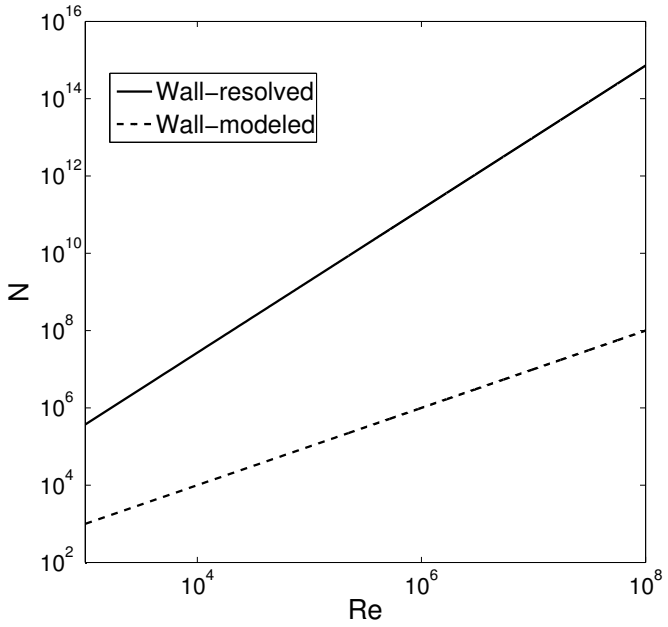

Figure 2.3: Number of mesh points needed for wall resolved and wall modeled LES as a function of the Reynolds number using Choi and Moin's estimates [7].

Wall-modeled LES is however limited in theory to simple flows, i.e fully developed turbulent boundary layers with no streamwise pressure gradient. This near-wall treatment has also been reported as prone to be impacted by the SGS model [59].

2.3 Modeling of the rotor/stator interface

A major difficulty in simulations of turbomachinery stages is located in the solver capacity of handling the interface between the immobile and the rotating blades. As already mentioned in section 1.4, performing unsteady simulations that accurately transfer the flow information between the stator and rotor domains is important for correct aerothermal predictions in both blade rows. However, such simulations pose three significant challenges:

- Number of blades per row:

  In a typical turbomachinery stage, the numbers of stator and rotor blades have no common divisor to prevent resonances between blade rows (usually one blade row has a prime number of blades). As a result, fully unsteady and geometrically

accurate simulations require meshing and simulating the entire 360 degree annulus of the stage [60].

- Necessary simulation time:

  Performing a numerical simulation of a turbomachinery stage requires a long runtime for the convergence of the simulation and the collection of enough data for post-processing. This runtime typically amounts to a few full rotations of the blade row [61].

- Numerical treatment of the interface:

  Transferring information from the stator to the rotor domain and vice versa should not introduce additional numerical errors and the order of the scheme must be in theory preserved.

Simulations that overcome all these difficulties come at a very high computational cost in terms of mesh points, necessary time steps and operations. During the design phase of turbomachinery stages, where a variety of potential geometries needs to be tested, the necessary computational resources and physical time for such simulations becomes prohibitive. These requirements have led to the development of different techniques specifically targeting the problems rotor/stator simulations and offer different levels of compromise between cost and accuracy. Below, the principles of three prominent methods are summarized.

Mixing plane model

This is the most elementary model for rotor/stator interactions developed by Denton and Singh [62] for steady state simulations. In theory it assumes an infinitely long distance between the rotor and the stator (i.e the wakes are perfectly mixed with the freestream flow) so an azimuthal average of the flow variables at the rotor/stator interface is possible. The averaged variables are then imposed as a boundary condition at the interface. This technique is widely used for single or multi-stage simulations. Different variables can be treated at the boundary (such as Riemann invariants or primitive variables) in an effort to ensure that the method is conservative and to avoid reflections from the structures arriving at the interface [63]. Note that more modern versions of the mixing plane method have been proposed that ensure flux conservation and non-reflectivity while retaining some flow variation [64].

The main advantage of this method comes from the fact that this azimuthal averaging process allows the simulation of a whole blade row by just one blade passage, making simulations computationally acceptable even for large multi-stage compressors and turbines. It also does not require long runtimes as only predictions of the time-averaged flow are targeted. The mixing plane model can also be used for flow-field initialization of simulations with more accurate techniques [65]. However, the infinite distance assumption between blade rows is not valid in modern compact turbine and compressor stages. The averaging also makes the method unsuitable for treating unsteady simulations.

Phase-lag method

The phase-lag (also called chorocronic) method [66] is a popular approach for unsteady simulations and has a widespread use in URANS simulations [5]. It is relatively affordable as simulating only one blade passage per row is sufficient. It is based on the hypothesis that the dominant unsteady phenomena are periodic and can be considered as waves spinning with the Blade Passing Frequency (BPF) and its harmonics. The BPF is the frequency at which a rotor, for example, is seeing the passage of a stator wake. It is a function of the rotational speed of the rotor and the number of blades of the neighboring blade row:

$$BPF_{stator} = \frac{N_{rotor}}{2\pi}\omega_{rotor} \quad \text{and} \quad BPF_{rotor} = \frac{N_{stator}}{2\pi}\omega_{rotor}. \tag{2.3}$$

In Eq. (2.3), N is the number of blades per row and ω is the angular velocity of the rotors. The spinning wave assumption implies that a blade passage sees the same flow at its azimuthal periodic boundaries and interface as its neighboring blade but with a time shift noted δt. This permits to simulate the passage of the wakes between blade rows while the domain is reduced to one passage per blade row. Figure 2.4 illustrates how the chorocronic method works in a model turbine stage. In the stator blade row for example, the blade passage located in the azimuthal position $\theta - \frac{2\pi}{N_1}$ sees at a time t the same flow F as its neighboring passage at position θ at a time $t - \delta t$. The time shift is the chorocronic period calculated using the formula:

$$\delta t = \left| \frac{\frac{2\pi}{N_{rotor}} - \frac{2\pi}{N_{stator}}}{\omega_{rotor}} \right|. \tag{2.4}$$

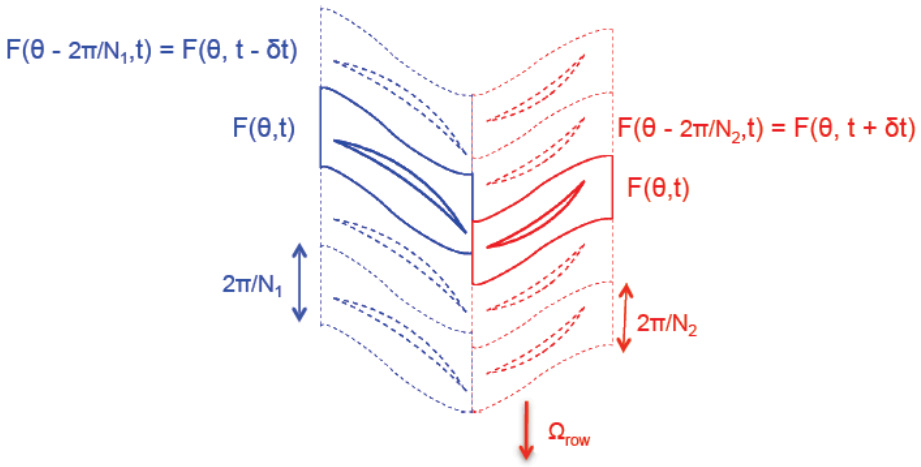

Figure 2.4: Chorocronic boundaries in a model turbine: the neighboring blade passages see the same flow with a time shift [5].

This allows to prescribe at the side boundaries with an angle θ_i and radius r at time t (with the subscript $i = 1, 2$ corresponding to the two azimuthal boundaries) the flow variables F_i from neighboring passages (calculated and stored from previous rotations) simply shifted by the chorocronic period:

$$F_i(x, r, \theta_i, t) = F_i\left(x, r, \theta_i - \frac{2\pi}{Z_i}, t - \delta t\right) = F_i\left(x, r, \theta_i + \frac{2\pi}{Z_i}, t + \delta t\right). \tag{2.5}$$

In theory, information from both past ($-\delta t$) and future ($+\delta t$) is required. In practice, this is achieved by storing the information at the boundaries from previous rotations and using them for the future. A variation of this method, called Shape-Correction (SC), was developed by He [67]. Instead of storing directly the flow variables at the boundaries, the method performs a Fourier decomposition of the signal and stores only their Fourier coefficients, reducing significantly the memory consumption. Multi-stage computations with a wide range of BPF's present is possible through a multi-frequency phase-lag [68]. One drawback of these methods is the relatively long convergence times, with several rotations of the stage being needed before simulations are converged [69]. Another drawback is that it only captures deterministic unsteady phenomena occurring at frequencies similar to the blade passage frequency and its harmonics. This can be very limiting at off-design conditions [45] or when transporting broadband phenomena.

Sliding Mesh method

This approach is the most widely used method for high-fidelity unsteady simulations. The flow variables at the interface are calculated through constant data exchange between the two domains at every time step through interpolation. As a result, a seamless interface is achieved. The method allows for precise simulations of the rotor/stator interactions and has been used extensively [65, 2, 70]. It is capable of capturing phenomena at all frequencies [71, 72] and does not include any of the cost reducing techniques. With the sliding mesh technique simulating one blade passage is not enough and the full 360^o domain is usually required for real turbomachinery stages. Since that would demand massive computer resources, sliding mesh is often complemented by applying the reduced blade count technique to the blade count of one or more blade rows in order to obtain a reduced azimuthally periodic domain.

To achieve this blade count change, the blades are while keeping the section and blade angles similar, thus minimally altering the flow field. Mayorca *et al.* [60] proposed a scaling based on cylindrical coordinates. For this approach, a scaling ratio for each blade row S is first defined:

$$S_{rotor} = \frac{\#\ of\ original\ rotor\ blades}{\#\ of\ scaled\ rotor\ blades}, \tag{2.6}$$

$$S_{stator} = \frac{\#\ of\ original\ stator\ blades}{\#\ of\ scaled\ stator\ blades}. \tag{2.7}$$

The overall scaling ratio is the following:

$$S_{overall} = \frac{S_{rotor}}{S_{stator}}. \tag{2.8}$$

Assuming that the axial direction follows the X coordinate (Y and Z are the other cartesian coordinates), the blades are scaled across the axial and circumferential coordinates (in a cylindrical coordinate system) using:

$$X_{scaled} = X \cdot S_{overall}, \tag{2.9a}$$
$$Y_{scaled} = R \cdot cos(S_{overall} \cdot \theta), \tag{2.9b}$$
$$Z_{scaled} = R \cdot sin(S_{overall} \cdot \theta). \tag{2.9c}$$

where R is the radius and θ the azimuthal angle of a point with cartesian coordinates (X, Y, Z).

Mayorca *et al.* [60] showed that for compressor blades, with reasonable blade count changes, such a scaling does not alter the operating point and averaged flow profiles. These results were further confirmed in [73, 74] for turbine blades. Note that the unsteady flow is impacted as the BPF's are modified and hence the associated unsteady flow dynamics. Additionally, the circumferential scaling has the effect of thickening more the blade towards the casing which may alter the thermal response of the blade.

LES requirements

The sliding mesh approach, being the most accurate and capable of treating broadband phenomena, is the obvious choice for LES of turbine stages. Indeed, it is the method employed in the first LES of compressor stages published in the literature [72, 75]. However, high-fidelity LES have challenging requirements for the rotor/stator interface treatment of the crossing flow features (turbulence, hot-streaks or acoustic waves):

- It should be capable of preserving the global accuracy of the numerical scheme.
- Ensure low dissipation.
- Ensure low dispersion.

The previously published LES of compressors [72, 75], based on codes usually employed for RANS simulations, use the same interface for both formalisms and the compliance to the mentioned requirements has not been established.

In the next chapter, an extension of the sliding mesh approach for the treatment of rotor/stator interactions is presented on the basis of a fully unstructured and hybrid LES flow solver. The objective here is to develop an interface treatment that is compatible with the reactive LES solver AVBP[1] and that is compliant with the guidelines for high-fidelity LES. The selected approach uses overset grids and is validated thoroughly on a series of academic test cases to ensure that it allows for high quality LES of rotor/stator simulations.

[1]The AVBP solver is developed by CERFACS and IFP Energies Nouvelles

Chapter 3

An overset-grid method for the treatment of rotor/stator interactions

Contents

3.1 Numerical schemes for the solution of the Navier-Stokes equations . . 26
3.1.1 Domain Decomposition for standard simulations 27
3.2 Principle of the overset method for rotor/stator interactions 27
3.3 Validation test cases 31
3.3.1 Acoustic waves traveling in a static coupled simulation 32
3.3.2 Convection of a 2D isentropic vortex 34
3.3.3 Turbulent pipe flow 41
3.4 Conclusions 45

The objective of the present chapter is to provide a description and validation of a developed overset grid method for the treatment of rotor/stator interfaces in high-fidelity LES. This approach relies on the reactive unstructured LES solver AVBP [76] and it is intended to comply to the strict requirement for high-fidelity LES, as described in the previous chapter. This chapter has also been the subject of a journal publication [77].

The overset grid method has been proposed in the past by several authors, such as Volkov [78], Magnus and Yoshihara [79], Starius [80], Atta and Vadyak [81], Benek *et. al.* [82, 83], Berger [84], Henshaw and Chesshire [85, 86]. It has recently been studied and applied for Computational AeroAcoustics (CAA) [87, 88, 89], coupling CFD/CAA [90], conjugate heat transfer problems [91], moving body applications [92, 93, 94, 95, 96] or to handle complex geometries with high accuracy [97, 98, 99, 100]. It has also been used in RANS of external and turbomachinery flows where it is commonly known as the Chimera method [82] and reported as providing an equivalent accuracy as the sliding mesh method [101]. In the specific RANS context where fields are smooth and independent of time, conservation is sufficient for the rotor/stator interface since the turbulence is

fully modeled or described by some extra conservation equations towards the steady state solution of the problem. Numerical requirements of RANS are hence limited to the interpolation scheme at the interface meshes that needs to be conservative, which is usually obtained by taking first-order area-based interpolation within the sliding mesh approach [102]. For LES, most of the flow structures are resolved so flow fields are time dependent and contain a large range of wave lengths covering all the scales from the geometry up to the finest local grid resolution. To preserve the quality of such simulations all this information should be transferred through the interface with as less influence as possible to maintain flow coherence, evolution as well as the numerical properties of the scheme. The primary objective is thus to avoid dissipating or dispersing the signal within the original context of the numerical scheme used away from this boundary. To meet such requirements, the overset grid method is of interest as increasing its accuracy is straightforward for structured meshes [103, 104, 105, 99, 90, 88, 98, 87, 97, 106], though it may lead to some complexity in the generation of these overlapping regions [107].

In the following, the overlapping moving interface is implemented based on a domain decomposition approach [108] with an unstructured compressible high-performance parallel LES solver (details are provided later in the chapter). The resulting strategy is hereafter called MISCOG for Multi Instance Solver Coupled through Overlapping Grids and is validated on several cases of increasing complexity. Convergence and numerical errors of the proposed method are first checked on canonical cases with both static and moving coupling interfaces. A specific attention is brought to the dispersive and dissipative errors introduced by the interface treatment. To do so, propagation of acoustic and vortical waves (an isentropic vortex) are considered before introducing the translating interface. The rotating interface is then tested on a three-dimensional turbulent pipe flow. A more realistic application on a turbomachinery stage is detailed in Chapter 4, with the numerical properties of the method exposed hereafter.

3.1 Numerical schemes for the solution of the Navier-Stokes equations

Before introducing the MISCOG method, it is useful to provide some information on the numerical approach of the AVBP solver.

First, the filtered flow equations are rewritten in a compact conservative form:

$$\frac{\partial \mathbf{W}}{\partial t} + \nabla \cdot \mathcal{F} = 0, \tag{3.1}$$

where $\mathbf{W}$ is the vector containing the conservative variables $(\rho, \rho\mathbf{U}, \rho E)^T$ and $\mathcal{F} = (\mathbf{F}, \mathbf{G}, \mathbf{H})^T$ is the flux tensor. For convenience, this flux is usually divided into two components, the convective flux ($\mathcal{F}^C$) and the viscous flux $\mathcal{F}^V$:

$$\mathcal{F} = \mathcal{F}^C(\mathbf{W}) + \mathcal{F}^V(\mathbf{W}, \nabla\mathbf{W}), \tag{3.2}$$

In AVBP, all numerical schemes implemented are expressed in the cell-vertex numerical discretization approach, for its compactness and effectiveness on parallel HPC

machines [76]. The cell-based residuals, *i.e.* the spatially dependent terms of the equations on each control volume Ω_j, are then calculated by integrating the fluxes over the cell as:

$$\mathbb{R}_{\Omega_j} = \frac{1}{V_{\Omega_j}} \int_{\partial\Omega_j} \mathcal{F} \cdot n \, dS, \tag{3.3}$$

where V_{Ω_j} is the cell volume and $\partial\Omega_j$ its boundary with normal vector n. Since the integration is obtained around a vertex, a distributed version of these cell-based residuals $\mathbb{R}_k$ is constructed via distribution matrices. One can hence express Eq. (3.1) into the semi-discrete scheme

$$\frac{d\mathbf{W}_k}{dt} = \mathbb{R}_k = -\frac{1}{V_k} \sum_{j|k\in\Omega_j} D^k_{\Omega_j} V_{\Omega_j} \mathbb{R}_{\Omega_j}, \tag{3.4}$$

where V_k is a control volume associated with a node k and $D^k_{\Omega_j}$ is the distribution matrix that weights the cell residual from the cell center Ω_j to node k [109, 110].

Several numerical schemes are available. Only two of those are presently considered. First, the Lax-Wendroff scheme (LW) is a 2^{nd}-order finite volume scheme in time and space, which corresponds to the accuracy of most commercial codes as well as most of the turbomachinery CFD tools available today [111]. Secondly, the Two-step Taylor-Galerkin finite element scheme TTG4A (4^{th}-order in time and 3^{rd}-order in space) provides improved LES quality on unstructured grids [112].

3.1.1 Domain Decomposition for standard simulations

In static (with stationary mesh elements) parallel computations, the computational domain is divided into several individual vertices-shared partitioned domains each of which is attributed to one processor using Domain Decomposition Methods (DDM) [108]. Figure 3.1(a) illustrates the conventional DDM static coupling process for a cell-vertex scheme. The cells $(\mathbf{L_{1,2}}, \mathbf{R_{1,2}})$ are grouped into two domains respectively denoted by **L** and **R** and contribute to the common node **a** cell residual. Indeed in cell-vertex schemes, the cell-based residuals are computed locally (*i.e.* for all individual cells, $\mathbf{L_{1,2}}, \mathbf{R_{1,2}}$) and scattered to the belonging vertices. Vertex **a** that is located at the interface therefore needs all the contributions from the neighboring partitions for the nodal residual to be evaluated following Eq. (3.4). In conventional approaches of static massively parallel codes, this is simply done through MPI network communications. However, in rotor/stator simulations computing the flow variables at the interface is more complex.

3.2 Principle of the overset method for rotor/stator interactions

The problem for the rotor/stator coupling is similar to the DDM problem described above except that the two domains **L** and **R** are moving (translating or rotating) relatively to

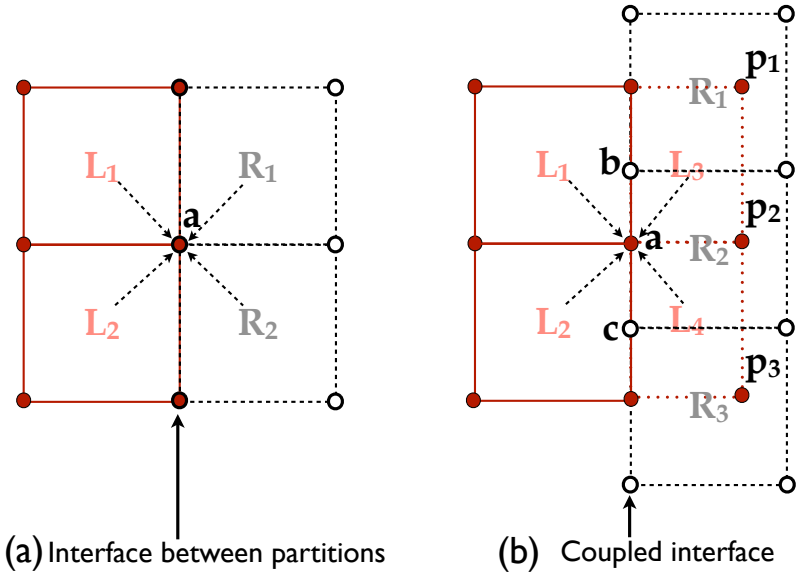

Figure 3.1: (a) DDM for cell-vertex schemes used in parallel computations and (b) the proposed method for rotor/stator interface. $\mathbf{L_{1,2,3,4}}$ (composed of: solid lines - edges and filled symbols for the vertices) and $\mathbf{R_{1,2,3}}$ (composed of: dashed lines - edges and open symbols for vertices) denote the cells on the left and right sides of a partitioned domain, respectively. In the case of a moving fluid boundary, points **a** of domain **L** and points **b**, **c** of domain **R** are the vertices to be coupled at the interface. Points $\mathbf{p_{1,2,3}}$ and $\mathbf{L_{3,4}}$ are additional vertices involved in the coupling when the overlapping method is introduced.

each other. Non-conformal vertices (shown in Fig. 3.1b) are hence present at a given instant and along the interface. Additional evaluations at every iteration are therefore needed if compared with static DDM. Numerically, several coupling methods are possible for such problems, all of which introduce the notion of interpolation for information reconstruction around or on the interface. In the implementation, Lagrange interpolators can be used for exchanging variables following:

$$\mathfrak{L}f = \sum_{i=1}^{n_{sh}} f(q_i)\,\phi_i, \tag{3.5}$$

where f is a function approximated by Lagrange polynomial elements and $f(q_i)$ are the function values at the vertices q_i; n_{sh} is the number of degrees of freedom of the element and ϕ_i are its shape functions. For nodes in an element, the interpolation coefficients are calculated based on the shape functions using the local coordinates of the elements. In the implementation two kinds of interpolation are available:

a) Interpolation using simple linear shape functions, *i.e.* barycentric interpolation or bilinear interpolations using $\mathbb{P}_1$ (triangular in $2D$ and tetrahedral in $3D$) and $\mathbb{Q}_1$ (quad in $2D$ and hexahedral in $3D$ respectively) elements, implying an order 2 for these operations and

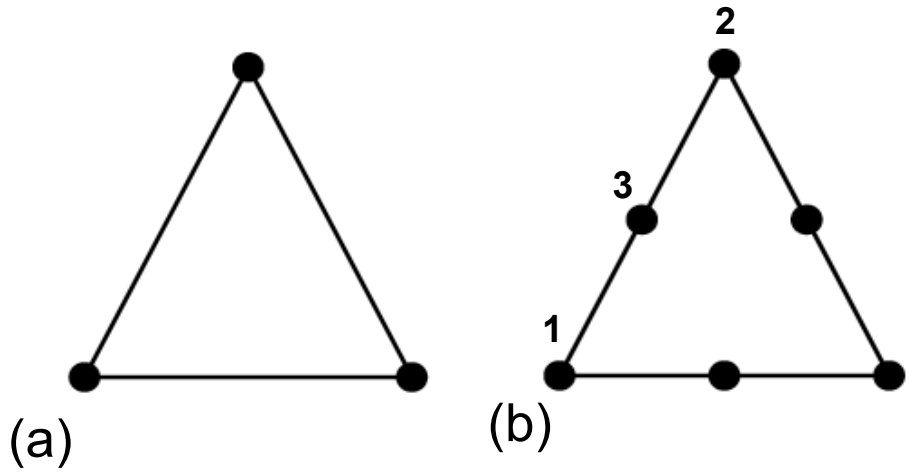

Figure 3.2: Linear (a) and quadratic (b) triangular elements.

b) 3rd order quadratic interpolation for use with the Taylor-Galerkin schemes. For such quadratic interpolation, the classic $\mathbb{P}_1$ elements (Fig. 3.2(a) shows a triangular $\mathbb{P}_1$ element), with the flow variables available only at the element corners, are not sufficient. Instead, $\mathbb{P}_2$ elements, with vertices present at the middle of the element edges are necessary, Fig. 3.2(b). Since most CFD solvers do not support such elements, the flow variables at the extra vertices need to be approximated without deteriorating the order of the interpolation. To ensure a 3rd order approximation in agreement with the high order schemes available in AVBP, Hermite interpolation is employed. For example, the flow variables will be approximated at node 3 in Fig. 3.2(b) using the flow variables from nodes 1 and 2, as well as the gradients of the variables readily available from the CFD solver. In this way a 3rd order interpolation is achieved by use of the corresponding Lagrangian interpolation.

The rotor/stator interface treatment may be introduced at various steps of the numerical scheme. *1*) Coupling fluxes before computing the cell-based residuals of Eq. (3.3) has the benefit of involving only the interface nodes limiting the number of unknowns and potential manipulations. Within such a context, the computed fluxes should be interpolated on the $2D$ coupled interface for a $3D$ computation as performed in the traditional sliding mesh approach for example [102]. *2*) An alternative is to couple nodal residuals. In this approach, each nodal residual $\mathbb{R}_a^L$, $\mathbb{R}_b^R$ and $\mathbb{R}_c^R$ are calculated by counting the contributions of all sub-domain local cells using Eq. (3.4) first. The contributions of each missing domain (*i.e.*: $\mathbf{R}_2$ residual contribution to node $\mathbf{a}$ for example) are then estimated by introducing an additive interpolation $\mathfrak{L}$ to obtain the vertex $\mathbf{a}$ residual at the interface for example,

$$\mathbb{R}_a = \mathbb{R}_a^L + \mathfrak{L}(\mathbb{R}_b^R, \mathbb{R}_c^R). \tag{3.6}$$

Such a scheme was however found to be unstable in the case of a rotating domain coupled to a static domain if using simple linear interpolation schemes. *3*) The last solution,

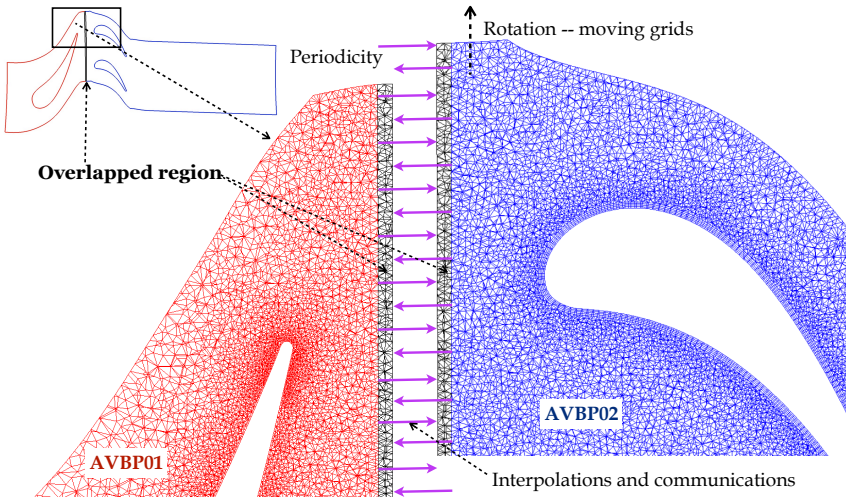

Figure 3.3: Communication framework of coupling rotor/stator interface.

retained in the following, consists in reconstructing the residuals using an overset grid method that directly exchanges the multi-domain conservative variables by interpolation.

To do so, as shown in Fig. 3.1(b), the overset grid approach is introduced by use of an extended domains $\mathbf{L}$, by two $\mathbf{L_{3,4}}$ or more ghost cells in the normal direction of the interface, so that the nodal residual of vertex $\mathbf{a}$ can be computed from available sub-domain cell-based residuals of $\mathbf{L_{1,2,3,4}}$. Note that $\mathbf{L_{1,2,3,4}}$ is obtained using the interpolated conservative variables within the overlap region to evaluate the right-hand side of Eq. (3.3). Note finally that cells $\mathbf{L_{3,4}}$ are geometrically overlapped with the domain $\mathbf{R}$ with points located in cells $\mathbf{R_{1,2,3}}$. In the more generic cases, the extent and topology of the duplicated cells will not coincide. The unknown conservative variables of the overset vertices $\mathbf{p_{1,2,3}}$ are hence approximated through an interpolation from the information of cells $\mathbf{R_{1,2,3}}$. The same procedure is used to compute the nodal residuals of $\mathbf{b}, \mathbf{c}$ in domain $\mathbf{R}$ that is also extended onto mesh $\mathbf{L}$ by two or more cells, since it is a two-way coupling.

This third approach is selected here as it is easily implemented externally from any base CFD code and yields high-order accuracy if used in conjunction with high order interpolation [90, 97, 98, 113, 88, 106]. In terms of methodology and overall strategy, the external code coupling is preferred over an internal implementation to extend the available LES solver so that it can deal with rotor/stator simulations. Hence two or more copies of the same LES solver (namely AVBP) each with its own computational domain and static DDM algorithm executing a given partitioning with a given target number of processes, are coupled through the parallel coupler OpenPALM [114]. The detailed implementation of such coupling includes: (1) find the enclosed cell; (2) calculate the local coordinates in the cell; (3) calculate the interpolation coefficients using a shape function; (4) calculate the interpolated value using Eq. (3.5). The current implementation [114] is compatible with the CGNS interpolation tool [115] and is external to the CFD code.

Figure 3.3 shows a typical communication framework for a rotor/stator coupling approach using the MISCOG method described above. For this case, the whole flow domain

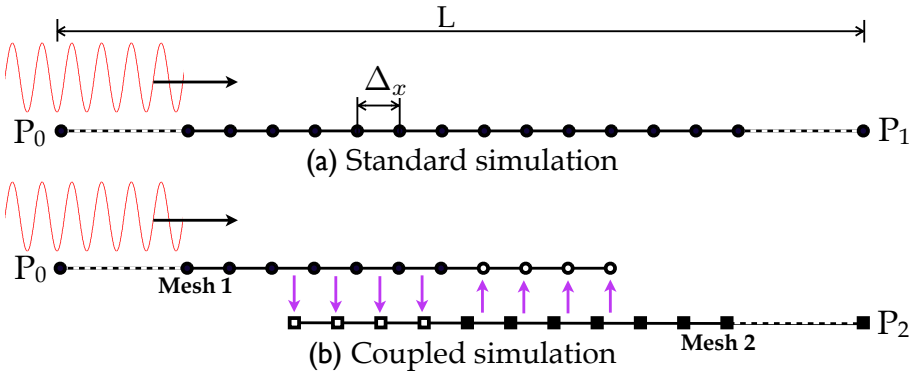

Figure 3.4: $1D$ acoustic wave propagation simulated by two approaches: (a) the stand-alone solver and (b) the equivalent coupled approach. The total length of the computational domain is L and the cell size is Δ_x.

should initially be divided into static (AVBP01) and rotating parts (AVBP02). For rotating parts, the code uses the moving-mesh ALE approach in the absolute frame of reference while the remaining unit simulates the flow in the stationary part in the same coordinate system [116]. The interfaces between the two units involving rotating and non-rotating parts are coupled with the overset grids by interpolating and then exchanging the conservative variables wherever needed and as described above. To do so, an efficient distributed search algorithm is implemented in the coupler OpenPALM to locate the points in parallel partitioned mesh blocks. This coupling algorithm will then update at each time step the information and carry the interpolation from one sub-MPI world to the next and vice-versa. Issues of numerical stability of the coupled solution and the convergence of this coupled problem are directly linked to the size of the overlapped region and the stencil of the numerical schemes selected [23].

3.3 Validation test cases

Before applying the described methodology in a realistic turbine stage, it is validated on a series of canonical cases. These cases are characterized by different levels of complexity and include both static and moving coupling interfaces for a comprehensive validation. Convergence and numerical errors of the proposed method are evaluated, as well as the dispersion and dissipation introduced by the interface treatment. Propagation of acoustic and vortical waves (an isentropic vortex) is first considered before introducing the translating interface. The rotating interface is then tested on a three-dimensional turbulent pipe flow. It is worth noting that other test cases have been performed but are not presented in this section. They can be found in the corresponding journal publication [77], included in this dissertation in Appendix D.

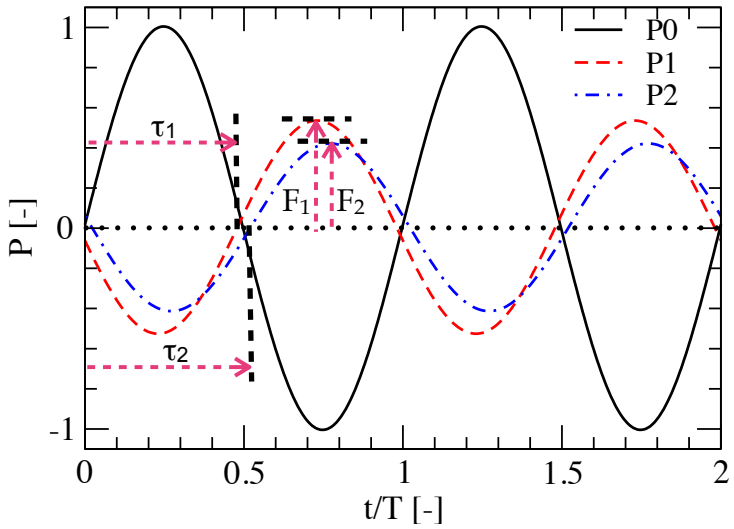

Figure 3.5: Inlet wave signal (P0) and signals at the downstream probe for the standard simulation (P1) and the coupled simulation (P2) as a function of time t normalized by the period T (mesh resolution of $\Delta x/\lambda = 0.125$ and LW scheme). Definitions of the gain factor F and phase-shift τ.

3.3.1 Acoustic waves traveling in a static coupled simulation

An accurate compressible LES should first transport acoustic waves properly. The first validation case is therefore the simple problem of a $1D$ propagating acoustic wave (Euler equation) in a domain whose boundary conditions are non-reflective, the acoustic signal covering the entire computational domain. Figure 3.4 illustrates the configuration for the reference and coupled simulations. In the latter, two overlapping $1D$ meshes are computationally communicating using MISCOG with the 2nd order linear interpolation. In the overlapped region, the meshes are non-coincident and the vertices from one mesh are located at the center of the corresponding cell in the other mesh so that interpolation errors are maximized. The conservative variables over several layers of nodes (1 to 5) on each side are coupled and will be updated based on the interpolated values of the other mesh at each time step.

The incoming acoustic wave is imposed at the left side boundary of the domain, Fig. 3.4, using the Inlet Wave Modulation (IWM) approach [117], which is equivalent to modulating the target velocity at the inlet as:

$$u_{inlet} = U_0 + \frac{P^A}{\rho_0 c_0} sin(2\pi f t). \tag{3.7}$$

The amplitude of the pressure perturbation is $P^A = 100\ Pa$. The temporal frequency is $f = 1000\ Hz$. A zero mean flow velocity is set ($U_0 = 0$), and the density $\rho_0 = 1.172\ kg/m^3$ and sound speed $c_0 = 347.469\ m/s$ of the mean flow correspond to atmospheric conditions. Navier-Stokes Characteristic Boundary Conditions (NSCBC) are used at both

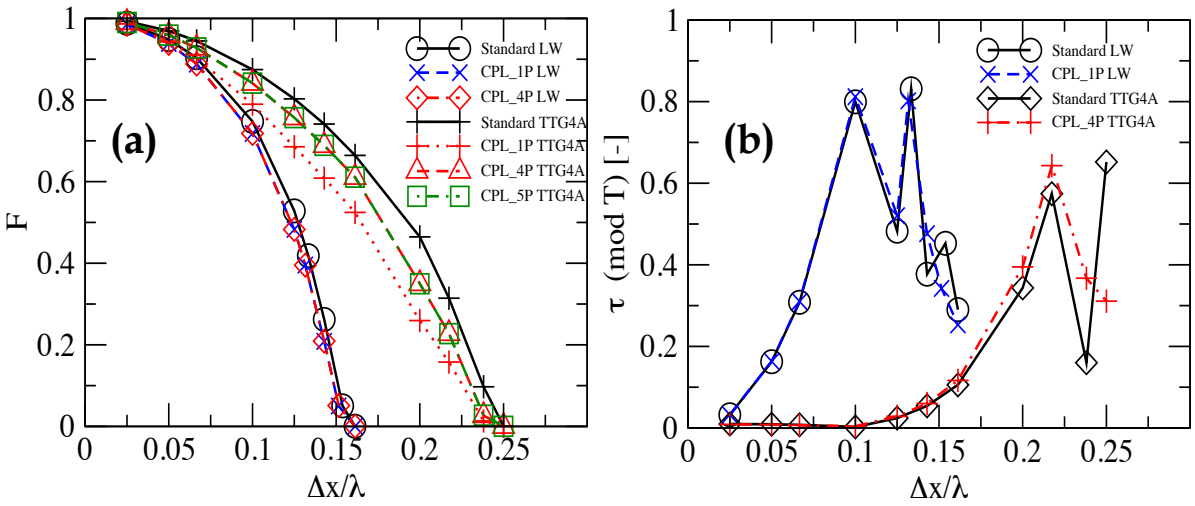

Figure 3.6: The gain factor F (a) and phase-shift τ (b) errors for both standard and coupled simulations. 1P indicates one overlapping cell, 4P four and 5P five overlapping cells each side of the interface.

inlet and outlet boundaries to prevent wave reflections [118]. The total length L of the computational domain is chosen to be 10 times the selected wave length, $\lambda = c_0/f$, which is then discretized by different mesh resolutions, $\Delta_x \in [\lambda/40, \lambda/4]$. To focus on the spatial discretization error, the time steps of all cases are set to a very small physical value $\Delta t = 6\ ms$, which corresponds to a Courant-Friedrichs-Lewy (CFL) number of 0.2 for the finest mesh ($\Delta_x = \lambda/40$) and 0.02 for the coarsest mesh ($\Delta_x = \lambda/4$). The two numerical schemes (LW and TTG4A) presented above are tested here.

Figure 3.5 shows the temporal evolution of this flow solution obtained with LW. The inlet wave signal (P_0) is compared with the outlet probed signal for the two different approaches (P_1 for the standalone computation and P_2 for the coupled one). Only two wave periods of the input signals are taken for a mesh resolution $\Delta_x = \lambda/8$. In the exact solution to such a problem the sine wave should be preserved and only a delay of $\tau_{ex} = L/c$ should be present at all frequencies. A gain factor F and a phase-difference τ between inlet and outlet signals are introduced for all simulations to assess the differences with this exact solution. The results of the standalone simulations then provide the dissipative and dispersive properties of the selected scheme. When comparing with the results of the coupled simulations, the additional contribution of the coupling scheme and particularly the effect of the interpolation can be assessed. Figure 3.6 quantifies both errors illustrated in Fig. 3.5. In Fig. 3.6(a), for large numbers of points per wave-length, all schemes show a small level of dissipation: the gain factor approaches unity in all cases as $\Delta x/\lambda$ decreases confirming the convergence of the discretized system (with or without interpolation). It also shows that dissipation increases as the number of points per wave-length decreases; F is almost vanishing when the mesh resolution is poor: $\Delta x/\lambda = 0.16$ for LW and

$\Delta x/\lambda = 0.25$ for TTG4A stressing the superiority of the Taylor-Galerkin schemes for compressible LES [119, 109]. Several coupled computations with varying numbers of overlapping points N_o are also shown in Fig. 3.6(a) ($N_o = 1, 4, 5$), to find its optimal value for both numerical schemes. Only one overlapped cell on each side is required for LW as confirmed by theoretical and numerical analyses [23]. Using one or four overlapped cells also yields very similar results. For TTG4A, four overlapping nodes are needed to cover the full stencil at the interface. As shown in Fig. 3.6(a) adding a fifth point on either side of the overlapped interface does not improve the gain factor curve, since it does not appear in the stencil. Figure 3.6(b) shows the phase errors for standard and coupled simulations. The curves indicate that interpolation does impact the results mainly at very poorly resolved scales.

All these results are consistent with conventional analysis of numerical schemes designed for LES and confirm that the proposed rotor/stator interface treatment meets LES requirements provided that the uncoupled discretization scheme is of high order to minimize numerical dispersion and dissipation. This desired result is however obtained only if used with a sufficient number of overlapping points. Results also confirm that the interface treatment comes with an increased dissipation at all resolutions. Increased dispersion appears mainly for poorly resolved wave lengths.

3.3.2 Convection of a 2D isentropic vortex

Accurate compressible LES also relies on the model and solver ability to resolve and transport vortices within a complex geometry. The second validation case is specifically chosen to address the ability of the proposed solution to resolve a $2D$ vortex traveling through the overlapped interface using Euler equations. The numerical setups are given in Fig. 3.7. The standard reference case, Fig. 3.7(a), has a single mesh composed of $2N_x \times N_x$ quad cells of size $\Delta_x = 20R_c/N_x$, where R_c is the radius of the vortex, covering a rectangular (x,y) domain of dimensions $[-20R_c, +20R_c] \times [-10R_c, +10R_c]$. For the coupled cases, two computational domains are provided in Figs. 3.7(b) and (c), and consist of two rectangular boxes with an overlapped region for which N_o points are present on each side of the interface. The first box covers a domain of $[-20R_c, N_o\Delta_x] \times [-10R_c, +10R_c]$ and is meshed with $(N_x + N_o) \times N_x$ quad cells (indicated as **Mesh A** in Fig. 3.7). The second box covers $[-N_o\Delta_x + \Delta_x/2, +20R_c] \times [-10R_c, +10R_c]$ and has $(N_x + N_o) \times (N_x + 1)$ quad cells (indicated as **Mesh B** in Fig. 3.7). Similarly to the first test case, the overlapped vertices are located at the center of the quad cells of the other mesh. Two types of coupled simulations are conducted: (1) a static coupling; (2) a coupling with a translating interface in which the second coupled mesh is periodically translating in the vertical direction in Fig. 3.7, at a constant speed of 100, 200 and 300 m/s (typical rotating speeds of relevant turbomachinery applications). NSCBC are used again at both inlet at outlet boundaries to avoid wave reflections. To prevent any problems from the domain boundaries, all lateral surfaces are set to be periodic. The simpler second order interpolation is employed for the data exchange between the domains.

An initial isotropic vortex [118, 120, 119] is imposed on a uniform mean flow going

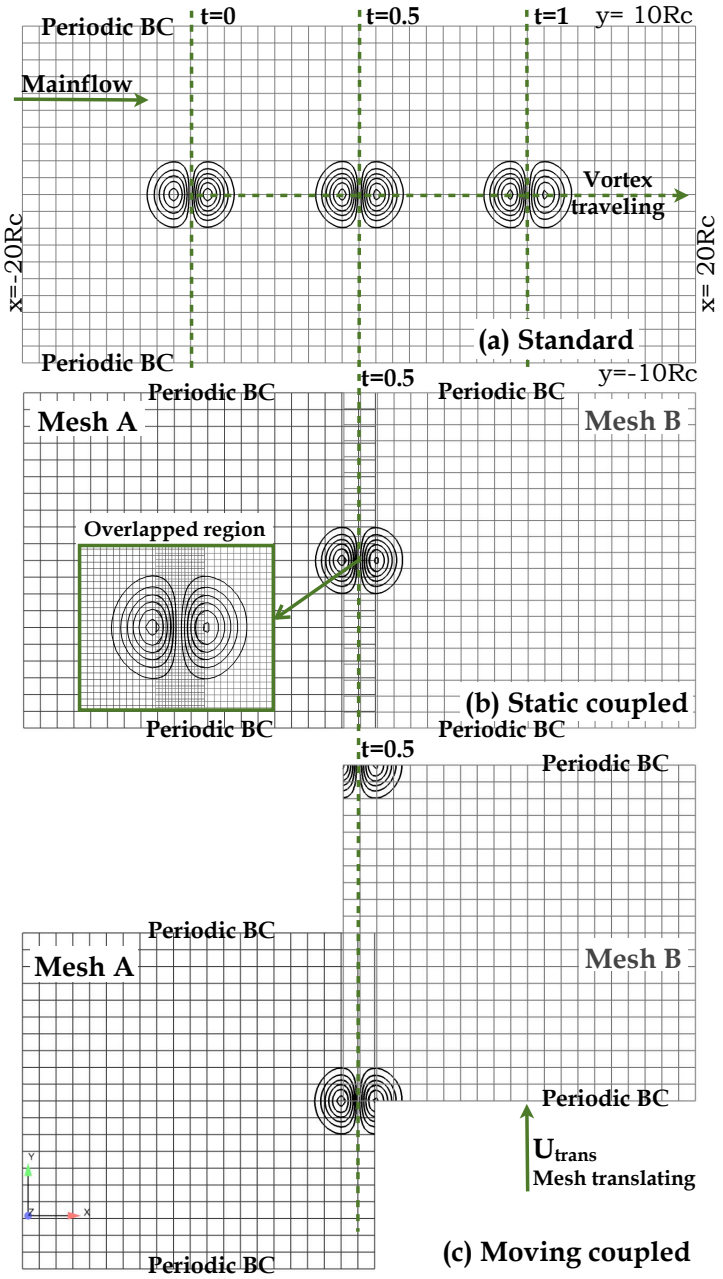

Figure 3.7: Schematic of standard and coupled simulations of vortex traveling: (a) Standard case; (b) Static coupled case (c) Moving coupled case: similar mesh sizes as the previous coupled case, except that mesh B is translating at speed of u_{trans}=100, 200 or 300 m/s. The mesh size is $\Delta_x = R_c/4$ with $N_x = 80$ and $N_o = 4$ (only one-fourth of grid points are shown). The inviscid vortex (with radius R_c), shown by isolines of lateral velocity, is initialized at time $t = 0$ and is traveling from left to right and passing through the interface ($t = 0.5$). Time t is normalized by the vortex convection time over travel distance, $20R_c/U_0$.

from left to right. It is based on the stream function

$$\Psi(x,y) = \Gamma e^{-r^2/2R_c^2}, \tag{3.8}$$

where Γ is the vortex strength and $r = \sqrt{(x-x_c)^2 + (y-y_c)^2}$ the geometric distance to the vortex center (x_c, y_c), initially located at $x_c = -10\ R_c$ and $y_c = 0$. R_c controls the size of the vortex. The resulting velocity and pressure fields simply read

$$\mathrm{u} = U_0 + \frac{\partial \Psi}{\partial y} = U_0 - \frac{\Gamma}{R_c^2}(y-y_c)e^{-r^2/2R_c^2} \tag{3.9a}$$

$$\mathrm{v} = -\frac{\partial \Psi}{\partial x} = \frac{\Gamma}{R_c^2}(x-x_c)e^{-r^2/2R_c^2} \tag{3.9b}$$

$$P = P_0 - \frac{\rho\Gamma^2}{2R_c^2}e^{-r^2/R_c^2}. \tag{3.9c}$$

where P_0 and U_0 stand for the reference background pressure field and flow velocity respectively. For the present simulations the different parameters are $R_c = 0.01556$ m, $P_0 = 101,300$ Pa, $\rho = 1.172$ kg/m^3 and a constant uniform flow $U_0 = 100$ m/s. Three levels of vortex strength $\Gamma = 0.036, 0.1$ and 0.5 m^2/s are chosen leading to velocity fluctuations $\mathrm{u}'_{max} = \mathrm{v}'_{max} = 1.4, 3.9$ and 19.4 m/s and pressure fluctuations $P'_{max} = 3.1, 24.1$ and 601.8 Pa respectively. The time steps are chosen to yield CFL= 0.07 to minimize temporal effects. Additional simulations are obtained for CFL= 0.7 as recommended for TTG4A [110].

Predictions for CFL= 0.07 are shown in Fig. 3.7 for the three simulation setups. In Fig. 3.7(a), the initial vortex evidenced by isolines of the transverse velocity component is convected with time by the main flow from left to right in the standalone setup. In Fig. 3.7(b) & (c) for the static and moving mesh respectively, the vortex has reached the center of the coupling interface. As evidenced by the isolines, the vortex is well preserved in the coupled cases even when it crosses the coupling interfaces.

Numerical convergence of the proposed coupled strategy is then addressed based on different mesh resolutions (N_x from 20 to 200), using both the LW and TTG4A schemes, with the quadratic mean errors of the instantaneous pressure field P (most sensitive variable)

$$L_2(P) = \|\epsilon_P\|_2 = \left[\sum V_i(\epsilon_{P,i})^2\right]^{1/2} \tag{3.10}$$

and the maximum error

$$L_\infty(P) = \|\epsilon_P\|_\infty = \max\left[|\epsilon_{P,i}|\right], \tag{3.11}$$

where $\epsilon_{P,i}$ is the difference between the nodal value of the analytical pressure field and the scheme value, and V_i is the area of the cell. The analytical fields are given by Eq.(3.9c) with the vortex center advected to the anticipated positions. Figures 3.8 and 3.9 show $L_2(P)$ and $L_\infty(P)$ curves as a function of the grid resolution at three dimensionless instants $t = 0.25$, 0.5 and 1, when the vortex is convected from the initial

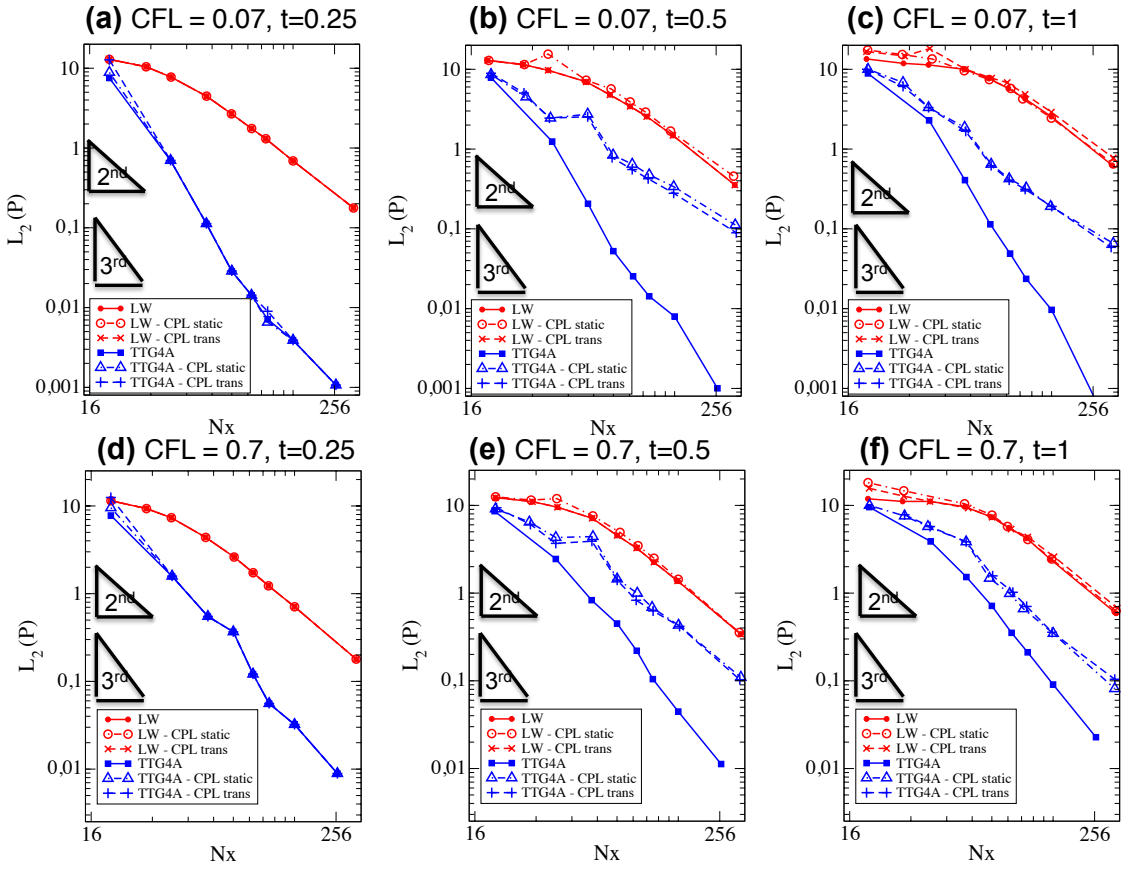

Figure 3.8: The quadratic mean errors of instantaneous pressure fields $L_2(P)$ versus mesh resolution N_x for different cases using the LW or TTG4A schemes. The pressure profiles are compared with the analytic profiles when the vortex reaches upstream of the interface ($t = 0.25$), the interface ($t = 0.5$) and the downstream of the interface ($t = 1$). The computations are using two sets of time steps with CFL= 0.07 (top) and CFL= 0.7 (bottom). The translation speeds for the translating coupled cases is $U_{trans} = 200$ m/s.

position $x = -10\,R_c$ at $t = 0$, to the positions $x = -5\,R_c$ (upstream of the interface) at $t = 0.25$, $x = 0$ (crossing the interface) at $t = 0.5$, and $x = 10\,R_c$ (downstream of the interface) at $t = 1$.

In Fig. 3.8(a), convergence at $t = 0.25$ is first checked for the small CFL number of 0.07. There are two sets of convergence plots with two different slopes, only depending on the numerical schemes. The coupled cases have the same errors as the standard one. As expected, simulations using LW recover the scheme 2^{nd}-order spatial accuracy, while simulations using TTG4A reaches a 3^{rd}-order accuracy or slightly above. In Fig. 3.8(b), convergence results are given at $t = 0.5$, when the vortex has reached the interface. In the coupled cases, all static and translating ($U_{trans} = 200$ m/s) have similar error levels and slopes for the LW, while the TTG4A cases demonstrate an increase of the error. Only a 2^{nd}-order spatial accuracy is ensured for both the LW and TTG4A simulations

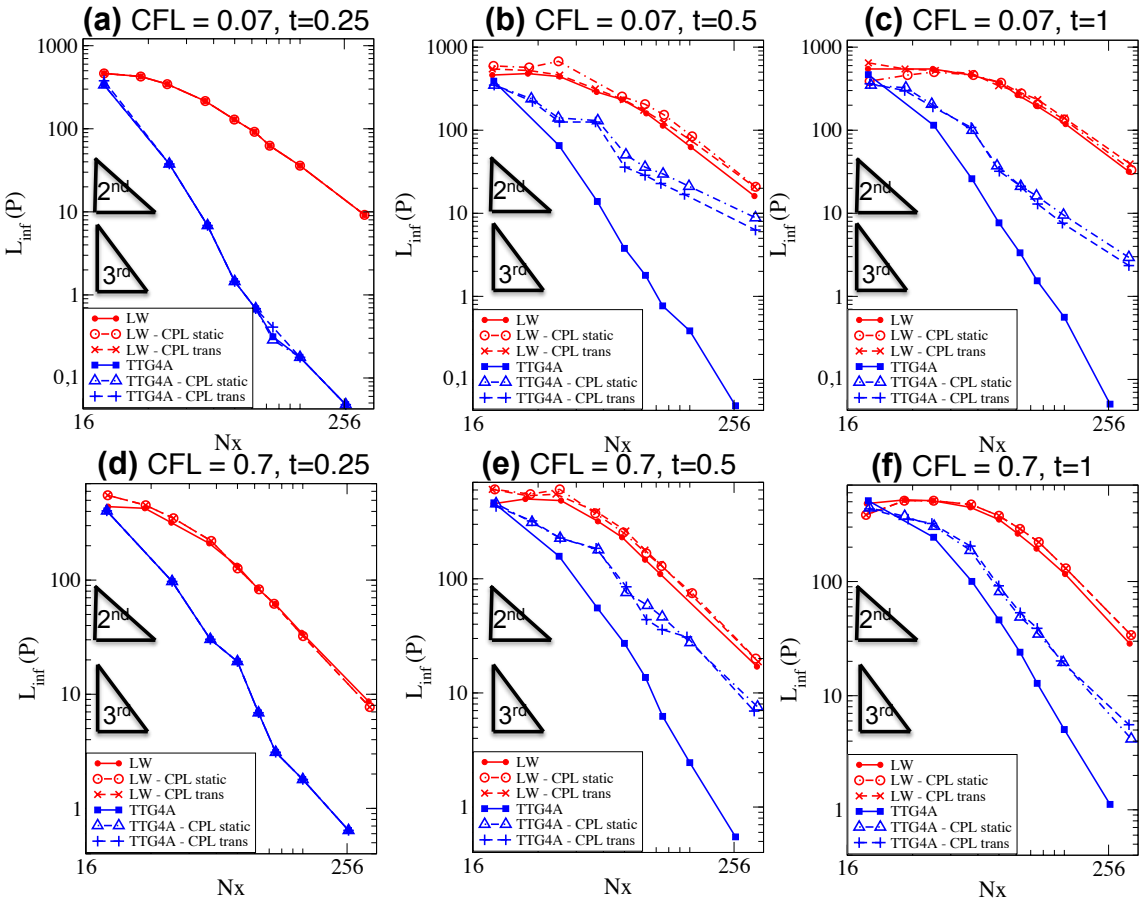

Figure 3.9: The maximum errors of instantaneous pressure fields $L_\infty(P)$ versus mesh resolution N_x for different cases using the LW or TTG4A schemes. The pressure profiles are compared with the analytic profiles when the vortex reaches upstream of the interface ($t = 0.25$), the interface ($t = 0.5$) and the downstream of the interface ($t = 1$). The computations are using two sets of time steps with CFL= 0.07 (top) and CFL= 0.7 (bottom). The translation speeds for the translating coupled cases is $U_{trans} = 200$ m/s.

respectively. This discrepancy, as will be shown in the next section, is due to the linear interpolation employed here. However, coupled simulations with TTG4A are almost an order of magnitude more precise than the coupled LW for any given grid resolution, as already evidenced in the above $1D$ test case. In Fig. 3.8(c), at $t = 1$, as before the 2^{nd}-order spatial accuracy for the two schemes are still recovered, even though the vortex has traveled $10R_c$ downstream the interface. Again, the mesh-translating coupled cases have similar error levels as the static ones. Figures 3.8(d)-(f) show the same converged results for CFL=0.7. The error levels have slightly increased due to what is perceived to come from the additional temporal error. All coupled cases again exhibit 2^{nd}-order accuracy for both LW and TTG4A (Figs. 3.8(e) and (f)). The translating coupled cases also have similar convergence rates as the static ones. The convergence of the maximum error (L_∞), presented in Fig. 3.9, is following the same trends as the quadratic mean errors.

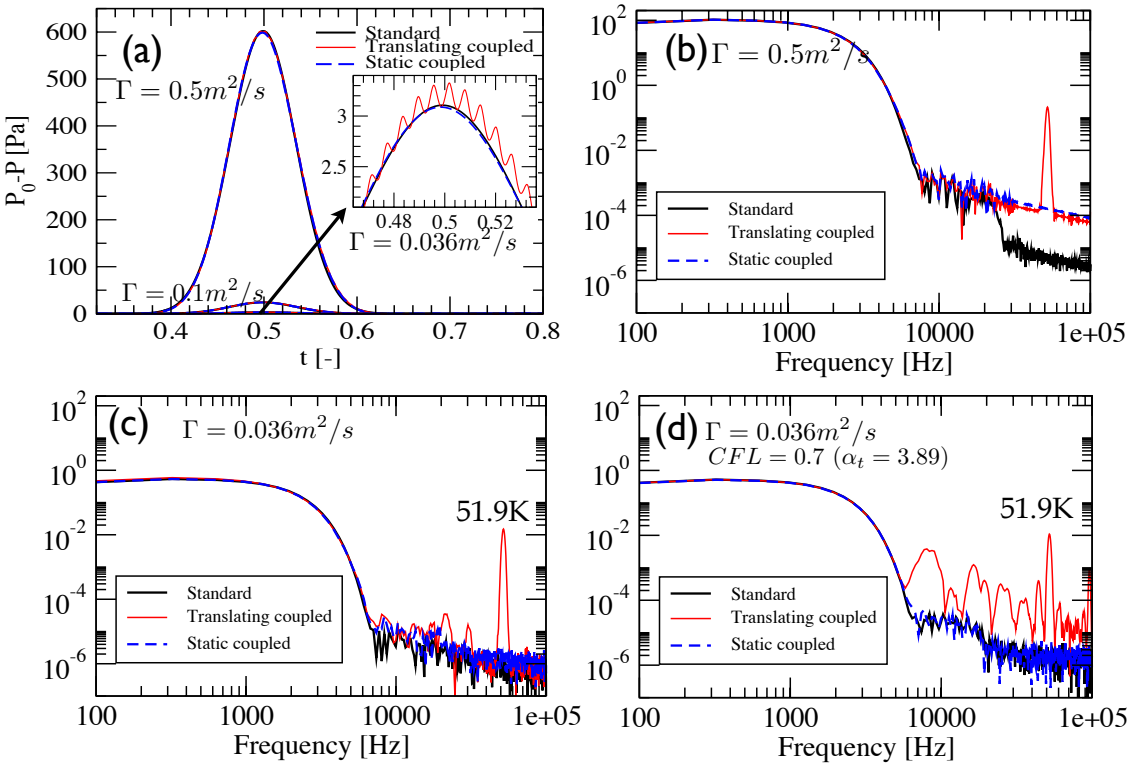

Figure 3.10: Temporal evolutions of pressure signals at the central position (0,0) of interface for different vortex intensities (top: $\Gamma = 0.5$ m^2/s; bottom: $\Gamma = 0.036$ m^2/s) in standard, static coupled and translating ($U_{trans} = 200$ m/s) coupled cases. Time traces (a) and spectra (b)-(c) for CFL=0.07. (d) Spectra for CFL=0.7.

Only the level of the error has changed, reflecting the difference on the computation of the norm.

Temporal evolution of the above simulations is now considered to assess the spurious errors introduced at every time step by the moving coupled domains. The following mesh resolution is chosen: $N_x = 80$ ($\Delta_x = R_c/4 = 3.89$ mm). Figures 3.10 show the time traces of the pressure signals monitored at the middle point of the overall computational domain for different vortex strengths. Figure 3.10(a) stresses that all temporal signals agree well with the standard simulation for a CFL of 0.07. Only high-frequency pressure fluctuations are introduced by the translating interface as evidenced in the zoom of the plot. When a standard FFT of the signal is performed in Figs. 3.10(b) and (c), these spurious oscillations are identified by a tone around 51.9 kHz independent of the vortex strengths and the coupling only introduces this additional high-frequency noise. When the CFL is increased to 0.7 in Fig. 3.10(d), the same conclusions can be drawn for all vortex strengths, except that additional humps appear around the tone.

The vortex strength is then set to $\Gamma = 0.5$ m^2/s. The pressure spectra are presented for different translating speeds $U_{trans} = 100, 200$ and 300 m/s in Fig. 3.11(a) and for different mesh sizes Δ_x in Fig. 3.11(b), all cases being summarized in Table 3.1. The

Table 3.1: Frequency f_{trans} of pressure signal spectra in translating coupled cases with different mesh sizes Δx and translating speeds U_{trans}.

Δx [mm]	U_{trans} [m/s]	f_{trans} [kHz]	$S_{trans} = \frac{f_{trans}\Delta x}{U_{trans}}$
3.8900	100	25.9	1.0075
3.8900	200	51.9	1.0095
3.8900	300	77.8	1.0088
2.5933	200	77.8	1.0088
1.9450	200	103.8	1.0094

frequencies of the spurious oscillations are clearly proportional to the translating speed and inversely proportional to the mesh size, as confirmed by the non-dimensional ratio or equivalent Strouhal number obtained as the ratio between these three parameters

$$S_{trans} = \frac{f_{trans} U_{trans}}{\Delta_x} = 1.0 \quad . \tag{3.12}$$

Interpolation error is indeed fluctuating in time as the position of donor cells evolves with time. The level of this numerical noise is however two orders of magnitude smaller than the main vortex signal and can be considered negligible as long as it does not interfere with LES resolved large-scale motions. Moreover, this high frequency noise decreases rapidly away from the middle point as shown in Fig. 3.11(c) and is higher than the typical frequencies of combustion and turbomachinery noise of interest. Finally, Fig. 3.11(d) clearly shows that the additional humps observed in Fig. 3.10(d) are related to the ratio of the translation period T_{trans} to the timestep Δt

$$\alpha_t = \frac{T_{trans}}{\Delta t} = \frac{\Delta_x / U_{trans}}{CFL \cdot \Delta_x / (U_0 + c_0)} \quad . \tag{3.13}$$

First, large values of α_t lead to less spurious frequency bands in the pressure spectra, and when T_{trans} is well resolved by the time step, only the peak translating frequency at 51.9 kHz can be seen. Secondly, poor sampling of T_{trans} leads to aliasing frequencies [121, 23].

Impact of the interpolation scheme

To verify the impact of the interpolation scheme on the order of accuracy of the coupling approach, the cases of Figs. 3.8 and 3.9 are recomputed with the 3$^{\text{rd}}$-order interpolation method. The quadratic mean and maximum error convergence plots are presented in Figs. 3.12 and 3.13 respectively. At $t = 0.25$, with the vortex not having reached the interface, results are similar as with the linear interpolation. Two sets of convergence plots with two different slopes are recovered, corresponding to the 2$^{\text{nd}}$ and 3$^{\text{rd}}$-order of accuracy of the two numerical schemes. However and in contrast to the simulations with linear interpolation, these different slopes are recovered at times $t = 0.5$ and $t = 1$ as

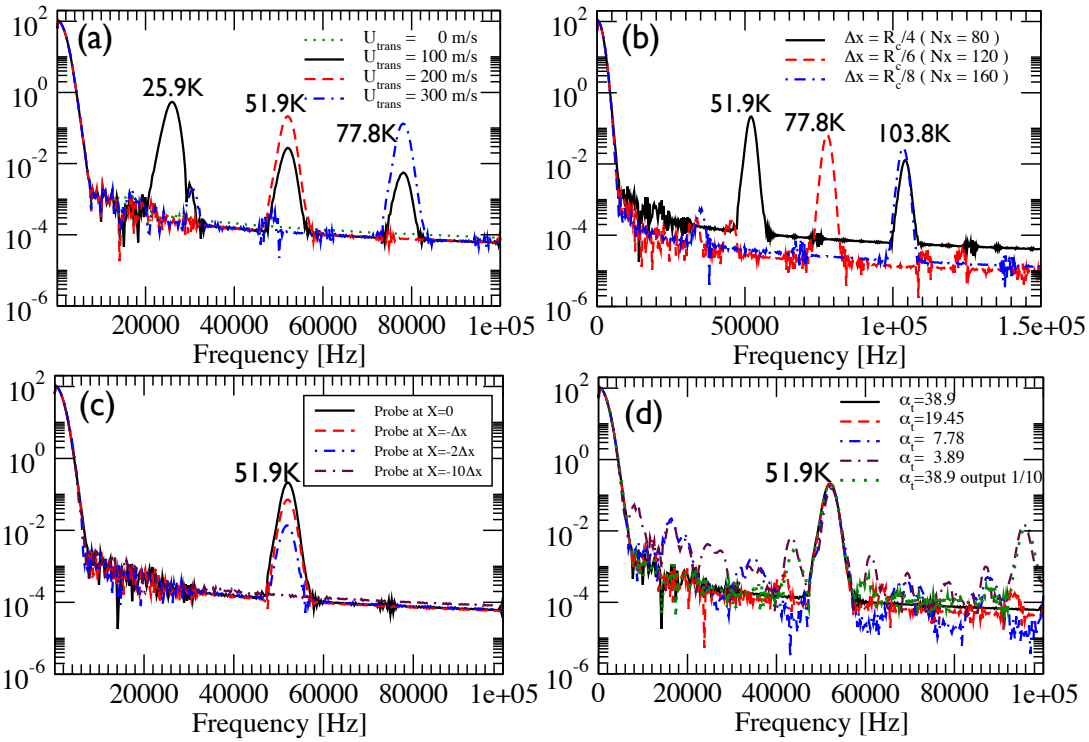

Figure 3.11: Spectra of pressure signals at the central position (0,0) of interface in translating coupled cases (CFL= 0.07; vortex intensity $\Gamma = 0.5$): (a) with different translating speeds, $U_{trans} = 100$, 200 and 300 m/s and mesh size $\Delta x = R_c/4$; (b) with different mesh sizes, $\Delta x = R_c/4$, $R_c/6$ and $R_c/8$ for a translating speed $U_{trans} = 200$ m/s; (c) at different monitoring positions for a translating speed $U_{trans} = 200$ m/s; (d) using different time ratios $\alpha_t = 38.9$, 19.45, 7.78 and 3.89.

well. While the LW simulations are not impacted, the 3$^{\text{rd}}$-order interpolation is indeed shown to be capable of preserving the order of the TTG4A scheme and a similar spatial accuracy is recovered between the standalone and coupled simulations.

These results naturally highlight that high-order schemes require high-order interpolation methods. Otherwise the rotor/stator interface can locally impact the crossing structures and reduce the order of the scheme. It is therefore clear that the interpolation should be at least of similar order as the numerical scheme to ensure minimum impact on the rotor/stator interactions, as anticipated.

3.3.3 Turbulent pipe flow

The third validation case is a three-dimensional cylindrical fully turbulent pipe flow. The set-up of the case is depicted in Fig. 3.14. The reference AVBP case consists of a single cylindrical pipe of length $L = 0.015\ m$ and radius $r_0 = 0.1\ L$. The coupled case consists of two pipes of equal length $L_1 = 0.00771\ m$ coupled using the MISCOG method. They are placed in such a way to keep the overall length of the case equal to L, thus forming

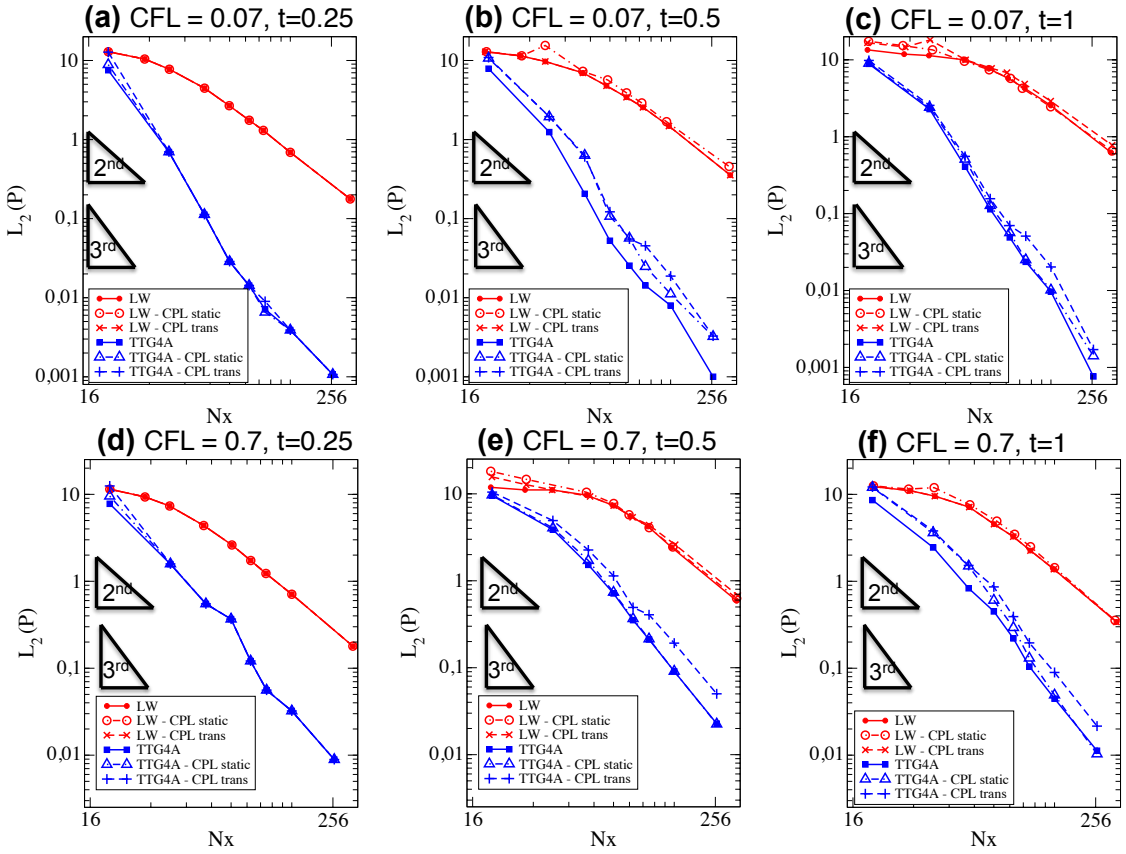

Figure 3.12: The quadratic mean errors of instantaneous pressure fields $L_2(P)$ versus mesh resolution N_x for different cases using the LW or TTG4A schemes using 3$^{\text{rd}}$-order interpolation. The pressure profiles are compared with the analytic profiles when the vortex reaches upstream of the interface ($t = 0.25$), the interface ($t = 0.5$) and the downstream of the interface ($t = 1$). The computations are using two sets of time steps with CFL= 0.07 (top) and CFL= 0.7 (bottom). The translation speeds for the translating coupled cases is $U_{trans} = 200$ m/s.

an overlap zone of 0.42 mm. The flow is coming from the left of AVBP01 and exiting from the right of AVBP02. Mesh rotation (at a constant speed of 9500 rpm), as used in typical turbomachinery simulations, is introduced in the second domain of the coupled case to evaluate any potential impact on the information crossing the interface. The wall boundary condition is not rotating so no impact from the mesh rotation should be visible in the flow.

The mesh employed is homogeneous, composed of tetrahedral cells of characteristic size $\delta = 0.1$ mm. The total mesh size is approximately 600k cells for the standard AVBP case and 310k cells per domain for the coupled case, with the extra cells accounting for the overlap zone. No mesh refinement is imposed near the walls as accurately resolving the boundary layer is beyond the scope of this test case. The bulk velocity targeted is $U_{bulk} = 100m/s$, resulting in a Reynolds number at 300 K equal to $Re = 20,000$. To achieve the desired bulk velocity and to approximate a realistic turbulent velocity inflow

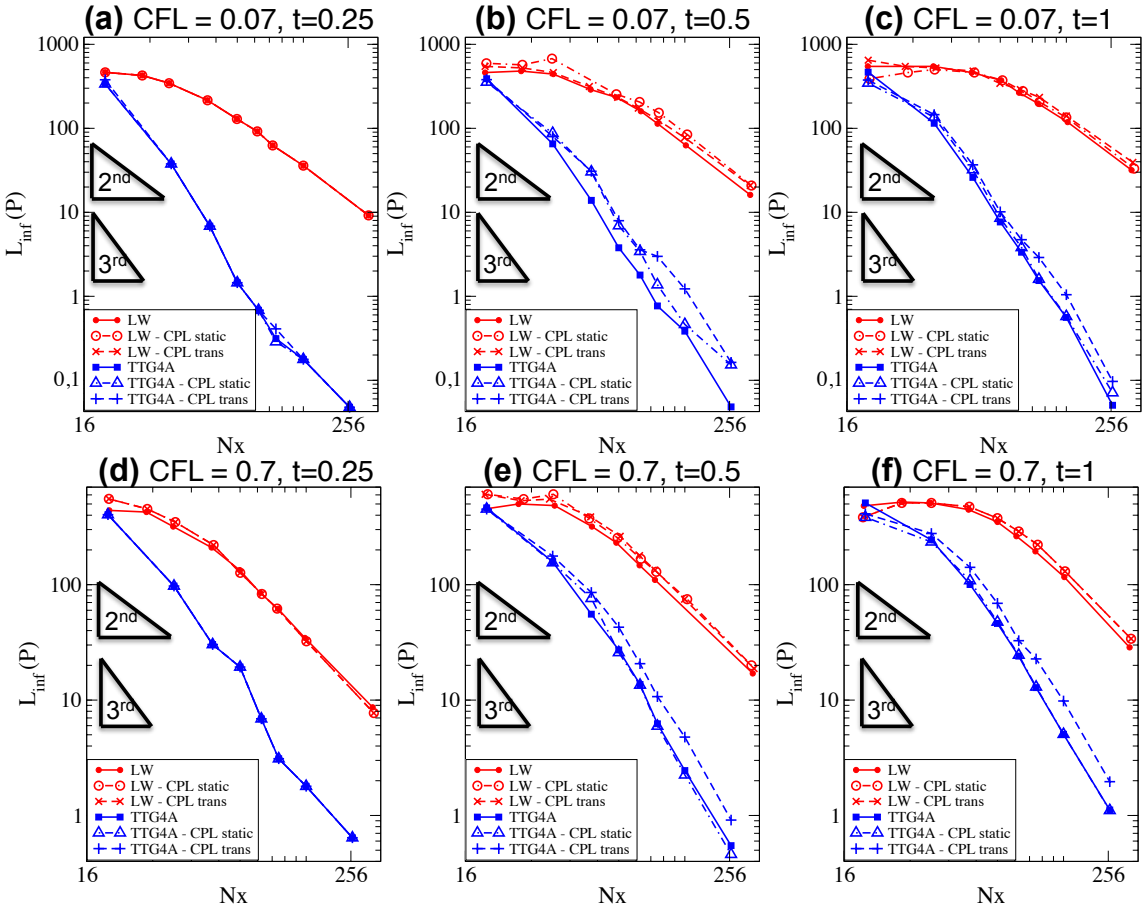

Figure 3.13: The maximum errors of instantaneous pressure fields $L_\infty(P)$ versus mesh resolution N_x for different cases using the LW or TTG4A schemes using 3$^{\text{rd}}$-order interpolation. The pressure profiles are compared with the analytic profiles when the vortex reaches upstream of the interface ($t = 0.25$), the interface ($t = 0.5$) and the downstream of the interface ($t = 1$). The computations are using two sets of time steps with CFL= 0.07 (top) and CFL= 0.7 (bottom). The translation speeds for the translating coupled cases is $U_{trans} = 200$ m/s.

profile, a mean velocity profile is imposed and follows an empirical power law of the form:

$$U(r) = U_{bulk}\frac{n^2}{2} * (\frac{2}{n} + 1) * (\frac{1}{n} + 1) * (1 - \frac{r}{r_0})^n, \tag{3.14}$$

where n is a profile factor that alters the slope of the radial profile (here it is $n = 1.7$). Homogeneous and isotropic turbulent fluctuations are also added on the velocity signal. They are formed using the Kraichnan/Celik method [122] and the Passot-Pouquet spectrum [123] and are introduced through the inlet using the NSCBC formulation [118] with the modification introduced by Guezennec *et al.* [124] for vorticity injection. The velocity fluctuations, like the mean velocity profile, are a function of the radius, to simulate the

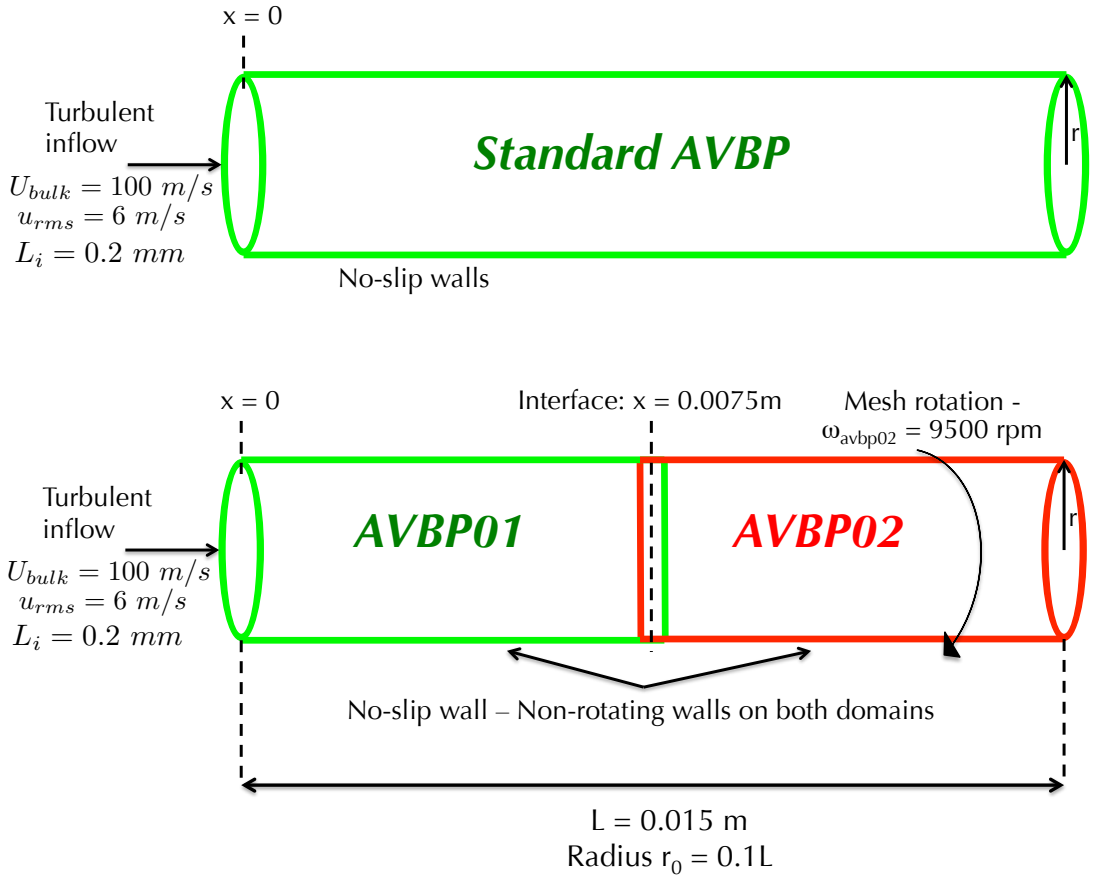

Figure 3.14: Numerical set-up of the pipe test case.

turbulent kinetic energy production occurring in turbulent boundary layers. The maximum value of the turbulent kinetic energy in the boundary layer K can be evaluated using:

$$K_{max} = \frac{U^{*2}}{\sqrt{C_\mu}} \tag{3.15}$$

where U^{*2} is the wall friction velocity and $C_\mu \approx 0.09$.

For Re between 2000 and 10^5, Tournier [125] proposes an evaluation of U^* using:

$$U^* = 0.03955 U_{bulk}^{\left(\frac{7}{4}\right)} \left(\frac{\nu}{2R}\right)^{\frac{1}{4}} = 0.03955 \frac{U_b^2}{Re^{\frac{1}{4}}} \tag{3.16}$$

The maximum value of K is typically reached at a non-dimensional distance to the wall $y^+ \approx 10$, where $y^+ = \frac{(R-r)U^*}{\nu}$.

The maximum value of the imposed fluctuations U_{pmax} is given by:

$$U_{pmax} = \sqrt{\frac{2K_{max}}{3}} = \sqrt{\frac{2}{3\sqrt{C_\mu}}} U^* \tag{3.17}$$

For this study the value of U_{pmax} is 8.6 m/s.

Then velocity fluctuations decrease to reach a minimum value of U_{pmin} at $r = 0$:

$$U_{pmin} = 0.5 U_{pmax} \tag{3.18}$$

The profile of the root-mean-square velocity imposed at the inlet is finally modeled using:

$$\sqrt{\overline{u_i'^2}}(r) = u_{rms}(r) = \begin{cases} U_{pmin} + (U_{pmax} - U_{pmin}) \left(\frac{r}{(1-\delta)R}\right)^2 & \text{if } r \leq (1-\delta)R \\ 0 & \text{if } r > (1-\delta)R \end{cases} \tag{3.19}$$

The mean u_{rms} imposed at the inlet is approximately 6 m/s. The integral length scales of the injected fluctuations is $L_i = 0.2\ mm$ that corresponds to approximately 8 integral length scales along the diameter of the pipe which should ensure relatively adequate statistical representation of the injected turbulence [126]. For all discussed results, the governing equations are resolved using the 2nd order LW numerical scheme along with linear interpolation for the data exchange in the overlap region.

Figure 3.15 shows the velocity magnitude of an instantaneous solution across the cylinder mid-plane for the standalone and coupled cases (at different instants). Both cases depict a similar flow field, with relatively small turbulent structures injected at the inlet evolving into more realistic and larger structures as they propagate through the pipe. Visually, the interface for the coupled case appears not to interfere with the turbulent structures crossing it. This can be further confirmed by a view of the interface (x-normal plane at $x = 0.0075m$) from the two different sides of the coupled simulation and shown in Fig. 3.16. It is evident that the differences in velocity, even with this very coarse mesh, are minimal, despite the interface and the rotation of the second domain. The mass flow difference between the two domains is 0.1%, highlighting minimal conservation issues despite the large cell size.

Comparisons between the coupled and standalone cases are performed on an averaged solution. The duration of the averaging is $12ms$, which corresponds to 80 flow-through times (computed using the pipe's bulk velocity). Figure 3.17 depicts the mean profiles (both time and azimuthally averaged) of the axial velocity and the turbulent kinetic energy as a function of the radius for the standard and coupled cases at the location of the interface of the coupled simulation (x = 0.0075 m). For the coupled case, the profiles are plotted for both domains to highlight any potential impact issued by the interface. Very good agreement is found between the two cases for both quantities, the biggest difference being observed for the peak of the kinetic energy.

3.4 Conclusions

LES recommendations point to the need for numerical schemes that are high order and centered to minimize numerical dissipation as well as dispersion of turbulent structures, a fundamental property for proper LES predictions. Yet, they are hard to apply for complex

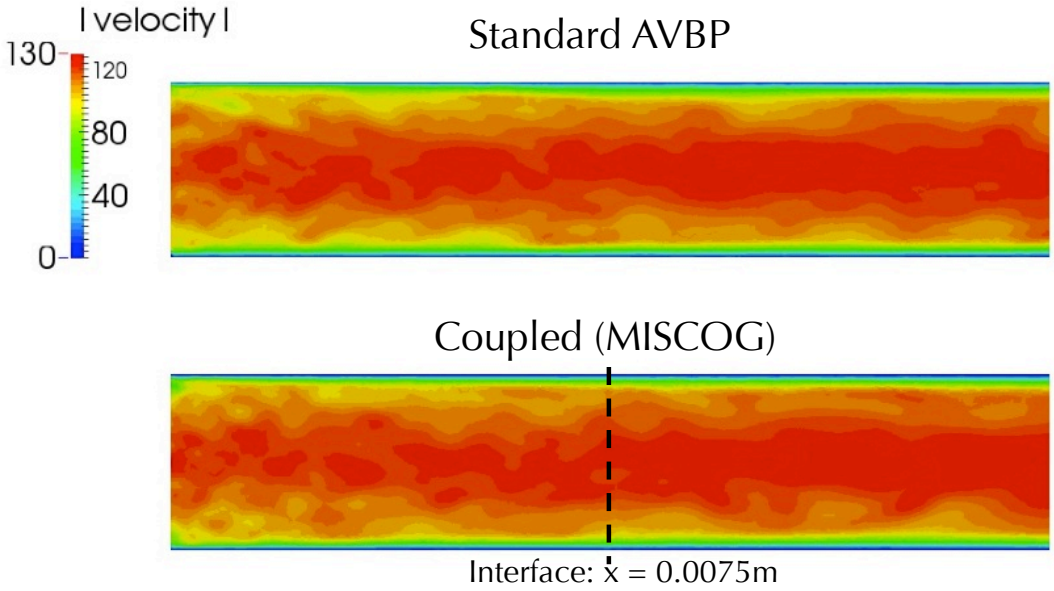

Figure 3.15: Velocity magnitude across the pipe of an instantaneous solution - Standalone AVBP (top), coupled simulation with MISCOG (bottom).

industrial, confined and rotating internal flows. To address this specific difficulty, coupling multi-copies of a massively parallel unstructured compressible LES solver AVBP with the parallel coupler OpenPALM is employed, the rotor/stator interface being treated with an overset grid approach, termed MISCOG.

Several numerical test cases with increasing degrees of complexity have been proposed to evaluate this solution for both translating and rotating interfaces. The coupling method is proven to handle acoustic and vortical wave propagation for both interfaces with an acceptable degree of accuracy for LES, provided that the overlapping region contains a sufficiently large number of points dependent on the selected numerical scheme. The proposed treatment almost recovers the dispersive and dissipative properties of the schemes of the stand-alone LES code. It also shows similar properties as the static cases with the exception of a high-frequency tone appearing as long as a proper sampling of the translation period is used. This tone is however weak (low level) and spatially localized close to the interface. For a fully turbulent problem, the turbulent fluctuations are found to be properly convected through the interface without significant dissipation and distortion even with an overlapping rotating interface.

With the numerical properties of the proposed coupling approach investigated, validation on a realistic rotor/stator configuration is still necessary before proceeding with real applications like combustor/turbine simulations. To this end, the next chapter details the numerical simulations of an experimental turbine stage using the MISCOG method.

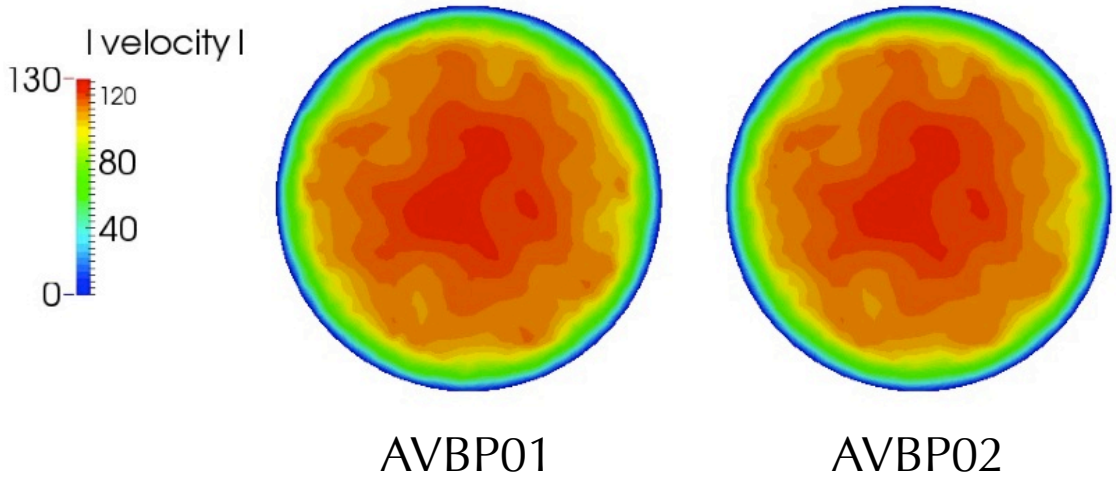

Figure 3.16: X-normal plane of the velocity magnitude at the interface for the coupled case - AVBP01 (left) and AVBP02 (right).

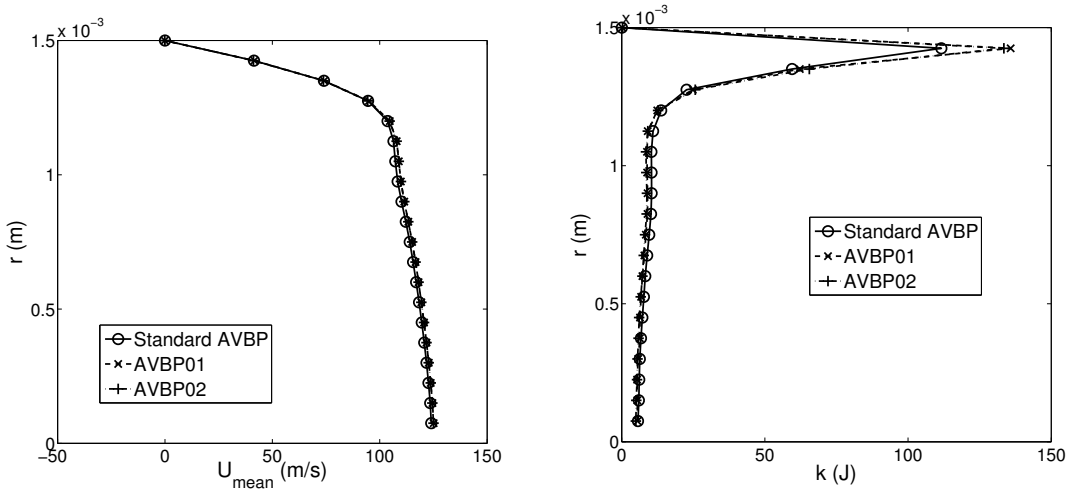

Figure 3.17: Mean axial velocity (left) and turbulent kinetic energy k (right) profiles as a function of the radius for the standard and coupled simulations at the interface.

Chapter 4

Large-Eddy Simulation of a transonic, high-pressure turbine stage

Contents

4.1 Applications of LES in turbomachines 50

4.2 High-pressure turbine flow characteristics 52

4.3 MT1 Turbine Stage 58

4.4 Simulation set-up 58

4.5 Global characteristics 65

4.6 Basic flow topology 66

4.7 Low resolution results 70

4.8 High resolution results 78

4.9 Conclusions 88

In this chapter, the MISCOG method is applied to a real rotor/stator configuration, the experimental high-pressure turbine MT1, installed in the Oxford Research Turbine Facility, Fig. 4.1. The available measurements [2] provide a good platform to validate the method in realistic turbine configurations. The study is parametric, with different SGS models and mesh resolutions investigated in an effort to explore as widely as possible the advantages and limitations of the method as well as establishing some guidelines on LES of such configurations. Note that a wall-modeled approach is followed throughout to reduce the computational cost and make the execution of this parametric study possible. A large part of the results detailed in this chapter have been presented in the ASME Turbo Expo conference [127] and submitted for publication in the Journal of Turbomachinery.

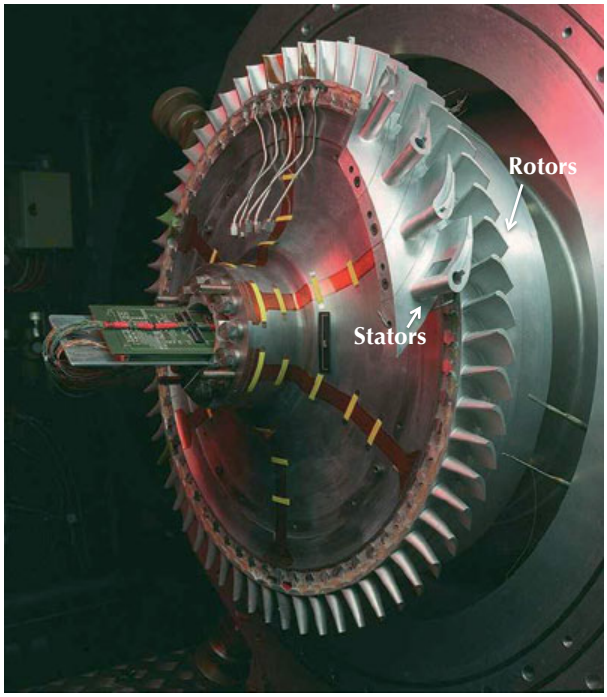

Figure 4.1: View of the experimental high-pressure turbine MT1 [2].

4.1 Applications of LES in turbomachines

Current industrial state-of-the-art in turbomachinery simulations usually relies on solving the RANS equations with a turbulence model to obtain the mean variables of the stationary flow field. In some cases where unsteady flow features at established frequencies are to be captured, the prevalent method is performing Unsteady RANS (URANS) simulations [14]. While both these methods are mature and come with an affordable computational cost, they are subject to several limitations. As mentioned in Chapter 2, they do not explicitly resolve any turbulent length scales and show deficiencies in predicting transition and flow separation [128]. This is very restrictive for turbomachinery flows, where there are complex flow phenomena, including boundary layer transition [9], flow separation and reattachment [14], vortex shedding and high levels of free-stream turbulence [32, 23].

Large Eddy Simulations (LES), designed to resolve a large range of the turbulent spectrum with an unsteady formulation [47], have long been considered promising for turbomachinery applications. However, due to the high computational cost associated with wall resolved LES and the limitations of classic wall models, only few studies have been performed so far in this field. Most of the investigated configurations are simple cascades or slices of the full 3D blades at both low and high Reynolds numbers. The first studies focused on LES of the low-pressure, low-Reynolds turbine blade T106 with impinging wakes [129, 130] or homogeneous inflow [131], a challenging case where a laminar separation bubble, Kelvin-Helmholtz instabilities and wake-induced transition can coexist. The success of these simulations in capturing all these phenomena, accompanied

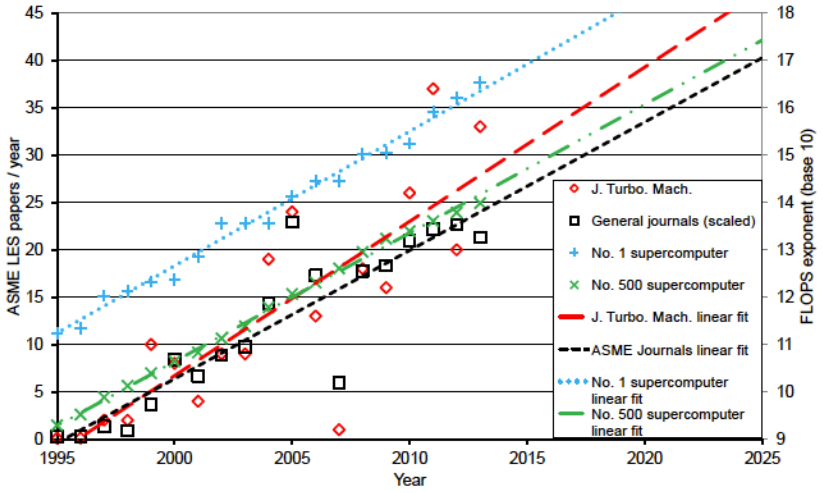

Figure 4.2: Number of published ASME papers on LES of turbomachinery and power of the Top 500 supercomputers for the last 20 years [8].

by the incompressible DNS of Wu and Durbin [50] for further validation of the results, showcased the potential of high-fidelity LES in turbine blades. These investigations, in conjunction with the increasing computational power, sparked an ever-increasing interest in the approach. Figure 4.2 presents in the same graph the number of papers on LES of turbomachinery blades in ASME journals/conferences and the increase in power of the top 500 supercomputers [43] for the last 20 years, as well as projections for the future through linear fits of the data [8]. It highlights the attention the field has received the last 15 years, as well as the correlation with the available computing power. It also shows that in the future such simulations will become more commonplace, following almost perfectly the predicted increase in available computational power.

Besides low-pressure turbine cascades, more recent studies focused on compressor blades with several authors performing LES of the NASA Rotor 37, a high-Reynolds number compressor rotor blade with shock/boundary layer interactions at the tip [132, 133, 134] and the V103 blade [135, 136], where the impact of incoming wakes on the transition mechanisms was analyzed. LES and hybrid LES of the aerothermal flow field around high-pressure turbine cascades are also available in the literature [14, 137, 44], with Collado *et al.* [23] and Bhaskaran and Lele [99] successfully capturing the impact of free-stream turbulence and transition on the heat transfer at the blade walls, contrary to RANS/URANS simulations. As heat transfer in turbine blades is crucial due to the high operating temperatures, LES of high-pressure turbine blades with internal blade cooling have also been coupled to heat transfer solvers to improve the thermal predictions [138, 139]. Finally, You *et al.* [140, 13] used LES to focus on a particularly challenging region of moving blades, the tip clearance, which is responsible for the generation of secondary flows and approximately a third of the total losses [141] of a stage. Apart from accurate mean flow predictions, the LES formalism allowed to highlight the evolution of turbulent stresses in that region and their influence on the viscous losses. More recently, Cahuzac

et al. [142] investigated the rotor tip clearance flows using LES with an aeroacoustics interest, reporting fair agreement on the measured profiles and spectra with experimental data from DLR. This is not an exhaustive list of all the LES of blade flows. Tucker [14] provides a thorough list of turbomachinery LES performed up to 2011 and Gourdain *et al.* a more recent list of compressor LES and hybrid LES [143], with the number of studies increasing considerably every year, as shown in Fig. 4.2.

LES studies of complete turbomachinery stages, including the critical part of rotor/stator interaction, also emerged. Tyagi and Acharya [144] simulated the stator/rotor interactions across a turbine stage using the immersed boundary method but only discussed shortly the flow topology. More recently, Rai [145, 146] evaluated in more detail the rotor/stator interactions across a slice of a compressor and low-pressure turbine stages respectively, while De Laborderie *et al.* [147] focused on the emitted noise from a slice of a 3D compressor stage. Gourdain [72, 148, 149] performed wall-resolved LES (up to almost 1 billion nodes) of the CME2 compressor stage, including the endwalls and tip clearance. Besides accurately predicting the mean flow variables, LES also provided information on turbulent structures and frequencies not present in URANS simulations and captured the transition of the boundary layer. Finally, similar conclusions were drawn by McMullan and Page [75], who performed LES on two different compressor stage configurations, emphasizing also the impact of the inflow turbulence on the aerodynamic field, notably the tip leakage flow. Regarding 3D turbine stages, to the author's knowledge, before the beginning of this PhD there was no LES of 3D turbine stages in the literature. This work is the first of its kind and it is aiming at providing a stepping stone for future high-fidelity LES of turbines by performing wall-modeled LES of a 3D HPT stage.

Before detailing the performed simulations and results, a short review of some turbine aerodynamic characteristics and secondary flows, particularly important in turbines due to the strong flow turning [150], is provided. The purpose is for this section to serve as a reference for the subsequent analysis of LES results and to reveal the flow complexity of such configurations.

4.2 High-pressure turbine flow characteristics

As mentioned in Chapter 1, the purpose of the HPT is to extract the necessary energy from the hot and high-energy gases to drive the compressor. Analyzing the velocity triangles in a 2D slice of a turbine stage is an intuitive and simple way to better illustrate its function [151]. The triangles of a typical configuration are depicted in Fig. 4.3. With such a model the velocities are analyzed at 3 stations: at the stator inlet (position 1), at the stator/rotor interface (position 2) and at the rotor exit (position 3). In Fig. 4.3, $\mathbf{V}$ corresponds to the absolute velocity vector, seen by the immobile stator blades, $\mathbf{W}$ is the relative velocity seen by the moving rotors and $\mathbf{U}$ is the velocity of the blades due to the angular velocity ω at a radius R. It can be seen that $\mathbf{V} = \mathbf{W} + \mathbf{U}$. In this example, the flow at the turbine inlet is axial (absolute velocity $\mathbf{V_1}$ with angle $\alpha_1 = 0$). As it passes through the stator, the absolute velocity increases with a large azimuthal component created by the flow turn, illustrated by the positive angle α_2. In this simple

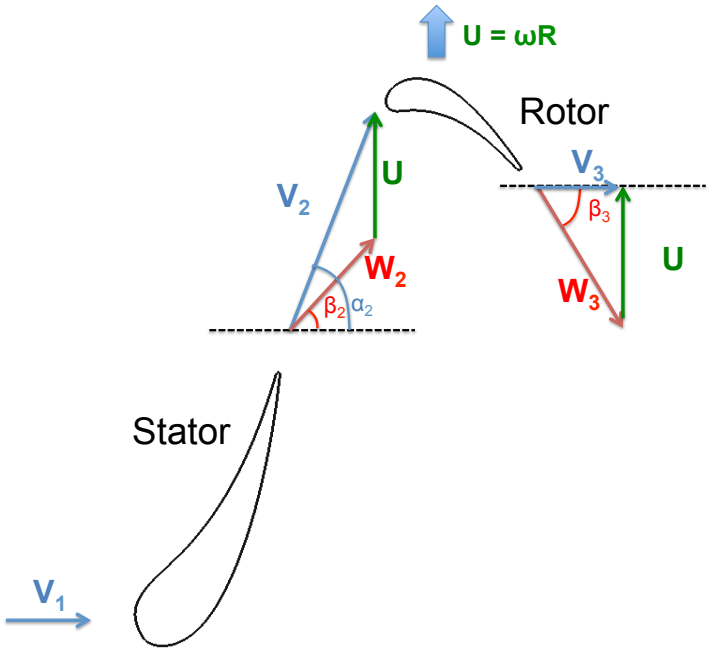

Figure 4.3: Typical velocity triangles across a turbine stage. Absolute velocity is V, relative velocity is W and U is the velocity due to the blade rotation.

approximation, the axial component of the velocity is equal at all 3 positions to ensure equal mass flow. The rotor on the other hand is moving. As a result, an observer sitting on the blade would encounter the relative velocity $\mathbf{W_2} = \mathbf{V_2} - \mathbf{U}$, coming at an angle β_2. As the flow goes through the blades it expands further and the previously large azimuthal component of the absolute velocity is reduced (in this example the flow has turned back to the axial direction, $\alpha_3 = 0$). The amount of work (or total enthalpy drop) extracted from the flow through this process can be straightforwardly calculated using Euler's relation [152]. For a constant radius, it reads:

$$\Delta H_i = \Delta(UV_{azim}) = -\omega * R * V_2 * cos(\alpha_2) \tag{4.1}$$

where V_{azim} is the azimuthal component of the absolute velocity. It shows that for an axial turbomachinery stage the changes in azimuthal velocity are responsible for the work (the negative sign used here indicates work extraction). Equation (4.1) is valid also for compressors, with the difference that the enthalpy of the fluid is increased.

From a purely aerodynamic point of view, the designer of a turbine is interested in achieving the necessary pressure drop with the maximum efficiency and the lowest possible losses. The principal sources of aerodynamic losses come from the flow boundary layers, the mixing of the wakes at the blade trailing edges, in the case of choked transonic turbines from shock losses, and finally from the secondary flows. The first 3 types are often grouped in the literature and called profile losses, while secondary flow losses are often split into endwall (hub and casing) and tip leakage losses [10, 153]. Heat transfer is

another source of entropy increase, hence contributing to the total losses in the turbine. Proportions are approximately 60-70% for profile losses and 30-40% for both types of secondary flow losses.

The generation of losses through viscous friction in boundary and shear layers is a mechanism known for some time (Denton [153] provides a thorough review of the mechanisms and different correlations for both boundary layer and mixing losses). However, the state of the boundary or shear layer is an important parameter to determine these losses accurately. In a HPT, the near-wall flow Reynolds number is usually high enough to trigger laminar-to-turbulent transition on the suction side of the blade. This transition usually occurs after the mid-chord of the blade, where an adverse pressure gradient is prevalent, and leads to higher skin friction and losses. While correlations for the transition region exist (e.g the correlation of Cebeci & Smith [154]), they are usually calibrated on flat plates or airfoils for certain free-stream turbulence levels. In real turbines, a large variety of transition scenarios of the boundary layer can be observed, such as by-pass transition of attached boundary layers, transition due to laminar separation bubbles, wake-induced transition from preceding blade rows and shock-induced transition [9]. The sensitivity of the phenomenon to the free-stream turbulence levels is also an important characteristic [99, 9]. Figure 4.4 depicts a map of different transition regimes as a function of the acceleration parameter (positive for accelerating flow and negative for decelerating) and the momentum Reynolds number [9]. It shows that, for high free-stream turbulence levels, by-pass transition is possible even in accelerating regions.

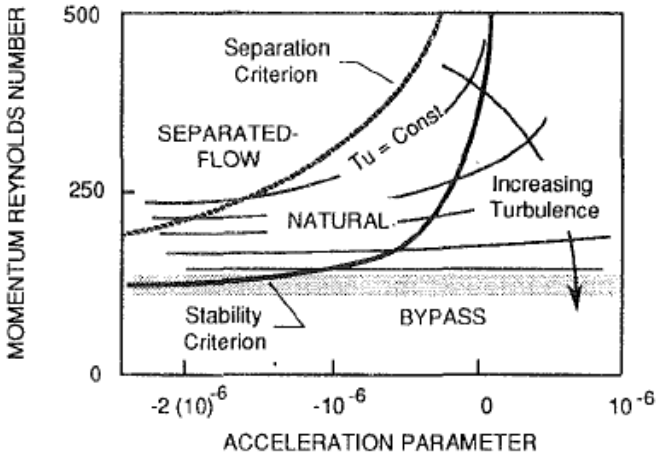

Figure 4.4: Topology of the different transition regimes as a function of the flow acceleration level and turbulence intensity [9].

Besides the boundary layer developing along the blades, boundary layers are also developing at the endwalls, i.e the walls of the channel in which the turbine is placed (casing on the top and hub at the foot of the blades). Endwall flow losses occur from the interaction of these endwall boundary layers and the blade passage that gives rise to secondary flows. They are considered to be the least understood sources of losses

and a significant amount of research has been performed on cascades since the 70's to understand them with several experimental studies establishing a qualitative idea of their form [155, 156]. Figure 4.5 (left) provides a visualization of the generation of secondary flows and their interactions in a cascade according to the model of Sharma and Butler [10]. The two principal secondary vortices evidenced here are *a*) the passage vortex and *b*) the horseshoe vortex occurring at the stator hub and casing as well as the rotor hub.

a) As the endwall boundary layer approaches the blade from the turbine inlet, due to the velocity deficit with respect to the freestream flow and the azimuthal pressure gradient between the suction and pressure sides, the flow is forced to turn towards the pressure side and rolls to form the passage vortex [141]. The pitchwise pressure gradient inside the blade passage then pushes the vortex towards the low-pressure suction side of the neighboring blade.

b) The horseshoe vortex is formed due to a different mechanism. With the endwall boundary layer facing an adverse pressure gradient from the blade stagnation point it can separate and form a double saddle point. This forces the boundary layer to roll up into a horseshoe vortex that is transported downstream in two different legs: one on the suction side and one on the pressure-side [157].

Note that as these vortices move downstream, they eventually interact with each other. The pressure-side leg of the horseshoe vortex has the same direction of rotation as the passage vortex, resulting potentially in merging structures migrating to the suction side. The suction-side leg, on the other hand, is rotating in the opposite direction and gets wrapped around the passage vortex as it propagates downstream. More complicated vortex flow fields and models have been proposed, with several smaller vortices developing around the principal ones, as in the model of Wang *et al.* [11] shown in Fig. 4.5 (bottom). These enriched views of the flow topology are however based on limited experimental flow visualizations and further validations are needed [156].

Regarding the influencing parameters of the secondary flows, the endwall boundary layer, i.e the wall normal total pressure gradient is a major parameter in the secondary flow development. Laksminarayana and Horlock [158] used the vorticity transport equation to show that in an inviscid flow, the radial pressure gradient governs the development of these structures in non-rotating blades. While the inviscid assumption may appear strong, considering that viscous effects are at the origin of the endwall boundary layer, the effect of viscosity on the dynamics of the developing vortices is negligible [141]. Prassad and Hendricks [30] using a similar analysis also showed that density gradients due to non-uniformities at the turbine inlet and modifications of the vane exit angle produce additional vorticity in the rotor passage. These findings were complemented by the recent experiments of Barringer *et al.* [159] and Colban *et al.* [160] who confirmed that the radial gradients of the inlet total pressure profile and the state of the endwall boundary layers impact significantly the secondary flows as well as the heat transfer across the NGV, with additional vortices appearing for certain inlet profiles. The azimuthal pressure gradients are also of importance, as they control the pressure-to-suction side migration of the secondary flows in the blade passage [141]. Finally, the residual combustor swirl arriving at

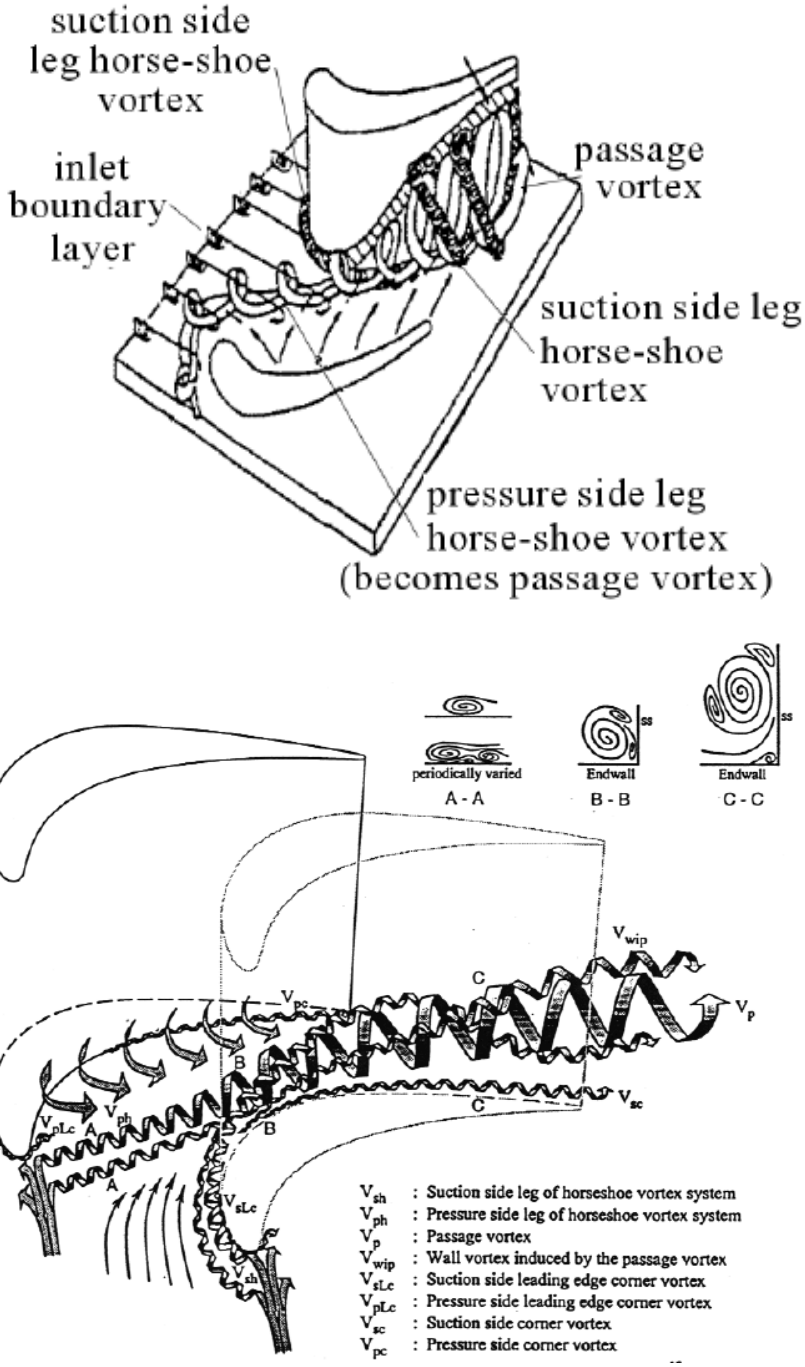

Figure 4.5: Secondary flow field in a cascade according to Sharma and Butler [10] (top) and according to Wang *et al.* [11] (bottom).

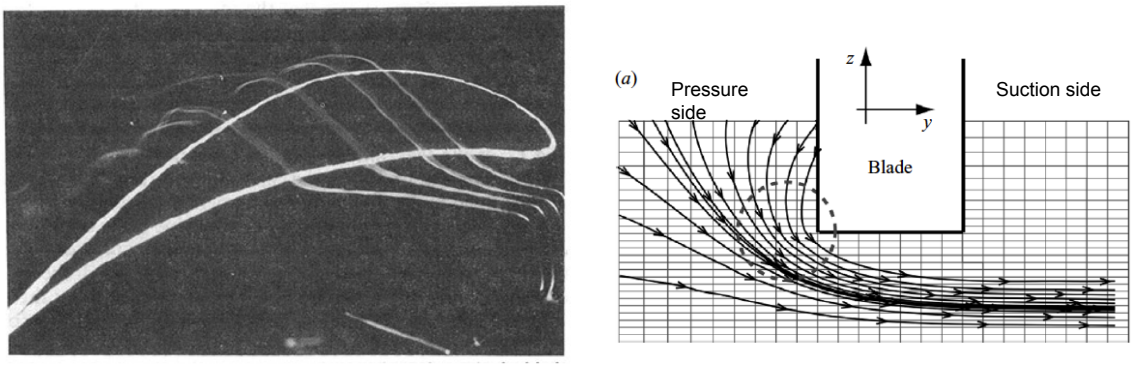

Figure 4.6: Smoke visualization of tip leakage in a turbine blade [12] (left) and schematic of the formation of the tip leakage flow on a thin blade [13] (right).

the HPT is known to impact the secondary flow development through the modification of the incident angles and generation of additional vorticity [4]. These results question the universality of correlations for secondary flows in realistic turbines and highlight further that the combustor/turbine interface is of paramount importance and needs to be taken into account if the correct flow field is to be reproduced or predicted.

In rotating blade rows, practical reasons impose a clearance between the moving blade tips and the immobile casing, as the mechanical and thermal forces at the blade are constantly modifying its effective shape during the different operating conditions and there is a manufacturing tolerance [161]. This tip clearance leads to the tip leakage flow, where fluid from the pressure side of the blade passes through this space to the suction side. Figure 4.6 (left) shows a smoke visualization of tip leakage in a turbine blade [12] and Fig. 4.6 (right) depicts a schematic of the formation of the tip leakage flow [13] for a compressor blade (the streamwise coordinate follows the x-axis). For relatively thin blades, the flow separates as it passes the pressure side corner and moves to the suction side to form the tip leakage vortex. If the blade thickness is larger, the flow can reattach on the blade tip before it reaching the suction side where it rolls to form a vortex. This latter mechanism has been reported in the literature to be the prevalent one for turbine blades [162, 153]. The tip leakage flow is formed primarily between 20 and 50% of the rotor chord [13]. Several experimental studies have tried to investigate the tip leakage flow both in cascades [162] and in annular turbines [16]. Numerical investigations have accompanied the experiments, but most attempts relied on Reynolds-Averaged Navier-Stokes (RANS) that model the turbulent fluctuations. Recently You *et al.* [140, 13] performed high-fidelity LES of the tip clearance flow of a rotor cascade, moving beyond mean flow predictions, as provided in RANS/URANS simulations, and shedding light onto the evolution of viscous losses issued in the leakage region.

The findings presented above highlight that turbine flows are highly complex. Finding universal correlations or low-order models is challenging and experimental predictions on realistic configurations are difficult to obtain due to the geometric complexities. Cascades alleviate some of the experimental difficulties but such flows present important differences compared to annular blade rows [163, 4], where secondary flows are considered to be more

confined. In this context, high-fidelity numerical simulations is one promising path to further our understanding of the flow physics in turbine stages and improve the predictive capabilities on new designs as well as the low-order models.

4.3 MT1 Turbine Stage

The investigated turbine configuration is the MT1 high-pressure turbine. It is an unshrouded, single stage, high-pressure experimental turbine designed by Rolls-Royce and measured in the frame of the European project TATEF-II[1]. It is a full scale turbine and works in engine representative conditions, forming a good database for validations of numerical methods and solvers in a realistic configuration. The stage consists of 32 stator and 60 rotor blades. The experimental data come from two different measurement campaigns and include pressure profiles across the stator blades at 3 different spanwise positions, across mid-span for the rotor blades as well as azimuthally averaged rotor exit profiles in the near and far field [2]. Heat transfer measurements were also performed but have not been employed in this investigation. Note that to complement the original database, Qureshi *et al.* [33] provide additional data on the secondary flow structures across the rotor blades.

Experimental facility

The test bench of MT1 is a short duration, rotating light piston wind tunnel designed for investigating turbine stages. Experiments were conducted initially at the QinetiQ Turbine Test Facility (TTF) in Farnborough, England. Later, the experimental apparatus was moved to the Oxford Turbine Research Facility. It has the capacity to create engine representative test conditions for turbines up to one and a half stages while both aerodynamic and heat transfer measurements can be performed simultaneously at a moderate cost [2]. Figure 4.7 shows a schematic of the TTF facility. To start the experiments, the turbine first needs to reach the desired rotation speed. Air from the high-pressure reservoir is then injected behind a piston upstream of the test section making the piston move forward, hence compressing and heating the air in front of it. When the desired inlet conditions in front of the piston have been achieved, a plug valve opens and mass flow is generated due to the pressure gradient across the stage. The duration of the tests is approximately 400 ms for each run. More details on the installation and the function of the facility are provided by Hilditch *et al.* [164].

4.4 Simulation set-up

Geometry and computational domain

The MT1 turbine allows for the periodic simulation of a quarter of the 360 degree annulus (8 stators and 15 rotors). To reduce the computational cost of such a simulation, the

[1]TATEF-II : Turbine Aero-Thermal External Flows 2

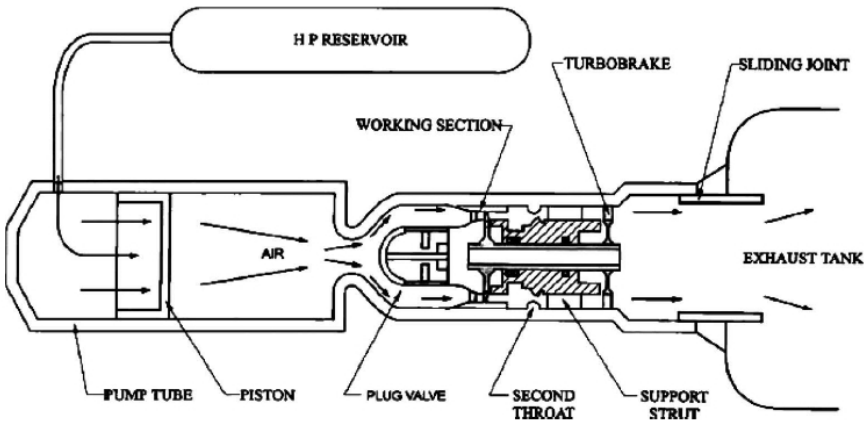

Figure 4.7: Schematic of the TTF facility.

reduced blade count technique is employed, as explained in Chapter 2. Hosseini *et al.* [73] performed numerical simulations of the MT1 turbine using different blade counts and concluded that the impact of the scaling on the mean aerodynamic flow field is minimal (as long as the solidity and the blade angles are maintained). In this study, a small scaling is performed on the stator side so the final blade count is 30:60 hence creating a periodic domain of 12 degrees. The distance to the inflow location from the stator leading edge is approximately a quarter of the stator chord length, while the distance from the rotor trailing edge to the outlet is two rotor chord lengths. The resulting domain, along with the decomposition of the turbine stage to the corresponding AVBP instances, can be seen in Fig. 4.8.

Mesh generation

Two different meshes are employed in this study. They are fully 3D hybrid meshes, with prism layers around the blades and tetrahedral elements on the vane and at the endwalls. Figure 4.9 provides an overview of the coarsest mesh, while Table 4.1 summarizes the main characteristics of these grids. The coarse mesh (MESH1) is composed of 8.1 million cells in total for the stator domain and 10.5 million cells for the rotor domain. It is designed to place the first nodes around the blade walls in the logarithmic region of a turbulent boundary layer, hence allowing for the law-of-the-wall to be used effectively while reducing the computational cost. Note also that the prisms have a low aspect ratio set to $\Delta x^+ \approx \Delta z^+ \approx 4\Delta y^+$, with four prism layers in total around each blade. The fine mesh (MESH2) is designed to improve the overall resolution and places nodes deeper in the boundary layers to capture the effect of the turbulent structures formed in the outer and logarithmic parts. Additional prism layers have been added, increasing the total number of prism layers to 10. The prisms also have an increased aspect ratio, i.e $\Delta x^+ \approx 10\Delta y^+ \approx 10\Delta z^+$ to reduce the computational cost. In the rotor tip region the coarsest mesh has only 6-7 cell layers, shown in Fig. 4.9b, to keep the mesh cell

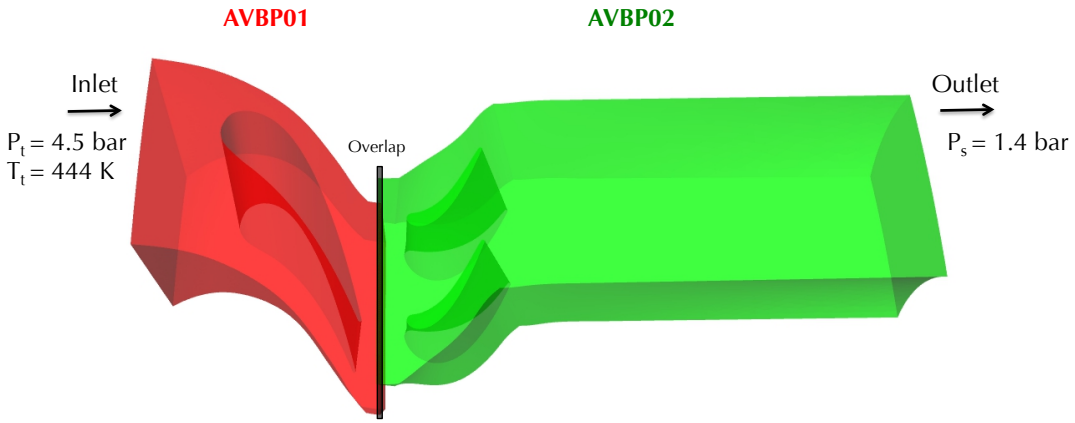

Figure 4.8: A view of the MT1 domain highlighting the decomposition of the turbine stage to the corresponding AVBP instances and the overlap between them for application of the MISCOG method.

count limited hence rendering the resolution rather limited in that area. The fine mesh (MESH2) has approximately 20 layers of cells in the tip clearance, allowing for a much better representation of the secondary flows developing in that region.

Figure 4.10 depicts estimated values of the non-dimensional wall distance y^+ from the computations across the stator and rotor blades at mid-span as a function of the curvilinear abscissa. The maximum y^+ values measured are approximately 100 and 12 for the stator (coarse and fine mesh respectively), where the thinnest boundary layers are encountered. Across the rotor blades, lower values are estimated with the exception of the trailing edge region, where the stator maximum y^+ is approached. The mesh with y^+ of 100 clearly necessitates the use of a logarithmic law-of-the-wall, since the first node from the wall is placed well within the logarithmic part of a turbulent boundary layer. For the finer mesh, y^+ indicates that across both blades most nodes are placed within the buffer region of a turbulent boundary layer [165] where the velocity profile switches from linear to logarithmic, hence justifying the use of a law-of-the-wall. Note that typical grid requirements for wall-resolved LES are $\Delta y^+ < 1$, $\Delta x^+ < 150$ and $\Delta z^+ < 40$ [56]. The y^+ estimations clearly confirm that the coarse cases do not respect the typical grid requirements for wall-resolved LES. The fine cases, however, do respect the requirement for the streamwise resolution Δx^+ on most of the blade surfaces and considering the use of a wall-law, this may create issues. These fundamental questions on near-wall modeling are however considered to be outside the scope of this work.

Boundary and Operating Conditions

The inlet and outlet boundary conditions follow the NSCBC formulation [118] and consist of imposing a total pressure, total temperature and flow angles for the inlet and a static pressure at the outlet. The total temperature measured experimentally is imposed at the inlet and corresponds to 444 K. The experimental value for the total pressure is 4.6 bar.

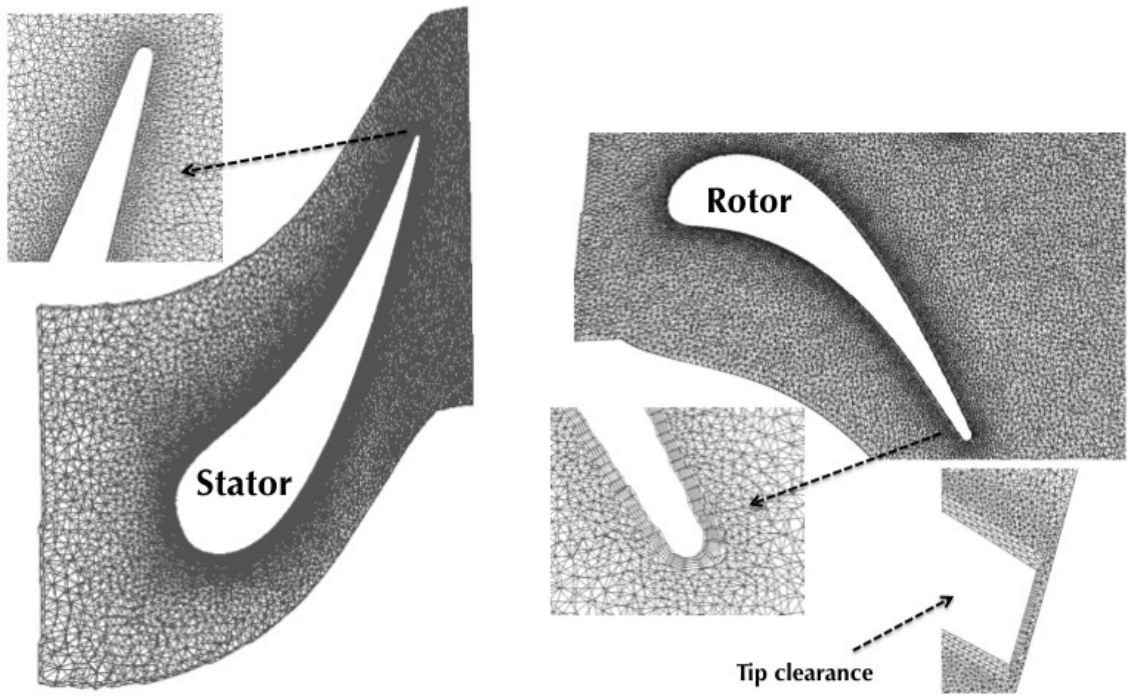

Figure 4.9: Cylindrical and x-plane cuts of MESH1.

	MESH1	**MESH2**
Stator cell count	8.1M	40M
Rotor cell count	10.5M	74M
Stator/Rotor prism layers	1/4	10/10
Max y+	100	12
$\frac{\Delta x+}{\Delta y+} = \frac{\Delta z+}{\Delta y+}$	4	10

Table 4.1: Main properties of the generated meshes.

With this setting preliminary results revealed that the LES had a mass flow surplus of approximately 2% linked to an underestimation of losses, as will be detailed further in section 4.5. To correct this surplus a reduction of the inlet total pressure was applied using the fact that for a choked turbine (such as this one) the reduced mass flow rate $\dot{m}_{red} = \dot{m}\sqrt{Tt}/Pt = 1$. A linear relationship between the actual mass flow rate and the inlet total pressure can thus be established to correct the mass flow. Based on this adaptation the inlet total pressure was decreased to 4.5 bar for all simulations. Note that to reduce the complexity in this parametric study, no turbulent fluctuations are injected at the inlet and walls are considered adiabatic, as indicated in Table 4.2 where all boundary conditions are summarized. The Reynolds number of the configuration, calculated using the stator blade chord and the velocity at the stator exit, equals 3 million.

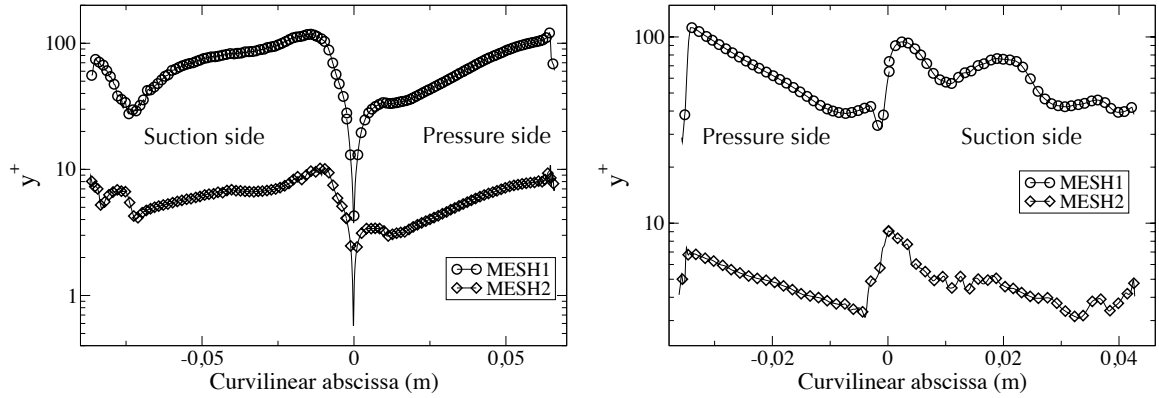

Figure 4.10: y^+ values for the two meshes across the stator (left) and rotor blades (right) at mid-span.

Rotational Speed (rpm)	9500
Inlet total pressure (Pa)	$4.5 * 10^5$
Inlet total temperature (K)	444
Mass flow (kg/sec)	17.4
Outlet static pressure (Pa)	$1.4 * 10^5$
Walls	Adiabatic
Re	$3 \cdot 10^6$

Table 4.2: Summary of the flow parameters.

Numerical scheme and initialization

The numerical scheme employed for this study is LW, second order in space and time [111]. No particular shock capturing techniques are employed apart from the application of some additional artificial viscosity around the shocks. The position of the shocks is evaluated by the Jameson sensor. Usually initialization of an unsteady turbine simulation typically uses a quick stationary RANS simulation (using the mixing plane approach) [65]. However, this option is not available in the solver. Due to the absence of an initial RANS solution, the computations are initialized by performing four full rotations on an initial mesh (very coarse) with uniform initial velocities. The obtained solution is then interpolated to the two meshes described above. Convergence of the simulation is determined by assuring that the mean thermodynamical variables and kinetic energy do not exhibit low temporal transients and that the oscillations around the mean value remain with the same amplitude. Approximately one extra rotation is enough to achieve convergence after interpolating to the fine meshes. An additional rotation is then necessary to acquire reliable time-averaged data.

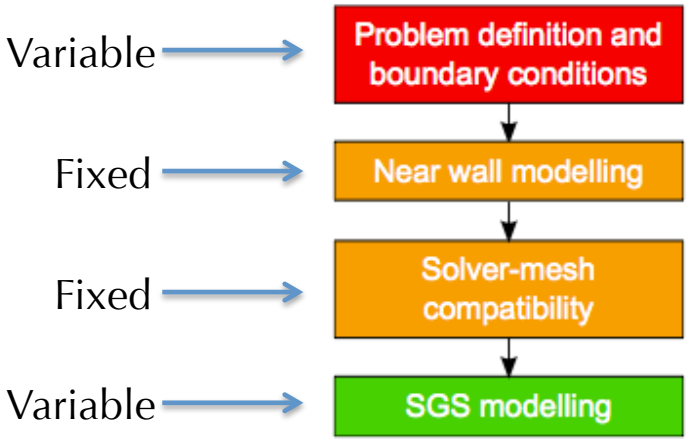

Figure 4.11: Practical LES hierarchy [14].

Objectives and cases investigated

The principal objective of this chapter is to validate the MISCOG approach in a realistic turbine configuration. In addition to that, as the literature lacks of simulations of this type, the sensitivity of such simulations needs to be evaluated to establish guidelines for future studies. Tucker *et al.* [14, 166] provide a hierarchy of the influencing parameters for LES, Fig. 4.11, commenting that the problem definition and boundary conditions have the highest influence, followed by the wall modeling, the mesh-solver compatibility and the SGS models. He also noted that in transitional flows, typically encountered in HPT, the importance of the SGS model increases. In this work, the wall treatment and boundary conditions are fixed and only one type of mesh is employed, hybrid prism/tetra meshes. The sensitivity analysis probes two other influencing parameters, the SGS model and mesh resolution.

	Smagorinsky	**WALE**	$\boldsymbol{\sigma}$
P1	NO	YES	YES
P2	NO	NO	YES
P3	NO	NO	YES

Table 4.3: Summary of the three sub-grid scale models, their constants and whether they satisfy the desired properties

First, a study of the effect of the SGS models is performed. In general, SGS models should be able to follow three universal properties. A primary property is that turbulence stresses are damped near the walls (they scale with y^3, where y is the wall-normal distance [167]), thus turbulent viscosity should follow the same behavior (named property P1). Additionally, two other desired properties are that turbulent viscosity should be zero in case of pure shear and pure rotation (property P2) as well as when there is isotropic or axisymmetric contraction/expansion (property P3) [168]. Property P1 is particularly

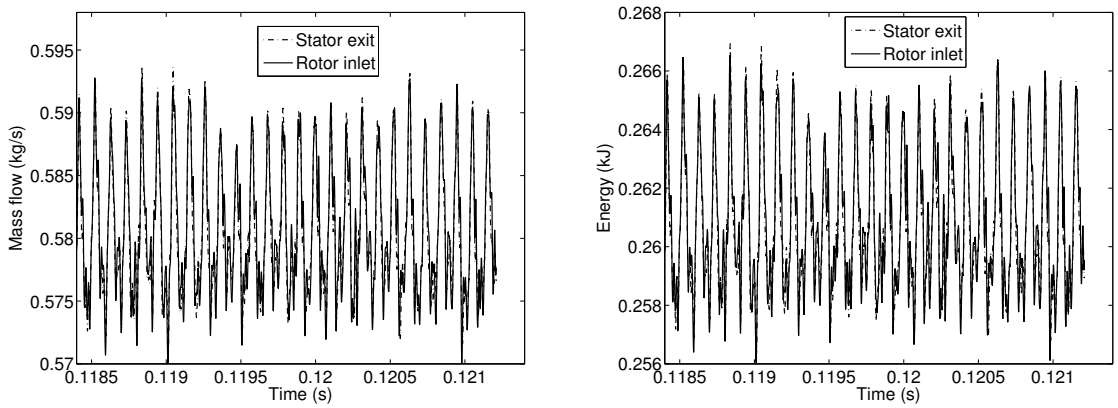

Figure 4.12: Mass (left) and energy (right) conservation at the rotor/stator interface.

critical for wall-bounded flows but not all models comply to it. Damping functions, such as the Van Driest function [169], exist but they can be cumbersome to use in complex geometries [170] and are not employed in this work. Here three different cases are computed, all employing MESH1 and altering only the SGS treatment. The models evaluated are the classic Smagorinsky model [171] (**Case 1**), the WALE model [57] (**Case 2**) and the σ model [168] (**Case 3**). Table 4.3 summarizes which of the desired properties are satisfied by the formulation of the three SGS models. The computational cost for a full rotation of the turbine stage is 6k CPU hours (approximately 2 days on 128 cores), thus permitting relatively quick results. An effect of the turbulent viscosity on the near-wall predictions with wall modeling has been reported in the literature [59] with the notable outcome being under or over prediction of the shear stress due to incorrect levels of turbulent viscosity affecting the calculations of the velocity gradients. Such effects should therefore be recovered here and impact both global and local predictions. They can also be further emphasized because of the relatively under-resolved mesh. More details on the formulation of each model are provided in Appendix A.

The second part tries to identify the influence of mesh resolution on the flow predictions. Besides the changes in the computed turbulent viscosity due to the reduced cell size (for all models the turbulent viscosity is a function of the filter width, or equivalently the cell size in solvers with no explicit filtering), the wall-modeled approach in LES is also particularly sensitive to the resolved flow variables and the turbulent fluctuations present in the outer layers [59, 172]. As a result, the improved resolution is expected to play a considerable role on the predictions. For this part, the fine mesh (MESH2) is employed with the three different SGS models (**Cases 4-6**) and results are compared to the coarse mesh. A summary of the cases investigated, their respective characteristics and cost (in CPU Hours) can be found in Table 4.4. It is evident that the increase in resolution leads to a large increase of the computational cost (2 orders of magnitude), due to both an increase of cell count in the domain and the decreased timestep since the numerical scheme employed is explicit in time.

The structure for the presentation of the results is the following: First, the flow

	Mesh	Timestep(sec)	SGS model	Cost (CPUh)	Wall-clock
Case 1		0.4e-7	Smago	6K	2 days
Case 2	MESH1	0.4e-7	WALE	6K	(128 cores)
Case 3		0.4e-7	σ	6K	
Case 4		5e-9	Smago	800K	15 days
Case 5	MESH2	5e-9	WALE	800K	(2048 cores)
Case 6		5e-9	σ	800K	

Table 4.4: Summary of the cases investigated in this study.

topology and characteristics are established on the basis of **Case 1**. Then, the sensitivity analysis for the three SGS models is presented. The results of these cases are compared to the available experimental data and against each other. The impact of the SGS model on the unsteady flow field and secondary flows is also evaluated. Finally, the cases with the refined MESH2 are analyzed and compared to the results already presented, while the advantages and limitations of the simulations are established.

4.5 Global characteristics

Conservation across the interface

An essential characteristic for the rotor/stator interface is to avoid any mass or energy losses. The overset grid method for the rotor/stator interface is based on linear interpolation of the conservative variables onto the overlapped cells, so it can be prone to conservation problems. As a result, a necessary step is to evaluate the mass and energy fluxes at the interface. Figure 4.12 shows the temporal evolution of the mass flow and energy surface integrals at the rotor/stator interface for **Case 1**, evaluated for both stator and rotor domain. The curves match almost perfectly, with the discrepancy in the mass flow being less than 0.06%. These plots allow to conclude that the conservation properties, even for the coarse cases, are adequate. The high level of mass and energy fluctuations also highlight the unsteady flow features at the interface, which will be more thoroughly analyzed in the following sections.

Operating point

Before any detailed analysis is performed, the operating point of each numerical case is examined. The computed mass flow and total pressure drop Pt_{in}/Pt_{out} across the turbine stage, for each case, is plotted in Fig. 4.13 where the target mass flow is shown by the vertical dash line. It is important to underline that the experimental total pressure drop across the turbine is not known. Experimentally the total-to-static pressure drop Pt_{in}/P_{hub} was measured, P_{hub} being the static pressure at the hub of the turbine. However, the exact measuring position of this pressure at the turbine exit duct is not known and as the duct is diverging (thus acting as a diffuser), knowing the measurement

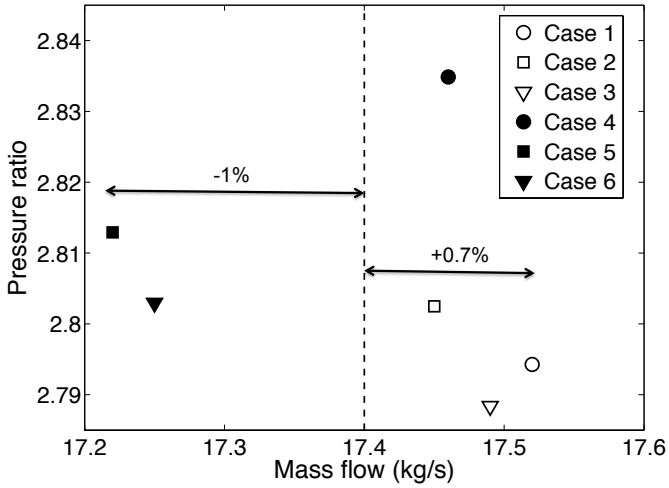

Figure 4.13: Operating point of the different cases analyzed. The target mass flow is shown with the vertical line.

position can become important. Despite this limit, a clear trend is observed for the numerical cases with the same SGS model: increasing the mesh resolution translates into an increased pressure drop across the stage and a reduced mass flow. The coarse **Cases 1-3** and the refined **Case 4** overestimate the mass flow by approximately 0.3-0.5%, while the finer cases with WALE and σ underestimate the target by 1%. This corresponds well with the fact that a reduction of the inlet total pressure was applied to achieve the correct mass flow; the coarse cases indeed largely underestimate the pressure drop across the turbine. The increased mesh resolution increases the pressure drop and reduces the mass flow. This suggests that, for a choked turbine such as this one, compensating the mass flow deficit of the refined simulations would require an increased inlet total pressure that is closer to the experimentally measured one. These findings highlight the difficulty for numerical simulations to adequately capture the aerodynamic losses and the associated flow mechanisms. Such a fundamental difficulty cannot be addressed here and besides the necessary mesh resolution it requires an extensive characterization of inflow conditions which are not available for this case. Finally, the tendency of under-predicting the losses in low resolution LES of turbomachinery stages has also been observed on previous simulations [148], with results improving as a wall-resolved LES is approached. It is worth noting that these mass flow differences are significantly higher than any losses observed at the stator/rotor interface between the two domains, highlighting that conservation is not an issue in these simulations.

4.6 Basic flow topology

As a first step, the main flow topology, including the identification of the secondary flows, is described on the basis of the predictions obtained from **Case 1**. Turbine flows

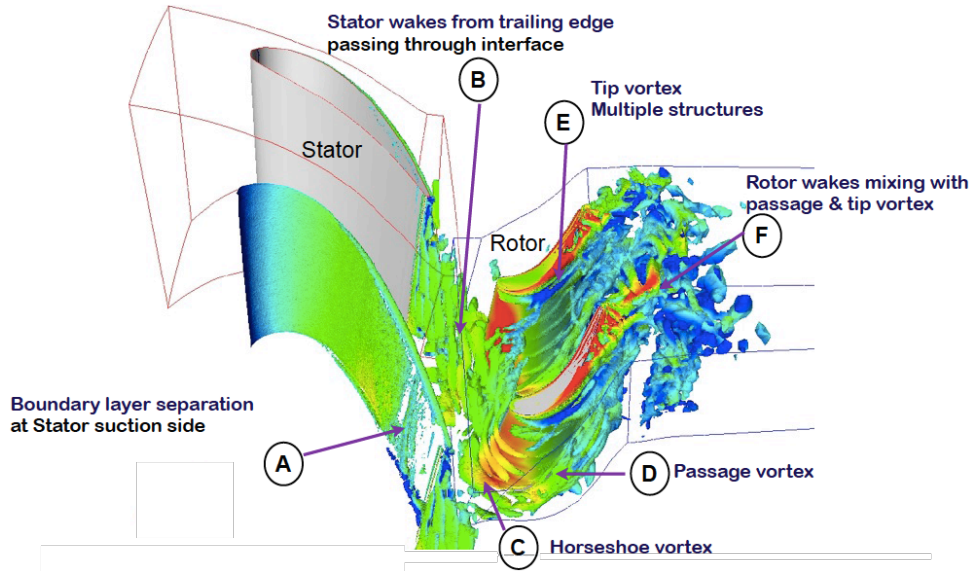

Figure 4.14: Isosurfaces of the Q criterion across the turbine stage.

are complex industrial configurations and the actual topology can vary considerably. First, the stator vane and near wall flows are known to be sensitive to boundary layer separation and transition. These phenomena impact the aerothermal load on the blade as well as the stator wake features. Second, in the rotor domain, besides the stator wakes being injected with a periodic and deterministic rate at the BPF, its flow topology is also significantly affected by the tip leakage flow, the passage vortex and subsequent potential interactions with the flow boundary layer around the blade.

Although highly complex, all LES produced here evidence most of these reported features, as seen in Fig. 4.14 where an iso-contour of the Q criterion [173] colored by the local absolute Mach number allows to identify:

(A) a boundary layer separation on the stator suction side,

(B) the stator wake entering the rotor passage,

(C) a horseshoe vortex at the rotor leading edge,

(D) the hub passage vortex,

(E) the tip vortex associated with multiple small scale structures,

(F) the mixing between the rotor wake and aforementioned passage and tip leakage structures.

To get a better idea of the form of the secondary flows, the Q-criterion can be computed based on a time-averaged velocity profile to remove the effect of the unsteady

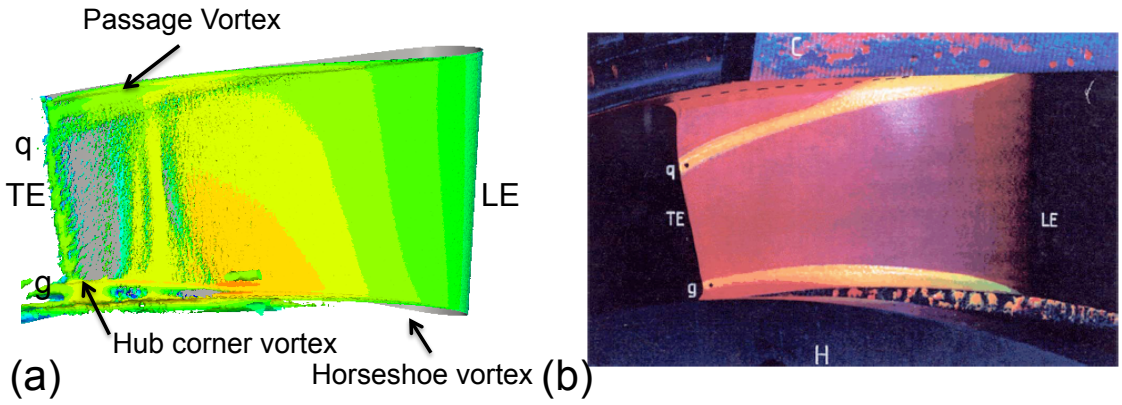

Figure 4.15: Q criterion of a time-averaged solution across the stator blade (a) and flow visualization of the secondary flows across the blade from experiments [15] (b).

wakes and turbulent fluctuations. Figure 4.15(a) depicts such isosurfaces across the stator suction side and is compared to flow visualizations obtained experimentally [15] and shown in Fig. 4.15(b). It can be observed that there exists a good agreement between the simulation and the experiments. Both at the hub and the casing, the development of the passage vortices is evidenced. These are the principal flow structures, with the one from the casing migrating strongly towards mid-span, while the one from the hub stays close to the endwall due to the radial gradients issued by the radial equilibrium and the profile of hub and casing. The isosurface of the Q-criterion obtained from the numerical simulation also allows to observe a small hub corner vortex close to the trailing edge.

Focusing on the rotor blades only, structures highlighted in Fig. 4.14 are once more evidenced more clearly in Fig. 4.16(a). Here, a time-averaged relative velocity field is employed to move to the rotor frame of reference. Focusing on the tip clearance and suction side of the rotor blade, Fig. 4.16(a) shows multiple tip leakage structures:

(E1) the induced tip clearance vortex,

(E2) the tip leakage vortex,

(E3) the tip separation vortex and

(E4) the scraping vortex

It is also noted that the tip separation vortex merges with the tip leakage vortex further downstream as they have the same sense of rotation. The scraping vortex is weak and gets dissipated rather quickly.

While no experimental flow visualization across the rotor path is available, these vortices are typical structures observed in similar configurations as described in [13], Fig. 4.16(b), and in [16], Fig. 4.16(c). To highlight further the development of these

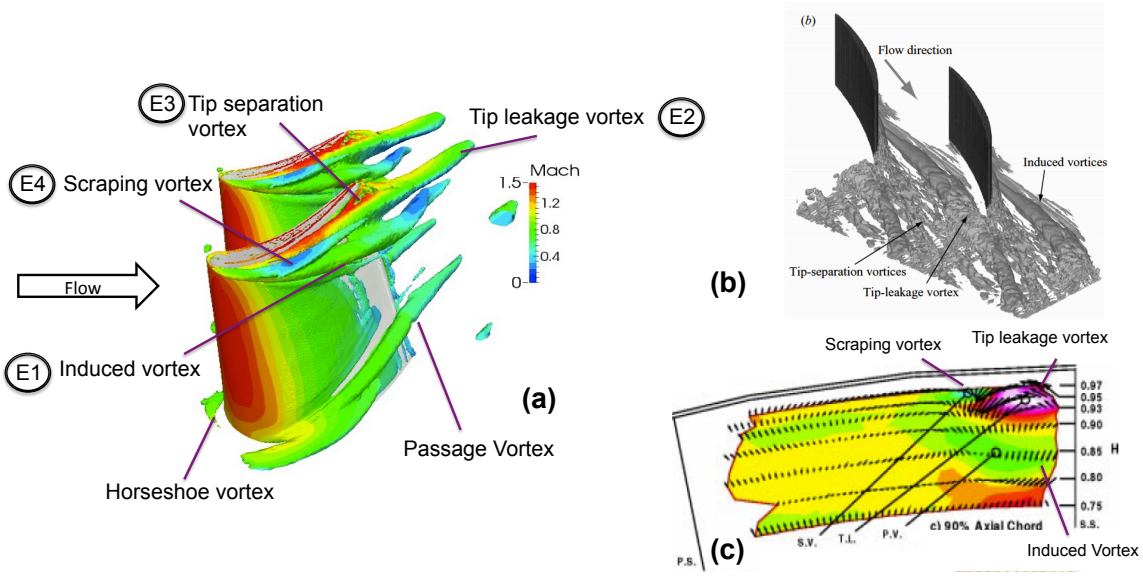

Figure 4.16: Q criterion of a time-averaged solution across the rotor blades (a) and tip clearance flow topology of a cascade from the LES of You *et al.* [13] (b) and from the experiments of McCarter *et al.* [16] (c).

flows the helicity, computed from a time-averaged relative velocity field, is plotted across the rotor domain at 50% of the chord, Fig. 4.17(a), and at the rotor exit, Fig. 4.17(b). Helicity provides information on the direction of rotation of the observed secondary and tip vortices, with negative helicity indicating a counter-clockwise rotation (seen from the front) and positive helicity indicating a clockwise rotation. At 50% of the chord, four principal structures are observed: the hub passage vortex, the tip leakage vortex, the induced vortex and the scraping vortex. The induced and scraping vortices have opposite directions of rotation to the other two ones, in agreement with the observations from the experiments of McCarter *et al.* [16] in Fig 4.16 or RANS predictions of high-pressure turbine stages from Wlassow [5]. The induced vortex is at the side of the tip leakage vortex and is moving around it while the hub passage vortex, that has migrated from the pressure side of the neighboring blade, is still close to the endwall and the rotor suction side. At the rotor exit, Fig. 4.17(b), the induced vortex has moved under the tip leakage vortex, while the scraping vortex is no longer present. The hub passage vortex has increased in size and migrated towards the mid-span of the passage. Note that the flow organization described above is present in all simulations.

In the following section, mean flow profiles are compared and gauged against the experimental data prior to a more detailed analysis on the unsteady features of the simulations using MESH1. An evaluation of the influence of the mesh resolution is then addressed, for which the predictions using MESH2 are specifically looked at.

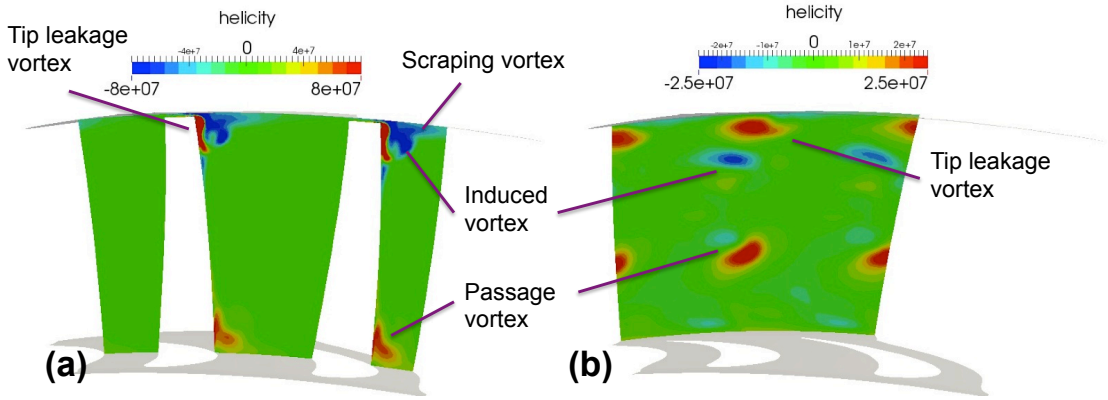

Figure 4.17: Helicity of a time-averaged relative velocity flow field.

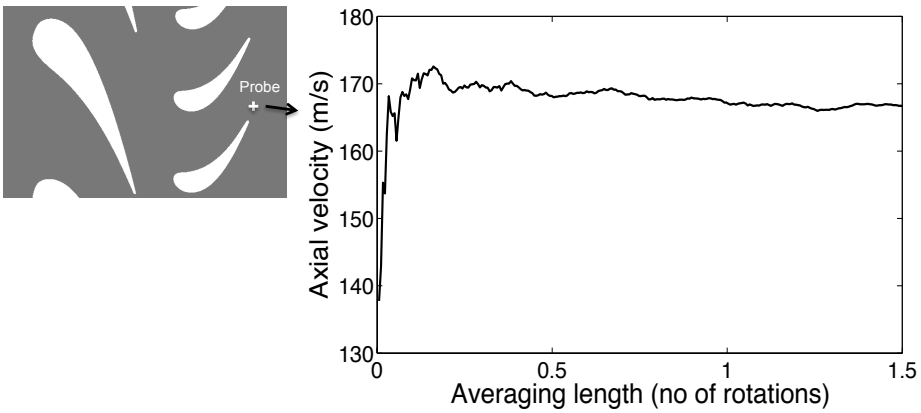

Figure 4.18: Time-averaged axial velocity at a probe in the rotor wake as a function of the averaging time.

4.7 Low resolution results

Mean Flow Field Predictions

Before analyzing the mean flow field, the adequacy of the averaging time is established on the basis of **Case 1**. To do this, the signal of the axial velocity from a simple temporal probe located in the rotor wake is used. This position is chosen to ensure that the probe is subjected to both unsteady blade wakes, responsible for a large part of the unsteadiness observed across a turbine stage. The signal is then averaged using different time lengths, up to 1.5 full rotations of the rotor, and the average axial velocity at the probe location is plotted. The result is shown in Fig. 4.18. It is evident that after approximately 0.8 rotations the averaged axial velocity reaches a converged value, hence the chosen runtime for obtaining time-averaged solutions of 1 rotation is sufficient.

The first step in evaluating the differences between each model is obtained by looking

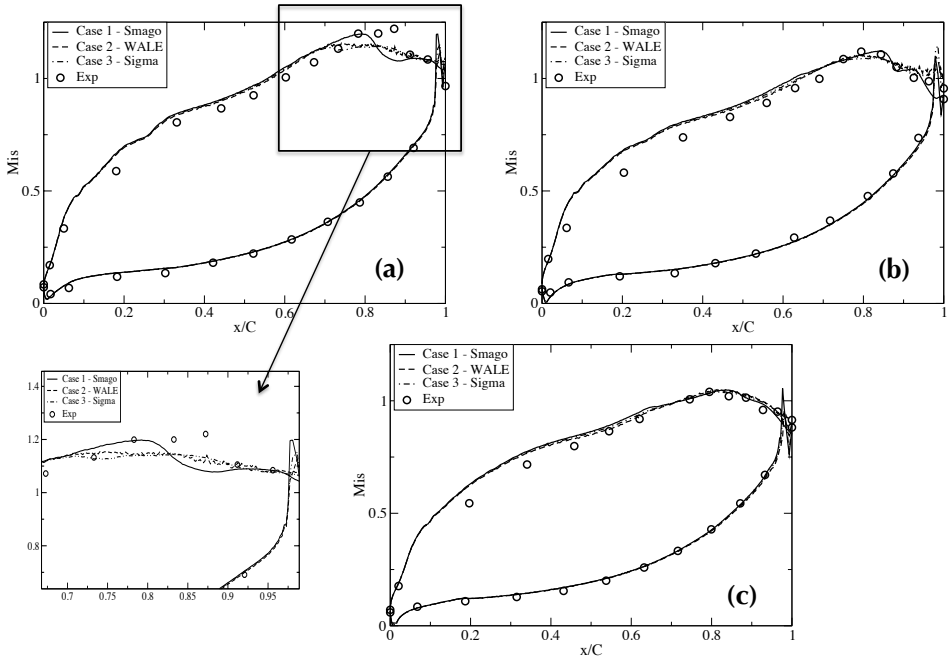

Figure 4.19: Isentropic mach number across the stator at 10% (a), 50% (b) and 90% span.

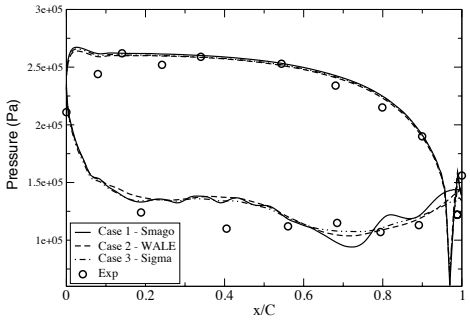

Figure 4.20: Static pressure across the rotor blade at mid-span.

at the pressure profiles across the blades. To do so, Fig. 4.19 shows the time averaged isentropic Mach number across the stator vane for the three SGS models (**Cases 1**, **2 & 3**) and for three different spans of the blade: 10, 50 and 90%. All three models predict similar behaviors across both the pressure and suction sides. Small differences exist near the trailing edge at 10% span, where a hub corner vortex exists, Fig. 4.15, and for which each model predicts a slightly different location of the separation point. This phenomenon leads to a plateau of the pressure profiles at the suction side near the trailing edge. At the other spans, the minor differences are related to the shock structures on the suction side. Reasons for such changes are differences in the boundary layer thicknesses as well as potential interactions of the outer boundary layer flow unsteady content with the law-of-the-wall model [59]. Typically, **Case 1** produces much stronger shock structures in the stator that are not present for **Cases 2 & 3**. Such findings emphasize the need for

accurate treatment of the modeling in the main stream along with an adequate coupling with the law-of-the-wall to guarantee the desired turbulent flow properties of Table 4.3. Similar findings are observed for the rotor, Fig. 4.20, if looking at pressure profiles across the blade at mid-span.

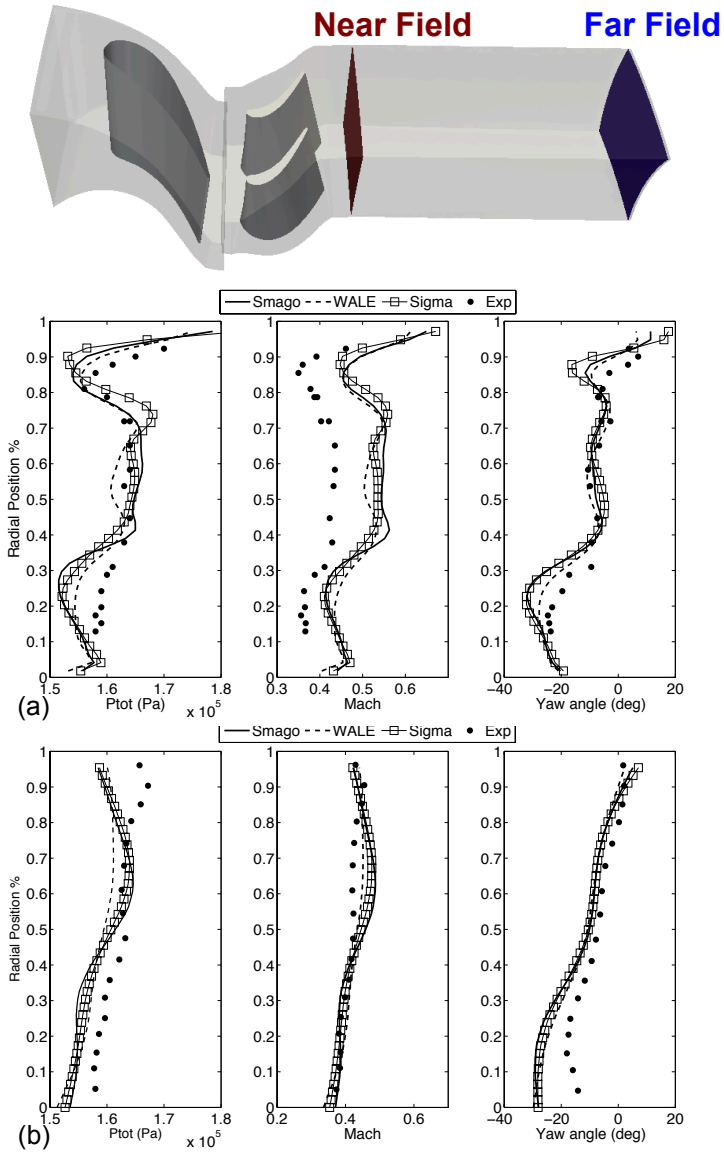

Figure 4.21: Radial profiles for **Cases 1**, **2**, **3** at the rotor exit (a) near field (b) far field.

Azimuthally and time-averaged radial profiles of several flow variables at the rotor exit obtained by LES and measured experimentally are shown in Fig. 4.21. Two exit stations are displayed: (a) the near field position located less than one rotor chord after the stage and (b) the far field station which is located approximately three rotor chords from the stage. All LES predictions show good qualitative agreement with the experiments at

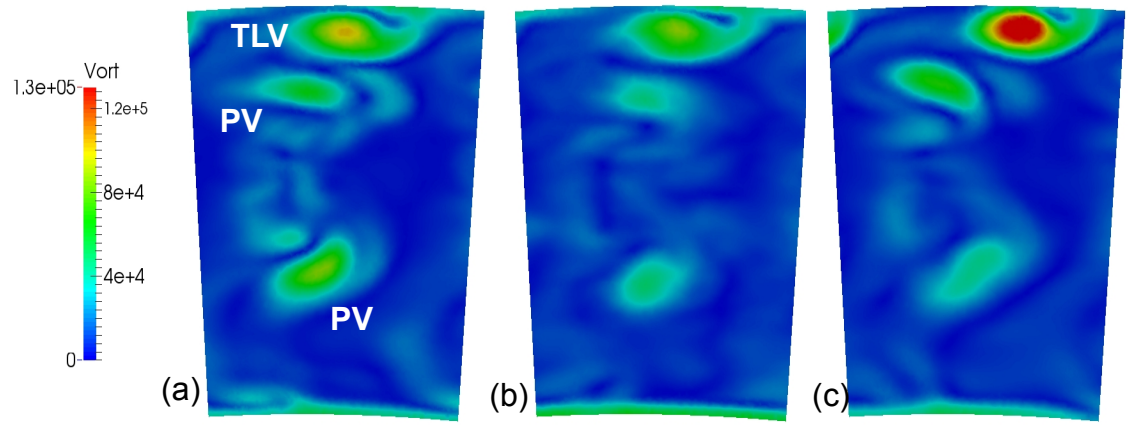

Figure 4.22: Vorticity of the mean velocity field at the rotor exit for **Case 1** (a), **Case 2** (b) and **Case 3** (c).

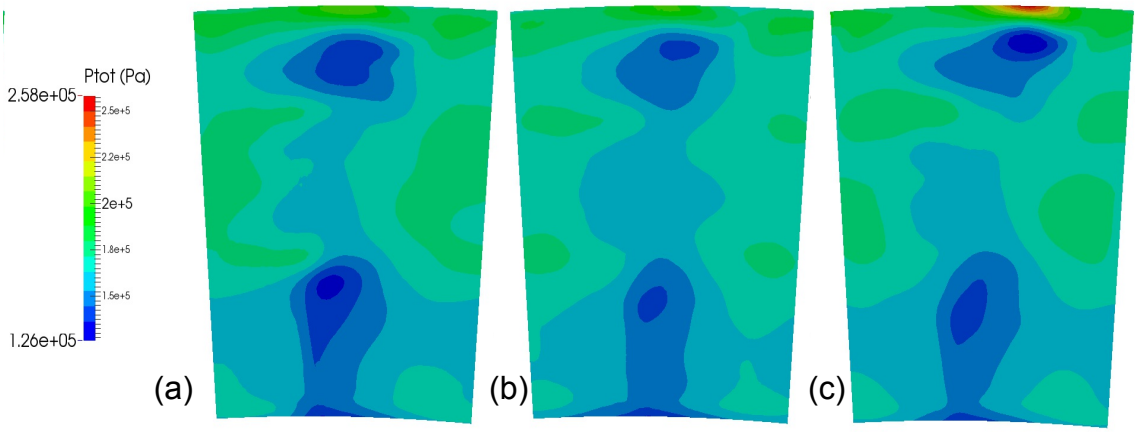

Figure 4.23: Total pressure of the mean velocity field at the rotor exit for **Case 1** (a), **Case 2** (b) and **Case 3** (c).

both locations, with **Case 2** producing slightly improved predictions for the flow exiting the rotor. Most differences with the experiments are concentrated in the hub and casing regions where further grid resolution would most likely improve the predictions. To better discriminate the impact of SGS on the LES predictions, magnitudes of the mean vorticity and mean total pressure in the near field rotor exit plane are provided respectively in Figs. 4.22 and 4.23. The three main structures evidenced from Figs. 4.14 and 4.16 are also reported here for clarity. Although the expected mean flow structures are reproduced by the three models, differences in energy content are clearly evidenced and are related to the different model properties which impact the overall loss prediction mechanisms. As anticipated, the tip leakage vortical structure is of crucial importance just like the casing flow and passage vortex strength for the lower radial part of the stream.

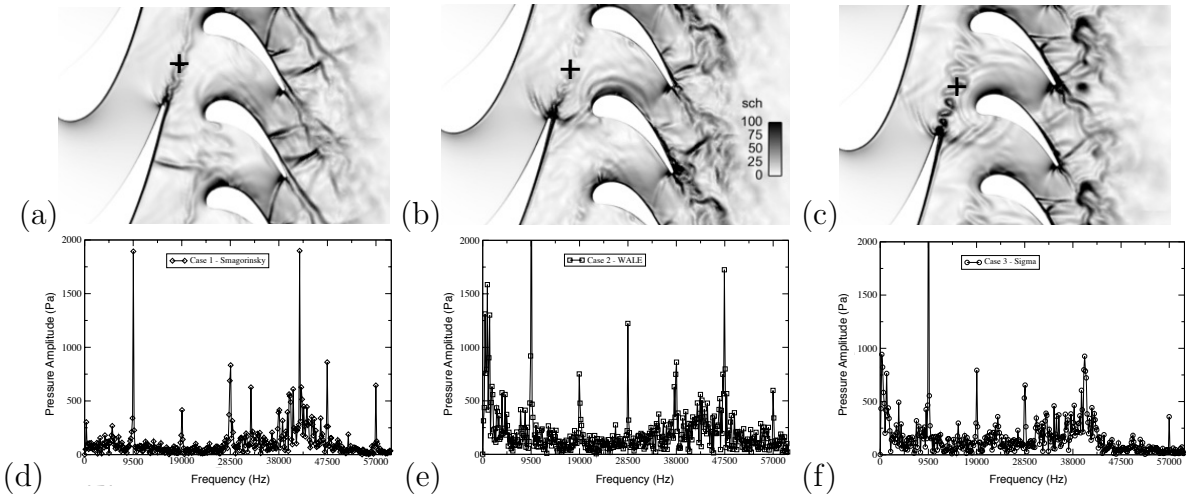

Figure 4.24: Instantaneous views of $\frac{||\nabla\rho||}{\rho}$ at mid-span (a)-(c) and FFT's of the pressure signal for the identified probe (d)-(f) for **Case 1** (a) & (d), **Case 2** (b) & (e) and **Case 3** (c) & (f).

Unsteady flow features

Looking at an instantaneous density gradient ($\frac{||\nabla\rho||}{\rho}$) at mid-span and across the flow field for the 3 cases, Fig. 4.24 (a)-(c), allows to evaluate the unsteady content of each simulation. Aside from the acoustic waves that propagate and impact neighboring blades, different flow patterns appear to be affected by the SGS models. Shock locations and strengths are not the same, although **Cases 2 & 3** converge to a similar flow picture, thus explaining the observed differences in Figs. 4.19 and 4.20. Stator wakes are also affected, as evidenced by the FFT's of pressure signals extracted from a probe and illustrated for the three LES in Fig. 4.24(d)-(f). From this diagnostic, multiple peaks appear with amplitudes differing depending on the SGS modeling used (recall that for this operating condition the rotor BPF equals 9.5 kHz). For all cases, the peaks related to the passing rotors are particularly clear. Higher harmonics, although clearly present, can however be altered by the modeling. Another expected peak is related to the Vortex Shedding (VS) from the trailing edge of the stator. For **Cases 1 & 3** it approaches 42 kHz. **Case 2** shows a much weaker peak over a wider range of frequencies with a particularly strong peak at the 5th harmonic of the rotor BPF. Such changes in spectra furthermore indicate that the energetic flow content issued by the three different SGS models can be very different.

In an attempt to distinguish the fully turbulent features from the deterministic rotor/stator interactions a triple decomposition is detailed in the following paragraphs. In turbine flows there is inherent unsteadiness due to the passing blades occurring at the BPF and its harmonics; the stator blades are subjected to the potential effects of the rotors behind them (and the rotor wakes from previous stages if a multi-stage turbine is analyzed) and the rotors encounter the stator wakes. This can be considered a deterministic phenomenon that is repeated in time, a fact exploited for example by the phase-lag

method. On top of these deterministic oscillations there are additional turbulent fluctuations generated by the flow, that are stochastic by nature, as well as other unsteady phenomena occurring at other frequencies. These will be superposed on the deterministic ones. This concept is illustrated more clearly in Fig. 4.25, which illustrates a pure deterministic oscillation that is repeated in time (here a simple sinusoidal function, solid line) and the result of the superposition of random fluctuations on that signal (dotted line). From this it is evident that calculating the root-mean-square of that signal after simple time averaging, without any additional treatment, will provide fluctuations that include both these components. In the turbine flow context, it is desirable to separate deterministic from stochastic oscillations as the modeling may impact each component differently and reveal more about the differences observed in the spectra. To this end, a triple decomposition is employed.

Triple decomposition analysis

For any flow where a deterministic or fixed frequency interaction is present and known, the following decomposition can be used to characterize the flow response at any point in time and space of the simulation [174],

$$u_i(x,t) = \overline{U_i}(x) + u_i'^{\mathrm{det}}(x,t) + u_i'^{\mathrm{stoc}}(x,t). \tag{4.2}$$

In Eq. (4.2), the overbar stands for the temporal average, $u_i'^{\mathrm{det}}(x,t)$ is the deterministic fluctuation of the field due to the passing blades in our case and $u_i'^{\mathrm{stoc}}(x,t)$ is the stochastic or remaining part of the turbulent signal. Postulating that $u_i'^{\mathrm{stoc}}(x,t)$ is not correlated to the deterministic oscillations $u_i'^{\mathrm{det}}(x,t)$, phase averaging of $[u_i(x,t) - \overline{U_i}(x)]$ results in an evaluation of $u_i'^{\mathrm{det}}(x,t)$ [174] and access to the three components of Eq. (4.2).

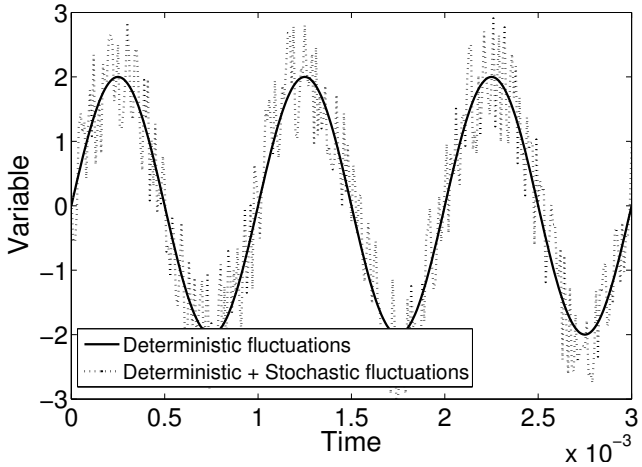

Figure 4.25: Deterministic oscillation (solid line) and deterministic oscillation with random fluctuations (dotted line).

Depending on the deterministic frequency selected for the decomposition, different contributions will be evidenced. Typically, if the rotor BPF is chosen (9.5 kHz), $u_i'^{\mathrm{det}}(x,t)$

will produce fluctuations induced by the flow modulation at that frequency: *i.e.* the potential flow oscillation imposed to the stator flow because of the relative and temporally evolving rotor blade position in the stator vane exit section. Likewise, if the stator BPF is chosen (4.75 kHz), the potential flow modulation imposed by the stator to the rotor vane will be evidenced by $u_i'^{\mathrm{det}}(x,t)$. To illustrate the SGS model effects on the distributions, energetic contents are constructed for the different fluctuating components: *i.e.* $\sqrt{\frac{1}{3}\,\overline{u_i'^{\mathrm{det}}u_i'^{\mathrm{det}}}}$ and $\sqrt{\frac{1}{3}\,\overline{u_i'^{\mathrm{stoc}}u_i'^{\mathrm{stoc}}}}$. Estimates are then azimuthally averaged and normalized by the radially dependent mean velocity norm (temporally and azimuthally averaged velocity norm) to produce dimensionless radial profiles of the deterministic and stochastic turbulent intensity distributions within the stage and respectively noted: $Tu_{\mathrm{det}} = \sqrt{\frac{1}{3}\,\overline{u_i'^{\mathrm{det}}u_i'^{\mathrm{det}}}}/||\overline{U_i}||$ and $Tu_{\mathrm{stoc}} = \sqrt{\frac{1}{3}\,\overline{u_i'^{\mathrm{stoc}}u_i'^{\mathrm{stoc}}}}/||\overline{U_i}||$ where $||\overline{U_i}||$ stands for the time average velocity vector norm. Note that in the remaining, all contributions are obtained out of a total of 400 LES snapshots equally spaced and covering 50 periods of each selected frequency (either the rotor or the stator BPF), the deterministic components being represented by 8 equally spaced phases of the targeted period.

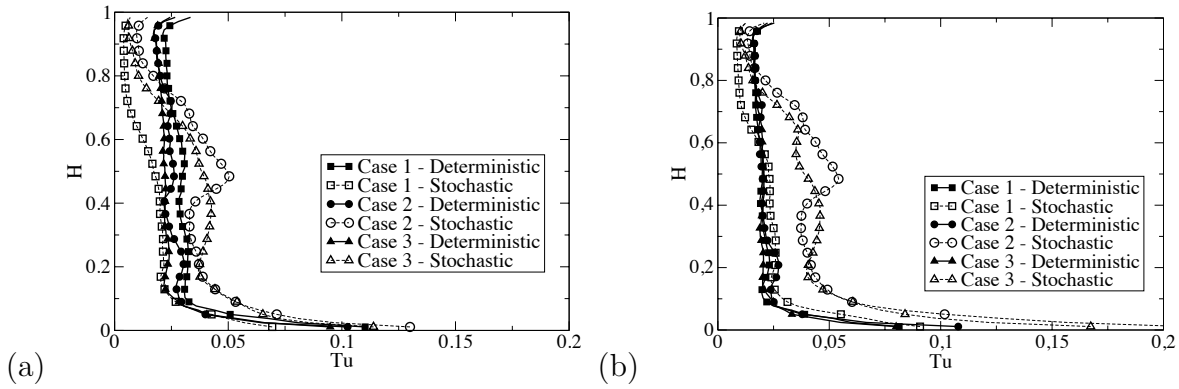

Figure 4.26: Radial profiles of the unsteady activity obtained at the rotor / stator interface for all three LES and based on a triple decomposition using (a) the rotor BPF (9.5 kHz) and (b) the stator BPF (4.75 kHz).

Typical results are provided in Figs. 4.26 & 4.27 for the rotor and stator BPF based decompositions. Only two sections in the stage are here presented: the rotor/stator interface, computed in the fixed stator domain and shown in Fig. 4.26, and the near field exit plane of the rotor, computed in the rotating rotor domain and shown in Fig. 4.27. At the interface, Fig. 4.26, deterministic turbulent intensities are rather insensitive to SGS modeling whatever the reference frequency used which confirms that such interactions are essentially geometrical (as expected). However, they are not insignificant and, with an azimuthal average having been introduced, this spatial dependency is seen over the entire height of the section. Stochastic contributions are on the other hand clearly influenced by SGS modeling. Although **Case 1** produces levels of stochastic flow activities of the same order as the deterministic one, **Cases 2 & 3** produce uncorrelated intensities as much as twice as high as the deterministic contribution. Looking further into the details

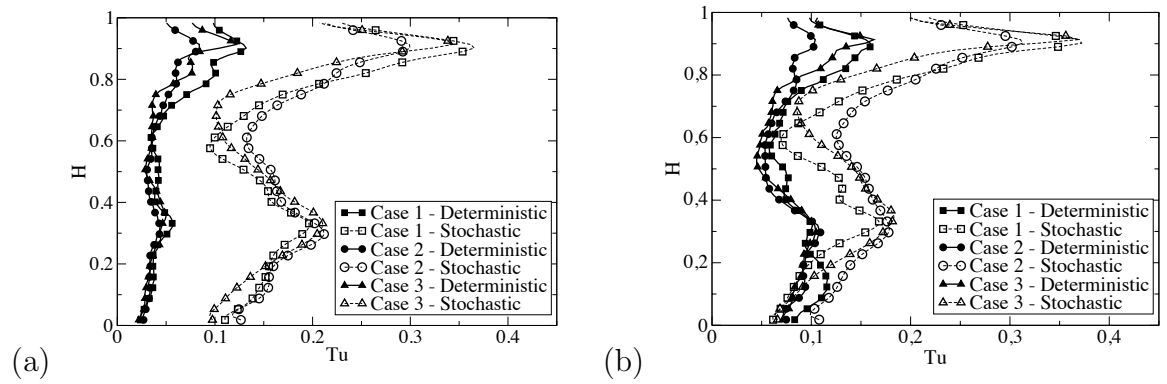

Figure 4.27: Radial profiles of the unsteady activity obtained at the exit of the rotor (near field plane of Fig. 4.21) for all three LES and based on a triple decomposition using (a) the rotor BPF (9.5 kHz) and (b) the stator BPF (4.75 kHz).

of these stochastic contributions issued by **Cases 2 & 3**, changes do locally occur around mid-span, issued by different stator wake profiles, further stressing the importance of SGS modeling.

At the near field exit plane, Fig. 4.27, conclusions slightly differ. First, deterministic activity is clearly impacted by the selected reference frequency. Levels obtained for the signal issued by the rotor BPF, Fig. 4.27(a), are indeed smaller than the one obtained for stator BPF, Fig. 4.27(b), as it corresponds to the second harmonic of the stator BPF, the principal frequency seen by the rotor, and is thus weaker. Furthermore and although azimuthal averages are applied, SGS modeling is seen to impact the deterministic components of the flow activity. For the rotor BPF based decomposition, Fig. 4.27(a), differences mainly appear in the region of the tip leakage flow whose extend and intensity is changing with SGS modeling. For the stator BPF based decomposition, the same observations are valid with a clear and bulk increase of the associated levels complemented by a response of the near hub and near casing flow in all cases. In their stochastic counterparts, local differences appear and are linked to SGS modeling but the overall levels seem unchanged between the different cases. The main impact observed here and linked to SGS modeling appears for the stator BPF based decomposition, Fig. 4.27(b), for which the three LES depict different extents of the stochastic activity issued by the near casing, tip leakage flow. Note finally that based on these two decompositions, the similar behaviors of the two contributions either obtained from the stator or rotor-BPF based decompositions, no conclusion on the flow organization in the rotor is captured by Fig. 4.26. This underlines that the observed flow differences between models in Figs. 4.24(a)-(c), in the rotor are independent of the deterministic rotor/stator interactions or turbulent stochastic content. Differences in shock patterns in the stator for example are therefore to be related to intrinsic modeling issues involving SGS modeling. In that respect, **Cases 2 & 3** really differ from **Case 1**.

The strong impact of the SGS modeling observed in the presented results, with different results for each model, is exacerbated by the relatively limited MESH1. As a result,

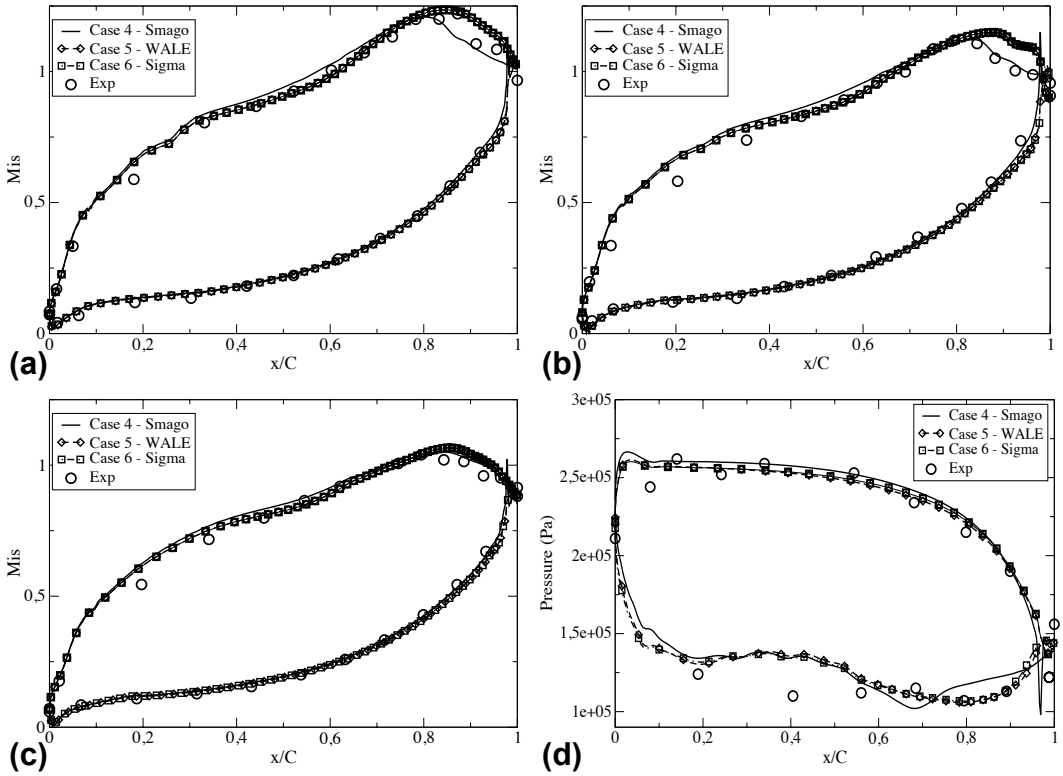

Figure 4.28: Isentropic mach number across stator blade at 10% span (a), 50% span (b), 90% span (c) and normalised pressure across the rotor blade at 50% span (d) for the cases employing MESH2.

further investigations are still needed using the refined MESH2. Improving the overall grid resolution will allow to evaluate whether the results obtain from the different models are similar to their low-resolution counterparts or whether there is a convergence to a common flow field.

4.8 High resolution results

For this part, the second set of predictions from Table 4.4 are investigated. **Cases 1-3** of the previous part are used for comparisons wherever deemed necessary. The objective is to investigate the impact of higher mesh resolution on the mean flow variables as well as on the general flow field and vortical structures. Since turbine flows are wall-dominated flows, the impact of the near-wall resolution is expected to be of particular importance. Indeed, reducing the cell size allows to resolve more turbulent fluctuations and ideally a more accurate unsteady representation of the flow field is expected. Note that the wall law continues to be applied since y^+ values obtained with this refined mesh place the first nodes in the beginning of the buffer region of a typical turbulent boundary layer.

Time-averaged predictions

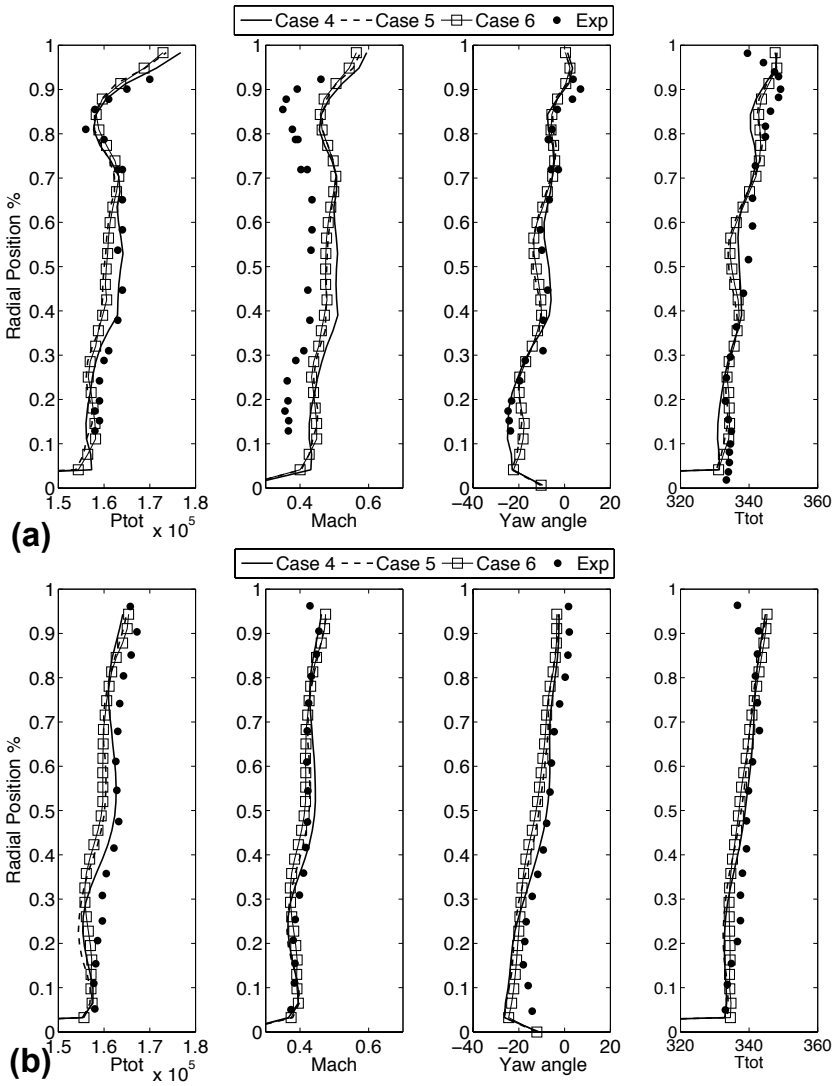

Figure 4.29: Rotor exit profiles in near (a) and far (b) field for the cases employing MESH2.

Figure 4.28 shows the isentropic Mach number and normalized pressure across the stator and rotor blades respectively for the three high resolution cases. The differences between them are only minor and are located mainly at the trailing edge of the stator at 10% span, where the hub corner vortex is present. It can be concluded that the mean pressure field is not significantly improved by the higher mesh resolution. The agreement with the experimental measurements remains fair like for the coarse cases. Figure 4.29 compares the azimuthally averaged radial profiles at the rotor exit. Both in the near and in the far field, there is a general improvement over **Cases 1 & 2**, Fig. 4.21, particularly in the tip clearance region where the number of cells has been increased from 6 to approximately 20 layers. The number of cells, however, is still insufficient and additional refinement

seems necessary for further improvement of the predictions, which is in agreement with the findings of You *et al.* [140]. Experimental trends are nonetheless better captured in the far field as well (where previously the cell size was much bigger). Overall, the mean thermodynamic variables agreement with the coarser mesh predictions, Figs. 4.19 - 4.21, is rather good although, when looking more into details, significant differences are observed.

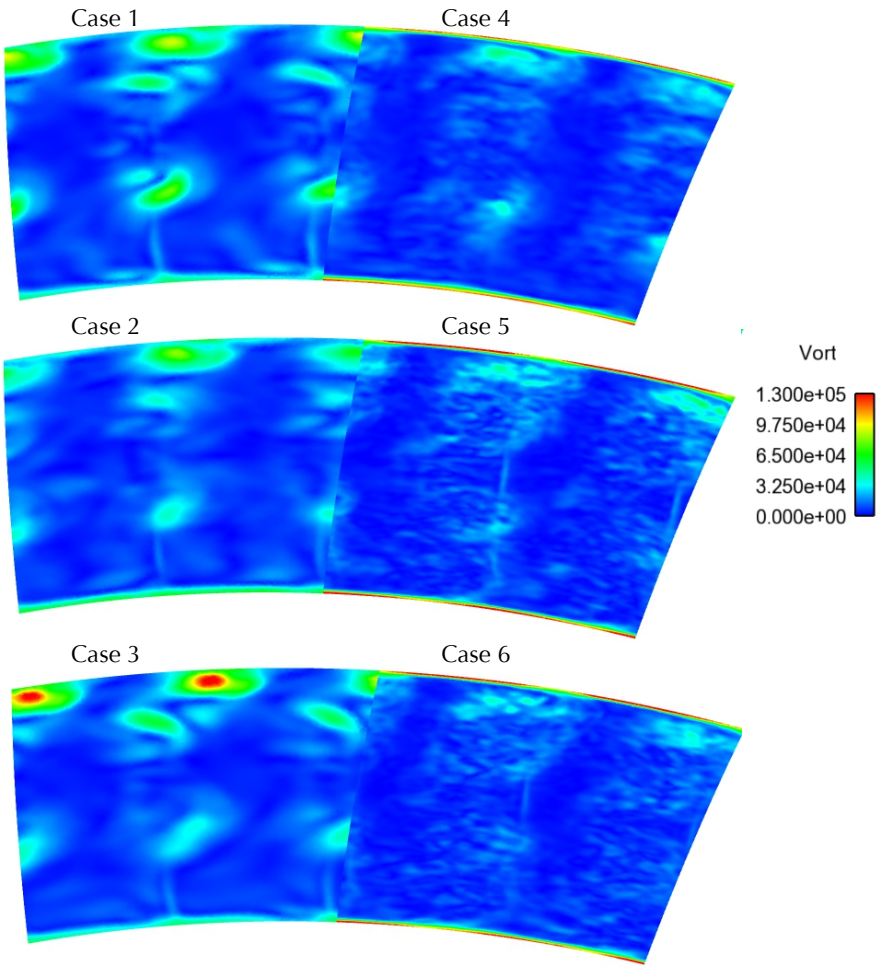

Figure 4.30: Vorticity magnitude comparisons at the rotor exit all cases grouped according to the SGS model employed.

First, the vorticity magnitude at the rotor exit (near field), calculated from a time-averaged velocity field, is plotted for all cases, Fig. 4.30. Each of the first three cases is plotted next to its corresponding high resolution case (same SGS model). Such comparisons serve to highlight the changes in the flow topology as well as in the position and strength of the secondary flows. The first observation is that the main secondary flows are recovered in all refined cases. Their positions also appear similar. Changes in their strength are, however, present with the high resolution cases (**Cases 4-6**) showing

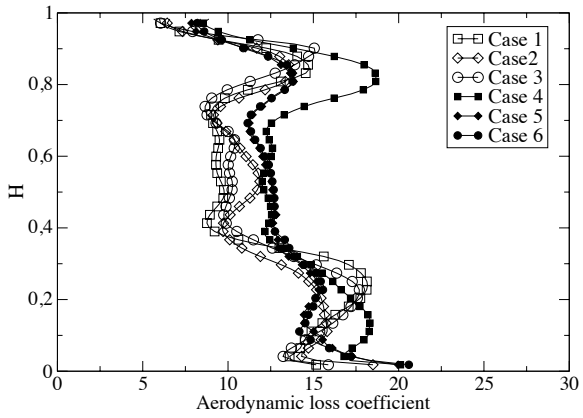

Figure 4.31: Azimuthally averaged loss coefficient as a function of the normalized radius for the six cases.

weaker vortices. The passage and induced vortices in particular appear much less pronounced. This is likely due to the higher effective Reynolds number flow that increases mixing and turbulent fluctuations, extracting energy from the coherent structures. At the same time, the endwall boundary layers become more pronounced with MESH2, a result of the increased near wall resolution. A relatively good coherence on the vortex positions between all the high resolution cases is also evidenced, a notable difference from the coarse **Cases 1-3** which showed differences both in the strength and placement of the tip-leakage vortices when compared with each other.

Findings obtained from the vorticity based analysis impact also the predicted aerodynamic losses. Figure 4.31 depicts the azimuthally averaged aerodynamic loss coefficient $\zeta(r) = (Pt_{in} - Pt_{out})/(Pt_{out} - Ps_{out})$ as a function of the radius for the 6 cases. It can be readily observed that with the higher mesh resolution losses are increased between 30 and 70% height, an indication of higher profile and mixing losses. Closer to the hub and the casing (20% and 80% of H respectively), where the secondary flow losses are prevalent, the high resolution cases show reduced values of the loss coefficient, in agreement with the weaker tip leakage flows and passage vortex of Fig. 4.30. Their respective contribution still remains pronounced with two distinctive peaks present near the hub and casing. The increase in profile losses is most likely the main contributing factor in the operating point differences identified between the cases and shown in Fig. 4.13. With respect to the coherence between the refined simulations, **Cases 5 & 6** are in excellent agreement with each other, while **Case 4** shows differences. The principal common point between these **Cases 5 & 6** is that their respective SGS model respects the property P1, the turbulent viscosity damping as the wall is approached. This property is essential in this type of flows and, in conjunction with the high resolution mesh that permits better resolution of the boundary layers, results to the computations converging to the same flow picture. **Case 4** on the other hand, dominated by excessive near-wall turbulent viscosity, does not produce the same predictions and convergence to either **Case 1** or **Cases 5 & 6** is

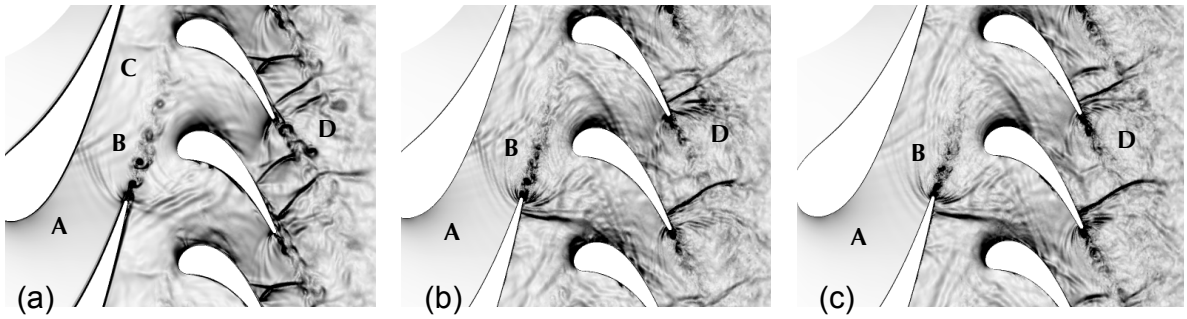

Figure 4.32: Instantaneous views of $\frac{||\nabla\rho||}{\rho}$ at mid-span for Cases 4 (a), 5 (b) and 6 (c).

not encountered.

Unsteady features

Looking at the density gradient for **Cases 4-6**, Fig. 4.32, to be compared to the coarse cases in Fig. 4.24, allows a quick overview of the unsteady activity across the turbine. With the refined mesh a much richer flow is revealed throughout with finer structures and increased acoustics. Figures 4.32(b,c) in particular reveal the strongest activity. A first notable difference is the evolution of the boundary layer for **Cases 5 & 6** (position A), where a much finer boundary layer appears compared to the coarse cases and **Case 4**. Clearly, the satisfaction of property P1 by the WALE and σ changes the boundary layer prediction. The reduction of the thickness with the increased near-wall resolution is also in agreement with the findings of Gourdain [148, 149] in a compressor stage, where refined meshes in conjunction with a non-intrusive LES model (the WALE model was employed solely in that work) resulted in thinner boundary layers. Differences are observed also in the stator wake and shock structures (Position B). The coherent vortex shedding depicted in Fig. 4.24 has been replaced by turbulent vortex shedding with vortices quickly braking up downstream. The trailing edge shock structure is also altered, with a very pronounced shock visible for **Cases 5 & 6** that interacts with the passing rotor blades in a similar fashion as in the high-pressure turbine stage of [175]. Recall that at Position C, **Case 1** was showing a double shock structure. In its corresponding refined prediction, **Case 4**, this is replaced by a much weaker single shock. Finally, Position D at the rotor exit is another area where major shock changes appear. **Case 4** depicts a blade with a pronounced λ shock at approximately 70% of the chord, that is seen to be sensitive to the passing stator wakes (it is of different strength for each rotor blade indicating that the strength of this shock is a function of the rotor phase with respect to the stator wake). It is followed by another shock near the trailing edge. The trailing edge shock, on the other hand, is the only major shock structure for **Cases 5 & 6**. As with the aerodynamic losses, there is an excellent agreement between **Cases 5 & 6** for the unsteady flow field as well, highlighting that indeed they predict a similar flow field.

Comparisons of the turbulent content of the flow can be useful to establish the changes in the turbulence cascade and turbulent production. To this end, a Power Spectral

Density (PSD) is evaluated for the axial velocity component signals recorded from probes located in the stators wake (same position as the probes shown in Fig. 4.24). Results are plotted in Fig. 4.33 using logarithmic scales in an effort to distinguish a turbulent cascade. The first finding is that the coarse **Cases 1-3** have pronounced peaks at the vortex shedding frequency and its harmonics, highlighting the more coherent and less turbulent nature of the vortex shedding from the stator trailing edge. Between peaks, differences are observed with the WALE and σ models permitting a narrow turbulent cascade to appear and an increased cut-off frequency compared to Smagorinsky. For the refined **Cases 4-6** results are very different. The cut-off frequency of the refined mesh is almost double the one of the coarse cases (approximately 800 kHz) and a pronounced turbulent cascade is visible. No particular peak appears, highlighting the strongly turbulent nature of the vortex shedding of this position. Another finding is the good agreement between these high-resolution **Cases 4-6** for which the effect of the SGS model is less pronounced.

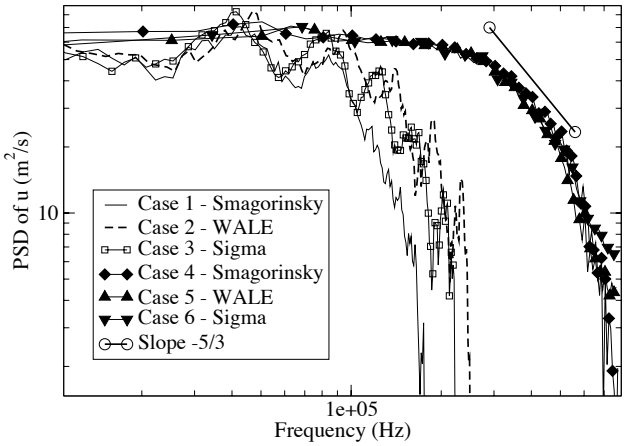

Figure 4.33: Power Spectral Density of the axial velocity signal recorded at a probe in the stator wake.

Near-wall characteristics

An area where significant improvement is expected with the refined mesh is the wall shear stress across the stator guide vane. In the present wall-modeled approach, the wall shear stress is calculated by a classic log-law that assumes a turbulent profile and uses flow information from the first node off the wall. In the stator of high-pressure turbines this procedure can create errors for two reasons: First, in regions where the boundary layer is not expected to be turbulent increased shear stress is predicted by the turbulent log-law, particularly at the suction side where the flow accelerates due to the blade curvature [176]. Second, if the turbulent viscosity is not zero close to the wall, as one expects, flow gradients and boundary layer profiles will be altered thus modifying the computed shear stress. On top of these two effects, the use of instantaneous flow variables, shown to be highly sensitive to the mesh resolution in LES, to calculate the

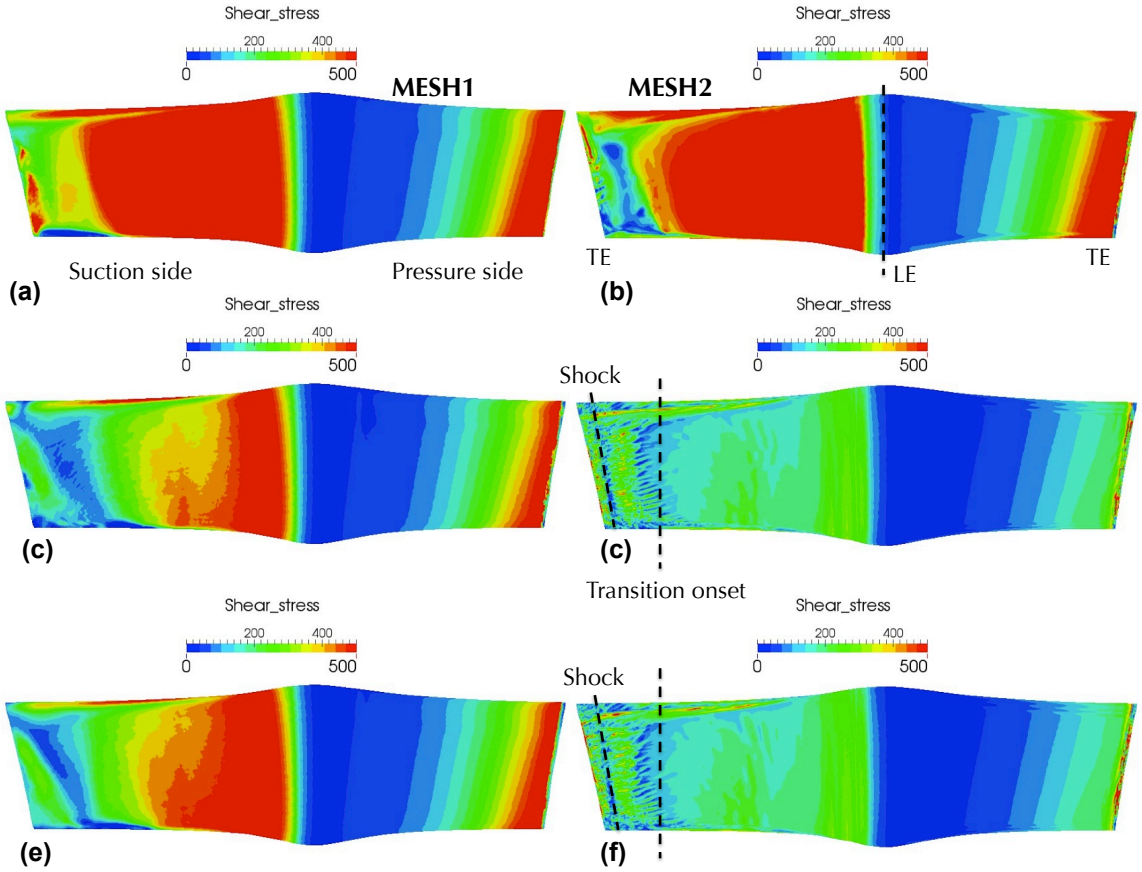

Figure 4.34: Shear stress across the stator blades for the two mesh resolutions. With the smagorinsky model (a),(b) - WALE model (c),(d) and σ model (e),(f).

wall shear stress from the analytical log-law can induce further errors [172].

Figure 4.34 depicts the shear stress at an instant across the stator for all 6 cases, with the blade opened to show both sides at the same time for clarity. The left side depicts **Cases 1-3** that use MESH1, while the right side shows **Cases 4-6** which employ MESH2. For **Cases 1 & 4**, that use the Smagorinsky model, the differences between MESH1 and MESH2 are minimal. It is evident that the turbulent viscosity produced in the boundary layer is a determining factor in the near-wall flow and the overall shear stress estimation. For the WALE and σ models, switching from MESH1 to MESH2 completely changes the shear stress profiles on the suction side of the blade. With the refined mesh, the overall levels of shear stress from the Leading Edge (LE) up to 50% of the chord are drastically reduced. In this area the flow accelerates strongly. The log-law turbulent formulation translates this accelerating region into increased wall shear stress based on a turbulent boundary layer formulation [176]. On the other hand, placing the first point deeper in the boundary layer, as is the case for the refined mesh, improves the boundary layer predictions and the velocity of the first node off the wall is reduced, thus reducing the shear stress value. Such an effect is not visible if the turbulent viscosity levels in this

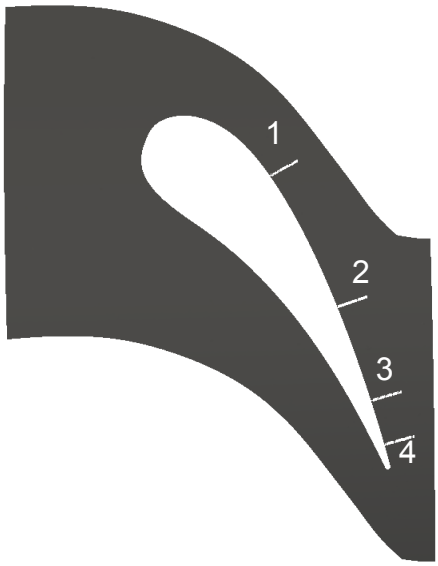

Figure 4.35: Positions across the suction side of the stator blade where the boundary layer profiles are plotted.

region are high. Another interesting point is that for **Cases 5 & 6**, Figs. 4.34(d,f), laminar-to-turbulent transition appears at around 70% of the chord, a characteristic not at all present for **Case 4**, despite the same mesh. This shows that, even with a turbulent log-law formulation and an unforced simulation, resolving more of the boundary layer with an appropriate SGS model allows more fluctuations to develop which can trigger transition. It also justifies the comment of Tucker [14] with respect to the importance of SGS modeling in transitional flows. Naturally, the point of the transition is highly sensitive to incoming free-stream turbulence [23, 9], which is not applied for this simulation, rendering the evaluation of the transition point irrelevant or at least questionable in this case. Commonality between all the different cases appears with respect to secondary flows, their traces being visible on the shear stress close to the hub and casing in a similar fashion as in Fig. 4.15(a). Finally, as with the previously presented results, **Cases 5 & 6** show remarkable agreement, the profiles being almost identical.

To investigate further the differences observed in the shear stress levels between the refined **Cases 4-6**, boundary layer profiles of the time-averaged tangential (parallel to the wall surface) velocity and turbulent kinetic energy are plotted at 4 different positions across the suction side of the stator blade at mid-span. These positions are highlighted in Fig. 4.35 and were chosen to correspond to the main findings from Fig. 4.34. The first 2 are placed in areas of relatively limited activity where the adverse pressure gradient starts developing. The third is where transition appears to be triggered in Figs. 4.34(d,f) and the fourth near the trailing edge, where in Figs. 4.34(d,f) a shock interacts with the boundary layer and a drop in the shear stress is observed.

Results are plotted in Figs. 4.36 and 4.37. The mean velocity profiles across the boundary layer in Fig. 4.36 are plotted as a function of y/δ, where δ is the boundary

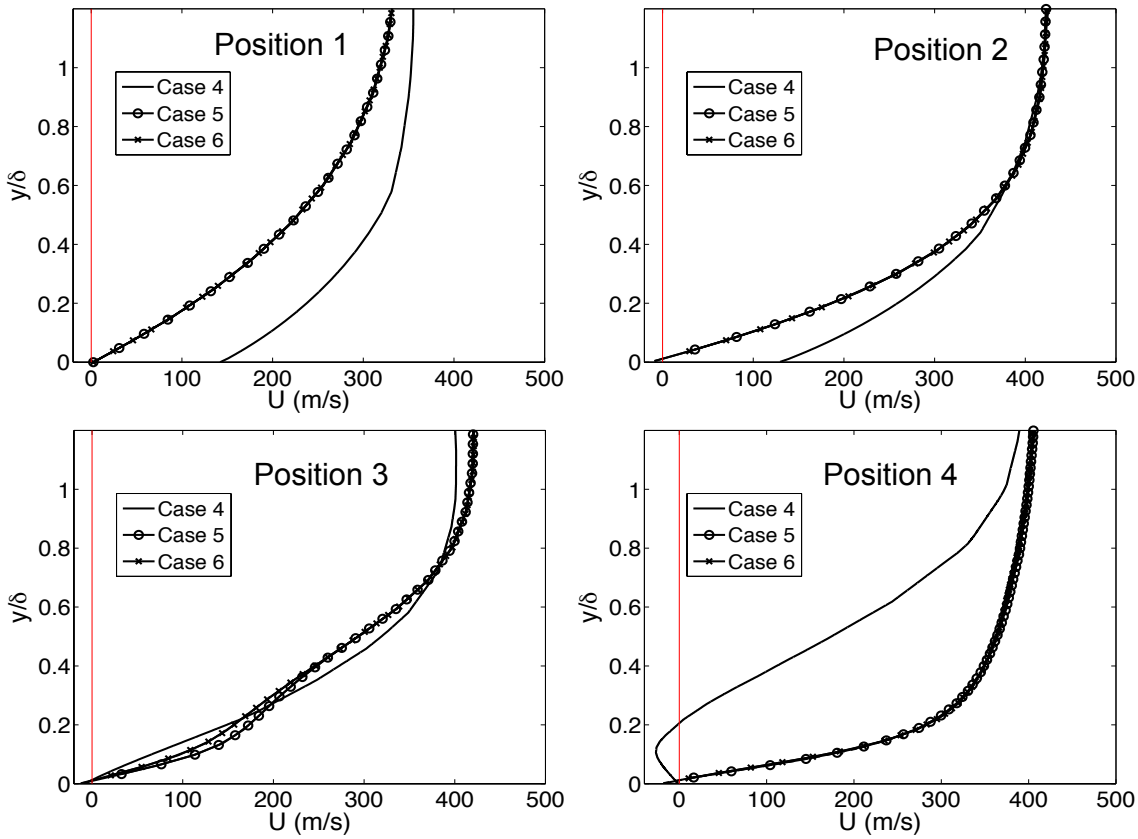

Figure 4.36: Wall tangential velocity across the boundary layer at 4 different suction side positions. The red line corresponds to zero velocity.

layer thickness defined as the wall-normal distance where the velocity is smaller than 99% of the free-stream velocity. The corresponding boundary layer thicknesses for each case and each measuring position are provided in Table. 4.5. For positions 1 and 2, the boundary layer appears laminar for all cases. However, **Case 4** exhibits a very limited slope, increased thickness and very high near-wall velocity compared to cases **Cases 5 & 6**. It is important to remember that the log-law allows for a slip velocity at the wall nodes. This velocity for **Case 4** is clearly over-predicted and leads to high shear stress by the log-law. In position 3, transition has been triggered and **Cases 5 & 6** show some characteristics of a turbulent boundary layer as different zones start to form near the wall, the linear viscous sublayer next to the wall followed by a buffer region and the logarithmic layer. **Case 4** on the other hand appears to have a negative slip velocity at the wall, a fact that agrees well with the drastically reduced shear stress in Fig. 4.34(b). In position 4, **Case 4** indicates that a separation bubble has been formed, with the region of negative velocities having been increased in thickness compared to position 3. For **Cases 5 & 6**, a negative slip velocity is evident at the wall. It appears to be linked to the shock present at this position, Figs. 4.34(d,f), as the shear stress decreases sharply. The increase of the shear stress right after position 4 indicates flow reattachment and highlights that there

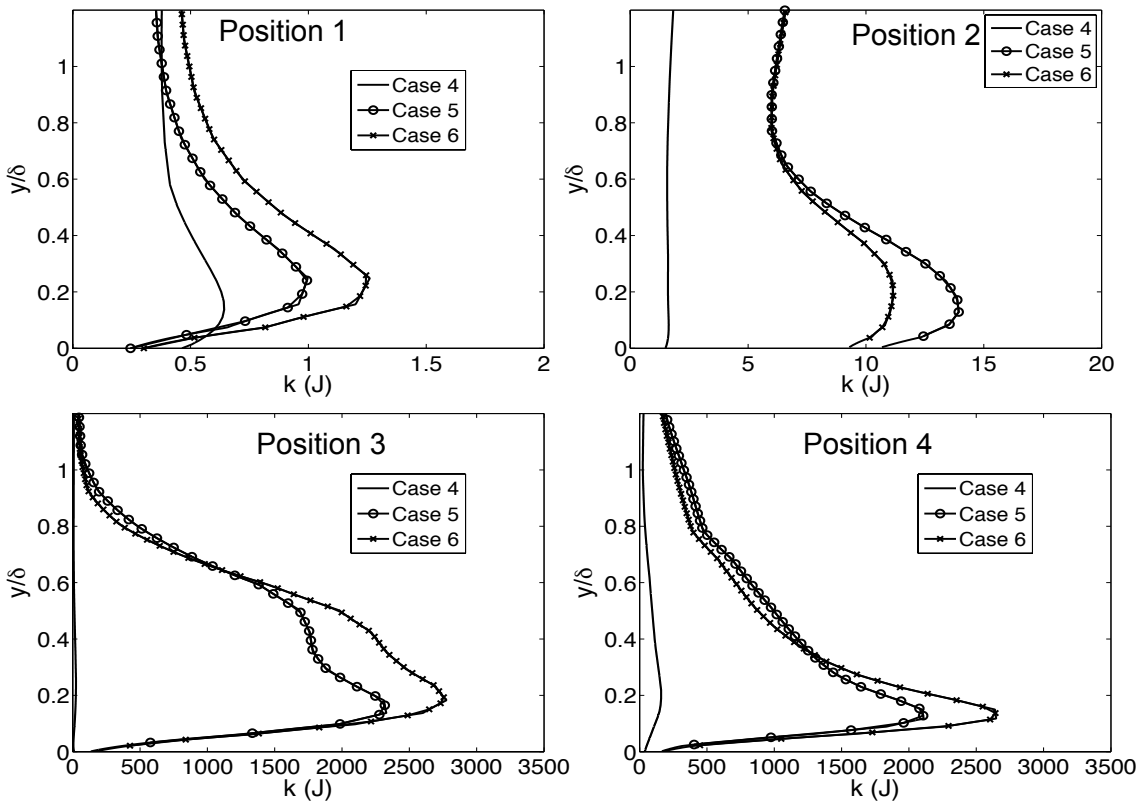

Figure 4.37: Turbulent kinetic energy across the boundary layer at 4 different suction side positions.

is shock/boundary layer interaction present.

These findings are confirmed by the turbulent kinetic energy across the boundary layer, Fig. 4.36. **Case 4** exhibits a very small level of fluctuations across the entire suction side. **Cases 5 & 6**, however, reveal strong near fluctuations developing at position 3, increasing by two orders of magnitude compared to position 2. This large increase indicates the development of a turbulent boundary layer. The high levels of fluctuations then continue up to the trailing edge. It is, however, important to note that increasing the near-wall resolution further and switching to no-slip solid boundaries would be essential if the entire production of the near-wall turbulent kinetic energy is to be captured (with the peak considered to be between $y^+ \approx 5 - 10$ [47]).

Further post-processing can be performed, for example phase averages, triple decomposition or spectra at other relevant positions in the flow. However, such post-processing in the refined cases requires significant computational and memory resources to run for sufficient time and extract snapshots at an increased sampling frequency. Such resources were not available at the time this thesis was written and such a work will take place in the near future.

	δ_1 **(m)**	δ_2 **(m)**	δ_3 **(m)**	δ_4 **(m)**
Case 4	$3.7 \cdot 10^{-4}$	$4.9 \cdot 10^{-4}$	$8.6 \cdot 10^{-4}$	$9.8 \cdot 10^{-4}$
Case 5	$6.8 \cdot 10^{-5}$	$1.3 \cdot 10^{-4}$	$1.7 \cdot 10^{-4}$	$2.7 \cdot 10^{-4}$
Case 6	$6.8 \cdot 10^{-5}$	$1.3 \cdot 10^{-4}$	$1.7 \cdot 10^{-4}$	$2.7 \cdot 10^{-4}$

Table 4.5: Boundary layer thickness δ for **Cases 4 - 6** at the different measuring positions, indicated by the subscript.

4.9 Conclusions

Several LES of the high-pressure experimental rotor /stator turbine stage MT1 have been performed using different SGS models with a wall-modeled approach. Despite modeling changes, overall mean flow results show qualitative and quantitative agreements with the experiments performed at the Oxford Turbine Research facility for all cases, even those with relatively poor resolution. Indeed, all the important flow characteristics and secondary flow features are revealed. However, an important sensitivity of the LES predictions to different modeling parameters is revealed here, particularly notable in the unsteady behavior of the flow. It is shown that SGS models, with their different turbulent flow characteristics, lead to different unsteady flow field responses characterized by different shock structures and more importantly different unsteady contents. Using SGS models adapted to wall-bounded flows results in flows with higher unsteadiness, hence, in flow fields likely to be more realistic. As expected, the basic Smagorinsky model proves to be too dissipative for these types of flows, even when a high resolution mesh is employed. In depth analysis of the different LES predictions based on a triple decomposition of the velocity field at different stations proved SGS modeling to be of critical importance especially at the exit of the stage where not only are the deterministic parts affected but so are the stochastic components. Such diagnostics also evidence the complexity of the rotor flow which is clearly affected by the stator exit unsteady flow content.

Increasing the mesh resolution shows minor changes on the mean flow predictions. However, decreasing the general cell size of the mesh and improving near wall resolution, combined with a model adapted for near-wall regions, not only increases the level of resolved turbulence but also changes the boundary layer thickness and near-wall dynamics. These changes alter the aerodynamic losses, shock structures and secondary flows as well as modify the operating point of the numerical simulations. The agreement between the high resolution simulations that use SGS models adapted for wall-bounded flows (WALE and σ) is also particularly noticeable. The unphysical behavior of the Smagorinsky model close to walls prevents, however, the corresponding case to converge to the corresponding flow field. These findings agree well with the LES literature, where damping functions (such as the Van Driest function [169]) or modified versions of the Smagorinsky model (such as the shear-improved Smagorinsky model [170]) are frequently used to correct this issue. The necessity of resolving more of the boundary layer is also highlighted as the simulations with $y^+ = 100$ show large differences between each other. As these simulations constitute the first LES of a HPT stage, the established conclusions can serve as necessary guidance for future simulations.

Part II

LES of combustor-turbine interactions

Chapter 5

Indirect combustion noise generation in a high-pressure turbine

Contents

5.1 Motivation 92
5.2 Indirect combustion noise state-of-the-art 93
5.3 DMD test case: 2D entropy spot propagation in a periodic channel . . 95
5.4 Turbine stage simulation set-up 99
5.4.1 Mesh 100
5.4.2 Numerical schemes 100
5.4.3 Boundary Conditions 101
5.5 Numerical Results 105
5.5.1 Overall flow topology 105
5.5.2 Dynamic Mode Decomposition of the LES flow field 107
5.5.3 Quantifying the indirect noise and comparisons with the compact theory 117
5.6 Conclusions 119

This chapter details the first application of the MISCOG method to combustion chamber/turbine interactions: the indirect combustion noise generated across a high-pressure turbine from temperature non-uniformities. As with most previous investigations of this process, a decoupled simulation of a turbine stage from the combustion chamber is performed. The consequence of this choice is that the temperature non-uniformities do not come from the unsteady combustion process. Instead, they are modeled by sinusoidal fluctuations introduced by boundary conditions in the turbine stage alone. The acoustic response of the turbine is then analyzed with a specific interest on the indirect noise generation mechanisms. A part of this work was performed during the author's participation to the Summer Program of the Center for Turbulence Research (CTR) at Stanford

University. Results have been published in the proceedings of the summer program [177], the ASME Turbo Expo 2015 conference [178] and will also appear in the Journal of Turbomachinery.

5.1 Motivation

According to the International Civil Aviation Organization (ICAO), the world passenger traffic has increased on average by 5.8% per year throughout this decade and the European Union predicts that without any substantial technological improvements, the number of people in Europe that will be affected by high levels of aircraft noise will double by the year 2026 [179]. Consequently, ACARE's Vision 2050 calls for increased research in the field to reduce the perceived noise by 65% until 2050, with respect to a new aircraft built in 2000. Engines are the main noise source in commercial and military aircraft. For helicopters, the main noise source is still and will remain for some time the rotor blades of the vehicle, hence reducing the significance of the gas turbine noise. Nonetheless, recent studies (for example in the frame of the TEENI project) clearly indicate traces of engine noise emitted from such aircraft.

The first studies on gas turbine noise, carried out by Lighthill [180], showed the importance of jet noise on the overall noise emitted by an aircraft. Lighthill showed that jet-noise scaled with the eighth power of the jet-exhaust speed, meaning that doubling the jet speed would lead to an increase of the acoustic intensity level by nearly 50 dB. The development of the turbofan engine alleviated significantly this issue thanks to the fact that the majority of the propulsion comes from a cold by-pass flow stream, with large mass flow and low speed, resulting in a drastically reduced jet noise. Jet noise has been reduced to the point that the noise emitted from the other components, notably from the fan, the compressors/turbines and the combustion chamber, is becoming more important. Figure 5.1 compares the noise contributions of the different gas turbine components and the noise directivity from an early turbojet engine and a modern turbofan engine. It is evident that in the latest designs fan noise is the prevalent source. However, as further reductions on fan noise are achieved, the relative importance of combustion noise, also called core noise, whose contribution stayed unchanged over the years, is increasing. This suggests that further research on combustion noise is essential if a continuous reduction of the overall engine noise levels is envisioned for the next years. This has led to a renewed interest in the topic with several dedicated EU projects forming the last five years, such as TEENI[1] and RECORD[2].

Combustion noise is principally a low-frequency noise generated in the combustion chamber of gas turbines and arising from two main mechanisms, as mentioned in Chapter 1. First, direct noise emanates from the acoustic waves created at the unsteady flame front and propagated through the rest of the engine. It is a source of noise that has received considerable attention in the past [181, 182, 183, 184]. Second, the unsteady combustion will give rise to low-frequency temperature fluctuations, or entropy waves,

[1]Turboshaft Engine Exhaust Noise Identification
[2]REsearch on Core Noise Reduction

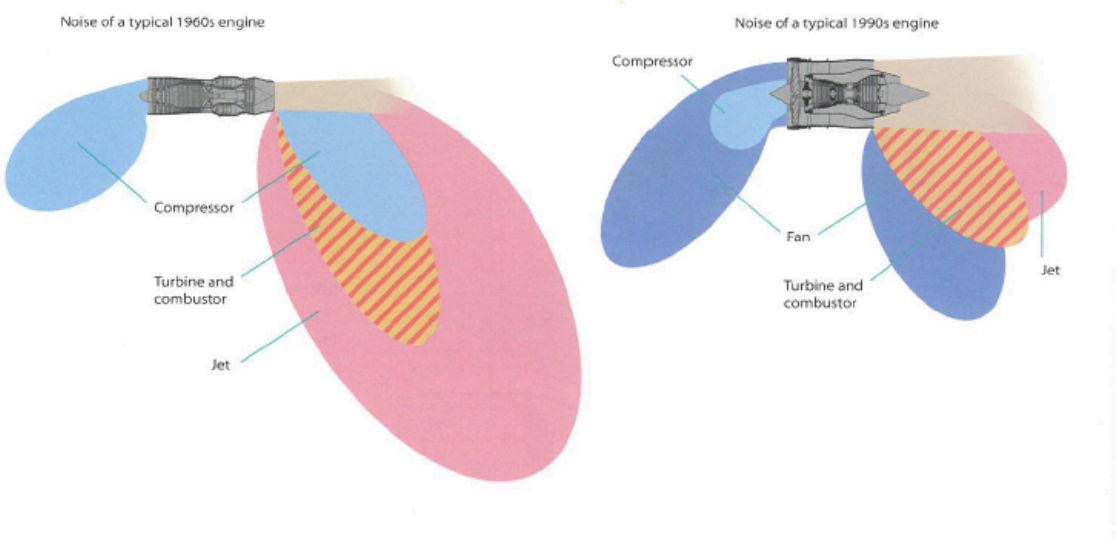

Figure 5.1: Noise emissions and directivity of gas turbine components - Typical 1960's turbojet engine (left) and a recent 1990's turbofan design (right) [17].

that are convected with the flow velocity to the combustor nozzle and turbine. There, the waves are subject to significant acceleration and distortion in the blade passages, generating acoustic waves in the process. This noise generation mechanism is called indirect and its importance is twofold: (a) it increases the noise signature of the engine and (b) the acoustic waves propagating upstream can impact the thermoacoustic stability of the combustion chamber [1, 35]. Leyko *et al.* [18] computed analytically the ratio between indirect and direct combustion noise for different operating conditions, modeling the flame in the combustor and the nozzle at the combustor exit as jump conditions. The results, Fig. 5.2, indicate that for the typical operating conditions of aeronautical gas turbines (red point), indirect combustion noise will likely be the dominant source of combustion noise. Yet its actual relevance remains controversial.

5.2 Indirect combustion noise state-of-the-art

Due to the complexity of a full 3D HPT, past theoretical and numerical studies have used simplified turbine-like geometries. The first in-depth analyses on turbine-like geometries focused on the propagation of entropy waves through quasi-1D nozzles. In this context, Marble and Candel [37] developed an analytical method to evaluate the transmission coefficients of acoustic and entropy waves propagating through a compact quasi-1D nozzle, its length being significantly smaller than the wavelength of the incoming waves. More recently, Duran and Moreau [34] proposed an analytical method to calculate the transmission coefficients of general quasi-1D nozzles, removing the compact nozzle assumption. These analytical methods, accompanied by numerical predictions from LES, have been evaluated on the experimental Entropy Wave Generator [40], with [18] and [42] reporting

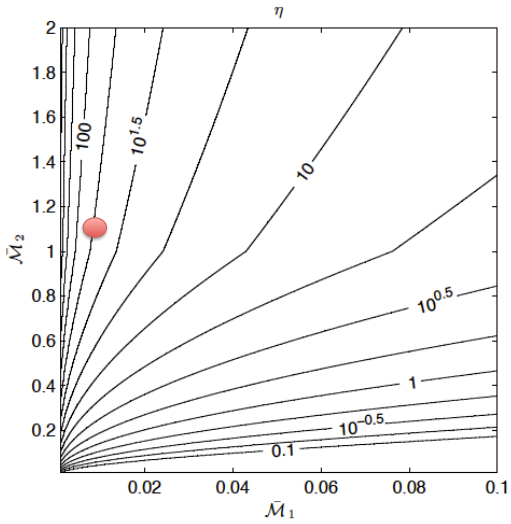

Figure 5.2: Estimation of the ratio η between indirect and direct noise by an analytic approach. The ratio η is plotted here as a function of the Mach number $\overline{M}_1$ representing the Mach number in the combustion chamber and at the nozzle inlet, and of the Mach number $\overline{M}_2$ representing the outlet nozzle Mach number - Typical combustor operating point indicated with a red point [18].

good agreement on both subsonic and supersonic operating conditions. The same problem was also treated theoretically by Howe [36], who used the compact hypothesis with an acoustic analogy and highlighted the impact of the entropy wave form on the generated noise. A potential coupling of indirect combustion with vortex noise from separated flow regions at the nozzle walls was revealed to be an influencing factor on the measured noise.

The theory of Marble and Candel for nozzles was extended to 2D compact blade rows by Cumpsty and Marble [38], taking into account the reorientation of the flow. This is achieved by imposing an additional constraint, the Kutta condition at the blade trailing edge. The method was originally conceived for a single blade row and tested against numerical simulations by several authors, both for compact and non-compact frequencies [185, 186]. It was extended to multi-stage turbines by Duran et al [187] and was compared against numerical simulations of a 2D high-pressure turbine stage as well as experimental results of [39] for a 3-stage turbine (NASA test case 1629).

The present work is the first numerical evaluation of the indirect combustion noise generated in a realistic, fully 3D, transonic high-pressure turbine. As it was observed in the previous chapters, the flow across a realistic turbine is much more complex than in 2D simulations, where no endwall effects are present and turbulence evolves differently. The operating point of these 2D studies was also subsonic [34, 185], instead of the typical transonic conditions encountered in real configurations. As a result, the mixing of the entropy waves as they go through the turbine and the indirect noise generation is expected to be altered. This simulation can, thus, serve as an additional validation of previous

simulations as well as to calibrate lower order models, such as the one developed in [18]. To do so, a train of sinusoidal entropy waves of constant frequency and amplitude is injected in the MT1 high-pressure turbine, detailed in Chapter 4, to model the entropy waves generated in a combustor (details on the entropy wave injections are provided in section 5.4.3). While combustion noise is broadband in nature, a monochromatic pulse allows to easily distinguish it from other turbine noise sources. Note that for this study, the Dynamic Mode Decomposition (DMD) is employed and deemed necessary for an adequate analysis of the predicted flow field [188].

Analyzing high-fidelity numerical simulations of flows characterized by complex, dynamic and non-linear systems can be particularly cumbersome. Such systems might be exceedingly hard to analyze directly by simple visualization or statistical techniques (either due to excessive memory demands or convergence issues). Advanced methods have emerged during the last decades to provide a detailed analysis of many flow fields. Dynamic Mode Decomposition is one of the most recent methods to appear [188] and it attempts to identify coherent single-frequency structures from a series of flow snapshots. The DMD has been selected here compared with other frequency-domain methods, for its robustness and the resolution capabilities with only few periods per frequency of interest included in the signal. Additionally, the method minimizes spectral leakage. It also provides both global information, in the form of spectra as well as the spatial structure of the computed modes.

In the following section, the method is validated on a simple 2D test case, illustrating the information that DMD provides and investigating its potential advantages and limitations. At the same time, the test case allows to validate the entropy wave injection through the boundary conditions. A description of the derivation of DMD is provided in Appendix C. The forced turbine simulations are presented in section 5.4 while section 5.5 discusses the results from the numerical simulations and quantifies the generated indirect combustion noise.

5.3 DMD test case: 2D entropy spot propagation in a periodic channel

To illustrate the DMD capabilities, a simple test case is employed: the propagation of an entropy wave across a 2D, periodic in the transverse coordinate, channel. To remove any diffusion effects, the Euler equations are resolved. The inflow consists of a uniform axial velocity $U = 10\ m/s$ at ambient conditions, i.e $T = 300\ K$ and $P = 1.01298\ bar$ respectively. At the inlet a sinusoidal entropy wave of frequency $f = 4\ kHz$ and amplitude $Tp = 20\ K$ is also introduced through the characteristic boundary conditions[2]. A schematic of the test case with the boundary conditions employed is presented in Fig. 5.3. For demonstration and validation purposes, DMD is also compared with the Fast Fourier Transform (FFT) of the signal recorded at a probe placed at the center of the channel.

[2]A description on the introduction of waves through the characteristic boundary conditions is presented in the next section

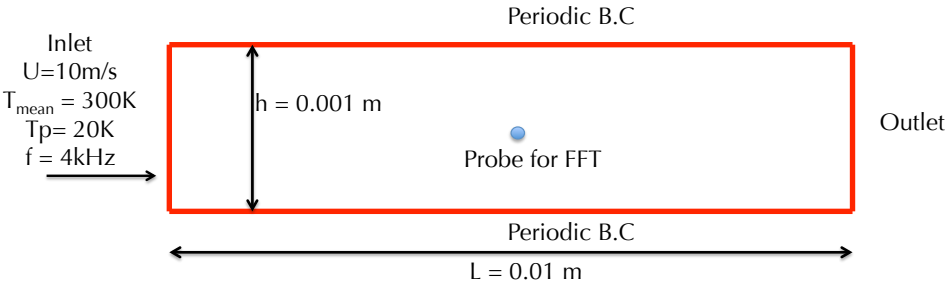

Figure 5.3: Schematic of the 2D test case and boundary conditions employed.

Figure 5.4: Instantaneous temperature flow field of the 2D test case.

The simulation run for four periods of the wave frequency and the sampling frequency for the flow field snapshots is 10 kHz. The sampling frequency at the temporal probe is the same as for the DMD and is chosen to be superior to the Nyquist frequency. Figure 5.4 depicts the temperature of the flow field obtained from an instantaneous solution. The form of the injected sinusoidal entropy wave with amplitude 20 K is evident. The entropy pulsation is convected by the flow and its wavelength can be easily computed: $\lambda = \frac{U}{f} = 0.0025\ m$.

The maximum and minimum temperature in the domain, as a function of time, are presented in Fig. 5.5(a). The recovered values correspond perfectly to $T \pm Tp$, highlighting that the entropy waves are injected correctly and no additional perturbations on the temperature are generated. An important requirement is that the forcing does not generate acoustic waves. If acoustic waves are generated by the boundary conditions they can pollute the indirect noise measurements. To verify that, the maximum and minimum pressure of the domain are also investigated, Fig. 5.5(b), and indicate that the difference between the two is less than $0.2Pa$, confirming that the entropy forcing is, indeed, "quiet".

Figure 5.6 depicts the temperature spectrum from the DMD analysis of the flow field snapshots along with the FFT of the temperature signal recorded at the temporal probe. It is evident that DMD captures correctly the introduced wave both in terms of frequency (4 kHz) and amplitude (20 K) with no other significant mode appearing. Note that comparatively and for this set of sampling frequency and signal duration the FFT is incapable to capture correctly neither the amplitude nor the frequency. Improving the frequency prediction would require increasing the FFT length to a size that divides

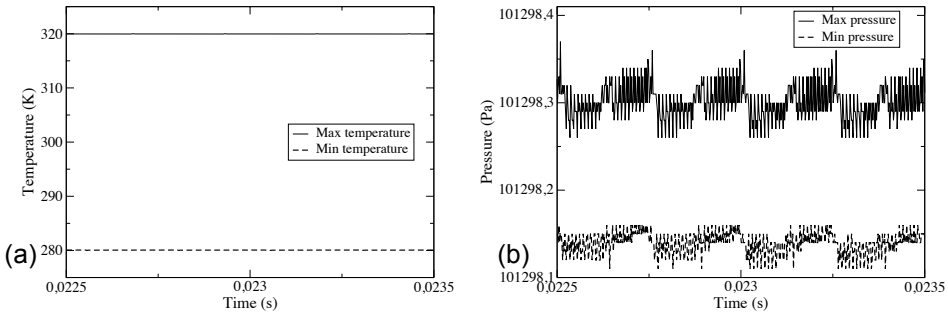

Figure 5.5: Maximum and minimum temperature (a) and pressure (b) across the domain as a function of time. Entropy forcing of amplitude 20 K is active.

the frequency of interest closer to an integer or use of the zeropadding technique in the signal. Improving the amplitude can only be obtained by simulating longer periods of the phenomenon. These difficulties typical of FFT analysis confirm that DMD can provide reliable information with a considerably reduced number of snapshots and without additional treatments.

To confirm further that DMD captures accurately the introduced waves, the spatial form of the 4 kHz mode, in terms of temperature modulus and phase across the domain, is presented in Fig. 5.7. The depicted temperature modulus (top) is, indeed, showing the right entropy wave amplitude with minimal variation across the domain, despite the fact that only 4 periods T of the phenomenon were effectively computed. The phase of the temperature, Fig. 5.7(bottom), provides information on the propagative direction of the waves. As it changes linearly across the axial direction and there is no variation across the transverse coordinate, purely axial propagating entropy waves are observed, as anticipated for this simple test case.

From these results, it is evident that DMD can provide a wide range of information, both global and local, at an affordable cost and high precision. To investigate further the limits of DMD, a parametric analysis of the temperature spectra is performed in the following: *a*) for a varying sampling frequency and a total runtime of 4 periods and *b*) for a varying runtime and a constant sampling frequency of 10 kHz.

Effect of sampling frequency

The first step is to evaluate the impact of the sampling frequency. A method capable of finding the oscillatory motions with low sampling frequencies is particularly advantageous: the memory requirements for storing the necessary information indeed would reduce drastically and the CPU cost decreases if the code does not need to pass through the routines that create solution files. These aspects are particularly important in large LES where storage requirements of a single solution file can be of the order of Gigabytes.

In this simple test case there are no other oscillatory phenomena present apart from the entropy forcing so the effect of the sampling frequency can be straightforwardly evaluated. The sampling frequency can be reduced up to the Nyquist frequency, that is twice the

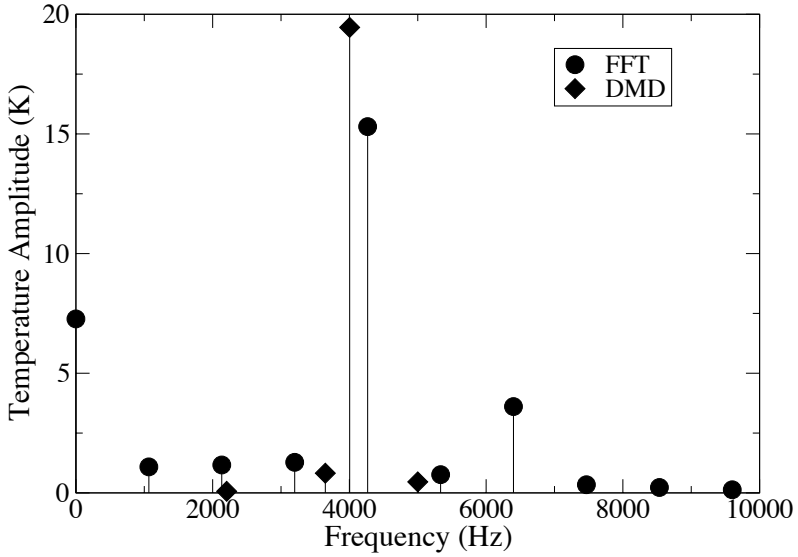

Figure 5.6: DMD temperature spectrum of the 2D test case and FFT of the temperature signal captured at a probe in the center of the channel.

frequency of the phenomenon of interest. Higher sampling frequencies are also tested. The temperature spectra for sampling frequencies ranging from $8-40$ kHz are presented in Fig. 5.8. The total runtime remains 4 periods of the entropy wave frequency. It is evident that even with the minimum possible sampling frequency of 8 kHz the pulsating mode is recovered, albeit with an overpredicted amplitude. For sampling frequencies of 10 kHz and higher the amplitude prediction improves considerably and the results reach the desired 20 K amplitude.

Effect of runtime

Another important parameter, apart from the sampling time, is the runtime during which the flow snapshots are recorded. It is desirable for any frequency domain method to be reliable after few periods of the oscillating phenomenon of interest have been simulated by the CFD solver. This limits the computational cost and facilitates the post-processing since again less memory is required to save and process the data. As was observed in Fig. 5.6, FFT has difficulties in recovering oscillatory phenomena with as few as 4 periods. Figure 5.9 depicts the DMD temperature spectra for different runtimes (hence different total number of snapshots) and constant sampling frequency of 4 kHz. It is evident that DMD recovers the mode with only 2 periods and with approximately the correct amplitude. A slight improvement on the amplitude prediction is the only outcome of the runtime increases. These findings highlight the potential of the method on more realistic flow configurations.

These findings suggest that DMD is a very reliable and robust method. However, as the proposed test case is very simple and lacks any stochastic fluctuations, a convergence

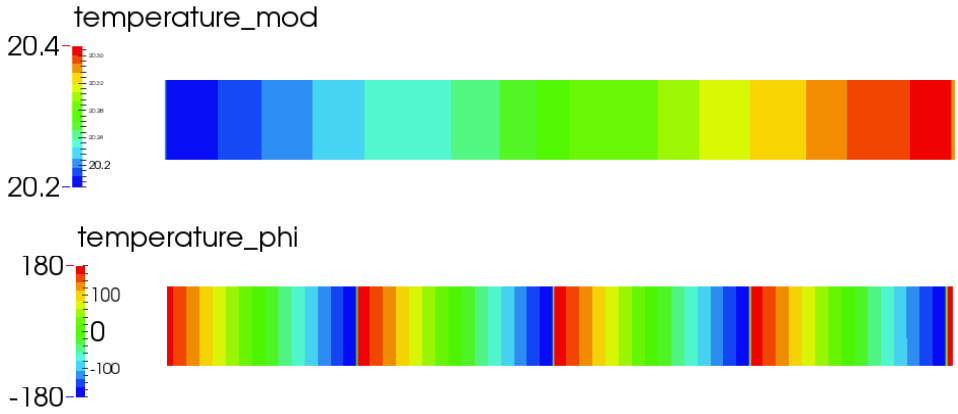

Figure 5.7: DMD 4 kHz mode - Temperature modulus (top) and phase (bottom).

study with respect to different runtimes is undertaken and detailed later for the turbine stage configuration. This will provide further insight on the method's capacities in very complex geometries and high Reynolds number flows.

5.4 Turbine stage simulation set-up

The objective of this chapter is to investigate the generation of indirect combustion noise across a fully 3D turbine stage. To this end, the transonic MT1 turbine stage [2] is chosen for this study as it provides a validated and realistic geometry of a high-pressure turbine. As in chapter 4 the scaled geometry is employed with 1 stator blade and 2 rotors (12 degree periodicity) to reduce the computational domain. Two simulations were performed: *a*) one with a steady inflow that serves as a reference case and *b*) one where an entropy wave train is introduced at the inlet to evaluate the indirect combustion noise generation process.

In the following, the principal flow characteristics are first identified for both the steady inflow and the forced cases. The analysis of the steady inflow reference simulation using DMD is performed and the most important natural modes are identified. The DMD global spectra of the forced case are then investigated against those of the steady inflow case to evaluate the impact of the incoming entropy waves on the noise generation of the turbine. Afterwards, the response of the flow field at the pulsation frequency for the forced case is examined in further detail on the basis of DMD and transmission coefficients are obtained for the generated acoustic waves. To finish, the results are compared to those obtained with the 2D theoretical model of [38] and 2D pseudo-LES of a similar turbine configuration [189].

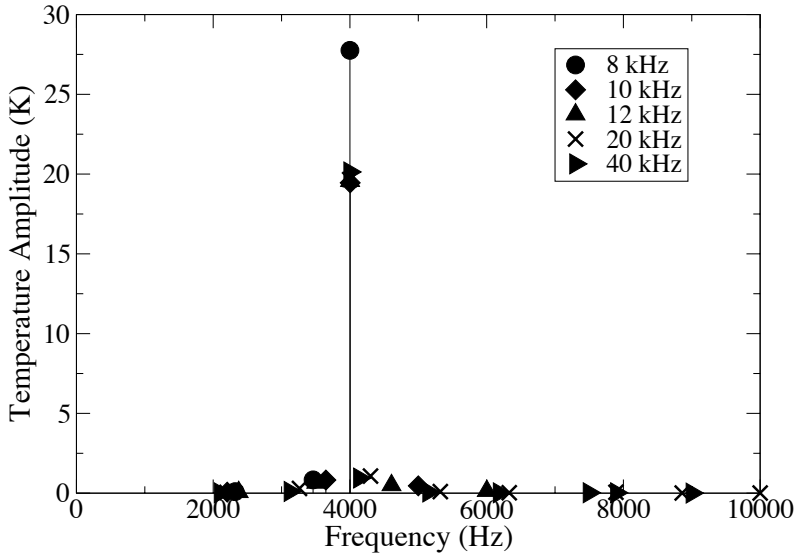

Figure 5.8: DMD temperature spectrum of the 2D test case for different sampling frequencies. Duration of the signal 4T.

5.4.1 Mesh

The mesh employed is, as for the previous MT1 simulations, a fully 3D hybrid mesh with 10 prism layers around the blades and tetrahedral elements in the passage and endwalls. Three views of the mesh are provided in Fig. 5.10. It is composed of 8.1 million cells in total for the stator domain and 10.5 million cells for the rotor domain. It is more refined than the coarse mesh used in Chapter 4 to improve the acoustic predictions and is designed to place the first nodes around the blade walls deeper in the logarithmic region. Note also that a low aspect ratio for the prisms, set to $\Delta x^+ \approx 5\Delta y^+ \approx 5\Delta z^+$, is maintained to permit a good resolution of streamwise/spanwise flow structures. In the rotor tip region, there are approximately 15 cell layers, as shown in Fig. 5.10(c), in an effort to keep the time step reasonable. In wall units, the maximum values of y^+ measured around the blade is approximately 50.

5.4.2 Numerical schemes

As in the previous chapters, the AVBP solver with the MISCOG method is used to perform LES of the MT1 turbine stage. The numerical integration in this chapter is handled by the two-step, finite-element TTGC [119] scheme that is 3rd order accurate in time and space and explicit in time. It is chosen over the cheaper LW scheme for its performance in handling acoustics, an important parameter in this problem. This scheme is used in conjunction with the Hermite-type 3rd order interpolation for the data exchange at the overlap zone, ensuring low dissipation and low dispersion of the rotor/stator interactions, while preserving the global order of accuracy of the numerical

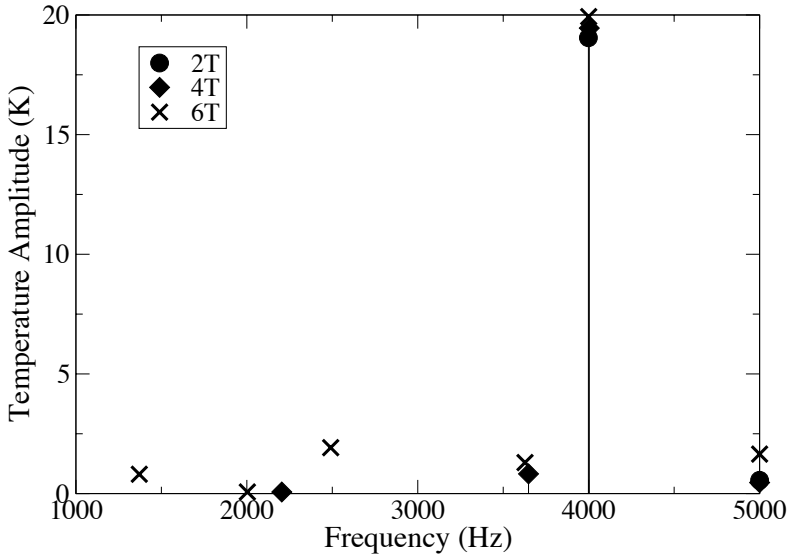

Figure 5.9: DMD temperature spectrum of the 2D test case for different runtimes. Sampling frequency 10 kHz.

Boundary	**Euler**	**Navier-Stokes**
Subsonic Inflow	4	5
Subsonic outflow	1	4

Table 5.1: Number of conditions required for a well-posed 3D simulation [25].

scheme. The computational cost for simulating the time corresponding to one 360-degree revolution of the turbine stage is 30K CPU hours.

5.4.3 Boundary Conditions

Performing numerical simulations requires from the user to specify certain boundary conditions at the domain limits. Table 5.1 presents the number of necessary conditions to ensure a well-posed problem near the boundaries [25]. In the LES context particular attention on the boundary conditions is required as the compressible LES formalism allows the resolution of acoustic waves generated by the flow, which will propagate and reach the boundaries of the domain. Imposing the necessary boundary conditions in a hard way will lead to the waves being reflected back into the domain thus modifying and polluting the flow field. As a result, treating these waves is necessary to ensure minimal reflection while respecting the user imposed flow parameters.

In AVBP, the boundary conditions follow the NSCBC formulation [118]. In this method, the flow is decomposed into characteristic waves crossing the boundaries using the Linear One-Dimensionsal Inviscid (LODI) relations. Figure 5.11 depicts the characteristic waves crossing an inlet and an outlet. Two acoustic waves (upstream propagating

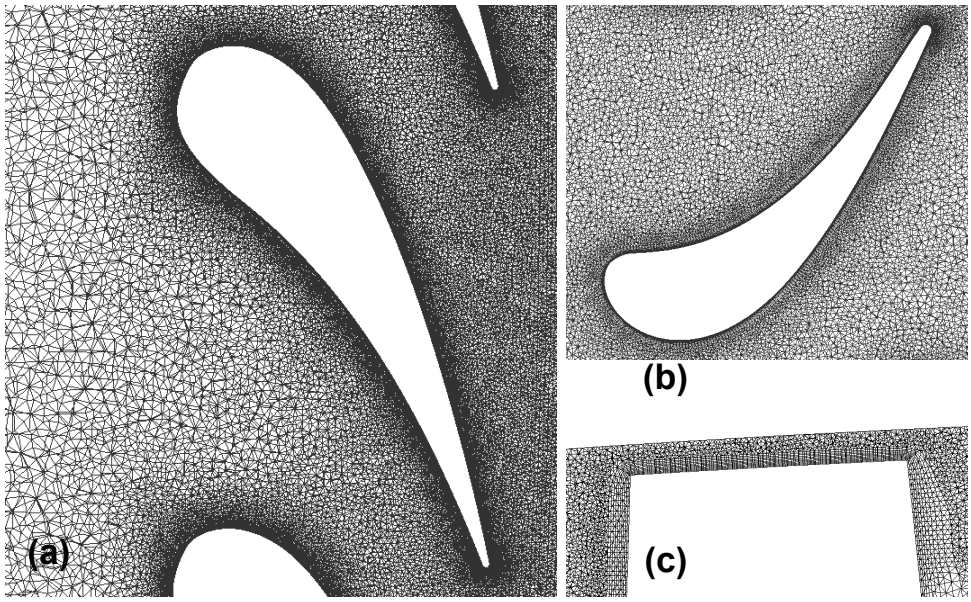

Figure 5.10: mesh view of the stator at mid-span (a) of the rotor at mid-span (b) and at the rotor tip (c)

w^- and downstream propagating w^+) are identified and are complemented by an entropy wave w^s and two waves related to transverse variations of the velocity. At the inlet, four of these waves are entering the domain so 4 physical conditions need to be specified. At the outlet one condition is sufficient as only the wave w^- is entering the domain at this position.

Outlet

At the outlet of the domain, Fig. 5.11 demonstrates that there is only one acoustic wave (w^-) coming in the domain that needs to be treated. With the NSCBC method, for the acoustic wave entering the domain from the outlet, w^-, one writes:

$$\frac{\partial w^-}{\partial t} - L^- = 0. \tag{5.1}$$

where L^- is the amplitude variation of the characteristic wave w^- that would enter the computational domain. For a perfectly non-reflecting boundary condition $L^- = 0$. In practice however this is not possible. In most commonly used outlet conditions, the user wants to impose a static pressure. To recover this desired property while being acoustically nearly non-reflection, a partially non-reflecting formulation is usually used:

$$L^- = K_p \frac{p - p_{ref}}{\gamma p_{ref}}. \tag{5.2}$$

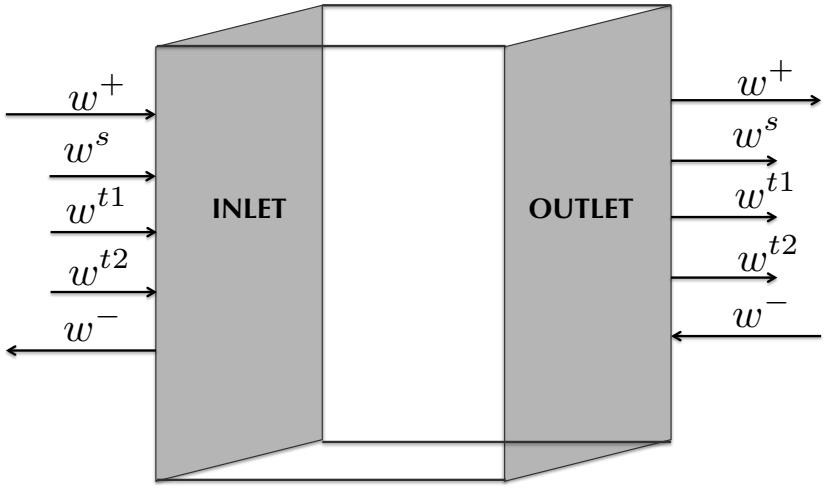

Figure 5.11: Characteristic waves crossing an inlet and outlet

In Eq. (5.2) K_p is the relaxation coefficient and p_{ref} the reference pressure imposed by the user. With this formulation, small values of the relaxation coefficient result in a less reflecting outlet, while large values ensure that the pressure is close to the user-defined target but wave reflection is stronger [190]. For real flow problems where locally 1D flow does not apply, a modification of the NSCBC, described by Granet *et al.* [191] can also be used, to ensure that vortices created by the blade wakes are leaving the domain without generating noise.

Inlet

At the inlet, the boundary is treated in a similar way. The user-specified physical conditions in the investigated case include the total pressure and the total temperature. The incoming acoustic wave (since now it is an inlet) will be a function of these 2 variables. The formula for the incoming acoustic wave reads:

$$\frac{\partial w^+}{\partial t} - L^+ = 0. \tag{5.3}$$

with the amplitude of the incoming acoustic wave written as [192] (transverse fluctuations are ignored):

$$L^+ = -\frac{e_c}{K_+} K_{tt}(Tt - Tt_{ref}) - \frac{T}{\rho K_+} K_{pt}(Pt - Pt_{ref}). \tag{5.4}$$

where e_c is the kinetic energy, Pt and Tt are the total pressure and temperature, K_{pt} is the relaxation coefficient on the total pressure, while $K_+ = \frac{(c+u_n)Tt}{2} + \frac{e_c T}{2c}$, u_n being the velocity normal to the boundary and c the speed of sound.

Rotational Speed (rpm)	9500
Inlet total pressure (Pa)	$4.56e5$
Inlet total temperature (K)	444
Mass flow (kg/sec)	17.4
Outlet static pressure (Pa)	$1.4 \cdot 10^5$
Wave amplitude (K)	20
Wave frequency (Hz)	2000

Table 5.2: Operating conditions of the MT1 turbine.

Note that no turbulent fluctuations are added at the inlet, as only pure indirect combustion noise generated in the turbine is investigated. For the forced simulations, sinusoidal entropy spots are introduced through the corresponding characteristic equation:

$$\frac{\partial w^s}{\partial t} - L^s = 0. \tag{5.5}$$

where w^s is the entropy wave. In an unforced simulation, $L^s = \frac{\rho(c+u_n)}{2C_pT}L^+ + \frac{\rho}{T}K_{tt}(Tt - Tt_{ref})$, with K_{tt} being the relaxation coefficient of the total temperature. For the forced simulations, one should instead write:

$$L^s = \frac{\rho(c+u_n)}{2C_pT}L^+ + \frac{\rho}{T}K_{tt}(Tt - Tt_{ref} - Tt_f^s) + \frac{\partial w_f^s}{\partial t}. \tag{5.6}$$

where $w_f^s = Asin(\omega t)$ is the entropy temporal signal of amplitude A and frequency ω injected in the domain and Tt_f^s is the fluctuation of the total temperature due to this wave.

For the forced LES, the frequency of the imposed waves is fixed at 2 kHz and the amplitude is 4.8% of the inlet total temperature. This value has been shown to generate acoustic waves of linear dynamics [185]. The reduced frequency of the forcing is $\Omega = fL_n/c_0 = 0.1$, with L_n being the rotor chord length, f the forcing frequency and c_0 the speed of sound at the turbine inlet. While combustion noise is usually associated to lower frequencies, 2 kHz was found to be approximately the limit of validity of the compact theory in 2D configurations [189] and renders the simulations more affordable. Additionally, due to the complexity of this high Reynolds transonic 3D turbine, a monochromatic pulsation is preferred over a more realistic broadband pulsation in an effort to distinguish pure indirect noise from other sources of noise more easily. Note that no acoustic waves are introduced into the computational domain by this approach, as was shown in section 5.3. The operating and boundary conditions employed in this work are summarized in Table 5.2.

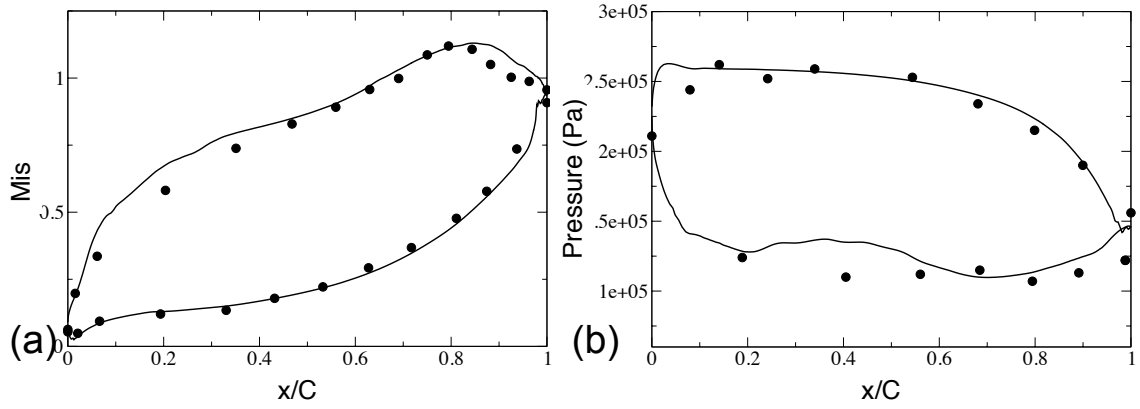

Figure 5.12: Time-averaged mid-span profiles of the isentropic Mach number across the stator blade (a) and of the static pressure across the rotor blades (b).

5.5 Numerical Results

5.5.1 Overall flow topology

The overall flow topology is analyzed for the two cases. First and in an attempt to validate the mean flow predictions with this mesh (of an intermediate resolution compared to MESH1 and MESH2 of Chapter 4), the isentropic Mach number and the static pressure across the stator and rotor blades are respectively shown on Fig. 5.12(a) and 5.12(b) at mid span for the steady inflow case. The agreement with the experimental measurements is fair and the plots correspond well with the results obtained in the previous chapters for this configuration.

Looking at the full 3D field, as before, a particularly complex flow field is revealed. Figure 5.13 depicts density gradient contours (in logarithmic scales) of the flow across a cylindrical cut at mid-span of the turbine for the steady inflow and pulsed cases, Figs. 5.13(a) and 5.13(b) respectively, complemented by a view in an x-normal plane near the rotor trailing edge for the steady inflow case, Fig 5.13(c). Some of the phenomena highlighted in Fig. 5.13 are the shock/boundary layer interaction on the suction side of both the stator and the rotor (positions A and B), vortex shedding from the trailing edge of the blades and the accompanying acoustic waves emitted (position C), as well as strong secondary flows developing at the endwalls (positions D and E), as observed in Chapter 4. For the pulsed case, Fig. 5.13(b), in addition to the previously highlighted phenomena, the planar entropy waves approaching the stator are also evidenced (position F). As these waves go through the stator passages they get distorted and partially mixed by the blade wakes before being cut by the passing rotors. The mixing and the developing turbulence clearly make the entropy waves less visible in the rotor domain.

Strong 3D secondary flows are highlighted by Q-criterion isosurfaces for an instantaneous solution of the unpulsed case, Fig. 5.14. It can be observed that on the stator suction side streaky structures are developing as the trailing edge is approached, which result in a flow boundary layer laminar-to-turbulent transition at the trailing edge and a

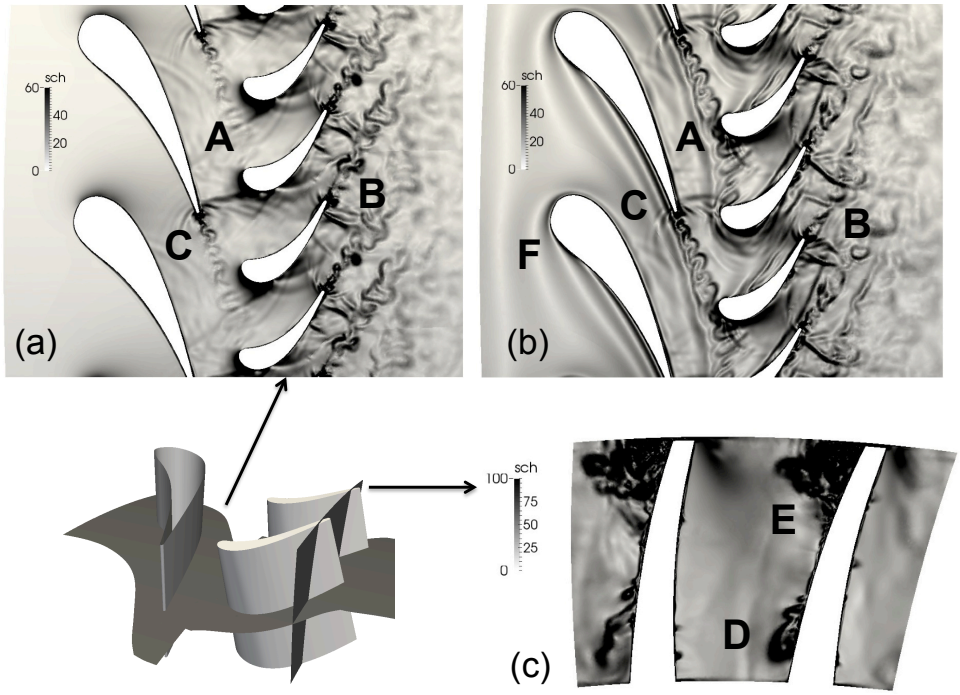

Figure 5.13: Contours $\frac{|\nabla\rho|}{\rho}$ of an instantaneous solution at mid-span for the steady inflow (a) and pulsed cases (b). Contours of the same variable and at an x-normal plane near the rotor exit for the steady inflow case (c).

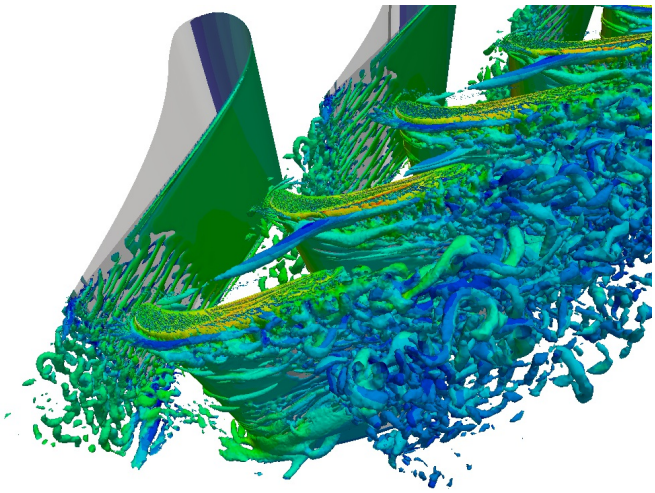

Figure 5.14: Q-criterion of an instantaneous solution across the turbine stage.

fully turbulent vortex shedding. These streaky structures differ from the low-resolution simulations of Chapter 4, Fig. 4.15, highlighting the effect of the mesh refinement on the near-wall predictions. Significant activity is also present at the rotor tip, where the tip leakage vortex dominates other unsteady activities.

5.5.2 Dynamic Mode Decomposition of the LES flow field

A frequency domain analysis is performed by applying DMD to a set of instantaneous flow fields to identify the most important noise-generating modes and their origins. It can also be effectively used to investigate both qualitatively and quantitatively the generated combustion noise.

To obtain converged and accurate statistics for the flow, especially in the highly turbulent rotor-blade wake, both the steady inflow and the pulsed simulations ran for a total of 10 periods of the pulsation frequency. As will be shown later in this section, the presence of turbulence necessitates this increase in runtime, in contrast to the findings in the simple 2D test case. To avoid aliasing, the sampling frequency needs to be high enough to include all the important high-frequency phenomena. In this case the vortex shedding from the stator trailing edge is the most significant and resolving it, as well as its first harmonic, is necessary. The necessary sampling frequency was determined to be 120 kHz using a simple FFT of a temporal signal recorded at a probe in the stator wake. Lower sampling frequencies were attempted (60 kHz and 30 kHz) but aliasing errors were present. Since DMD is memory consuming, the decomposition is performed at cylindrical blade-to-blade planes at mid-span with the signal including the six principal primitive variables: pressure, temperature, the three velocity components and density. For the pulsed case, a set of x-normal planes at the inlet and outlet of the turbine stage is also employed to measure the incoming/outgoing acoustic and entropy waves as well as the

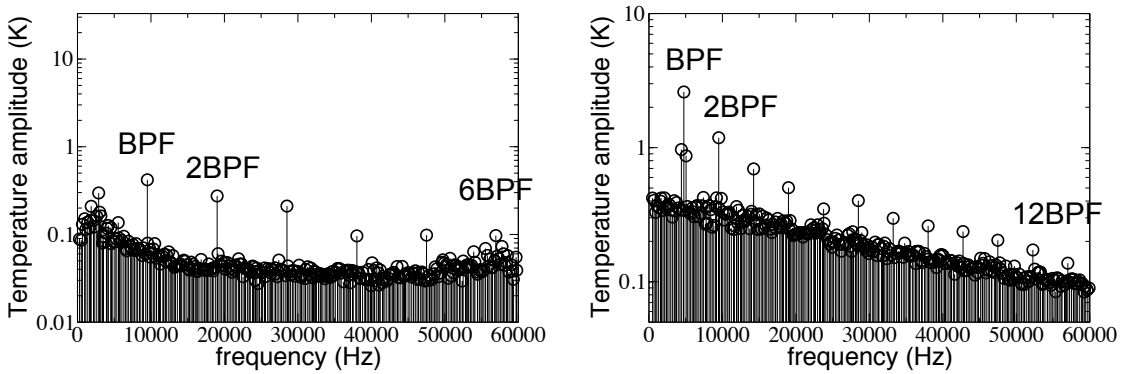

Figure 5.15: DMD temperature spectrums of the stator (left) and rotor domain (right) at mid-span - Steady inflow case.

associated transmission and reflection coefficients.

DMD of the steady inflow case

Before analyzing combustion noise generated in the forced case, DMD is performed for the steady inflow case to evaluate the principal sources of activity in the MT1 turbine. Figures 5.15 and 5.16 show the DMD temperature and pressure spectra of the flow in the stator (left) and rotor (right) domains (azimuthal cuts) for the unforced LES. Note that for this specific configuration, the BPF is 9.5 kHz and 4.75 kHz respectively in each domain. The depicted frequency range is 0-60 kHz, which corresponds to the sixth harmonic of the BPF for the stator and the twelfth for the rotor. It is evident both in the temperature and pressure spectra that the rotor/stator interactions are dominant, with the highest peaks located at the BPF of each domain and its harmonics. The second frequency band characterized by increased amplitudes is observed around the sixth harmonic of the BPF for the stator domain. These modes are related to the vortex shedding and the acoustic waves generated from the stator trailing edge. The corresponding mode (12 BPF) in the rotor domain is much weaker. The spatial structure of the BPF mode for each domain (9.5 kHz and 4.75 kHz), along with the common 57 kHz mode (6 BPF for the stator and 12 BPF for the rotor domain) can be visualized to identify the areas of highest amplitudes.

Figure 5.17 shows the temperature and pressure modulus and phase of the BPF mode at mid-span for each domain. In the stator domain, the highest amplitude both for pressure and temperature occurs near the suction side and close to the trailing edge (position 2 in Figs. 5.17(a) and 5.17(c)). This area of the blade is the closest to the passing rotors and thus experiences the largest fluctuations. The fluctuations originating in this area do not stay confined but also propagate upstream, principally through the stator suction side (position 1). In the rotor domain, the BPF corresponds to the rotor blades encountering the passing wakes from the stators. From the temperature and pressure phases, Figs. 5.17(b) and 5.17(d), it can be seen that at the rotor inlet (position 3) the

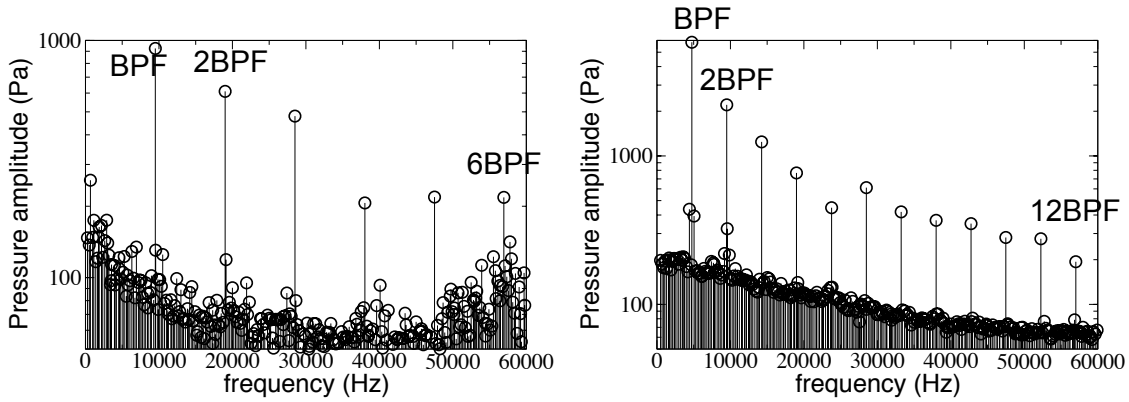

Figure 5.16: DMD pressure spectrums of the stator (left) and rotor domain (right) at mid-span - Steady inflow case.

wake comes at a very high angle, almost perpendicular to the axial direction as the phase changes in the azimuthal direction and stays constant in the axial one. As we go through the rotor passage the flow is turned by the blades and exits the passage with a much shallower angle (position 4).

The temperature as well as pressure modulus and phase of the 57 kHz mode (6 BPF and 12 BPF for the stator and rotor respectively) are depicted in Fig. 5.18. The principal area of activity is the stator trailing edge, where strong acoustic waves are generated. These waves are linked to the oscillating shear layers issued by vortex shedding from the stator wake. The waves generated on the pressure side propagate towards the suction side of the neighboring blade (position 1), while the ones formed from the suction side shear layer tend to move upstream (position 2). It is worth noting though that this activity appears to be largely confined between the stator blades. These observations obtained from DMD seem to match well the phenomena observed in Fig. 5.13(a), position C. In the rotor domain, as seen in the spectra of Figs. 5.15 and 5.16, the effect of the waves is largely attenuated with only the trailing edge showing noticeable amplitude.

DMD results of the forced case

Figures 5.19 and 5.20 show respectively the DMD temperature and pressure spectra of the flow in the stator (left) and rotor (right) domains (azimuthal cuts) for the stationary and forced LES. The depicted frequency ranges of Figs. 5.19 and 5.20 cover up to a frequency equal to the BPF (as seen in each domain) plus the forced Entropy Wave Frequency (EWF) 2 kHz. For the steady inflow case, Figs. 5.19 and 5.20 reveal that there is no mode at the pulsation frequency. For the forced LES, pure entropy waves are injected which create a distinctive peak in Fig. 5.19, seen both in the stator and rotor domains. Furthermore and although no acoustic forcing is imposed by the entropy waves, Fig. 5.20 reveals that a pressure mode with a distinctive peak appears at the forcing frequency. This indicates that acoustic waves have been generated, confirming the

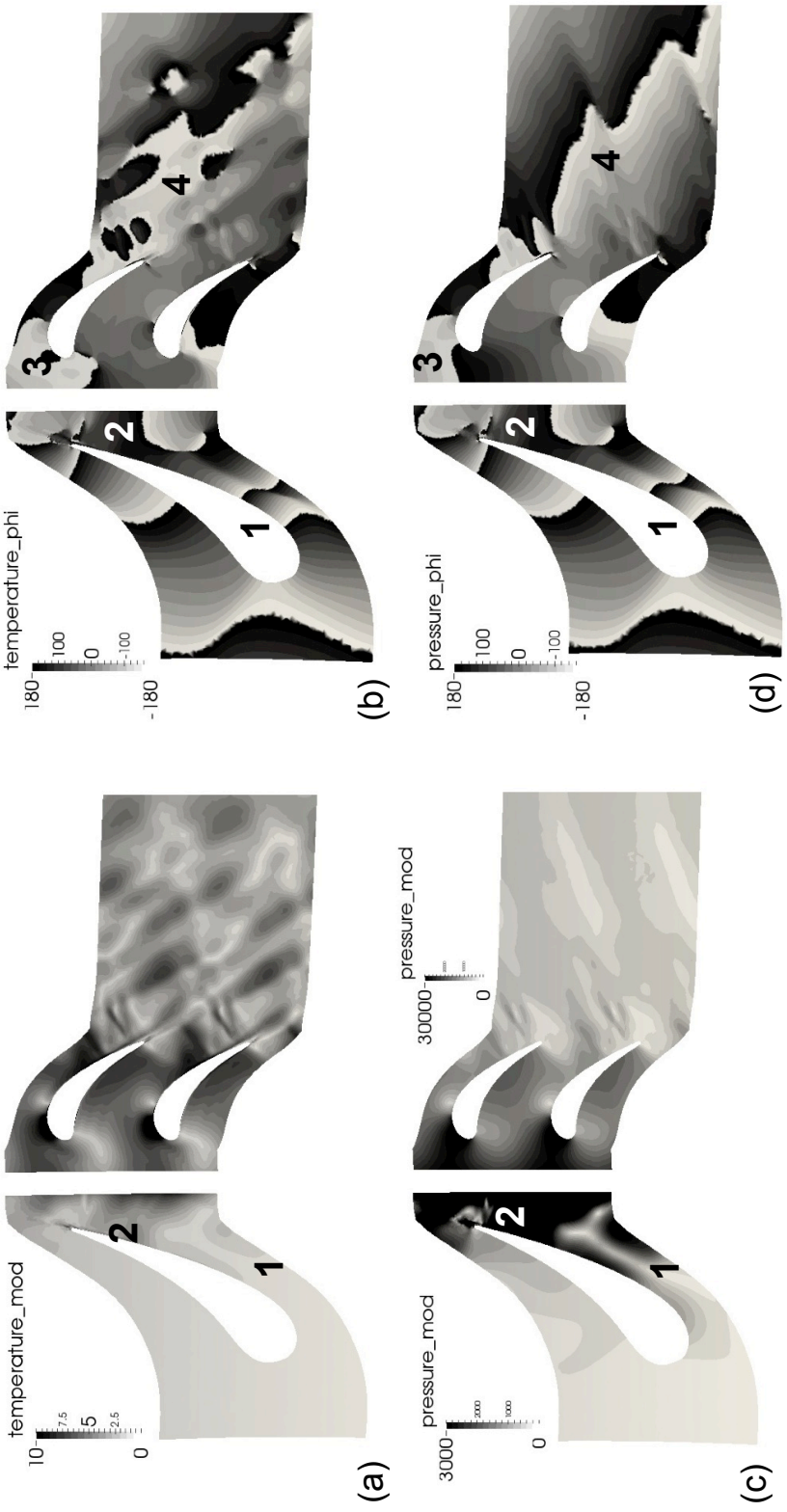

Figure 5.17: DMD BPF mode at mid-span - Modulus and phase of the temperature (a and b) and pressure (c and d) respectively.

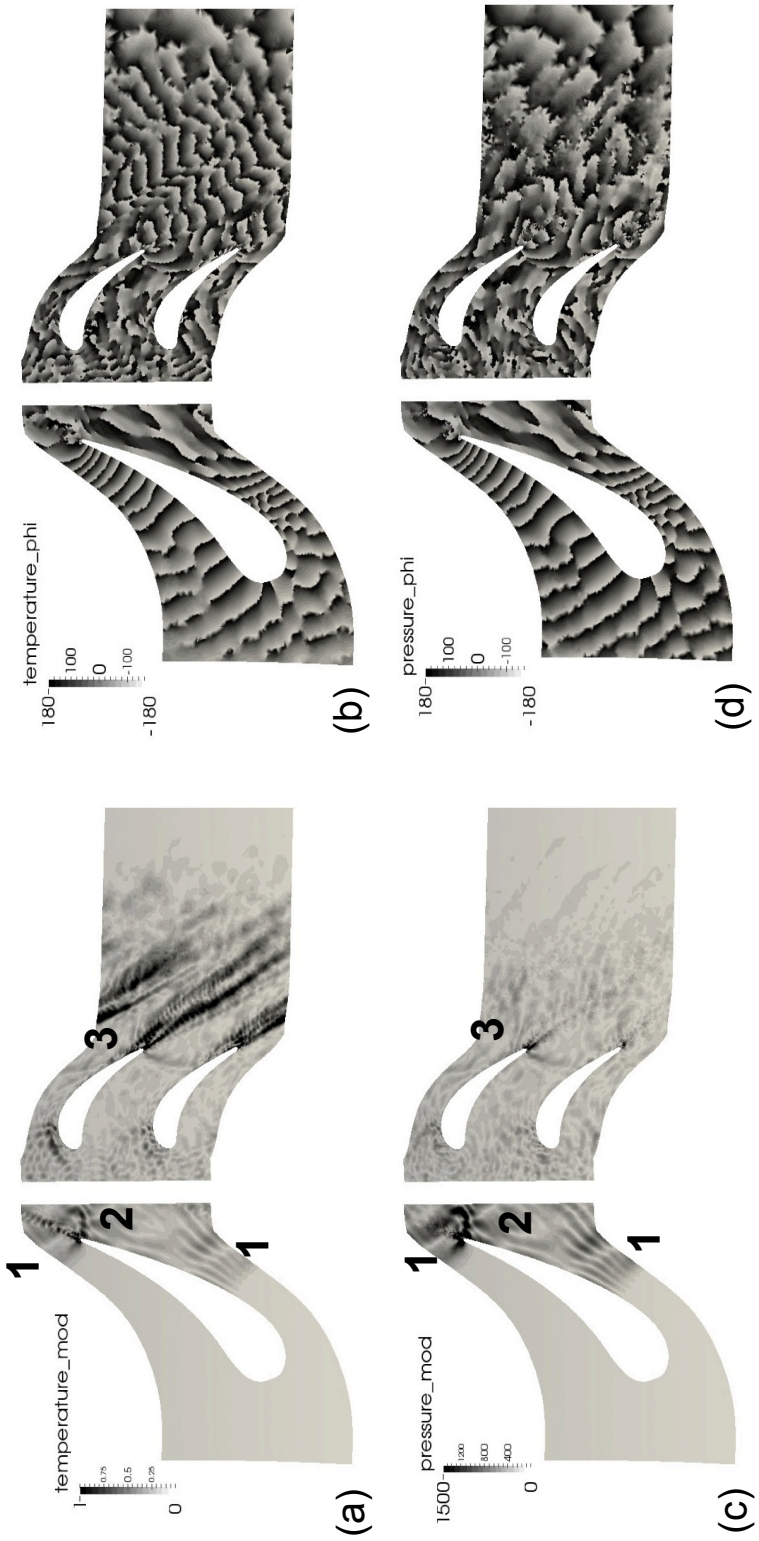

Figure 5.18: DMD 57 kHz mode at mid-span - Modulus and phase of the temperature (a and b) and pressure (c and d) respectively.

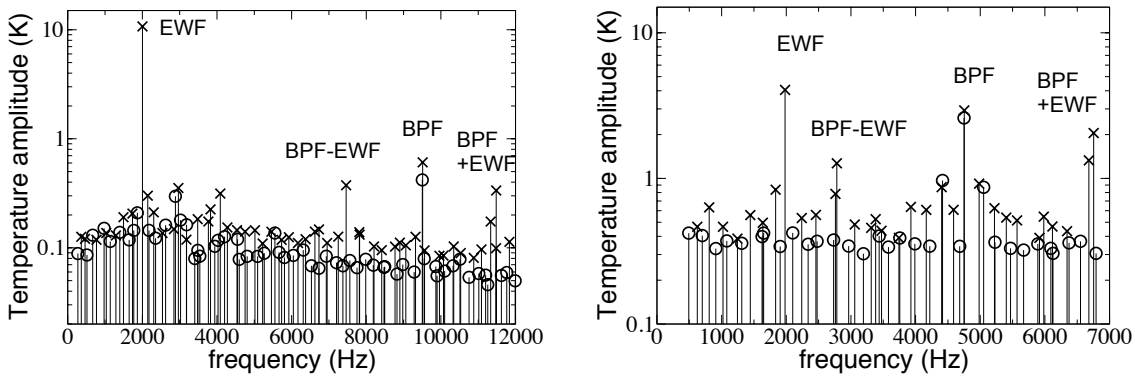

Figure 5.19: DMD temperature spectra of the stator (left) and rotor domain (right) at mid-span - Steady inflow case (∘) and pulsed case (×).

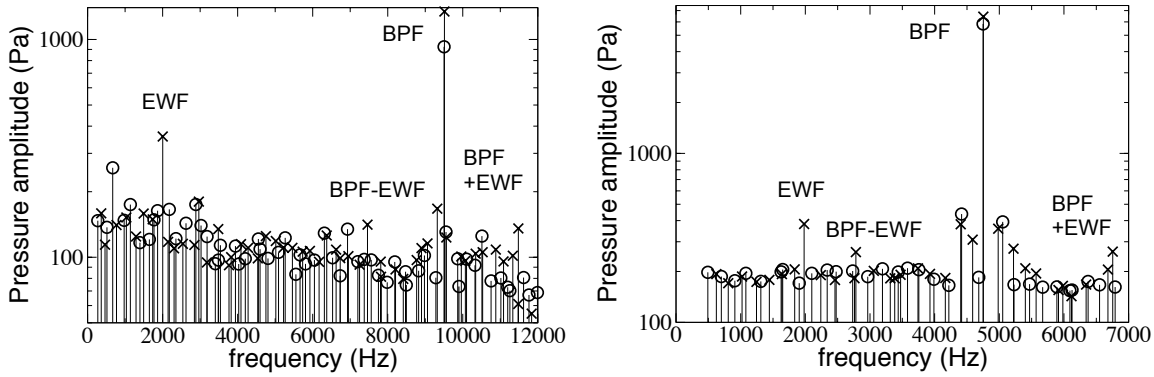

Figure 5.20: DMD pressure spectra of the stator (left) and rotor domain (right) at mid-span - Steady inflow case (∘) and pulsed case (×).

indirect noise generation mechanism. The imposed EWF also leads to the appearance of interaction modes between the BPF and this forcing with noticeable pressure peaks arising at $BPF \pm EWF$. This type of interaction between combustion noise and rotor/stator tones, yielding scattered tones, has also been measured on full scale engine tests [193].

The mode of primary interest obtained by DMD corresponds to the one at the EWF. Its spatial form can be visualized to identify the spatial activity at the origin of the EWF pressure peak present in Figs. 5.19 and 5.20. The modulus and phase of temperature, as well as pressure of the DMD mode are depicted in Fig. 5.21 at mid-span. The temperature modulus at the inlet, Fig. 5.21(a), is almost uniform and equal to 20 K, corresponding to the plane entropy waves injected in the domain. The phase at the same position, Fig. 5.21(b), indicates that the waves in this area are simply convected by the flow and remain planar. Further downstream in the blade passage, the modulus gets distorted with a reducing maximum value as found in previous 2D propagation studies in a stator [18] and in a turbine stage [189]. The phase also reveals an asymmetric distortion of the planar waves. This distortion is caused by the strong flow acceleration and turning

imposed by the blades. An azimuthal component of the velocity vector is created, with the higher velocity near the suction side resulting in an asymmetric propagation velocity across the azimuthal coordinate. In the rotor domain, due to the rotation the blades see rather uniform entropy waves, with the phase at the rotor inlet being practically planar and perpendicular to the axial direction. As these waves pass through the rotors, they get deformed in a similar fashion as in the first blade row. Such strong distortions of the injected entropy wave at both the stator and the rotor lead to scattering in additional azimuthal modes [18]. This energy redistribution mechanism can explain the additional peaks observed in the pressure and temperature spectra of Figs 5.19 and 5.20.

As anticipated in the discussion based on Figs. 3 and 4, convected temperature spots produce pressure waves in both blade rows at the forcing frequency. The pressure modulus and the phase of the DMD mode at EWF, pictured in Figs. 5.21(c) and 5.21(d), reveal a complex pressure field. A significant peak of the modulus exists between the suction side at 20% chord length and the trailing edge on the pressure side, as the domain is periodic in the azimuthal direction (position 1). In this area the phase hardly changes, Fig. 5.21(d), suggesting an excited cavity mode that stays confined between the blades, making it irrelevant to combustion noise where only propagating waves are of interest. The second area of high pressure modulus can be observed on the suction side close to the trailing edge (position 2), with the sharpest peak corresponding to a shock. In the rotor domain, both the pressure modulus and phase appear to simply follow the flow, with a smooth change of phase throughout indicating simple wave propagation. To finish, a large peak in the pressure and temperature modulus at the trailing edge of the blade corresponds to another trailing edge shock (position 3). At the outlet, the acceleration of the temperature spots through the rotor as well as the acoustic waves generated in the stator and transmitted in the rotor are strong enough to yield a significant pressure trace (non-zero modulus) that sticks above the broadband level. All these features identified in the stator and rotor domains are at the root of the indirect combustion noise emitted and will be quantified later in this work.

Convergence of the DMD

One of the advantages of DMD is the quick convergence of the method, particularly when dealing with oscillatory motions [188, 194] as shown in the 2D test case. The case of 3D turbine stage, however, is much more complex. While the phenomenon of interest consists of oscillating acoustic and entropy waves of known frequency, it coexists with broadband turbulence, shocks, blade wakes, boundary layers and secondary flows that might alter the convergence of the DMD in terms of temporal resolution and overall length of the treated simulations. To evaluate this potential source of uncertainties, DMD on the pulsed case at mid-span is performed with a varying number of snapshots and the same constant sampling frequency, i.e the length of the simulation is modified.

Figures 5.22 and 5.23 depict the DMD temperature and pressure spectra of the pulsed case for five different simulation runtimes, each equal to a multiple of the period $T = \frac{1}{EWF}$, which relates to the primary frequency of interest in this work. The sampling frequency for the snapshots is constant and equal to 120 kHz, as in the previous section. The first

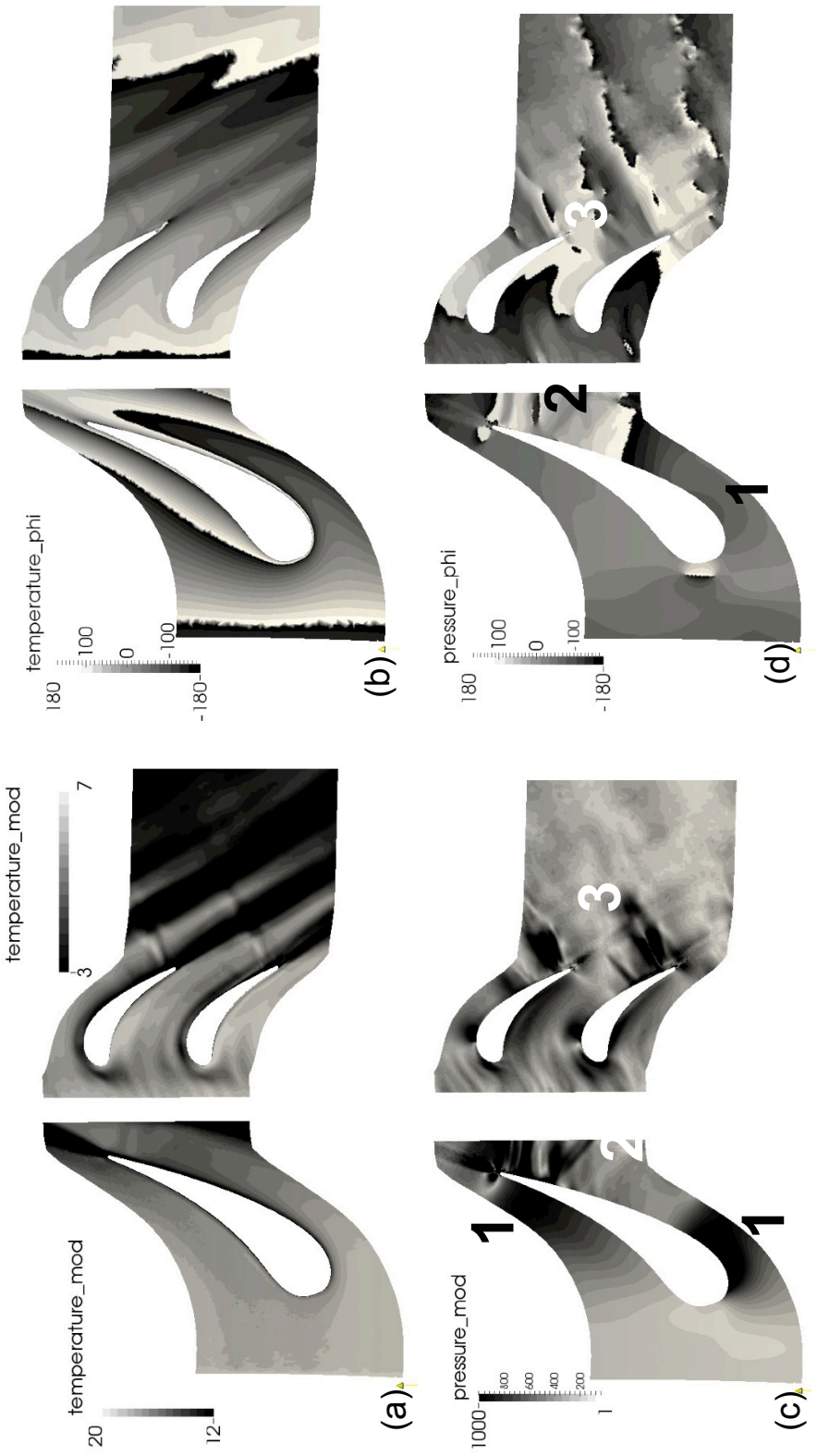

Figure 5.21: DMD 2 kHz mode at mid-span - Modulus and phase of the temperature (a and b) and pressure (c and d) respectively

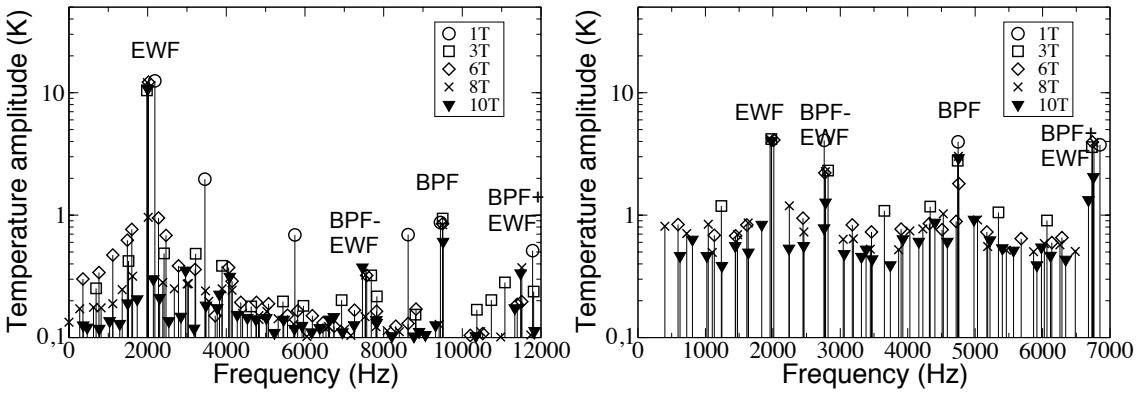

Figure 5.22: DMD temperature spectrums of the pulsed case with different number for different runtimes - stator (left) and rotor domain (right) at mid-span.

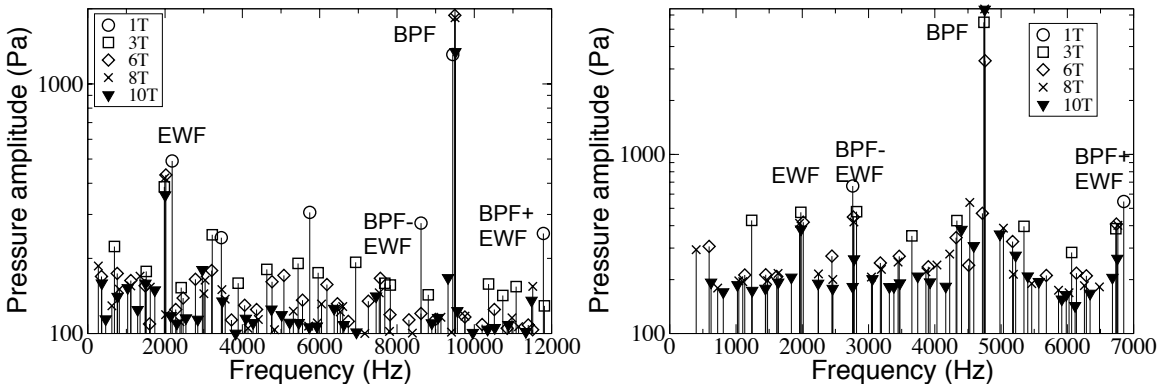

Figure 5.23: DMD pressure spectrums of the pulsed case with different number different runtimes - stator (left) and rotor domain (right) at mid-span.

conclusion that can be drawn is that for the EWF amplitude there is good agreement for all runs with a duration above $3T$. For a run time of $1T$, EWF in the stator is found to be shifted to slightly above 2 kHz, while in the rotor domain no mode at 2kHz is present. Regarding the BPF mode, a relatively good agreement is also observed, particularly for runtimes above $6T$. Most differences appear for the interaction modes $BPF \pm EWF$, where a trend of reduced pressure amplitudes appears as the run-time increases. Regarding the overall spectra, it can be observed that, as more snapshots are added to the signal, the amplitudes of the modes with irrelevant frequencies drop. This indicates that non-coherent broadband phenomena, such as turbulent fluctuations, are present and should not be interpreted as coherent or significant modes. For the cases with $1T$ and $3T$ of total runtime, for example, there are several notable peaks that either disappear or are largely reduced when more snapshots are added. Note that for the EWF, where combustion noise will occur, 6 periods T of run-time and above appear adequate for the method to converge.

These results highlight that DMD is more robust when treating purely coherent periodic phenomena. Its use in fully turbulent flows, with stochastic fluctuations and broadband noise present, makes the method prone to reveal more coherent modes than actually present. These flows, therefore, require longer runtimes compared to basic test cases to eliminate such discrepancies. To alleviate this shortcome, a modified version of DMD, called Sparsity-Promoting DMD has been recently developed [195].

Sparsity-Promoting DMD

The spectra of Figs. 5.19 and 5.20 reveal that several other modes are also present around the EWF. Combining this with the fact that the amplitudes of irrelevant modes can require a large amount of snapshots for convergence, it is desirable to be able to evaluate the most important contributions in terms of noise generation and eventually clean up the spectra. To do so automatically a modified version of the DMD has been developed [195] and called the Sparsity-Promoting DMD (SPDMD). This advanced version of DMD aims at selecting the long-standing coherent modes that generate noise while removing the fast decaying ones, typically present because of turbulence, by employing a user-defined regularization parameter that controls the balance between accuracy and a dataset with a reduced set of modes.

In the following, the SPDMD is performed on pressure using the same set of instantaneous flow fields as in the previous sections, to identify the most important noise-generating modes in the flow. The intention of this analysis is to verify that this optimized method will recover the pulsation mode and confirm its significance. Figure 5.24 depicts the original pressure DMD spectrum with all the modes present complemented by the sparsity-promoting spectrum superimposed for the turbine inlet and outlet respectively. Both diagnostics provided in Fig. 5.24 are measured at the x-normal inlet and outlet planes for the pulsed case, as it is where the combustion noise will be measured. It can be seen that at the stator inlet the algorithm keeps only the pulsation mode, as expected. At the rotor exit, even though many more modes exist (caused by the local high turbulence levels), the mode corresponding to the BPF and the pulsation frequency are chosen

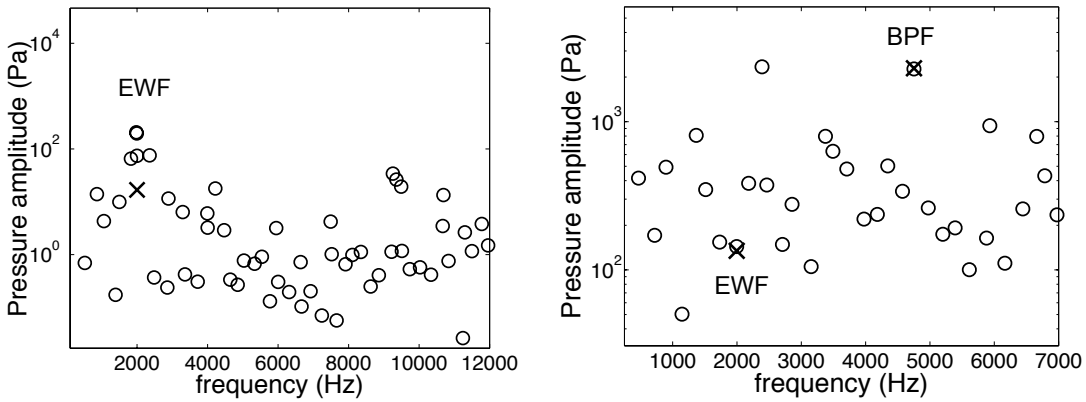

Figure 5.24: Sparsity-Promoting DMD at the stator inlet (left) and rotor outlet (right) - Original DMD modes (∘) and SPDMD selected modes (×).

as the most coherent ones. It can further be noted that the algorithm retains the EWF mode despite its weak amplitude.

These findings confirm the importance of the indirect combustion noise with respect to other flow phenomena, as well as the ability of DMD to extract it. It also shows that SPDMD can be an appealing method for the analysis of real combustors. With realistic entropy waves generated at flame fronts being broadband and not monochromatic, such a method has the potential of quickly identifying the entropy modes that are most probable to generate indirect noise and thus provide more guidance for the design. However, in this monochromatic study the frequency of the indirect noise is known a priori, as it corresponds to the user-defined EWF so the standard DMD method is sufficient.

5.5.3 Quantifying the indirect noise and comparisons with the compact theory

The noise that is measured in this study is the result of a pulsated, realistic 3D turbine with several flow features present (notably the secondary flows at the hub and casing of the stator, the tip leakage flow at the rotor, the complete 3D shock structures and the shock-boundary layer interactions). In terms of noise generation, it can be compared with the 2D compact theory of Cumpsty and Marble [38]. Numerical results from 2D pseudo-LES (using the MISCOG approach and a simple mesh deformation technique) of a simplified turbine stage described in detail in [189] serve as an additional complement to the theory and the full 3D simulations. It is worth noting that Duran *et al.* [34] commented that for his configuration (a modified version of the MT1 turbine stage at mid-span with a 30:30 blade count) 2 kHz is approximately the limit after which the compact assumption is not valid.

To measure the transmission of the generated acoustic waves, DMD is performed at the inlet and outlet x-normal planes. Assuming that at these locations the waves are 1D plane waves, the downstream propagating acoustic wave can be calculated as

$w^+ = \frac{p'}{\gamma\overline{p}} + \frac{u'}{\overline{c}}$, the upstream propagating acoustic wave as $w^- = \frac{p'}{\gamma\overline{p}} - \frac{u'}{\overline{c}}$ and the entropy wave $w^s = \frac{p'}{\gamma\overline{p}} - \frac{\rho'}{\overline{\rho}}$. The overline in these expressions indicates time averaged quantities, the prime indicates fluctuations and the heat capacity ratio γ is assumed to be constant throughout, while u indicates the axial component of the velocity. The formulation of these waves is dimensionless. The transmission coefficients of interest are the entropy wave attenuation $Ts = \frac{w_2^s}{w_1^s}$, the acoustic wave reflection $Ra = \frac{w_1^-}{w_1^s}$ and the acoustic wave transmission $Tr = \frac{w_2^+}{w_1^s}$, with the subscript 1 indicating the turbine inlet. The subscript 2 refers to the turbine outlet and w_1^s is the forced entropy wave imposed at the inlet.

The procedure to construct the characteristic waves and measure the transmission coefficients at the inlet and outlet of the turbine stage can be decomposed into 5 steps:

1. Perform DMD of the principal flow variables at an x-normal plane both at the inlet and outlet of the turbine.

2. Isolate the mode of interest (EWF in this case) and form the temporal fluctuations of the variables.

3. For each point in the plane construct the 1D plane waves using the reconstructed fluctuations and a time-averaged solution.

4. Perform surface averaging and calculate the transmission coefficients.

Applying this procedure at the inlet of the turbine stage is straightforward, since there is no free-stream turbulence imposed. However, as the flow goes through the turbine it generates broadband fluctuations. While DMD allows an easy filtering of all irrelevant frequencies, turbulence or hydrodynamic phenomena whose frequency coincides with the pulsation frequency will be present in the signal and can therefore modify the evaluation of the transmission coefficients. As a result, at the rotor outlet an extra step is added before step (4): a hydrodynamic filtering based on the Characteristics Based Filtering (CBF) method [196] is applied to separate hydrodynamics from acoustics knowing their different propagation velocities. To apply this filtering, the waves are measured in 3 outlet x-normal planes in close proximity (instead of just 1). The Taylor hypothesis and the known wave speed are then used to correlate the data between the 3 planes at different physical times following the formula:

$$w_a = \frac{1}{3}\sum_{i=0}^{2} f(x - i\Delta x, t - \frac{i\Delta x}{u_p}) \tag{5.7}$$

In Eq. (5.7), f is the wave of interest, w_a is the filtered wave, Δx is the distance between the planes and u_p is the wave speed, i.e $\overline{u} + c$ for w^+ and $\overline{u}$ for w^s.

Results, obtained with the procedure described above, are summarized in Fig. 5.25, where they are also compared to the theory and 2D numerical predictions. For the compact theory and 2D simulations, predictions across a broad frequency range are available. The 3D predictions are close to the 2D ones, while the compact theory predicts stronger upstream propagating generated noise and slightly lower transmitted noise. Regarding

the entropy wave transmission, the results of the 3D simulation suggest that at the turbine outlet the injected wave has been dissipated more than in the 2D simulations, while the theoretical approach neglects the entropy wave attenuation process. Concerning the acoustic waves generated at the forcing frequency, for the downstream propagating acoustic wave, the two numerical simulations are in reasonable agreement. For the upstream propagating wave, the 3D simulation predicts a small decrease in strength compared to the 2D prediction, probably because of the choked operating condition that prevents acoustic waves generated downstream the sonic line to travel towards the turbine inlet.

5.6 Conclusions

In this chapter, the indirect combustion noise generation mechanism across a high-pressure turbine has been investigated. It is achieved by performing LES of a 3D high-pressure turbine stage subject to a constant-frequency entropy wave train pulsation. To simplify the data processing, the flow field and the generated noise are analyzed through the Dynamic Mode Decomposition of instantaneous snapshots at several positions across the turbine and the results are compared with a steady inflow case. When no wave forcing takes place, the strongest noise-generating mechanisms are revealed to be the rotor/stator interactions occurring at the BPF and its harmonics, followed by weaker activity due to the stator vortex shedding and trailing edge acoustic wave generation. When entropy wave injection is activated, a distinctive high-amplitude mode at the pulsation frequency is generated, as well as interaction modes with the blade passing frequency. The influence of the entropy waves is also captured by the sparsity-promoting DMD, a modified DMD algorithm that provides an accurate reconstruction of the flow field with few well-selected modes. Despite the presence of broadband turbulence and non-linear interactions, the blade passing frequency and pulsation modes are shown to be the most important ones. For the forced frequency, a detailed analysis of the 3D LES predictions is performed and the results are compared with the compact theory [38] as well as 2D simulations of a similar turbine configuration. While the theory overpredicts the noise levels, the 3D LES of the choked transonic HP turbine reveals that the entropy waves get highly distorted and weaker as they are transmitted to the following stages if compared to 2D results or the compact theory (unlikely to generate any additional indirect noise). The transmitted acoustic waves to the consequent stages remain strong, and will equally contribute to the indirect noise as in the 2D simulations. The reflected acoustic waves are slightly weaker than in 2D predictions and much more attenuated than in the compact theory.

This chapter also serves as the first application of MISCOG on a combustion chamber-turbine interaction problem. While the problem is treated in a decoupled fashion from the combustor, the method proves to be capable of capturing the complex generation mechanisms of indirect combustion noise in a fully 3D high-pressure turbine stage where rotor/stator interactions are important. These results, thus, can provide some degree of confidence that the method is capable of treating a fully coupled combustion chamber-turbine problem.

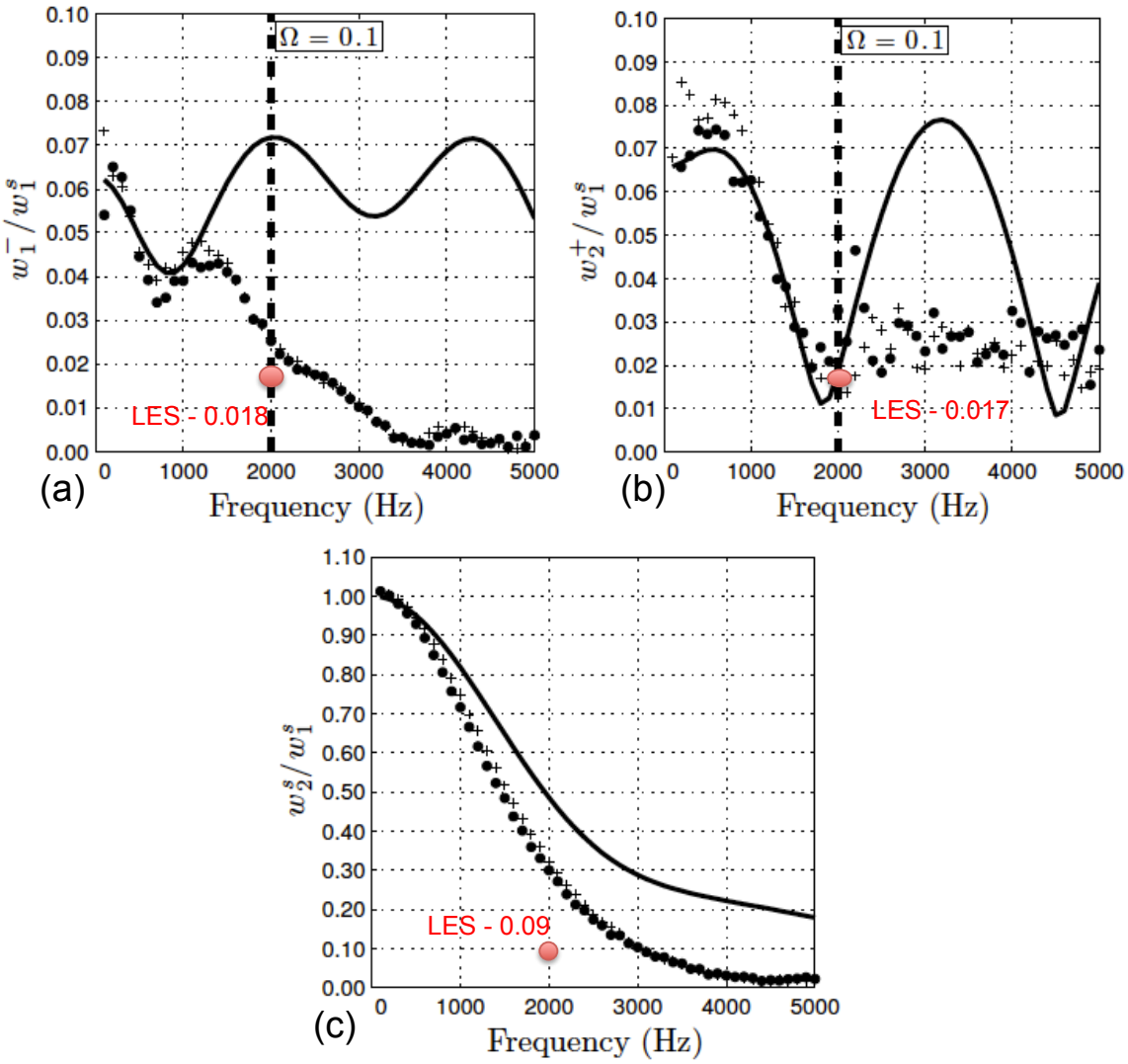

Figure 5.25: Transmission coefficients - a) Ra b) Tr and c) Ts - Compact theory (solid line), 2D simulations (+ and •) and LES (•)

Chapter 6

LES of an industrial combustion chamber-turbine system

Contents

6.1 Multicomponent simulations of gas turbines 122
6.2 Hot-streak migration across turbines 125
6.2.1 Segregation effect 125
6.2.2 Other parameters influencing the hot-streak migration 126
6.3 LES of an industrial high-pressure turbine stage 129
6.3.1 Standalone turbine geometry 129
6.3.2 Mesh 130
6.3.3 Boundary conditions 132
6.3.4 Numerical setup and initialization 133
6.3.5 Results 133
6.4 Fully coupled combustion chamber-turbine simulation 141
6.4.1 Geometry 141
6.4.2 Mesh 142
6.4.3 Combustion modelling 142
6.4.4 Initialization and numerical set-up 144
6.4.5 Results 146
6.5 Conclusions 152

In this chapter, the MISCOG method is used to perform combustor-turbine LES of a helicopter engine, the focus being placed on the aerothermal interactions in such systems. Before presenting the numerical simulations, the literature on previous multi-component simulations of gas turbines and on the migration of combustor-generated non-uniformities across turbines is reviewed. Although the main objective here is to illustrate the capacity of MISCOG to treat the full combustor-turbine LES flow of real industrial configurations, the turbine is first investigated alone. Comparatively to the simulations of Chapter 4, increased fidelity is introduced by imposing realistic time-averaged temperature profiles at the inlet of this standalone turbine LES, provided by an existing LES of the combustion chamber. Comparisons of the aerodynamic flow field with standard steady-state RANS simulations that employ the cheaper mixing plane method for the rotor/stator interface (provided by Turbomeca) permits the comparison of the results of this first complex turbine stage LES with the typical industrial simulation method.

The second part of this chapter is dedicated to a fully coupled, multi-species and reactive LES of the entire combustion chamber-HPT system. With this approach, all the heterogeneities at the combustor outlet can be propagated in real time through the turbine, thus taking into account all combustor-turbine interactions in time and space. This last simulation highlights the potential of the developed methods for future multi-component simulations of gas turbines and is compared to the standalone turbine LES. Although such predictions remain at this stage preliminary and clearly require further efforts, both simulations are compared with a focus on the migration of temperature non-uniformities across the entire turbine stage.

Note that a large part of the presented simulations was performed during a 3-month secondment at Turbomeca, in the frame of the project COPA-GT. For confidentiality reasons, figures that include temperature and pressure have been normalized by the total temperature and total pressure at the turbine inlet issued by the thermodynamic cycle of the engine.

6.1 Multicomponent simulations of gas turbines

The advantages of coupled multi-component simulations, complemented with the increasing computational resources, have sparked considerable interest since the beginning of 2000's. A first full engine simulation was produced for the General Electric GE90 engine by Turner *et al.* [19] within the NASA Numerical Propulsion System Simulation (NPSS) program. For this simulation, dedicated solvers for each component were used, the unstructured National Combustion Code for the combustion chamber [197] and the structured multi-block APNASA code for the turbomachinery stages. Both codes are steady-state RANS solvers employing the $k-\epsilon$ turbulence model [198]. This work relied on a turbomachinery-combustor coupling method developed earlier [199, 200] which ensured mass and total enthalpy conservation and resulting efforts were oriented towards the capacity of such a tool to recover the main cycle parameters of the engine. Despite the success of the simulation in capturing such engine data (Fig. 6.1 presents the error on the prediction of the main thermodynamic parameters across the engine compared

to experimentally measured values), the RANS approach and the modeling of significant technological effects, such as the tip clearances of the rotating machineries or coolant injections, were found to impact the predictions significantly [201].

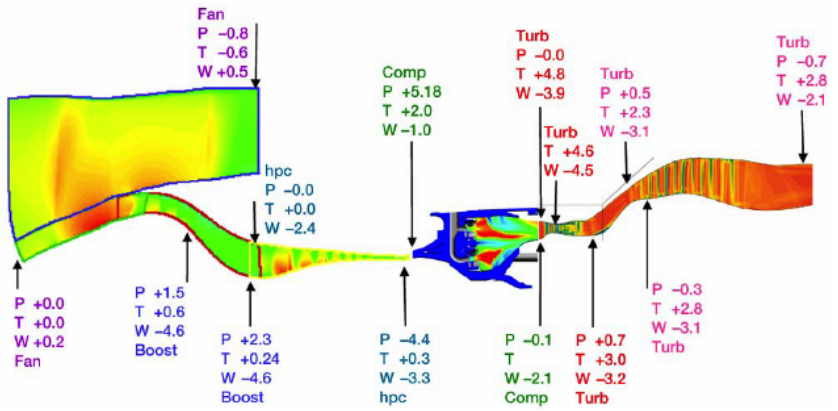

Figure 6.1: Full GE90 simulation comparison to engine cycle data. Percent difference in total pressure (P), total temperature (T) and flow rate (W) from experimentally measured values [19].

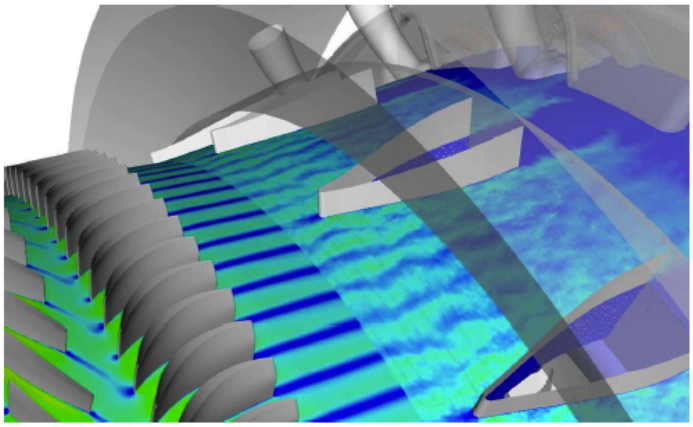

Figure 6.2: LES/RANS interface at the compressor exit with turbulent fluctuations superimposed at the time averaged RANS solution [20].

To increase the fidelity of such multicomponent tools, combustor simulations switched to solvers based on the LES formalism, considered more accurate than RANS for this component [202]. For the wall-bounded high-Reynolds turbomachinery parts, the (U)RANS approach was retained. The most notable work using this type of coupling was the full engine simulation performed at Stanford University in the framework of the ASCI project [20, 21]. The principal challenge with this different approach is in the handling of the interfaces between the different solvers and formalisms: *a*) at the RANS/LES interface, located at the compressor exit, turbulent fluctuations need to be reconstructed and

injected in the LES domain and *b*) the LES/RANS interface placed at the turbine inlet needs a specific treatment to ensure a smooth transition and conservativity. Difficulties were also added due to the fact that the combustion chamber solver was incompressible compared to the compressible turbomachinery solver.

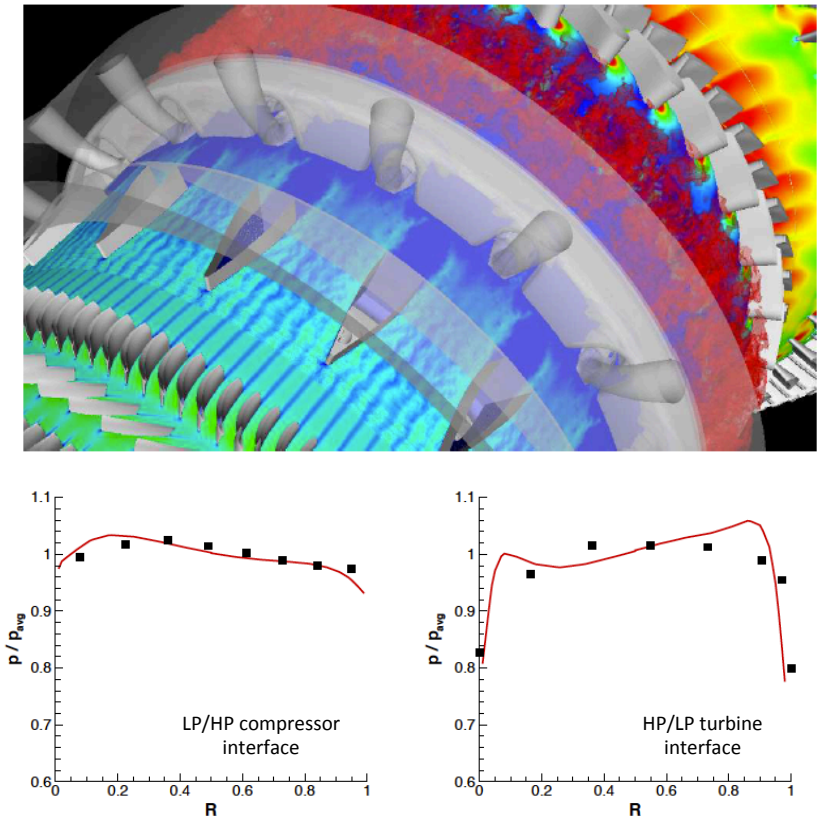

Figure 6.3: View of the high-pressure flow field from the full engine simulation (top) and radial pressure profiles at two different engine positions (bottom)[21].

For the reconstruction of turbulent fluctuations at the RANS/LES interface, Medic *et al.* [20, 203, 204] proposed a recycling technique. In this approach the turbulent fluctuations are calculated in parallel "on the fly" by a periodic duct LES with similar conditions as those prevailing at the combustor inlet. Obtained fluctuating fields were then superposed to the time averaged RANS profile and used at the LES inlet, Fig. 6.2. On the other side of the combustion chamber, to overcome the difficulties between the incompressible-compressible solver coupling, Schlüter *et al.* [205, 206] proposed the use of the body force method: the LES domain has an overlapping region with the RANS domain and within this region the mean velocity of the LES solution is driven towards the RANS solution with the addition of body forces. The final full engine simulation, combining LES and RANS, depicted very realistic flow fields and the existing measurements for the pressure radial profiles at two different engine locations (low-pressure/high-pressure

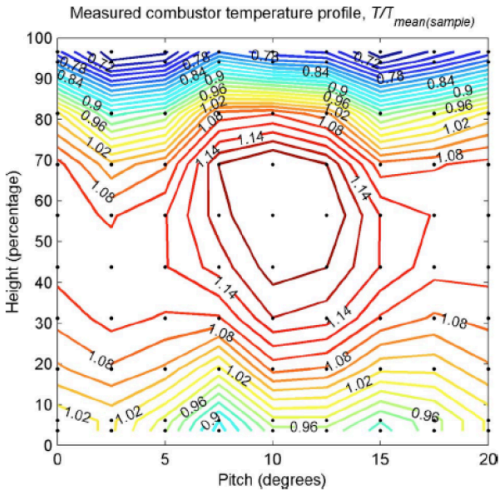

Figure 6.4: Typical combustor outlet temperature profile [22].

compressor interface and the corresponding turbine interface) showed a generally good agreement with the simulation, Fig. 6.3.

6.2 Hot-streak migration across turbines

As mentioned in Chapter 1, the combustion chamber generates temperature heterogeneities, turbulence and swirl that propagate and migrate across the turbine stage. Figure 6.4 depicts a typical time-averaged temperature profile at a combustor exit highlighting the large temperature differences across the sector. The thermal load of the blade rows, already constrained by the high mean operating temperatures, is altered considerably by these heterogeneities. This necessitates consequently a good prediction of the migration of the non-uniformities if an optimal design of the blade and its cooling systems is to be obtained. The importance of the combustor-turbine interactions can be better highlighted if one considers that an under-prediction of the blade temperature by just 15 degrees (when the inlet temperatures are well over 1500 K) can reduce the expected life duration of the turbine by half. Note that different physical effects and features are important on the migration of temperature heterogeneities across turbine stages, as detailed below.

6.2.1 Segregation effect

An important consideration when trying to predict the migration of temperature non-uniformities in the rotor blades of a turbine stage is the segregation effect first described in [207]. If the Mach number and flow angles are considered constant, fluid of higher temperature will have an increased absolute velocity at the stator exit due to the increased speed of sound, while cold gases will be slower. As a result, when the rotational velocity

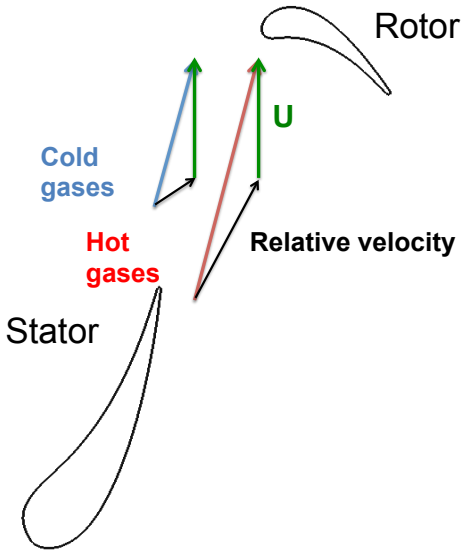

Figure 6.5: Schematic showing the segregation effect.

is added at the stator/rotor interface, the relative velocity angle seen by the rotor blades is different as illustrated in Fig. 6.5. While for both hot and cold gases the flow angle of the absolute velocity is the same, the higher magnitude of the hot gas velocity creates a relative velocity with a higher angle and magnitude. In real turbines with hot streaks, this leads to a preferential migration of the hot gases towards the pressure side of the rotors as confirmed experimentally by Butler *et al.* [208]. An interesting thing to note is that this phenomenon is fully unsteady. As a result, predictions from steady-state numerical simulations, which are prevalent at the design stage of a turbine, cannot take such effects into account.

6.2.2 Other parameters influencing the hot-streak migration

Figure 6.4 depicts a hot spot located in the center of the sector and contained between 40 and 60% of the span. This specific alignment of the non-uniformities can be however altered by the relative placement of the fuel injectors and the dilution holes present in the combustion chamber. As a consequence, a lot of research has been performed to evaluate the effect of the azimuthal and radial placement of hot-streaks on the resulting temperature profiles across the blade passages. Additional flow characteristics at the turbine inlet are also know to affect the heat load on the blades. Among others, the free-stream turbulence and length scales along with the residual swirl from the combustor are of crucial importance.

- Effect of the fuel injector and vane clocking

The principal parameter in hot-streak migration is considered to be the azimuthal placement, also called clocking, of the hot spots with respect to the blade leading edge.

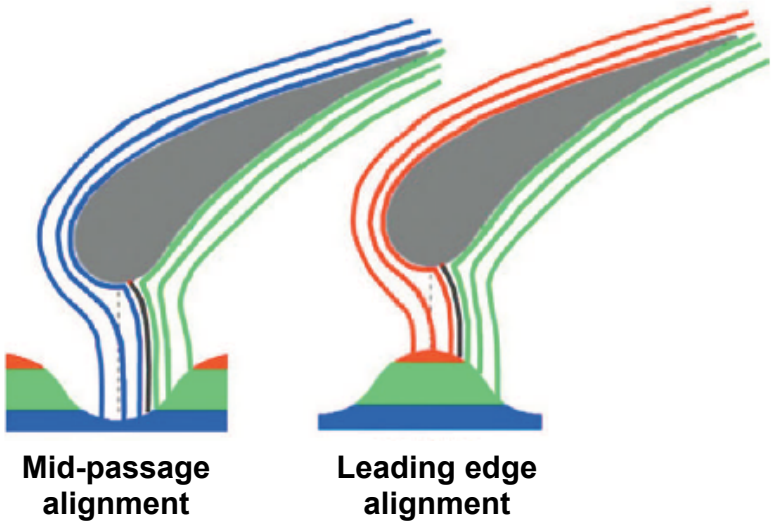

Figure 6.6: Effect of clocking on the NGV heat load [15].

Povey *et al.* [15] performed a numerical and experimental investigation of the effect. A significant increase in the heat transfer on the suction side of the stator (also called Nozzle Guide Vane, NGV) was observed when the hot part was aligned with the blade leading edge, while aligning the hot streak with the blade passage was reducing it, as shown in Fig. 6.6. Although the latter alignment can be beneficial for the stators, it can prove to be damaging for the rotor if the segregation effect is taken into account. In realistic geometries, the distance between blade rows is small and the flow at the outlet of the stator is not uniform. The wake region has a velocity deficit compared to the free-stream. Aligning the hot flow with the leading edge would direct the hotter, higher velocity gas in the wake region, reduce the velocity deficit and help cancel the segregation effect. As a result, the heat load on the rotor pressure side can be reduced. This has been confirmed by He *et al.* [26], in a thorough study of different hot-streak counts in the heat loads across the MT1 turbine stage.

- Impact of the hot-streak radial position

Besides the azimuthal placement of the non-uniformities, there is also evidence of the importance of the radial position of hot-streaks. In fact, small contained hot-streaks around mid-span are shown to have little impact on the blade heat load close to the endwalls. More specifically, Povey *et al.* [15] observed a decrease of the heat load as the temperature is decreased locally near the endwalls. On the contrary, when hot-streaks are enlarged they can interact with the secondary flows, the passage vortices being able to transport hot, high-energy fluid from the free-stream towards the hub and casing boundary layers, thus increasing the heat load at these locations [29]. Similar conclusions were drawn by Roback and Dring [28], when the position of the hot streak is moved radially towards either the hub or the casing. Finally, note that additional radial

migration of the non-uniformities can exist because of the radial pressure gradients and buoyancy effects for example [30].

- Influence of the free-stream turbulence

Apart from the mean temperature nonuniformities, the flow at the exit of the combustion chamber is also highly turbulent. Colban *et al.* [160] measured in experimental combustor simulators turbulence intensities up to 30% at the leading edge of the first turbine blade row. Similar results were measured by Barringer *et al.* [209], who also found a correlation between the turbulent length scales and the size of the dilution holes in the combustion chamber. Such levels of turbulence are known to impact the aerodynamic and thermal flow field of the turbine, as well as the hot-streak mixing.

A number of experimental and numerical investigations have shown a significant increase of the heat transfer of blades when high levels of turbulence are present at the inflow [23, 99]. Indeed, the incoming eddies interact with the blades and get stretched, forming long longitudinal structures, Fig. 6.7, that enhance the heat transfer, particularly on the pressure side. On the suction side, the strong flow acceleration alleviates this effect in the first half of the blade [23, 210]. However, as the flow decelerates when it approaches the trailing edge, laminar-to-turbulent transition of the boundary layer can be observed and is affected by the vane turbulent flow. A turbulent boundary layer is known to enhance the mixing of high momentum, high temperature fluid from the outer layer with the low momentum fluid of the inner layer, resulting in a considerable increase of the heat transfer to the blade walls. Free-stream turbulence is one of the principal ways transition can be triggered and is shown to influence the position where it occurs, thus impacting the overall heat load of the blade [9, 31]. It has also been shown that free stream turbulence does not decay across the turbine and that additional turbulent kinetic energy is produced around the stagnation points [210]. Interactions of turbulence with hot-streaks have also been investigated. Jenkins *et al.* [32] reported that medium levels of free-stream turbulence render the hot streak more compact and enhance temperature gradients.

- Influence of swirl

Recent experimental and computational work from Qureshi *et al.* [4, 33] indicate a considerable impact of the residual flow swirl at the turbine inlet, generated in the combustion chamber, on the aerothermal flow field across a high-pressure turbine stage. At the NGV, the swirl is altering the incidence angle of the flow, thus modifying the aerodynamic flow field and secondary flows. These changes naturally lead to significant local alterations of the heat transfer, particularly near the endwalls. Across the rotor the changes are less significant [33]. Nonetheless, the overall heat transfer should be increased as swirl is likely to enhance the free-stream turbulence levels and hence the near-wall mixing.

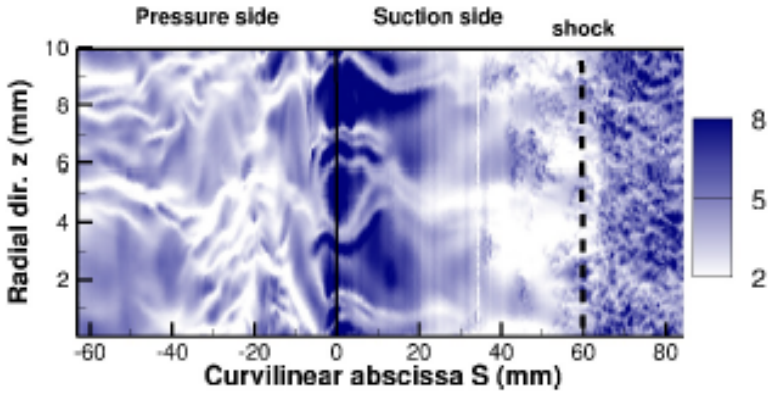

Figure 6.7: Heat transfer coefficient across a high-pressure NGV under the influence of free-stream turbulence [23]. The turbulence alters the thermal flow field, forms elongated structures and enhances the heat transfer.

6.3 LES of an industrial high-pressure turbine stage

The findings of previous research efforts on the migration of temperature non-uniformities underline that there is a strong coupling of the HPT and the combustor during the operation of a gas turbine. Important phenomena, such as the turbulence levels and length scales, cannot be accurately modeled in standalone HPT simulations, thus highlighting the potential gains in prediction accuracy issued by a fully coupled combustion chamber-turbine simulation. However, before illustrating the MISCOG ability to treat such complex industrial flows, the industrial HPT stage LES is first simulated to validate the proposed methodologies in an industrial turbine. To increase the fidelity of these simulations, a temperature hot-spot is imposed at the inlet and its migration across the turbine stage is studied. Comparisons with RANS, the preferred method for quick numerical predictions at the design phase, are also shown at this occasion for key performance figures.

6.3.1 Standalone turbine geometry

The high-pressure turbine geometry is selected from an existing engine of Turbomeca. It is an unshrouded design, similar to the MT1 turbine analyzed in the previous chapters. An advantage of the selected engine is that, parallel to this work and in the frame of the European project COPA-GT, Turbomeca performed LES of the corresponding combustion chamber, used here to determine the inlet profiles of this HPT simulation.

As with the MT1 geometry, the reduced blade count technique is employed in the rotor to reduce the computational domain to an azimuthally periodic extension of the combustor simulation (considered in the next section) with 1 stator and 2 rotors. However, the geometry set-up used in this chapter demanded the scaling of the rotors to be done in the cartesian coordinates instead of the cylindrical ones as proposed by Mayorca *et al.* [60] and used in the simulations of Chapter 4. As a result the blade angles and the

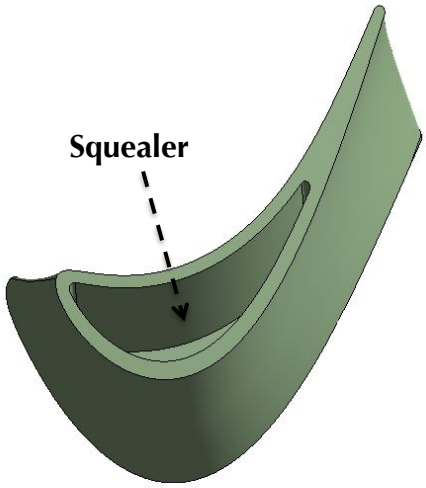

Figure 6.8: Rotor geometry with squealer.

mean flow will be significantly altered compared to the true geometry. It is also worth noting that the geometry used corresponds to a cold geometry, meaning that the thermal expansion of the blades due to the high operating temperature is not taken into account. The CAD source file uses a multi-zone approach where the combustor-turbine system is segmented in 3 zones to facilitate the coupled simulations: the combustion chamber, the stator and the rotor domains. For this case, i.e the standalone turbine LES, only the latter two parts are employed.

Besides the blades, a real HP turbine has complex technological effects that weren't present in the experimental MT1 turbine: fillets, internal blade cooling channels and holes that inject fluid in the main passage, as well as cavities in the hub and casing between the blade rows. Additionally, it is not uncommon for rotors to have squealers, which are obtained by removing material from the central area of the blade tip, Fig. 6.8. Such a process reduces the weight and mechanical forces applied to the blade. It also permits a reduced tip clearance to be achieved by the manufacturing [211]. Frequently, most or all of these specificities are omitted in CFD simulations as typical turbomachinery solvers use structured meshes and therefore require considerable effort to take them into account. The chosen configuration for LES retains only a squealer of depth approximately the one of the real blade and with a flat bottom, as it was assumed to be the most significant technological effect [5]. It is worth highlighting that here the unstructured approach allows for easier inclusion and meshing of even the most intricate technological aspects of the turbine geometry.

6.3.2 Mesh

As with the other turbine cases, a hybrid mesh approach is used, Fig. 6.9. Around the blades 5 layers of prisms are added to improve the near wall resolution, while tetrahedral

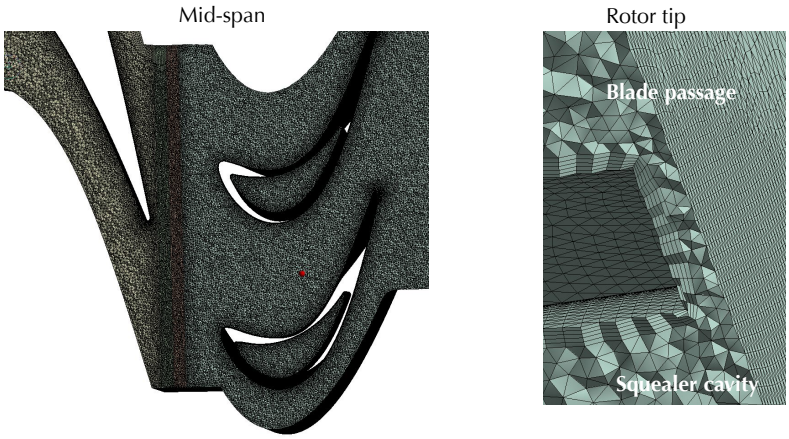

Figure 6.9: Views of the mesh at mid-span (left) and at the rotor tip (right).

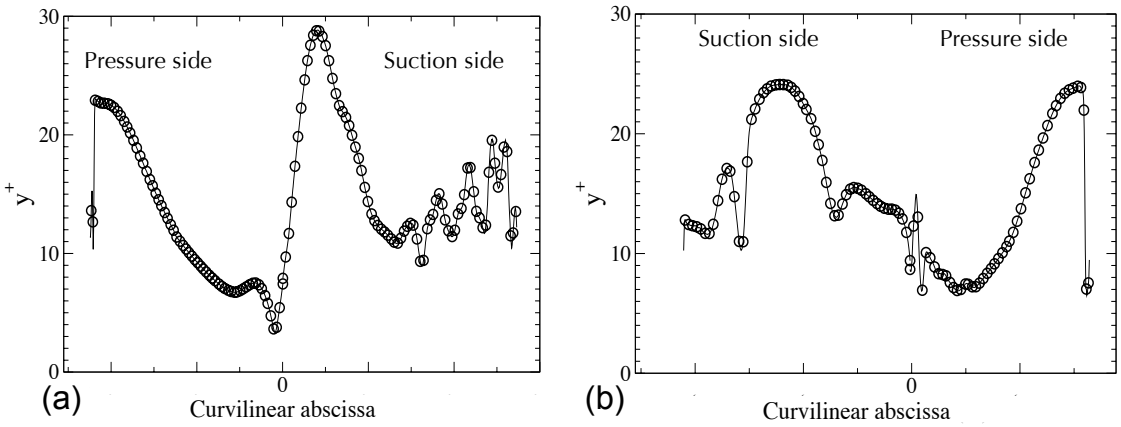

Figure 6.10: Distribution of y^+ across the stator (a) and rotor (b) blades at mid-span.

elements are employed in the passages and near the endwalls. On the rotor blade, the prism layers follow not only the form of the blade but also the squealer, Fig. 6.9 (right). The tip clearance is smaller than 0.5 mm. To keep the timestep acceptable, 7 cell layers are placed in that area. The total cell count is 25 million cells (10 million cells in the stator and 15 in the rotor domain). The maximum y^+ across the blades is approximately 30, Fig. 6.10. While this value is not within the guidelines for wall-resolved LES, it is significantly improved compared to the coarse MT1 mesh despite the limited cell count. This is due to the smaller power of helicopter engines, which translates to reduced turbine sizes and Reynolds number compared to the large airplane engines (the MT1 turbine is a representative configuration of an airplane engine). This improved resolution is followed however by a small time-step, $\Delta t = 8 \cdot 10^{-9}\ s$.

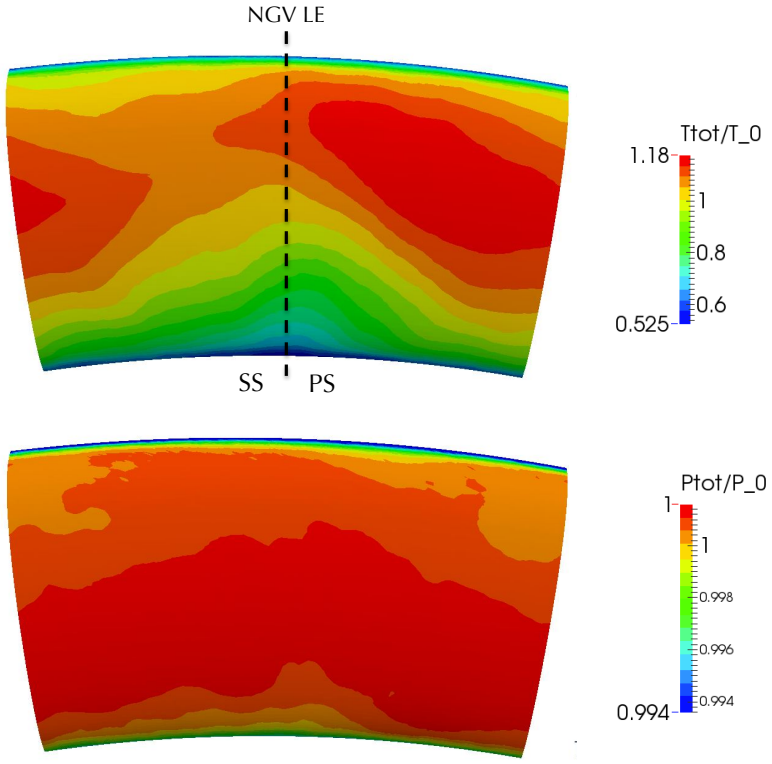

Figure 6.11: Non-dimensional total temperature (top) and pressure (bottom) profiles imposed at the turbine inlet.

6.3.3 Boundary conditions

As with most turbine stage simulations, the total temperature and pressure are prescribed at the inlet. Instead of imposing a homogeneous total pressure and temperature at the turbine inlet, realistic profiles constructed from a time-averaged solution of previous standalone combustor LES of the same engine were used. To this end, the principal flow variables are interpolated from the combustion chamber simulation exit section to the turbine inlet surface. Then using this information, the Mach number and total temperature are calculated as well as the total pressure using the isentropic relation. Note that the solver uses a variable heat capacity ratio γ. However, as RANS simulations of turbines often use a constant γ, an average value of γ is used to construct the inlet conditions in order to stay as close as possible to the RANS simulations of this configuration.

Another characteristic of this industrial turbine is that the real geometry has coolant air injected through cavities located between the stator and rotor hub, casing as well as through the stator trailing edge. These injections lead to an increase of the overall mass flow across the turbine stage. Taking into account these injections is costly, as that demands meshing the small cavities, penalizing the computational cost both in terms of mesh size and timestep. The typical approach for simulating their impact on the mass flow is by scaling the turbine inlet total temperature profile accordingly. Note that the

temperature variation across the inlet plane is preserved. The imposed total pressure is calculated from the total temperature using the isentropic relationship before applying the total temperature scaling.

The imposed profiles of total temperature and pressure, divided by the mean total temperature and pressure, are shown in Fig. 6.11 with the leading edge of the NGV depicted by the dashed line, along with the pressure and suction sides (PS and SS respectively) of the blade. As observed here, the hot-streak is centered at approximately 50-60% radius and towards the pressure side of the blade. This alignment indicates that the pressure side of the blade is likely to experience a higher thermal load. Note that the segregation effect can be exacerbated by such an alignment as described in section 6.2.1. Finally and contrarily to the fully integrated combustor-turbine LES, all standalone turbine stage computations use air to stay closer to the single-species formulation of most turbomachinery CFD solvers.

At the outlet of the turbine a static pressure is imposed. All walls are considered to be adiabatic.

6.3.4 Numerical setup and initialization

The Lax-Wendroff numerical scheme, 2nd order in space and time, is employed [111]. For SGS closure, following the findings and conclusions established in Chapter 4, the WALE model is employed in an effort to improve the near-wall predictions.

Initialization of the simulation is performed as before, through the use of a coarse mesh with 7 million cells in total. For these simulations, the 2D inlet profiles were not yet available so homogeneous inlet total pressure and temperature were applied. The initial flow field was simply uniform velocities throughout. After 3 rotations on the coarse mesh, the solution resembles the flow field of a turbine and is then interpolated onto the finer mesh. An additional 2 rotations with the realistic inlet profiles are performed to converge the flow on the fine mesh and a full rotation follows to obtain time-averaged data. RANS simulations are performed using the multi-block structured elsA code [212] using the same inlet profiles as the LES along with the $k - l$ two equation turbulence model of Smith [213] for closure. The rotor/stator interface of the RANS simulations is treated with the mixing-plane model.

6.3.5 Results

Performances

As mentioned in section 6.3.1, the rotor geometry of the turbine has been considerably modified compared to the real machine. This is expected to impact the aerodynamic flow field significantly. To quantify the effect of this modification some typical 0D performance figures measured from the LES of the scaled turbine are compared to RANS predictions of the correct geometry (without any scaling). RANS predictions of the scaled geometry are also presented to establish any similarities with the LES. Note that no squealer is included in the RANS domain which might have an impact on these figures. The

performance metrics of interest are (the subscripts *in* and *out* indicate turbine inlet and outlet respectively):

- Turbine total pressure ratio π_T

  It allows to evaluate the work extraction performed by the turbine and associated aerodynamic losses through the ratio of the total pressure at the inlet to the total pressure at the turbine exit:

  $$\pi_T = \frac{Pt_{in}}{Pt_{out}} \tag{6.1}$$

- Mass flow $\dot{m}$

- Degree of reaction R_d

  The formula for the degree of reaction reads:

  $$R_d = \frac{h_{rin} - h_{rout}}{ht_{in} - ht_{out}} \tag{6.2}$$

  where h and ht are the static and total enthalpy respectively, the subscript rin indicating the rotor inlet and $rout$ the rotor exit.

  R is a convenient metric to determine how the static pressure drop is distributed across the turbine blades. Values larger than 0.5 indicate that most of the drop occurs in the rotor blades, while values lower than 0.5 indicate that most of the flow acceleration takes place in the stator blades (impulse turbine).

- Isentropic efficiency η_{is}

  It is one of the best indicators of the quality of an aerodynamic design. It evaluates how close the expansion across the turbine stage is to the ideal isentropic expansion. For a perfect gas with constant heat capacity ratio, it is straightforwardly evaluated as:

  $$\eta_{is} = \frac{1 - \frac{Tt_{out}}{Tt_{in}}}{1 - \left(\frac{Pt_{out}}{Pt_{in}}\right)^{\frac{\gamma-1}{\gamma}}} \tag{6.3}$$

  Dedicated turbomachinery CFD solvers usually work with a constant heat capacity ratio γ and a mean value is applied in Eq. (6.3). In our case however, a reactive variable heat capacity ratio solver is used. As a result, calculating the isentropic efficiency with a variable γ, based on tabulated gas properties and described in [214], is preferred. Note that in this process the necessary surface averages needed at the different measuring stations (to render the result 0D) are performed using internal Turbomeca standards.

	LES	RANS (modified geometry)
π_T	-1.5%	-2.5%
$\dot{m}$	+1%	-0.1%
R_d	+65%	+75%
η_{is}	-0.4%	-4%

Table 6.1: Summary of 0D performance differences between LES and RANS with the modified geometry to RANS with the standard geometry.

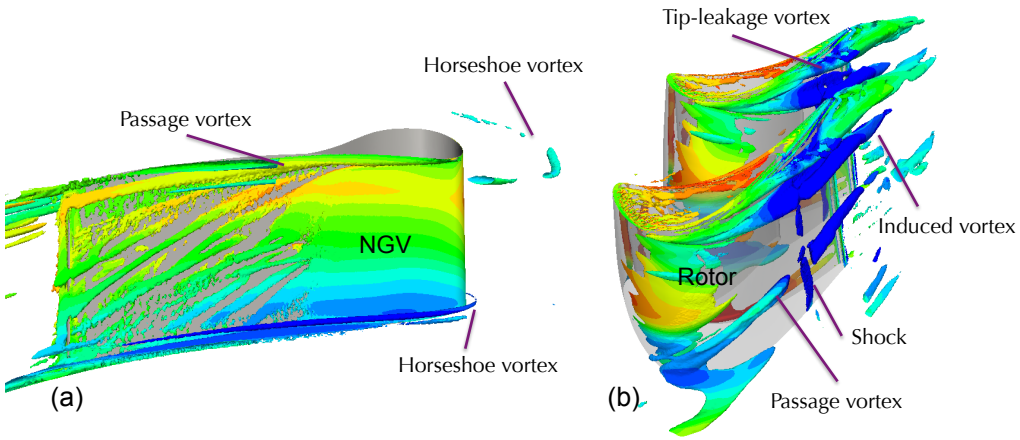

Figure 6.12: Isosurfaces of the Q-criterion across the NGV (a) and the rotor blade (b) calculated based on a mean flow and colored by the temperature.

Results are summarized in Table 6.1 where the differences between LES and RANS of the scaled turbine to the RANS of the unscaled geometry are presented. From Table 6.1 it is evident that the rotor blade scaling results in a small reduction of the total pressure drop across the turbine. Likewise, the isentropic efficiency is also reduced, especially for the RANS simulations where a drop of 4% is observed. The biggest change appears in the degree of reaction, where both scaled simulations yield a large increase of R_d. RANS simulations in particular, show a very large increase of the degree of reaction pointing to a significant reduction of the pressure drop across the NGV. In fact, since only the rotor blades have been modified, it becomes evident that the rotor/stator interactions impact directly the NGV aerodynamic loading and the flow is not comparable to the real engine flow. This is a typical problem encountered in real applications of CFD for which full annulus simulations are required if a high-fidelity rotor/stator interface, capable of transporting broadband phenomena, is demanded.

Mean flow topology

In the following, as the geometry modifications have been shown to be considerable and to have effectively altered the flow field, only the flow organization and predictions from the LES, which is the focus of this dissertation, are analyzed.

Isosurfaces of the Q-criterion computed from time-averaged velocities, colored by the mean local temperature, are shown in Fig 6.12. A typical flow field appears and secondary flows are recovered. The horseshoe and passage vortices are visible in the NGV and rotor hub, as well as the tip leakage and induced vortices developing in the tip clearance. One can also note that the horseshoe vortex at the NGV casing is developing further upstream compared to its counterpart at the hub. This behavior has also been observed on previous LES of the combustor+NGV system (internal Turbomeca simulations) or URANS of this turbine [5] (with the unscaled geometry). Another observation is that at around 50% of the NGV chord, streaks develop in the boundary layer, indicating the beginning of laminar-to-turbulent transition, although the near-wall mesh resolution is not sufficient to capture accurately such a process (Δz^+ and Δy^+ do not respect the criteria for accurate near-wall LES). These streaks are not horizontal and instead appear to migrate towards the hub. This orientation can be linked to the radial pressure gradients in this region. The temperature coloring allows to evaluate the influence of the secondary flows in the turbine heat load. The horseshoe vortices appear to be transporting colder flow from the endwalls to mid-passage, a phenomenon already observed before by Wlassow [5].

Hot streak migration

The hot-streak migration across the turbine is analyzed in detail in an attempt to qualify this standalone simulation in light of the physics discussed in section 6.2. Figure 6.13 depicts the temperature distribution across the NGV blade row at different axial positions. At the turbine inlet, Fig. 6.13(a), the hot-streak is located between the blades and at approximately 60% radius. At 10% of the chord length, Fig. 6.13(b), the distribution has already been altered around the blades: on the suction side there is a radial migration towards the casing (position B) and the horseshoe vortices from the hub and the casing (positions A and C) transport colder fluid from the endwalls towards the mid-passage. Further down the passage, Figs. 6.13(c,d), the secondary flows grow considerably. This leads to a further confinement of the hot-streak with comparatively cooler endwall temperatures. At these positions, the radial pressure gradient is now seen pushing the hot-streak towards the hub (position B). At the stator exit, Fig. 6.13(d), an additional area of higher temperature appears, near the casing on the blade suction side (position D). The casing horseshoe vortex is indeed located further away from the blade and the gap is filled by hot fluid is transported by the passage vortex instead as in [5].

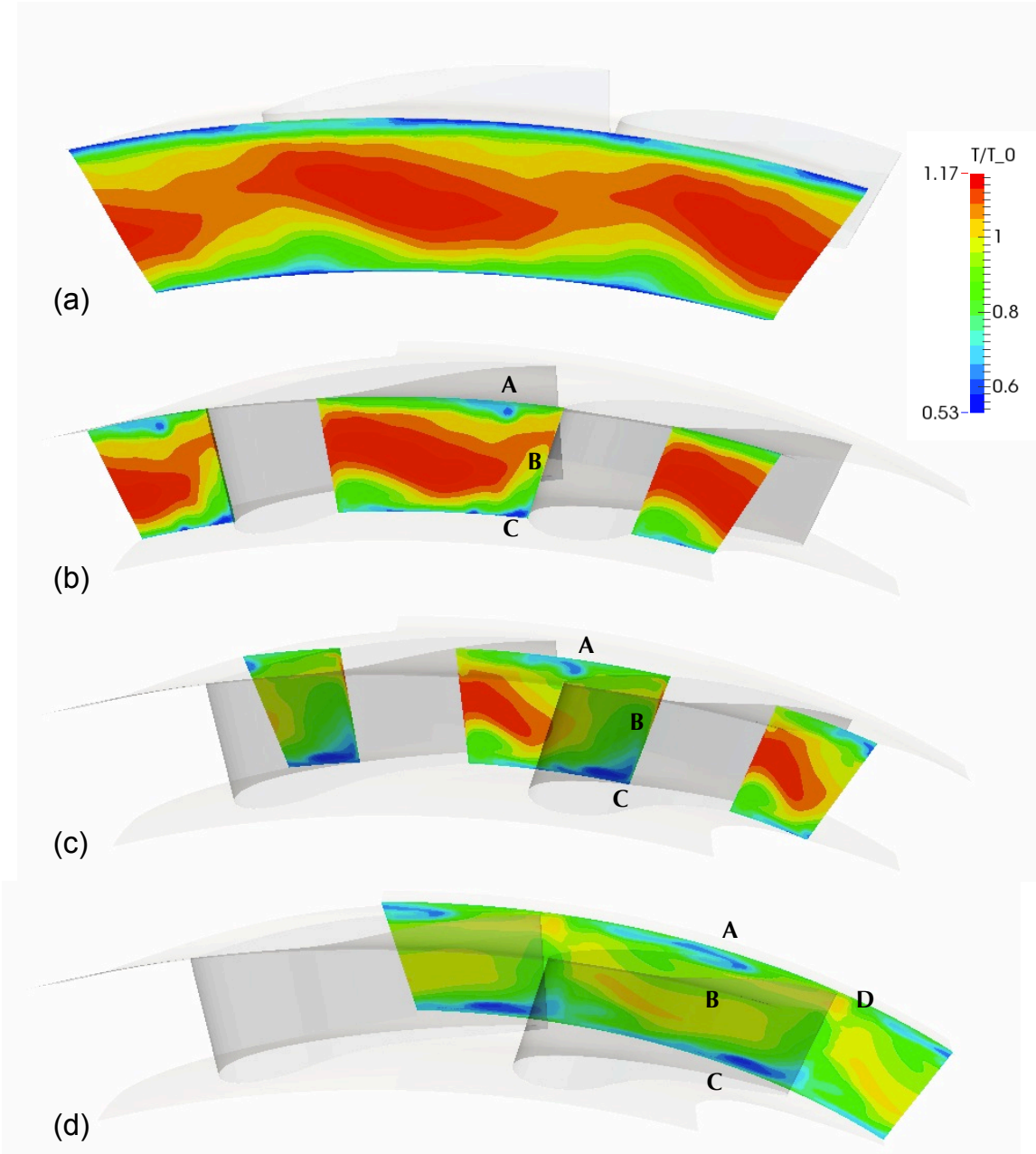

Figure 6.13: Temperature across the NGV passage - Turbine inlet (a), 10% of the chord (b), 60% (c) and at the NGV exit (d).

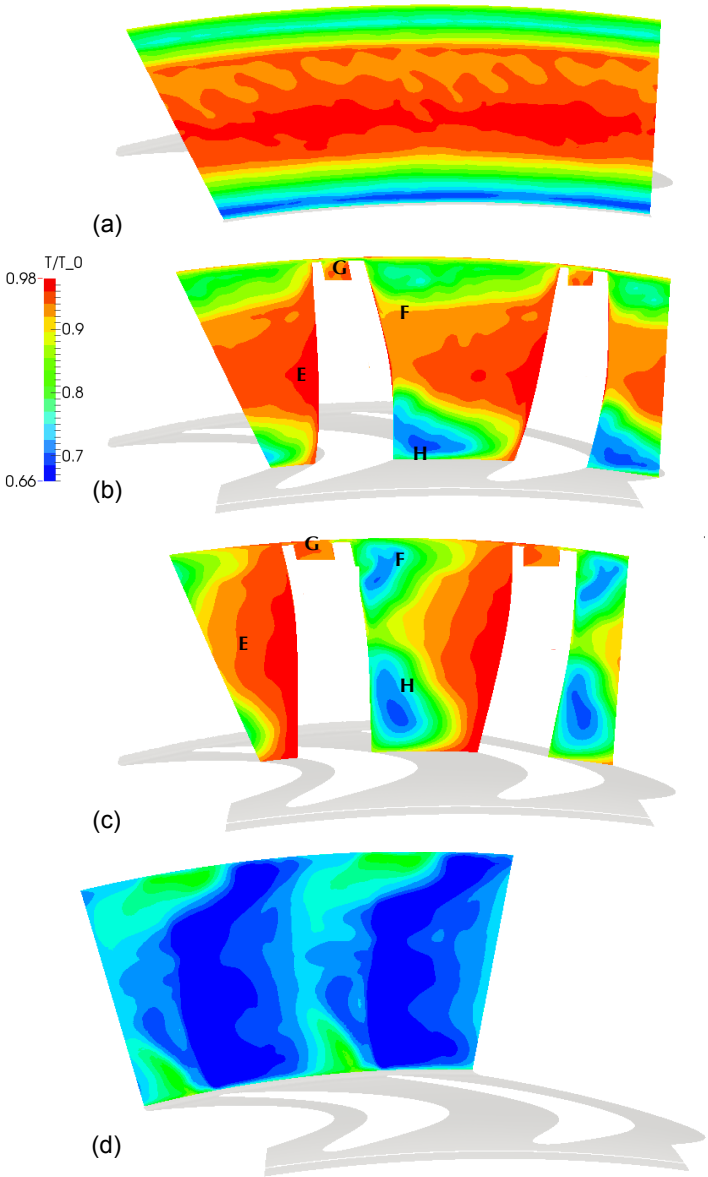

Figure 6.14: Temperature across the rotor passage - Rotor inlet (a), 10% of the chord (b),50% (c) and at the rotor exit (d).

In the rotor domain, Fig. 6.14, at the inlet a more uniform flow with mainly radial temperature gradients is seen by the blades due to the high-speed rotation, Fig. 6.14(a). The peak of the hot-streak appears now closer to the hub than at the NGV inlet, at approximately 40% height. Further down the passage, Fig. 6.14(b,c), four different phenomena that impact the migration of the hot-streak are observed. First, the hub secondary flows create a zone of colder fluid (position H), similar to the stator hub. Another region of interest is indicated by position E, which locates near the pressure side of the blade and where high temperatures are encountered. This feature can be explained by the segregation effect, which in this case is emphasized further by the mid-passage clocking of

the hot-streak as shown in [26], suggesting a preferential migration of the hot-streak to the rotor pressure side. Note that a radial migration of the streak towards the casing is also observed. The last interesting area relates to the tip clearance and the squealer. As already described, between 20 and 50% of the blade chord, the tip clearance flow passes from the pressure side to the suction side. Due to the higher temperature at the pressure side, this flow would lead to a high temperature tip leakage vortex region (position F). However, because of the presence of the squealer, the tip leakage flow is altered with a large part of the thermal load being transferred to the squealer (position G). It results in a lower temperature tip leakage region compared to the pressure side. Finally, at the rotor exit, the temperature is further decreased by the strong flow acceleration near the rotor trailing edge.

To evaluate the radial position of the hot-streak in the turbine, azimuthally averaged temperature profiles are plotted as a function of the radial coordinate. Figure 6.15 depicts such profiles for three different positions: the turbine inlet, the rotor/stator interface and the turbine outlet. First, at the turbine inlet the hot-streak is centered around 50-60% height with a temperature profile reducing smoothly towards the endwalls. Second, at the stator/rotor interface, the radial migration of the hot-streak towards the hub issued by the flow going through the stator blade is clearly seen: the maximum temperature drops from an initial location approximately 60% height to 40%. Heating near the endwalls is also present. Finally, at the rotor exit the hot-streak has moved towards the casing. Note that at this section the flow expansion has considerably decreased the static temperature levels and while significant turbulent mixing has taken place, a heterogeneous profile is still observed.

Blade wall temperature distributions across the stator and rotor are finally presented in Fig. 6.16. For clarity, the blade surface is opened around the leading edge (LE) and the previously highlighted features of Figs. 6.13 and 6.14 are also reported here. On the stator suction side, Fig. 6.16(a), the radial migration of the hot-streak can be observed, first towards the casing and then towards the hub (position B). The hub endwall flow effect is also evident on this view. On the rotor blade, Fig. 6.16(b), the preferential migration of the hot-streak to the pressure side is also seen with a large area of high temperature dominating the surface. On the suction side, high temperatures are confined to a narrow area near the LE, while the secondary flow regions (positions F and H) show decreased heat loads. Overall, although not detailed here, qualitative agreement with older URANS predictions [5] is found for the stator vane with some differences in the rotor domain most likely due to the blade modification.

While the aerodynamic flow field is shown to be strongly impacted by the rotor scaling, this LES of the HPT allows to conclude that *a*) the MISCOG method can handle complex industrial configurations and that *b*) generally established trends for the hot-streak migration are recovered (segregation effect, secondary flow effects etc). Based on these findings, a coupled reactive combustor-turbine LES was attempted and is detailed in the following section. The interest of this specific simulation, other than demonstrating its feasibility, is principally in the aerothermal response of such flows, i.e to evaluate the changes issued by the now fully unsteady, turbulent hot-streak arriving at the turbine when compared to the standalone HPT LES that employed a time-averaged hot-streak

at the inflow boundary condition.

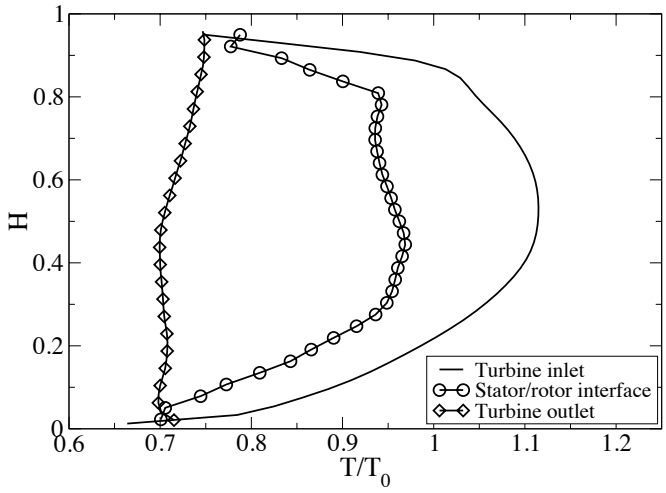

Figure 6.15: Azimuthally averaged temperature profiles at three different axial positions as a function of the height.

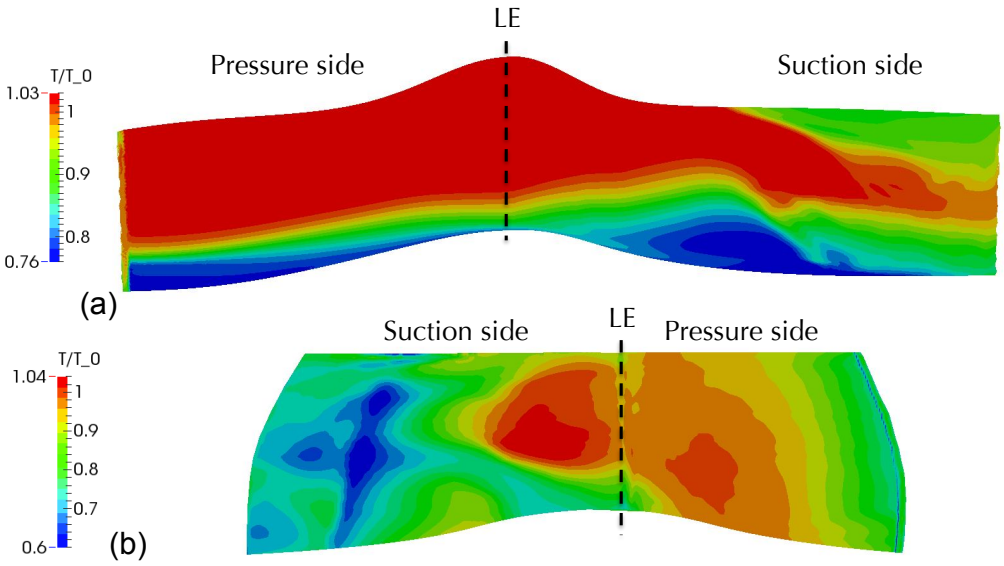

Figure 6.16: Blade wall temperature of the stator (a) and rotor (b) blades - Blade surface is opened around the Leading Edge (LE) for clarity.

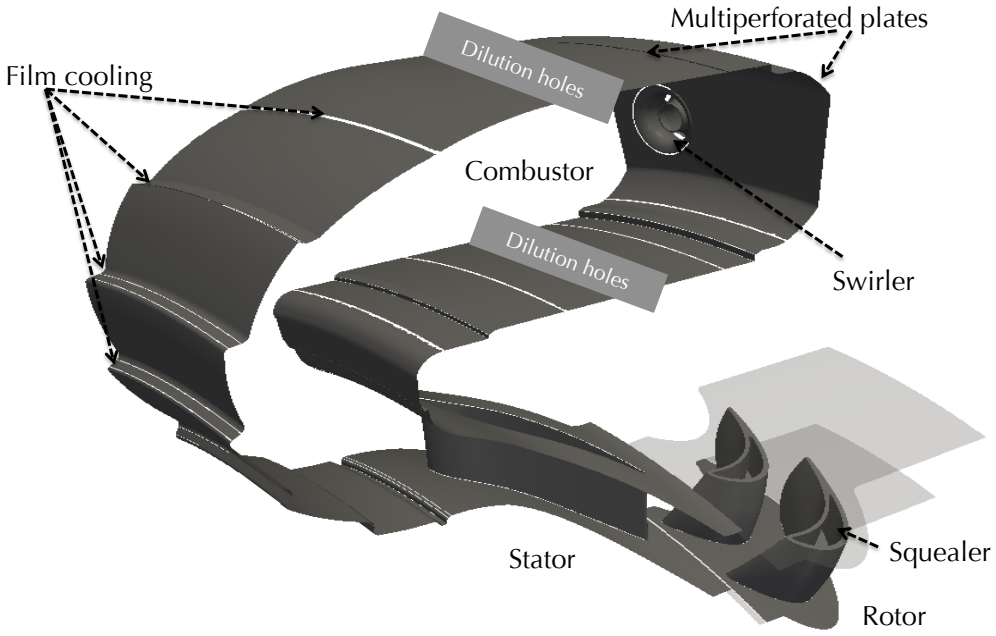

Figure 6.17: View of the combustion chamber-turbine geometry with important technological aspects highlighted.

6.4 Fully coupled combustion chamber-turbine simulation

After using the MISCOG method to evaluate the hot-streak migration on a standalone HPT computation, the full combustion chamber-turbine configuration is now simulated. This computation is the first of its kind with no physical interface between combustor and turbine thus allowing for unparalleled fidelity on the combustor-turbine interactions. Note that we now consider a multi-species simulation with reactions activated because of the combustion chamber. The rotor domain is multi-species as well but no reaction is taking place as the combustion process is assumed to be finished at this point.

6.4.1 Geometry

The geometry used for the turbine is exactly the same as in the previous section. The difference is that the combustion chamber geometry previously ignored is now connected to the computational domain, forming with the NGV a single static domain that will be simulated by one AVBP instance while the rotor is handled by a second AVBP instance. The combustion chamber is a reverse flow chamber. Air coming from the compressor arrives in a large plenum surrounding the main chamber and enters the combustor through the swirler, dilution holes and cooling devices. Although simulations with the combustor plenum have been reported in the literature [215], the less costly and simpler approach of using mass flow injections through the combustor liner and main flow paths is preferred.

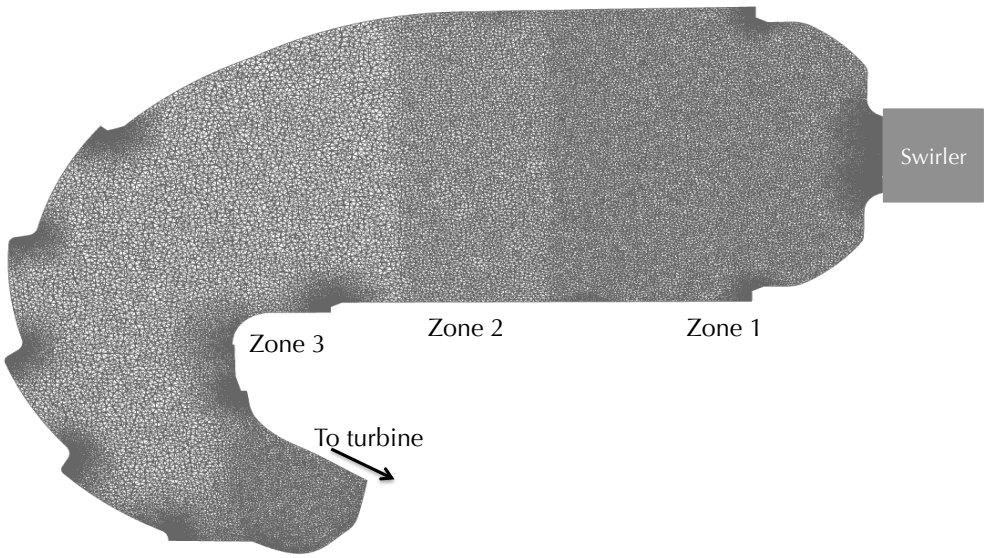

Figure 6.18: View of the combustion chamber mesh with the different refinement zones.

This chamber includes all the typical features found in modern RQL combustors: a swirler to help stabilizing the flame, multi-perforated plates, film cooling and dilution holes. The general geometry and some of the combustor features are depicted on Fig. 6.17.

6.4.2 Mesh

The mesh of the combustion chamber was generated using ANSYS Mesher and is a fully tetrahedral grid. The size of the chamber mesh is approximately 30 million cells, bringing the total cell count of the coupled simulation to 55 million cells. A view of the combustor mesh is provided in Fig. 6.18. The swirler and fuel injector regions are particularly refined before being gradually coarsened through three different user-defined zones. The coarsest zone corresponds to the beginning of the re-orientating elbow located in front of the turbine. As the turbine is approached, mesh refinement takes place again to adapt the grid to the wall-bounded turbine geometry and yield a mesh resolution adequate with the use of a law-of-the-wall as tested in Chapter 4. Note that all film cooling slots are explicitly meshed while the holes of the multi-perforated plates are not. Instead, a homogeneous model [216] is used to take into account the mass flow injected through this effusion cooling system.

6.4.3 Combustion modelling

A major difference introduced in this simulation compared to HPT simulations is the combustion process of kerosene taking place in the chamber. This process is characterized by several chemical reactions that convert the fresh gases (kerosene and air) into combustion products through a flame front interacting with the turbulence generated in

the chamber. Both these aspects need therefore to be taken into account.

The chemical process of hydrocarbon combustion typically involves hundreds of species and thousands of reactions with detailed models involving between 200-250 species and over 1500 reactions [217]. However, the cost of resolving all the species transport equations and computing the reaction rates of such chemical models is prohibitive. To reduce the cost, simplified chemical schemes have been developed where only a certain number of important reactions and species are retained. Such models attempt to fit the principal flame properties of the reduced scheme to the detailed reference chemistry. In this case, a 2-step/6 species model, presented in Eq.(6.4) and described in detail in [218], is employed. It has been shown to provide good accuracy on the burnt gas temperature as well as laminar flame speeds over a large range of equivalence ratios [217].

$$Kerosene + 10O_2 \Rightarrow 10CO + 10H_2O \tag{6.4a}$$

$$CO + 0.5O_2 \leftrightarrow CO_2 \tag{6.4b}$$

For the simulation, the fuel is injected directly in a gaseous form, ignoring the process of atomization and evaporation. This approach was chosen as previous LES of the combustion chamber performed by Turbomeca, using both gaseous and liquid fuel, showed minimal influence on the hot-streaks.

The flame/turbulence interaction is modeled using the Dynamic Thickened Flame (DTF) model [219]. In typical aeronautical combustor LES the mesh resolution is insufficient to accurately resolve the thin flame front and its wrinkling created by its interactions with turbulence. The DTF model is introduced to provide this information, as detailed hereafter.

Following the theory of laminar premixed flames [25] the flame speed S_L^0 and the flame thickness δ_L^0 of a premixed front may be expressed as:

$$S_L^0 \propto \sqrt{\lambda_t A} \quad \text{and} \quad \delta_L^0 \propto \frac{\lambda}{S_L^0} \tag{6.5}$$

where λ_t is the thermal diffusivity and A the pre-exponential constant. Increasing the thermal diffusivity by a factor F, the flame speed is kept unchanged if the pre-exponential factor is decreased by the same factor. This operation leads to a flame thickness which is multiplied by F and more easily resolved on a coarser mesh. While in reacting zones diffusion and source terms issued from the thickened reaction are well resolved, the effect of turbulence is solely represented by the efficiency function E [219, 25]. Note also that the molecular and thermal diffusion should not be over-estimated by a factor F in mixing zones where no combustion occurs (it would yield over-estimated mixing and wrong flame positions). Dynamic thickening is thus introduced to account for these points [219]. The baseline idea of the DTF model is to detect reaction zones using a sensor S and to thicken only these reaction zones, leaving the rest of the flow unmodified. In terms of implementation, thickening depends on the local grid resolution and therefore locally

adapts the combustion process to reach a numerically resolved flame front. Concerning the modeling, the flame sub-grid scale wrinkling and interactions at the SGS level are supplied by the efficiency function [219, 25]. This type of approach is commonly used in similar configurations [202, 215, 220]. More details on the formulation of the DTF model are provided in Appendix B.

6.4.4 Initialization and numerical set-up

For this multi-species case, appropriate initialization of the full configuration is more complex, the reason being that the high-pressure turbine simulation presented in the previous section was single-species. The followed initialization process can be summarized in 4 steps and makes use of a combustor+NGV LES of the same engine performed at Turbomeca:

1. Multi-species conversion of the high-pressure turbine simulation

   An instantaneous solution of the single-species turbine domain is converted to a multi-species field (with the 6 species present in the combustor simulation), with the help of the AVBP toolbox that is well-adapted for such operations. The mass fraction of each species specified in this new solution is considered constant throughout the domains. Inlet boundary conditions (including now the injection of different mass fractions for each species) are obtained from the combustor LES used for the initialization of the standalone HPT simulation. This HPT multi-species simulation is then run until converged.

2. Extraction of the rotor domain.

3. Attachment of the rotor domain to the combustion chamber + NGV LES converged solution using MISCOG.

4. Run until convergence.

As previously, the Lax-Wendroff scheme is used [111]. Converging the fully integrated combustor-turbine simulation required 4 rotations and an additional 3 rotations (5 ms) were performed to obtain averaged solutions for a total computational cost of 600K CPU hours. Note that while the averaging time is increased compared to the simulations of Chapter 4, it is smaller than the usual averaging time employed in combustor simulations (typically larger than 10 ms). It is also important to note that in this coupled simulation there is no possibility of scaling the total temperature at the turbine inlet as no boundary condition is present there. As a result, the mass flow across the turbine is reduced by approximately 8% compared to the previous standalone HPT simulation. Correcting this flow rate would require either additional coolant injection through the film cooling slots or injecting the coolant flow realistically across the turbine at the designed positions and slots. However, as the main objective of this study is principally to demonstrate the capacity of the developed tools to handle such complex industrial configurations,

the turbine coolant flows have not been included in the simulation. It is, nonetheless, envisioned and easily applicable.

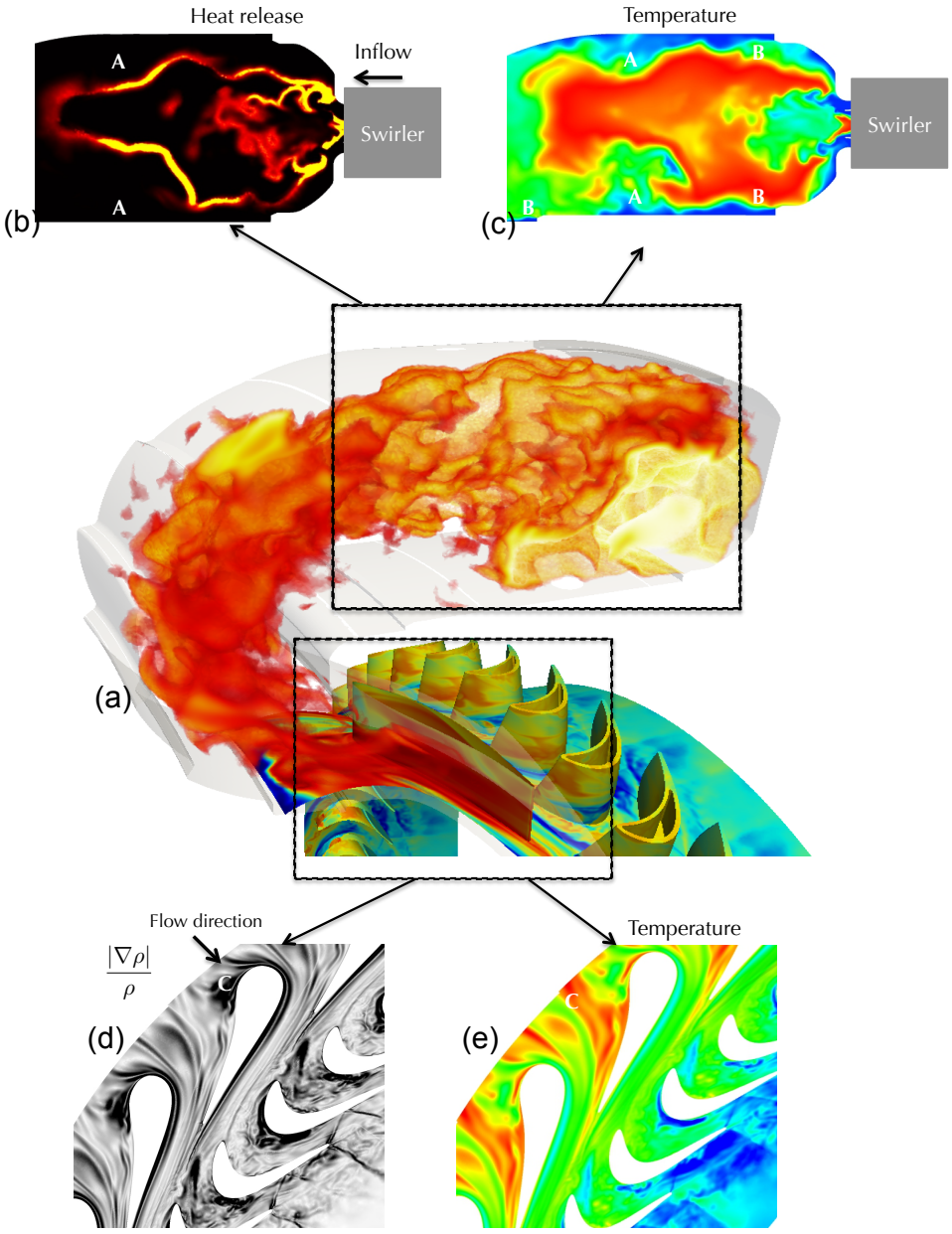

Figure 6.19: Instantaneous flow field of the coupled combustor-turbine simulation. The central image depicts temperature isosurfaces and the blade surface temperature. The top images present the heat release and temperature around the flame front (zoomed) and at the bottom the $\frac{|\nabla\rho|}{\rho}$ and temperature at mid-span across the turbine are depicted.

6.4.5 Results

In the first part of the results the overall flow field of the fully coupled combustor-turbine simulation is presented. It is followed by a more in-depth analysis of the hot-streak generation and migration across the turbine, where comparisons with the standalone HPT LES are also performed. Besides demonstrating the capacities of the developed methodologies in real aeronautical configurations, the emphasis is put on the aerothermal flow, i.e evaluate the changes on the blade temperatures issued by the unsteady inflow heterogeneities.

Overall flow field

Figure 6.19 presents a view of the aerothermal flow field across the combustor and the HPT obtained from an instantaneous solution of the fully integrated LES. The isosurfaces of temperature in the chamber highlight the generation of the hot-streak which will then impact the turbine, Fig. 6.19(a). The top images, Figs. 6.19(b,c), correspond to a zoomed view around the flame front and depict the heat release or temperature flow distribution, while zoomed views in the turbine are provided at the bottom, Figs. 6.19(d,e).

In the combustion chamber a primary high-temperature zone is clearly visible and spans the entire sector width, Fig. 6.19(a). This area is characterized by significant heat release, Fig. 6.19(b), and is usually designed so that most of the combustion process takes place there. This zone is usually delimited downstream by fresh air injected through the dilution holes (Positions A in Figs. 6.19(b,c)). These jets insert fresh air that locally quenches the flame, constraining the combustion to the primary region. It can be noted here that the dilution from the bottom holes appears here to be more effective penetrating deeper in the chamber. Overall, the mass flow, angle and the number of these dilution jets are seen here to contribute significantly in shaping the hot-streaks which for this burner is localized near the upper liner. Film cooling (Positions B in Figs. 6.19(b,c)) prevents the hot gases from touching the liners. The other noticeable feature is that by the time the flow starts turning towards the turbine, the hot-streak becomes more compact. From Fig. 6.19(b), it is also evident that some combustion continues past the primary zone (downstream of positions A). It however remains highly localized confirming an adequate design for this combustor.

When the flow is examined at the turbine entry, Figs. 6.19(d,e), the higher temperature fluid appears aligned with the NGV pressure side (Position C in Figs. 6.19(d,e)), as was the case in the standalone HPT simulation, with strong fluctuations superposed to it.

Time-averaged predictions

Turbine inlet

The principal interest of a coupled combustor-HPT simulation lies in its capacity to naturally introduce all the heterogeneities in the HPT domain. The principal non-uniformity of interest at the turbine inlet is usually the time-averaged temperature profile. Figure 6.20 depicts the mean static temperature at the turbine inlet plane of the standalone

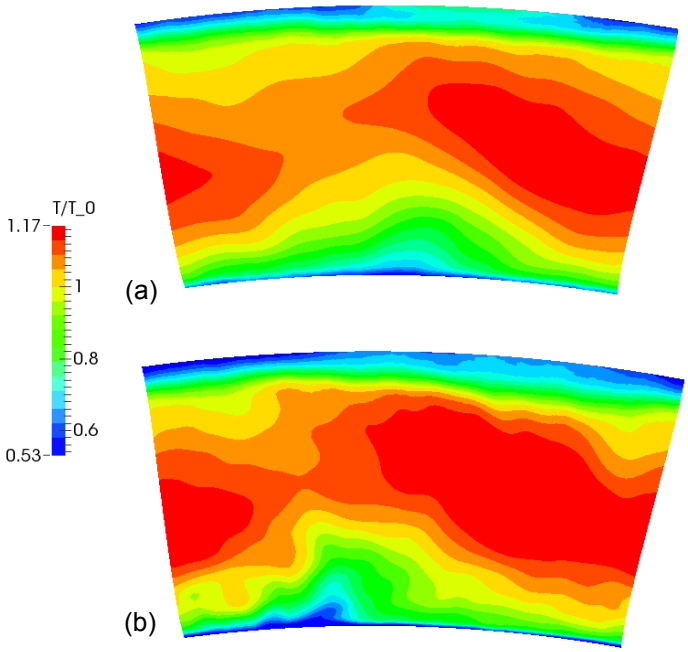

Figure 6.20: Static temperature at the turbine inlet - HPT LES (a) and combustor/HPT LES (b).

HPT simulation compared to the one issued by the coupled combustor-HPT simulation. Both simulations reveal a similar hot spot with some differences observed near the endwalls, particularly near the hub. This is explained mainly by the fact that as the inlet temperature profile of the HPT simulation comes from a combustor-only LES which cannot take into account the interactions of the endwall cooling flows with the turbine blades and secondary flows. Note also that other perturbations observed in Fig. 6.20(b) can also be attributed to the relatively short averaging time of the coupled simulation (5 ms).

To obtain a more quantitative view of the turbine inlet characteristics, Fig. 6.21 presents various azimuthally averaged quantities, computed at the turbine inlet from the combustor/HPT and the HPT simulation (for the mean temperature only as no temporal fluctuations were imposed) and plotted as a function of the height. Figure 6.21(a) presents mean temperature profiles while Fig. 6.21(b) and Fig. 6.21(c) respectively correspond to the temperature rms (divided by the local mean temperature, contrary to other figures that are normalized by the cycle total temperature at the turbine inlet) and the turbulence intensity. The temperature of the coupled simulation has been scaled to agree with the temperature imposed at the inlet of the HPT computation to make the comparisons reliable. Based on Fig. 6.21(a), the mean temperature profiles are qualitatively and quantitatively similar, with a small difference observed on the maximum level of the hot-streak and at around 20% height which is explained by the hub flow differences observed in Fig. 6.20. As for as the unsteady profiles at the turbine inlet, the coupled simulation reveals considerable and inhomogeneous activity. The temperature

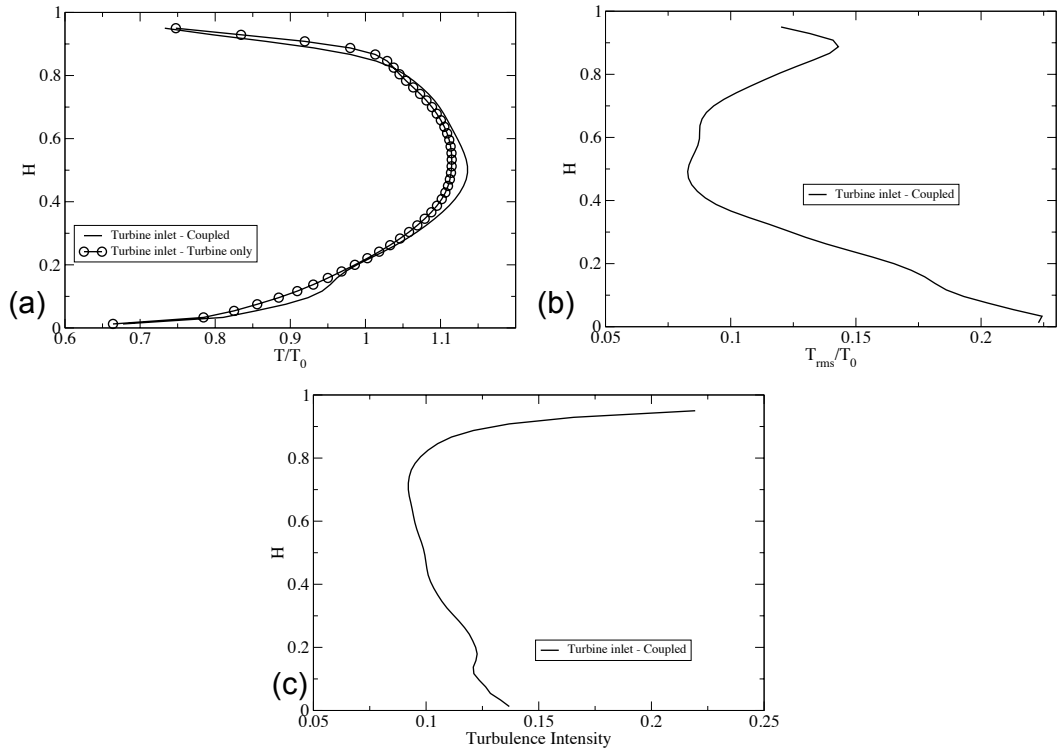

Figure 6.21: Turbine inlet profiles of the coupled combustor/HPT and HPT simulations - Temperature (a), temperature fluctuations (b) and turbulence intensity (c).

fluctuations, Fig. 6.21(b), are over 20% near the endwalls. These levels are explained by the strong mixing of the hot-streak with the cooling flows injected just upstream of the NGV. At mid-height, where less perturbations from technological effects are present, fluctuations are around 10% of the average temperature of the main stream.

The turbulence intensity distribution depicts similar trends as the temperature fluctuations. Higher levels of turbulence occur near the endwalls, where turbulent flow mixing between free-stream and cooling flows occurs while lower unsteadiness is encountered at mid-height. The latter one results principally from the convection of combustor-generated turbulence to the turbine inlet. It is worth noting though that the intensity does not drop under 10% at any radial position, in agreement with the significant turbulence levels observed previously in the literature [160]. These findings confirm that the coupled simulation is indeed capable of transporting all combustor-generated heterogeneities to the turbine. Furthermore, these extracted profiles can provide information that can prove valuable to improve the boundary conditions imposed in standalone turbine simulations.

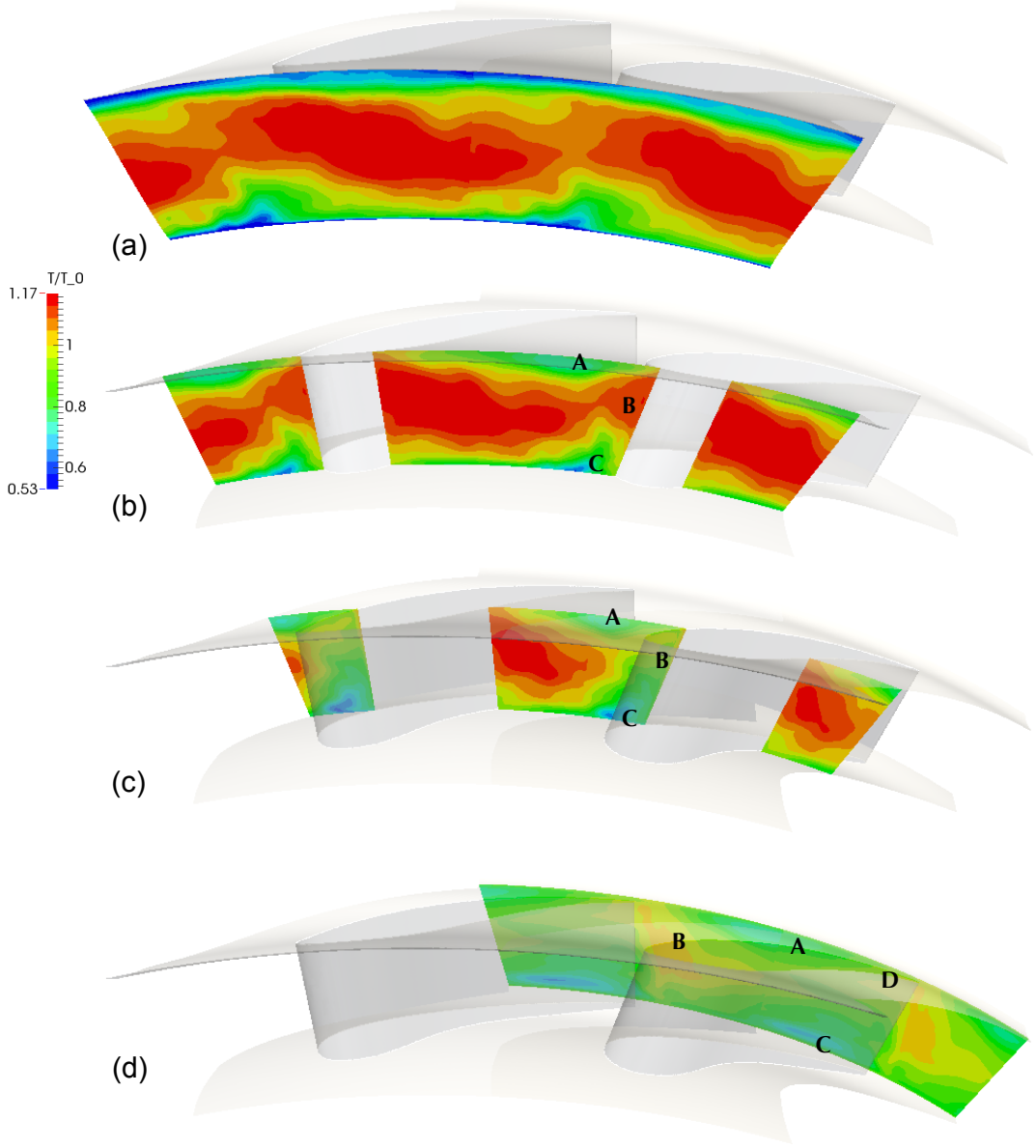

Figure 6.22: Temperature across the NGV passage for the coupled simulation - Turbine inlet (a), 10% of the chord (b), 60% (c) and at the NGV exit (d)

Hot-streak migration

Having evaluated the turbine inlet flow, the hot-streak migration across the turbine for the coupled simulation is analyzed in more details and is compared to Figs. 6.13-6.14, obtained from the standalone HPT LES. Figure 6.22 depicts the temperature distribution across the NGV blade row at different axial positions. The overall trends observed in the standalone HPT simulation are recovered. As observed before, at the turbine inlet the hot-streak is still oriented between the blades and at approximately 60% radius. At 10%

of the chord length similar trends are observed as with the HPT simulation, notably the radial migration towards the casing at the suction side (position B). However, positions A and C are now hotter, probably because of the improved mixing from the high turbulence levels, a trend that continues further down the passage, Figs. 6.13(c,d). Additionally, position C appears slightly further away from the blade, highlighting a slightly modified horseshoe vortex evolution. Further downstream, the hot-streak is migrating towards the hub, only less aggressively than in the standalone HPT simulation. At the stator exit, the hot spot is found to be more homogeneous and mixed out and present at a higher radius, if compared to the elongated one of Fig. 6.13. The endwall temperatures are also noticeably higher.

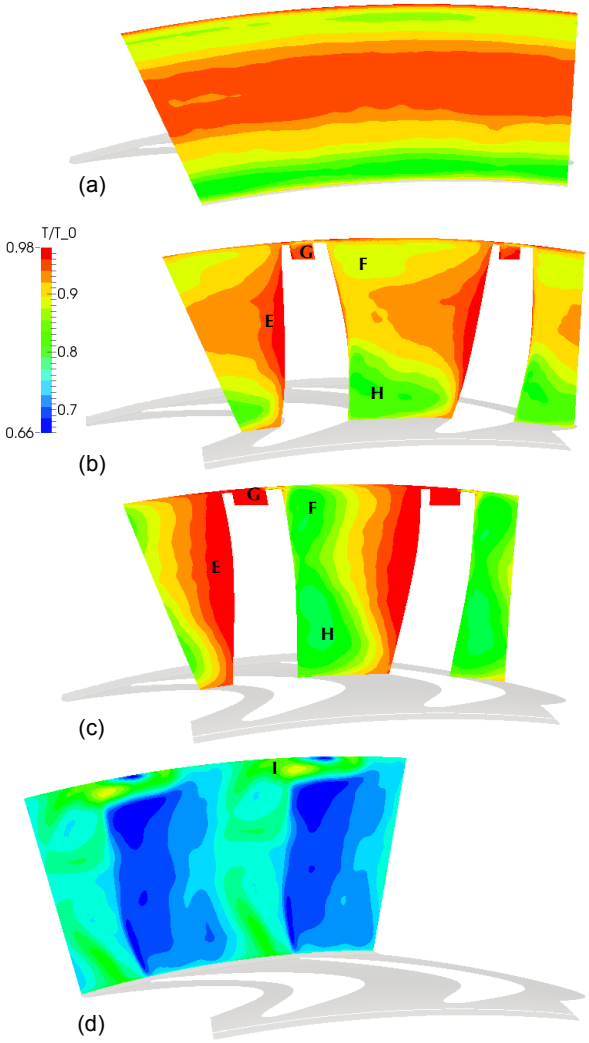

Figure 6.23: Temperature across the rotor passage for the coupled simulation - Rotor inlet (a), 10% of the chord (b), 50% (c) and at the rotor exit (d).

In the rotor domain, Fig.6.23, the hot-streak enters the domain at a radial position

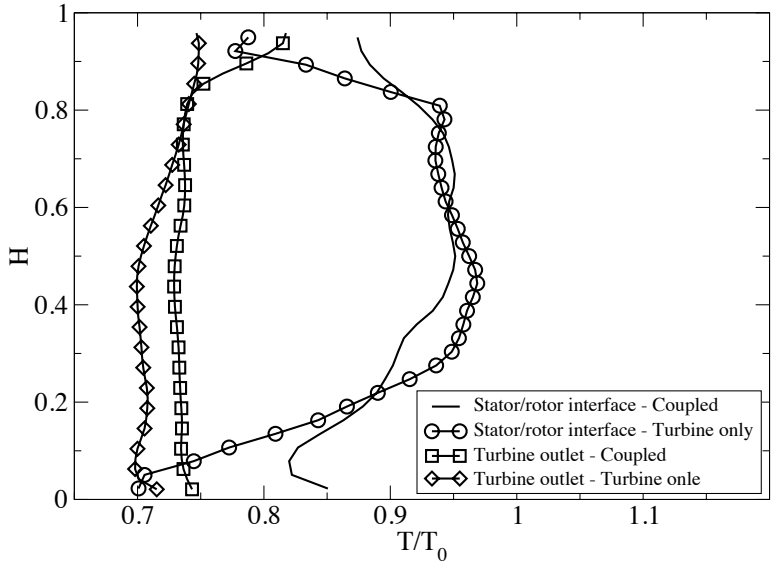

Figure 6.24: Azimuthally averaged temperature profiles at the stator/rotor interface at the the turbine exit as a function of the height.

that is higher than the HPT simulation, approximately 50-60% height. Further down the passage the different phenomena that impact the migration of the hot-streak are still evident. In position E, the pressure side of the blade, the segregation effect is particularly pronounced, the rotor pressure side being impinged by very hot fluid. The radial migration towards the casing appears also enhanced compared to the HPT simulation. The cooler positions F and H present because of the effect of the hub secondary flows, are still encountered but with increased temperature values. The same temperature increase appears in the squealer (position G), with the flow entering this cavity from the pressure side being slightly hotter. At the rotor exit, the cooler tip leakage flows move towards a lower span and hot fluid, previously on the pressure side of the blade and obstructed by the blade and squealer, is now moving towards the casing (position I).

Comparing the azimuthally-averaged temperature at the stator/rotor interface and at the rotor exit can be a more convenient way to quantify the differences observed in the hot-streak migration across the turbine for the two simulations. Such results are presented in Fig. 6.24. At the interface, there is only a fair agreement between the two simulations and for 20-80% of the span. The coupled simulation shows that the endwalls have considerably higher temperatures, the peak at 40% height is now less pronounced and a flatter profile is observed, pointing to a better mixed hot-streak. This trend is recovered at the turbine exit as well, along with an overall increase of the temperature levels by approximately 50 K. As observed in Fig 6.23, the tip leakage flow, that transports hot fluid from the pressure side to the casing, is also more pronounced. These findings highlight that the coupled combustor-turbine simulation does show important differences in the aerothermal predictions, particularly near the endwalls, and that the unsteady

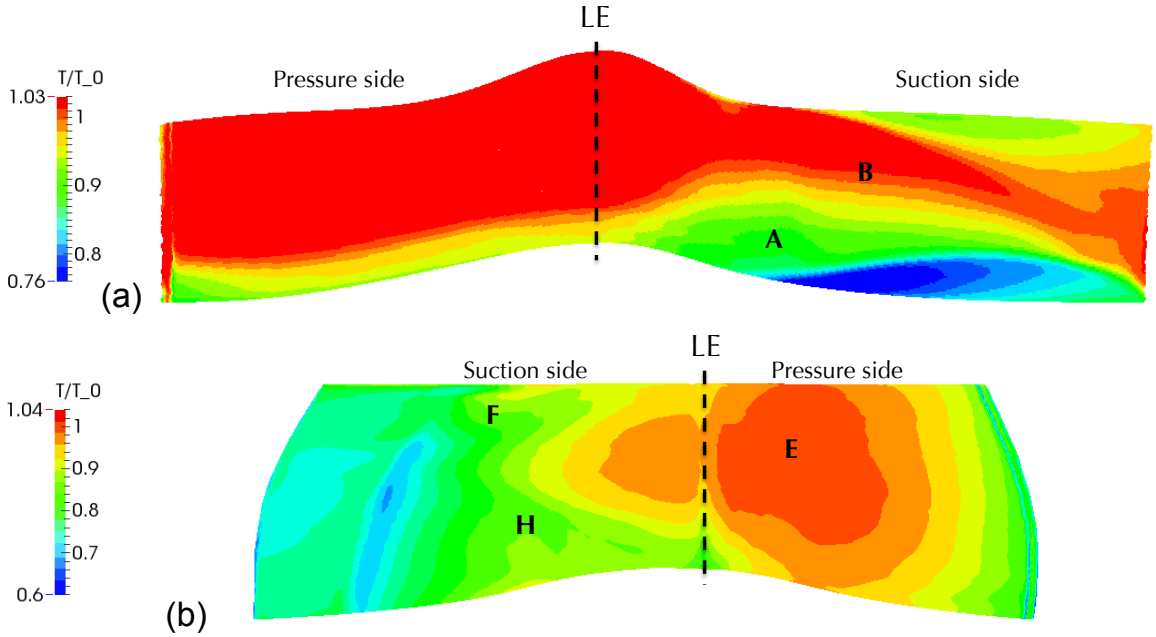

Figure 6.25: Blade wall temperature of the stator (a) and rotor (b) blades for the coupled cases - Blade surface is opened around the Leading Edge (LE) for clarity

inflow alters the migration of the non-uniformities.

The temperature contours across the stator and rotor blades are finally presented in Fig. 6.25. As before, the blade surface is opened around the leading edge (LE) for clarity and the observed features of Figs. 6.22 and 6.23 are depicted. On the stator suction side the radial migration of the hot-streak can be seen, first near the casing and then towards the hub (position B). At the trailing edge a spread of the high-temperature region is observed. The hub endwall flow effect is now slightly altered with the cold fluid staying nearer to the hub and arriving closer to the trailing edge compared to Fig. 6.13. On the rotor blade, the preferential migration of the hot-streak to the pressure side is now more pronounced, with a large area of high temperature dominating the pressure side. It is also shifted towards the casing compared to Fig. 6.16, explaining the higher temperatures observed near the casing in Fig. 6.24. On the suction side, the high temperatures observed near the leading edge at mid span are reduced, while the cooling effect of the secondary flows (positions F and H) is now less pronounced (the endwalls experience higher temperatures so cold air transport is not as efficient).

6.5 Conclusions

In this chapter an industrial application of the MISCOG methodology was presented: a HPT LES and a fully coupled reactive combustion chamber-HPT LES of a real helicopter engine. The objective of these simulations was to study the migration of combustion-

generated heterogeneities in the turbine. The HPT simulation had a time-averaged hot-streak imposed at the inlet and was used to provide a first evaluation of the solver's capacity to handle industrial configurations and predict the migration of time-averaged temperature non-uniformities across a turbine stage. While a necessary modification of the rotor geometry was shown to be significant, changing considerably the aerodynamic flow field of the turbine, the results highlight the potential of the developed methodologies for this type of simulations. The combustor-HPT simulation, allowing the propagation of all heterogeneities generated in the chamber, confirmed that the turbine inflow is very rich in turbulent structures and contains strong temperature fluctuations. Both simulations recover established trends, such as the segregation effect or the impact of secondary flows on the aerothermal flow field of the turbine or the migration of the non-uniformities. However, the coupled combustor-HPT LES indicates that while the time-averaged temperature field at the NGV entry is not changing significantly, the migration across the turbine and the thermal load on the blades can be impacted by the highly unsteady nature of the incoming flow. The relatively limited wall resolution and the geometry modification do not allow for a more detailed evaluation of the turbine losses and performance with accuracy. However, with the necessary tools and guidelines established, such a study can be straightforwardly undertaken in the near future.

General conclusions and perspectives

The constant growth of the aviation sector, along with the increasingly restrictive environmental and noise regulations, are driving considerable research in the field of gas turbines. Improving the numerical predictions of the aerothermal flow field of the high-pressure turbine and the combustion chamber/turbine interactions are at the forefront of this effort. Increasing the fidelity of numerical simulations for these components can help unlock considerable gains:

- In efficiency, as optimized or less over-engineered designs with respect to cooling flows and heat loads can be targeted.
- In development costs, as less time on test benches will be required to confirm the numerical computations and finalize the designs.

Current industrial state-of-the-art predictions treat HPT and combustors in a completely decoupled way. With this approach large errors on the critical blade thermal loads are not uncommon and the acoustic interactions between the two components are lost. This dissertation is proposing a coupled approach to the combustor-HPT interactions problem using the high-fidelity LES formalism.

Part I of the thesis is focusing on the numerical treatment of rotor/stator interfaces in an LES context, an essential part for any turbomachinery stage simulation. An overset grid method is proposed to treat such problems in a rigorous fashion that is compatible with the reactive LES solver AVBP. The properties of the interface are shown not to impact the characteristics of the numerical schemes on a series of academic test cases of varying complexity. The approach is then validated on a realistic HPT stage against experimental measurements. As this type of simulation has not been undertaken before, a sensitivity analysis with respect to SGS models and mesh resolution is performed. The results are in good agreement with the measurements and information on the time-averaged and unsteady content of turbine flows is extracted and analyzed.

Part II focuses on applications of the developed methodologies for the prediction of two different types of combustor/turbine interactions.

- The first is the indirect combustion noise generation across a HPT stage, occurring due to the acceleration of combustor-generated temperature non-uniformities (entropy waves) as they propagate through the turbine. The investigation does not

consider the combustor. Instead entropy waves are injected through the boundary conditions at the turbine inlet to simulate the effect. DMD is employed to post-process the results and analyze both the overall turbine noise mechanisms and the indirect noise generation. The measured acoustic waves are compared to predictions from an analytical theory or 2D simulations and are found to be of similar quality. The entropy waves on the other hand are found to be more attenuated as they pass through the turbine.

- The second application is a fully-coupled combustor-HPT simulation that investigates the interactions between the two components from an aerothermal point of view. The unsteady characteristics of flow at the turbine inlet are analyzed along with the migration of the temperature heterogeneities. A standalone HPT simulation serves as a benchmark to compare the impact of the fully coupled approach. Results show that strong turbulence and temperature fluctuations arrive from the combustion chamber with a large radial variation and they potentially have a considerable impact on the blade surface temperatures as they go through the blade passages, as modified migration patterns are observed and enhanced mixing.

Following this dissertation, several directions of further work and improvements can be identified on the topics discussed in this work:

- Different methods to computationally accelerate the rotor/stator interface can be evaluated, such as tabulating the interpolation coefficients or recalculating the interpolation coefficients less frequently. Methods that reduce the computational domain to one blade passage per blade row while avoiding the modification of the blade counts can also be evaluated, such as the time-inclined method [221] or the phase-lag method [66]. However, such methods have not been tested in an LES context and need to be able to conform with the strict requirements for high-fidelity LES and transport correctly broadband phenomena.

- Perform LES of the MT1 HPT with the addition of inlet turbulent fluctuation. The results, particularly if the high-resolution mesh is used, can allow to establish some conclusions on the impact of free stream turbulence on the predictions in conjunction with wall-modeled LES.

- A wall-resolved LES of the MT1 HPT stage can be performed to improve the validation of the method on this realistic configuration. Such a simulation can also provide more information on the general capacity of LES to predict aerodynamic losses, transition, tip clearance flows and heat transfer, areas where considerable gains are expected from the LES formalism. Additionally, it can serve as a benchmark and provide a solid database for future comparisons, for example with lower cost simulations experimenting with novel wall models. However, the cost for such a simulation is expected to be be upwards of 5M CPUhours due to the explicit time integration of the solver.

- Concerning indirect combustion noise, a simulation with multifrequency forcing can be performed to examine the levels of the generated noise as a function of the frequency. The realistic fully-coupled combustor/turbine simulation can also be continued and analyzed from this perspective to evaluate the combustion noise generated across the turbine from real entropy fluctuations instead of model entropy waves. Studies of non-linear effects should also be performed, as the simulations revealed non-linear interactions that could impact the generated noise.

- Finally, computing the fully coupled case using a more accurate representation of the industrial geometry (the rotor was strongly modified) will allow to establish more reliable conclusions on the aerothermal flow field across the turbine. Such predictions from a real configuration with an accurate turbine inflow will also help to validate observations and conclusions drawn from cheaper RANS/URANS simulations and correlations or other low-order models.

The biggest challenge that is envisioned after this Ph.D is a fully coupled LES investigation of the entire high-pressure spool of a gas turbine: high-pressure compressor, combustion chamber and high-pressure turbine. The proposed tools are not only applicable to single-stage turbine configurations but in multi-stage compressor/turbines as well. Such a simulation can be within reach only if the necessary computational resources become available in the future, which first requires an accurate evaluation of the CPU cost of such simulations. The biggest difficulty in this evaluation is to determine the minimum number of blades/combustor sectors that have to be used in order to obtain a good ratio between accuracy loss due to scaling and computational cost gains. An additional parameter for this evaluation is the engine type, as large gas turbines typically have multi-stage compressors and turbines while smaller helicopter engines have one or more centrifugal compressors.

The information that could be extracted is considerable and of interest for all three components. For example, the off-design predictions in compressors could be addressed by such tools and they can also contribute to the understanding of thermoacoustic instabilities in the combustors as well as the combustion noise transmission and hot-streak migration across the turbine.

Part III

Appendices

Appendix A

Equations of fluid motion

A.1 Navier-Stokes equations

Fluid flow is characterized by a set of partial differential equations, which describe the conservation of mass, momentum (Navier-Stokes equations) and energy in a compressible fluid (using Einstein's summation):

$$\frac{\partial \rho}{\partial t} + \frac{\partial \rho u_i}{\partial x_i} = 0 \tag{A.1}$$

$$\frac{\partial}{\partial t}\rho u_i + \frac{\partial}{\partial x_j}\rho u_i u_j = -\frac{\partial P}{\partial x_j}\delta_{ij} + \frac{\partial T_{ij}^{(v)}}{\partial x_i} \tag{A.2}$$

$$\frac{\partial \rho E}{\partial t} + \frac{\partial}{\partial x_j}(\rho u_j E) = \frac{\partial q_i}{\partial x_i} + \frac{\partial}{\partial x_j}(u_i(P\delta_{ij} + T_{ij}^{(v)})) + \dot{\mathcal{Q}} \tag{A.3}$$

In Eqs. (A.1)-(A.3), E is the total energy of the fluid, $\mathbf{u}$ is the velocity vector, ρ is the fluid density, $\mathbf{T^{(v)}}$ is the viscous stresses tensor, q is the heat flux and $\dot{\mathcal{Q}}$ is a heat source term (if existing). Finally, this set of equations is accompanied by the perfect gas law:

$$P = \rho r T \tag{A.4}$$

where r is the specific gas constant of the fluid and is equal to $r = R/W$, where W is the molar mass of the fluid and R is the molar gas constant equal to 8.314472 J/K/mol. The viscous stress tensor for Newtonian fluids (such as air) can be computed as:

$$T_{ij}^{(v)} = -\frac{2}{3}\mu\frac{\partial u_k}{\partial x_k}\delta_{ij} + \mu\left(\frac{\partial u_i}{\partial x_j} + \frac{\partial u_j}{\partial x_i}\right) \tag{A.5}$$

where μ is the dynamic viscosity of the fluid. It is a function of the temperature, and throughout this work it follows a power law with respect to a reference viscosity and temperature:

$$\mu(T) = \mu_{ref}\left(\frac{T}{T_{ref}}\right)^{-0.695} \tag{A.6}$$

Finally, the formula for the heat flux q reads:

$$q_i = -\lambda \frac{\partial T}{\partial x_i} \tag{A.7}$$

In Eq. (A.7), λ is the heat conduction coefficient, calculated using the Prandtl number Pr (assumed constant) using $\lambda = \frac{\mu C_p}{Pr}$.

These equations describe the flow in the absolute frame of reference. If the equations are to be resolved in the relative frame of reference for rotating blades, as if an observer was sitting on the blade surface, the velocity is switches to the relative velocity for which 2 additional forces impact its evolution. These are *a*) the centrifugal force $f_v = \omega^2 R$, where ω is the angular velocity, R the radius, and *b*) the Coriolis force $f_{cor} = -2\omega \times W$, where W is the relative velocity. The relative and absolute velocities are linked through the formula $\mathbf{V} = \mathbf{W} + \mathbf{U}$, as shown in section 1.3, with $\mathbf{U}$ being the rotational velocity of the blade.

Reacting flows are governed by the same equations complemented by the fact that the combustion of hydrocarbons leads to a large number of different species constantly created and consumed by chemical reactions. As a result, species conservation equations are introduced and the energy equation is modified to account for the reaction characteristics and forces exerted on the species [25]. For $k = 1, ..., N$ components the species conservation equation reads:

$$\frac{\partial \rho Y_k}{\partial t} + \frac{\partial}{\partial x_j}(\rho u_j Y_k) = -\frac{\partial}{\partial x_j} J_{j,k} + \dot{\omega}_k \tag{A.8}$$

and the energy equation reads:

$$\frac{\partial \rho E}{\partial t} + \frac{\partial}{\partial x_j}(\rho u_j E) = \frac{\partial q_i}{\partial x_i} + \frac{\partial}{\partial x_j}(u_i(P\delta_{ij} + T_{ij}^{(v)})) + \dot{\mathcal{Q}} \tag{A.9}$$

In Eq. (A.8), V_k is the diffusion velocity of species k, Y_k is the mass fraction, $J_{i,k}$ is the diffusion flux for species k and $\dot{\omega}_k$ is the reaction rate for species k.

The heat flux is modified to take into account the flux due to the diffusion of the species:

$$q_i = -\lambda \frac{\partial T}{\partial x_i} - \rho \sum_{k=1}^{N} J_{i,k} h_{s,k}, \tag{A.10}$$

where $h_{s,k}$ is the sensible enthalpy of species k. In Eqs. (A.10) and (A.8), $J_{i,k}$ is formulated as:

$$J_{i,k} = -\rho \left(D_k \frac{W_k}{W} \frac{\partial X_k}{\partial x_i} - Y_k V_i^c \right) \tag{A.11}$$

where X_k is the molar fraction of species k, D_k is the diffusion coefficient of the species k and V_i^c is a correction velocity to ensure mass conservation [25].

The diffusion coefficient of species k is calculated as:

$$D_k = \frac{\mu}{\rho S_{c,k}}, \tag{A.12}$$

where $S_{c,k}$ is the Schmidt number of species k. Finally, the correction velocity V_i^c is computed as:

$$V_i^c = \sum_{k=1}^{N} D_k \frac{W_k}{W} \frac{\partial X_k}{\partial x_i}. \tag{A.13}$$

It is important to note that the gas constant r of the fluid is now dependent on the molar mass of the mixture W, computed as:

$$\frac{1}{W} = \sum_{k=1}^{N} \frac{Y_k}{W_k} \tag{A.14}$$

A.2 Filtered Navier-Stokes equations

LES was first introduced in 1963 by Smagorinsky [171], in an attempt to directly simulate the large eddies existing in turbulent flows while modeling those in the sub-grid scales. For compressible flows, a spatial mass-weighted Favre filtering is performed [25]:

$$\overline{\rho}\tilde{f}(x,t) = \int_{-\infty}^{\infty} \rho f(x') G(x - x') dx' \tag{A.15}$$

where f can be any variable and G is the filter function. The overbar denotes a filtered variable while the tilde denotes the Favre filter operation $\tilde{f} = \frac{\overline{\rho f}}{\overline{\rho}}$. Thus, a RANS-like decomposition $f = \overline{f} + f'$ still exists, however $\overline{f}$ is the filtered variable and not its statistical or temporal average. It is noted that the filter function satisfies the normalization condition:

$$\int_{-\infty}^{\infty} G(x) dx = 1 \tag{A.16}$$

Performing the filtering allows to resolve the large scales of turbulence, while cutting off the smaller ones. The filter width Δ allows also to determine the extent of the resolved scales compared to the unresolved ones. Applying the filtering to the equations of motion (assuming that the filter is homogeneous and the filtering operation commutes with the gradient) yields for the mass conservation:

$$\frac{\partial \overline{\rho}}{\partial t} + \frac{\partial \overline{\rho} \tilde{U_j}}{\partial x_j} = 0. \tag{A.17}$$

Similarly, the filtered momentum and energy equations become:

$$\left[\frac{\partial \overline{\rho}\tilde{U}_i}{\partial t} + \frac{\partial \overline{\rho}\tilde{U}_i\tilde{U}_j}{\partial x_j}\right] = -\frac{\partial}{\partial x_j}[\overline{P}\delta_{ij} - \overline{T}_{ij}^{(v)} - \tau_{ij}^r], \tag{A.18}$$

$$\frac{\partial \overline{\rho}\tilde{E}}{\partial t} + \frac{\partial}{\partial x_j}(\overline{\rho}\tilde{E}\tilde{U}_j) = -\frac{\partial}{\partial x_j}[\overline{u_j(P\delta_{ij} - \tau_{ij})} + \overline{q}_j + q_j^r] + \overline{Q}. \tag{A.19}$$

The species equation becomes:

$$\frac{\partial \overline{\rho}\tilde{Y}_k}{\partial t} + \frac{\partial}{\partial x_j}\left(\overline{\rho}\tilde{u}_j\tilde{Y}_k\right) = \frac{\partial}{\partial x_j}\left[\overline{J}_{j,k} + J_{j,k}^r\right] + \overline{\dot{\omega}_k}. \tag{A.20}$$

Equations (A.18) - (A.20) give rise to similar closure problems as in RANS, notably for the residual stress τ_{ij}^r, the residual heat flux q_j^r and the sub-grid scale diffusive species flux vector $J_{j,k}^r$. They are respectively defined by:

$$\tau_{ij}^r = \widetilde{U_iU_j} - \tilde{U}_i\,\tilde{U}_j, \tag{A.21a}$$

$$q_i^r = \overline{\rho}\left(\widetilde{U_iE} - \tilde{U}_i\,\tilde{E}\right), \tag{A.21b}$$

$$J_{i,k}^r = \overline{\rho}(\widetilde{u_iY_k} - \tilde{u}_i\tilde{Y}_k). \tag{A.21c}$$

These terms represent the unresolved turbulent length scales that the mesh is incapable to capture. This concept is illustrated in Fig. A.1, where a set of eddies is superposed to a numerical grid. The larger red eddies are the ones that can be resolved with a few cell points available per eddy diameter, while the blue ones are too small to be captured by the mesh and will be removed by the filtering operation. For a good quality LES, the mesh construction should be such to enable the resolution of the large eddies well into the inertial sublayer of the turbulent spectrum, while cutting off the small scales that contain only a small part of the turbulent kinetic energy [54].

A.2.1 LES modeling

While the sub-grid scales hold a small portion of the kinetic energy (Chapman [54] suggests that LES should be able to resolve around 90% of the total turbulent kinetic energy), they are responsible for the dissipation of energy in the turbulent cascade. As a result, ignoring them would result very quickly in energy accumulating in the system. To rectify this, modeling is required by means of a so called Sub-Grid Scale (SGS) model, in an attempt to mimic the real behavior of the finest turbulent scales onto the resolved field. To achieve this objective, as with several RANS turbulence models, the Boussinesq approximation is commonly employed. For the SGS stress, the Boussinesq approximation links it to the filtered rate-of-strain. It reads for compressible flows [25]:

$$\tau_{ij}^r - \frac{\delta_{ij}}{3}\tau_{kk} = -2\nu_t\left(\tilde{S}_{ij} - \frac{\delta_{ij}}{3}\tilde{S}_{kk}\right) \tag{A.22}$$

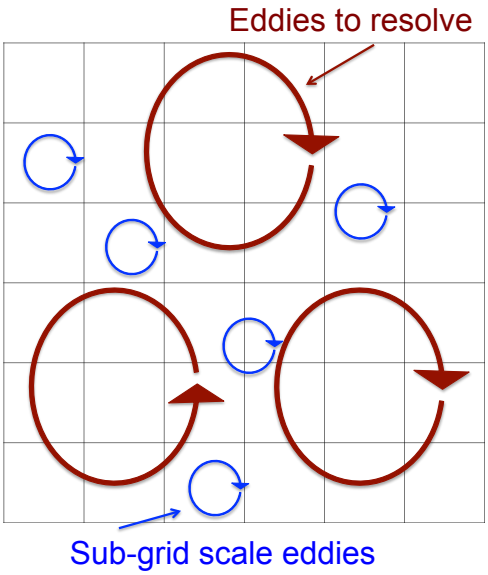

Figure A.1: The LES concept: large turbulent scales can be resolved by the mesh while the smaller ones have to be modeled

In Eq. (A.22) $\overline{S}_{ij} = \frac{1}{2}\left(\frac{\partial \overline{U}_j}{\partial x_j} + \frac{\partial \overline{U}_j}{\partial x_i}\right)$ is the filtered rate-of-strain tensor and ν_t is the turbulent viscosity that is to be closed. Several SGS models exist in the literature.

Below, a short description of three commonly used SGS models employed in this thesis is provided.

- Smagorinsky SGS model [171]

  It is the most elementary model developed for LES. It has the advantages of being easy to implement and robust. It is often used in conjunction with wall modeling to avoid numerical instabilities. The formula for the eddy viscosity reads:

$$\nu_\tau = l_S^2 \overline{\mathcal{S}} = (C_s \Delta)^2 \sqrt{2\overline{S}_{ij}\overline{S}_{ij}} \tag{A.23}$$

  In Eq. (A.23) l_S is the Smagorinsky length scale and C_s is the Smagorinsky coefficient, usually taken to be around 0.18.

- Wall Adapting Local Eddy-viscosity model (WALE) [57]

  Developed by Nicoud et al [57], the WALE model aims at capturing the change of scales close to walls without using a dynamic approach, such as the one proposed by Germano [222], therefore reducing the computational cost. Contrary to the simple Smagorinsky model, WALE model disappears in cases where there is pure shear.

$$\nu_\tau = (C_w \Delta)^2 \frac{(s_{ij}^d s_{ij}^d)^{3/2}}{(\tilde{S}_{ij}\tilde{S}_{ij})^{5/2} + (s_{ij}^d s_{ij}^d)^{5/4}} \tag{A.24}$$

with s_{ij}^d being:

$$s_{ij}^d = \frac{1}{2}(\tilde{g}_{ij}^2 + \tilde{g}_{ji}^2) - \frac{1}{3}\tilde{g}_{kk}^2\delta_{ij} \text{ with } \tilde{g}_{ij} = \frac{\partial \tilde{u}_i}{\partial x_j}, \tag{A.25}$$

- σ model [168]

  The σ model, developed by Nicoud et al [168], attempts to satisfy all the above mentioned properties P1-P3. Instead of being based on the strain rate tensor, its operator is formulated based on the singular values $(\sigma_1, \sigma_2, \sigma_3)$ of the velocity gradient tensor:

$$\nu_\tau = (C_\sigma \Delta)^2 \mathcal{D}_\sigma \text{ with } \mathcal{D}_\sigma = \frac{\sigma_3(\sigma_1 - \sigma_2)(\sigma_2 - \sigma_3)}{\sigma_1^2}, \tag{A.26}$$

  where $C_\sigma = 1.5$. It is the most recently developed of all the models employed, hence its capacity in handling more complex configurations has not been tested.

As with RANS models, SGS models are not perfect and might not follow certain universal flow properties and erroneously introduce additional turbulent viscosity. Besides modeling the sub-grid scales, all SGS models should be able to follow three universal properties. A primary property is that turbulence stresses are damped near the walls (they scale with y^3, where y is the distance from the wall [167]), thus turbulent viscosity should follow the same behavior (named property P1). Additionally, two other desired properties are that turbulent viscosity should be zero in case of pure shear and pure rotation (property P2) as well as when there is isotropic or axisymmetric contraction/expansion (property P3) [168].

Table A.1 summarizes which of the desired properties are satisfied by the formulation of the three SGS models.

	Smagorinsky	**WALE**	$\boldsymbol{\sigma}$
P1	NO	YES	YES
P2	NO	NO	YES
P3	NO	NO	YES

Table A.1: Summary of the three sub-grid scale models, their constants and whether they satisfy the desired properties

The SGS contribution to the heat flux is modeled simply as:

$$q_i^r = \lambda^t \frac{\partial \tilde{T}}{\partial x_i} + \sum_{k=1}^{N} J_{i,k}^r \overline{h}_{s,k} \tag{A.27}$$

In Eq. (A.27) λ^t is a modified heat conduction coefficient, calculated based on a constant turbulent Prandtl number, here assumed constant and equal to $Pr_t = 0.6$, and the turbulent viscosity as:

$$\lambda^t = \frac{\nu_t C_p}{Pr_t} \tag{A.28}$$

Similarly, the SGS diffusive species flux vector is computed as:

$$J^r_{i,k} = -\overline{\rho}\left(D^t_k \frac{W_k}{W}\frac{\partial \tilde{X}_k}{\partial x_i} - \tilde{Y}_k \tilde{V}^{c,t}_i\right) \tag{A.29}$$

where $D^t_k = \frac{\nu_t}{S^t_{c,k}}$, with $S^t_{c,k}$ being the turbulent Schmidt number, here equal to 0.6 for all species.

Appendix B

Combustion modeling

A difficult problem is encountered in Large Eddy Simulations of premixed flames: the thickness δ_L^0 of a premixed flame is generally smaller than the standard mesh size Δ_x used for LES. For this reason, the Dynamic Thickened Flame (TF) model has been developed to facilitate the resolution of flame fronts on a LES mesh. To achieve that, the flame is thickened by multiplying the diffusive fluxes by a thickening factor $\mathcal{F}$. This flame thickening factor is dynamically determined to have a maximum value in the flame zone and decrease to unity in non-reactive zones as:

$$\mathcal{F} = 1 + (\mathcal{F}_{max} - 1)\mathcal{S} \tag{B.1}$$

where $\mathcal{S}$ is a sensor to determine the flame position depending on the local temperature and mass fractions and $\mathcal{F}_{max} = \frac{N_c}{\Delta_x}\delta_L^0$ with N_c being the number of cells used to resolve the flame front. The necessity for a sensor becomes evident if one considers that in non reactive zones, where only mixing takes place, the molecular and thermal diffusions will be overestimated by a factor $\mathcal{F}$ if a non-dynamic approach is employed. In these zones, the thickening factor should be corrected to go to unity.

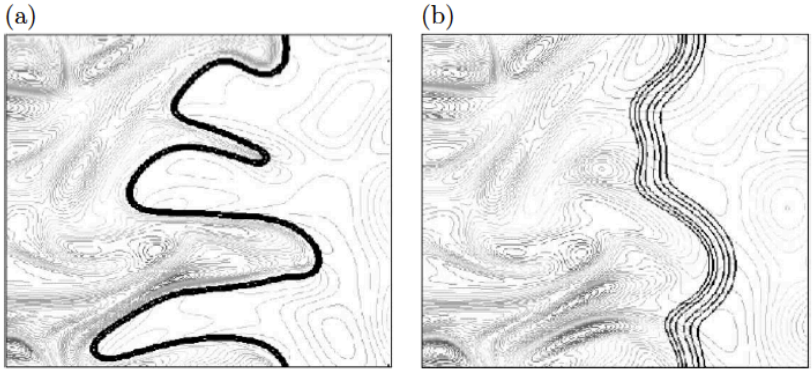

Figure B.1: Direct Numerical Simulation of flame/turbulence interactions by Angelberger *et al.* [24] and Poinsot and Veynante [25]. (a) non-thickened flame and, (b) thickened flame ($\mathcal{F} = 5$)

In turbulent flows, simply thickening the flame front is not enough as the interaction between turbulence and chemistry is altered: eddies smaller than δ_L^0 do not interact with the flame any longer. As a result, the thickening of the flame reduces the ability of the vortices to wrinkle the flame front. As the flame surface is decreased, the reaction rate is underestimated (Fig. B.1). In order to correct this effect, an efficiency function $\mathcal{E}$ has been developed from DNS results and implemented into AVBP. The formula for the efficiency function is defined as the wrinkling ratio between the non-thickened reference flame and the thickened flame and it reads:

$$\mathcal{E} = \frac{\Xi(\delta_L^0)}{\Xi(\delta_L^1)} = \frac{1 + \alpha\Gamma\left(\frac{\Delta_e}{\delta_L^0}, \frac{u'_{\Delta_e}}{S_L^0}\right)\frac{u'_{\Delta_e}}{S_L^0}}{1 + \alpha\Gamma\left(\frac{\Delta_e}{\delta_L^1}, \frac{u'_{\Delta_e}}{S_L^0}\right)\frac{u'_{\Delta_e}}{S_L^0}} \tag{B.2}$$

In Eq. (B.2), Γ corresponds to the integration of the effective strain rate induced by the turbulent scales between the Kolmogorov dissipative scales η_K and the filter width Δ_e, i.e the scales affected by the flame thickening. It is formulated as:

$$\Gamma\left(\frac{\Delta_e}{\delta_L^0}, \frac{u'_{\Delta_e}}{S_L^0}\right) = 0.75 exp\left[-\frac{1.2}{(u'_{\Delta_e}/S_L^0)^{0.3}}\right]\left(\frac{\Delta_e}{\delta_L^1}\right)^{2/3} \tag{B.3}$$

where S_L^0 and δ_L^0 are the laminar flame speed and thickness when no thickening takes place and $\delta_L^1 = \mathcal{F}\delta_L^0$. The variable α is a constant of the model and u'_{Δ_e} is the SGS turbulent velocity that is computed using a Laplacian operator described in [219]:

$$u'_{\Delta_e} = c_2\Delta_x^3|\frac{\partial^2}{\partial x_j \partial x_j}\left(e_{lmn}\frac{\partial \overline{u_n}}{\partial x_m}\right) \tag{B.4}$$

The energy and species conservations equations with the combustion modeling become:

$$\begin{aligned}\frac{\partial \overline{\rho}\tilde{E}}{\partial t} + \frac{\partial}{\partial x_j}(\overline{\rho}\tilde{E}\tilde{U}_j) =& -\frac{\partial}{\partial x_j}\left[\overline{u}_j P\delta_{ij} - 2\mu\tilde{u}_i(\tilde{S}_{ij} - \frac{1}{3}\tilde{S}_{kk}\delta_{ij})\right] \\ &+ \frac{\partial}{\partial x_j}\left[C_p\mathcal{E}\mathcal{F}\frac{\mu}{Pr}\frac{\partial \tilde{T}}{\partial x_j}\right] \\ &+ \frac{\partial}{\partial x_j}\left[\sum_{k=1}^{N}\left(\mathcal{E}\mathcal{F}\frac{\mu}{Sc_k}\frac{W_k}{W}\frac{\partial \tilde{X}_k}{\partial x_i} - \overline{\rho}\tilde{Y}_k(\tilde{V}_j^c + \tilde{V}_j^{c,t})\right)\tilde{h}_{s,k}\right] \\ &+ \frac{\mathcal{E}\overline{Q}}{\mathcal{F}}\end{aligned} \tag{B.5a}$$

$$\begin{aligned}\frac{\partial \overline{\rho}\tilde{Y}_k}{\partial t} + \frac{\partial}{\partial x_j}\left(\overline{\rho}\tilde{u}_j\tilde{Y}_k\right) =& \frac{\partial}{\partial x_j}\left[\mathcal{E}\mathcal{F}\frac{\mu}{Sc_k}\frac{W_k}{W}\frac{\partial \tilde{X}_k}{\partial x_i} - \overline{\rho}\tilde{Y}_k(\tilde{V}_j^c + \tilde{V}_j^{c,t})\right] \\ &+ \frac{\mathcal{E}\dot{\omega}_k}{\mathcal{F}}\end{aligned} \tag{B.5b}$$

Appendix C

Theory of Dynamic Mode Decomposition

The output of a typical numerical solver is a series of M instantaneous solutions (snapshots), saved every user-specified timestep Δt (significantly larger than the timestep of the simulation). In DMD, each snapshot is treated as a vector of length N (usually the number of grid points times the flow variables to be analyzed). Memory constraints normally dictate that $N >> M$. The data from the solutions can hence be represented by the following set of vectors:

$$\mathbf{V}_1^N = \{\mathbf{v}_1, \mathbf{v}_2, \mathbf{v}_3, ..., \mathbf{v}_N\} \tag{C.1}$$

In Eq. (C.1). $\mathbf{V}_1^N$ has a size of $N \times M$ and can be split into two sets, each of size $N \times (M-1)$:

$$\mathbf{V}_1^{N-1} = \{\mathbf{v}_1, \mathbf{v}_2, \mathbf{v}_3, ..., \mathbf{v}_{N-1}\} \tag{C.2a}$$

$$\mathbf{V}_2^N = \{\mathbf{v}_2, \mathbf{v}_3, \mathbf{v}_4, ..., \mathbf{v}_N\} \tag{C.2b}$$

An unknown matrix A is introduced that transforms any snapshot $\mathbf{v}_i$ in the data sequence over one time step Δt:

$$A\mathbf{v}_i = \mathbf{v}_{i+1} \tag{C.3}$$

where A is a linear operator that can be considered an approximation to the Navier-Stokes equations. Applying the propagation matrix to the entire dataset $\mathbf{V}_1^{N-1}$ gives:

$$A\mathbf{V}_1^{N-1} = \mathbf{V}_2^N \tag{C.4}$$

The characteristics of the operator A can be studied through its eigenvectors Φ_n and eigenvalues λ_n, which provide mode structures and frequencies respectively. However, the matrix A is either unknown or too large and a lower dimension approximation is usually looked for.

To do so, ff the number of snapshots M is large enough, the solution vectors become linearly dependent leading to:

$$v_N = \sum_{i<M} \alpha_i v_i + e_N \tag{C.5}$$

where e_N is the residual that tends to 0 as the number of snapshots M is increasing.

Using Eq. (C.5) and introducing a companion matrix S of size $(M-1)\times(M-1)$ and of the form:

$$S = \begin{pmatrix} 0 & 0 & \cdots & 0 & \alpha_1 \\ 1 & 0 & \cdots & 0 & \alpha_2 \\ 0 & 1 & \cdots & 0 & \alpha_3 \\ \vdots & \vdots & \ddots & \vdots & \\ 1 & 0 & \cdots & 1 & \alpha_{M-1} \end{pmatrix} \tag{C.6}$$

we can write:

$$A\mathbf{V}_1^{N-1} = \mathbf{V}_2^N = \mathbf{V}_1^{N-1} S \tag{C.7}$$

Equation (C.7) indicates that the modes of A, of size $(N-1)\times(N-1)$, can be looked for in the reduced matrix S. There are several formulations for the S matrix in the literature, for example by expanding $\mathbf{V}_1^{N-1}$ via a Singular Value Decomposition (SVD) [188] or a QR-decomposition [223]. In this work, the variant proposed by [224] is used. In this approach, the operator S is reformulated using Eq. (C.7):

$$S = (\mathbf{V}_1^{N-1})^{-1}\mathbf{V}_2^N \tag{C.8}$$

First, introducing the SVD, one can write:

$$\mathbf{V}_1^{N-1} = U\Sigma W^H \tag{C.9}$$

where U and W are unitary matrices and Σ is diagonal. The superscript ^{H} indicates the conjugate transpose of the matrix.

Then, the inverse of $\mathbf{V}_1^{N-1}$ is computed using a Moore-Penrose pseudo inversion [225] as:

$$(\mathbf{V}_1^{N-1})^{-1} = W\Sigma^{-1}U^H \tag{C.10}$$

From Eq. (C.9), U can be straightforwardly computed: $U = \mathbf{V}_1^{N-1}W\Sigma^{-1}$. Introducing it in Eq. (C.10) and replacing the whole expression in Eq. (C.8) the companion matrix can be computes as:

$$S = W\Sigma^{-1}\Sigma^{-1}W^H(\mathbf{V}_1^{N-1})^H\mathbf{V}_2^N \tag{C.11}$$

Considering the diagonalization:

$$(\mathbf{V}_1^{N-1})^H \mathbf{V}_1^{N-1} = W\Sigma^2 W^H \tag{C.12}$$

the matrices W and Σ can be also computed from an eigenvalue decomposition of $(\mathbf{V}_1^{N-1})^H \mathbf{V}_1^{N-1}$.

The last step is to solve the eigenvalue problem $Ss_n = \mu_n s_n$ where s_n and μ_n are the eigenvectors and eigenvalues of S. Note that the eigenvectors Φ_n of the matrix A, which correspond to the DMD modes, are simply the projection of s_n onto the snapshot basis:

$$\Phi_n \quad = \mathbf{V}_1^{N-1} s_n \tag{C.13}$$

The associated complex angular frequency of the modes follows:

$$\omega_n = \frac{ln(s_n)}{\Delta t} \tag{C.14}$$

Finally, the global amplitude of each dynamic mode is defined simply as its $\mathcal{L}_2$ norm, $||\Phi_n||_{\mathcal{L}_2} = \sqrt{\Phi_n \cdot \Phi_n}$, allowing to discriminate energetically significant modes.

Appendix D

MISCOG method - Journal of Computational Physics

Journal of Computational Physics 274 (2014) 333–355

Contents lists available at ScienceDirect

Journal of Computational Physics

www.elsevier.com/locate/jcp

An overset grid method for large eddy simulation of turbomachinery stages

Gaofeng Wang [a,b,*], Florent Duchaine [a], Dimitrios Papadogiannis [a], Ignacio Duran [a], Stéphane Moreau [b], Laurent Y.M. Gicquel [a]

[a] CFD team CERFACS, 42 avenue Gaspard Coriolis, 31057 Toulouse Cedex 1, France
[b] Université de Sherbrooke, Sherbrooke, QC J1K 2R1, Canada

ARTICLE INFO

Article history:
Received 19 October 2013
Received in revised form 25 April 2014
Accepted 4 June 2014
Available online 11 June 2014

Keywords:
Large eddy simulation
Turbomachinery
Rotor–stator interactions
Overset grids

ABSTRACT

A coupling method based on the overset grid approach has been successfully developed to couple multi-copies of a massively-parallel unstructured compressible LES solver AVBP for turbomachinery applications. As proper LES predictions require minimizing artificial dissipation as well as dispersion of turbulent structures, the numerical treatment of the moving interface between stationary and rotating components has been thoroughly tested on cases involving acoustical wave propagation, vortex propagation through a translating interface and a cylinder wake through a rotating interface. Convergence and stability of the coupled schemes show that a minimum number of overlapping points are required for a given scheme. The current accuracy limitation is locally given by the interpolation scheme at the interface, but with a limited and localized error. For rotor–stator type applications, the moving interface only introduces a spurious weak tone at the rotational frequency provided the latter is correctly sampled. The approach has then been applied to the QinetiQ MT1 high-pressure transonic experimental turbine to illustrate the potential of rotor/stator LES in complex, high Reynolds-number industrial turbomachinery configurations. Both wave propagation and generation are considered. Mean LES statistics agree well with experimental data and bring improvement over previous RANS or URANS results.

1. Introduction

Computational Fluid Dynamics (CFD) has been developed over the past few decades and has been intensively used as a design tool of gas turbines for propulsion or power generation systems. Because of increasing market and environmental constraints that target high efficiency, high power to weight ratio, low noise and high reliability, current and next generation of gas turbine engines will require improved CFD tools. Indeed to contribute efficiently to our understanding and thereby produce better engines, unsteady physical and chemical phenomena that take place in these engines need to be better apprehended. This in the long term will have to be addressed for each sub-component, but also in a fully integrated way: *i.e.* simulating at once the compressor, the combustor and the turbine [1]. In the specific context of CFD, Large Eddy Simulation (LES) [2] is a good candidate and has already been used to simulate the combustor of gas turbines [3,4] and some specific isolated parts of turbomachinery applications [5–13], but few applications are today available in turbomachinery stages [14–17]. In fact, CFD for turbomachinery still remains a challenge because of the high Reynolds and Mach-number

* Corresponding author at: CFD team CERFACS, 42 avenue Gaspard Coriolis, 31057 Toulouse Cedex 1, France.
E-mail address: gaofeng.wang@usherbrooke.ca (G. Wang).

http://dx.doi.org/10.1016/j.jcp.2014.06.006
0021-9991/

flows, the importance of several loss mechanisms that greatly impact the operating condition and efficiency of these components as well as mixing effects between hot stream from the combustion chamber and fresh cooling gases, multi-species flows, rotation and technological effects. Current industrial turbomachinery simulations usually involve Reynolds-Averaged Navier–Stokes (RANS) or Unsteady RANS (URANS) equations, which rely on turbulence models [18,19] to predict the mean flow fields in these elements. For the known rotor/stator interactions, URANS is necessary to capture the unsteady deterministic interactions that are present in these configurations [20]. Today the computational cost of RANS or URANS is acceptable for engineering applications and explain their daily use in real applications. However such tools show limits whenever used for testing off-design point computations [14] or even at design conditions when transition to turbulence or secondary flows play major roles. The modeling needed with RANS or URANS limits engineers from further efficiently improving the devices and expensive test benchings of multiple concepts are still mandatory today.

With the rapid development of High Performance Computing (HPC) [21], recent efforts have been made on the prediction of the complex turbulent flows around isolated parts with high-fidelity fully unsteady LES (see review by Tucker [22]). Although much more computationally intensive than RANS, LES can alleviate the modeling efforts by explicitly resolving the temporal and spatial evolutions of the large flow structures while filtering out the smaller ones [23,24]. Preliminary demonstrations show that LES can resolve flows with transitions, separations [5,6,13] and thereby improve heat transfer predictions on structured or unstructured meshes [8,10,12]. Tip-clearance flow predictions [7] have also been addressed successfully with LES. McMullan and Page [14] have demonstrated that LES can predict surface pressure on the Monterey cascade with a sufficiently refined mesh. Algorithmic developments complemented by high performance massively parallel machines allow today to have LES solvers capable of handling 21 billions unstructured tetrahedral cells with a very reasonable speed-up [25] making use of up to one million cores at once [26,27]. Following the analysis of Tucker [28], this capability seems to be approaching LES requirements of most gas turbines in aircraft applications. The application to real machines is currently being investigated and three configurations of compressor stages [14,16,17] and one transonic turbine stage [15,29] have already been reported: a scaled last stage of the Cranfield BBR compressor with a Reynolds number based on the stator midspan chord of $Re = 180{,}000$, the Cambridge axial compressor ($Re = 350{,}000$), the CME2 axial compressor ($Re = 500{,}000$) and the MT1 axial turbine ($Re = 2{,}600{,}000$). Even in these first LES predictions of compressor or turbine stages, numerical challenges are still present. First, the high computational costs relate to the complexity of these flows with high Reynolds numbers $Re \sim O(10^{5-7})$, which impose large grids. Secondly, the modeling difficulty comes from an adequate resolution or modeling of the wall flow physics since it may have a dramatic impact on the main blade-channel flow and vice-versa. Thirdly, current LES codes require high spatial and temporal accuracy [30] that may not survive at the rotating interfaces to yield adequate and relevant unsteady predictions of component interactions. Indeed the numerical treatment of a rotating interface will impact the overall discretization-scheme quality and properties. Typically, resolved vortical, acoustic and entropy waves should travel with the flow and therefore cross the interface without being significantly altered by the numerical treatment to preserve the LES nature of the solver in this region.[1]

The last point is crucial for turbomachinery stage simulations and is rarely discussed or validated in reported LES [29]. In an attempt to provide validation of the interface treatment for LES of turbomachinery, a coupling interface based on overset grids is presently proposed and studied with specific emphasis on the resulting scheme properties. The overset grid method has been proposed and developed for instance by Volkov [31], Magnus and Yoshihara [32], Starius [33], Atta and Vadyak [34], Benek et. al. [35,36], Berger [37], Henshaw and Chesshire [38,39]. It has recently been studied and applied for Computational AeroAcoustics (CAA) [40–42], coupling CFD/CAA [43], conjugate heat transfer problems [44], moving body applications [45–49] or to handle complex geometries [8,50] with very high accuracy [51,52]. It has also been used in RANS of external and turbomachinery flows where it is commonly known as the Chimera method [35] and reported as providing an equivalent accuracy as the sliding mesh method [53]. In the specific RANS context where fields are smooth and independent of time, conservation is sufficient for the rotor/stator interface since the turbulence is fully modeled or described by some extra conservation equations towards the steady state solution of the problem. Numerical requirements of RANS are hence limited to the interpolation scheme at the interface meshes that needs to be conservative, which is usually obtained by taking first-order area-based interpolation within the sliding mesh [54]. For LES, most of the flow structures are resolved so flow fields are time dependent and contain a large range of wave lengths covering all the scales from the geometry up to the finest local grid resolution. To preserve the quality of such simulations all this information should be transferred through the interface with as less influence as possible to maintain flow coherence, evolution as well as the numerical properties of the scheme. The primary objective is thus to avoid dissipating or dispersing the signal within the original context of the numerical scheme used away from this boundary. To meet such requirements, the overset grid method is of interest as increasing its accuracy is straightforward for structured meshes [8,40,41,43,51,52,55–58], though it may lead to some complexity in the generation of these overlapping regions [59]. Overset unstructured meshes have also been developed in the past decade [60–64] and are recently being considered for a high-order interface treatment [42,65].

In the following, the overlapping moving interface is implemented based on a domain decomposition approach [66] with an unstructured compressible high-performance parallel LES solver. The resulting strategy is hereafter called MISCOG for Multi Instance Solver Coupled through Overlapping Grids. The details of the coupling and associated numerical features are

[1] Conventional LES numerical schemes should be high order and centered to minimize dispersion and dissipation. Note that such schemes are by nature highly oscillatory and therefore become unstable and strongly modified by inadequate numerical treatment at the interface.

given in Section 2. Convergence and numerical errors of the proposed method are then checked on canonical cases with static or moving coupling interfaces in Section 3. A specific attention is brought to the dispersive and dissipative errors introduced by the interface treatment. Propagation of acoustic and vortical waves (an isentropic vortex) are first considered and the translating interface is introduced. The rotating interface is then tested on a rotating cylinder. Finally two examples of the developed methodology for wave propagation and generation in an actual turbine, involving both translating and rotating interfaces, are presented in Section 4. The new LES tool is applied to the QinetiQ MT1 high pressure turbine [67], which has both high Reynolds and Mach numbers typical of modern turboengines.

2. Numerical method and implementation

The objective of the present section is to provide a description of the numerical methods retained for the treatment of the rotor/stator interface problem using the overset grid method. First, governing equations, numerical schemes and formalisms present in the CFD code are exposed followed by the presentation of the numerical approach introduced to deal with the exchange of information at the interface belonging to the fixed and rotating domains.

2.1. Governing equations

The filtered LES unsteady compressible Navier–Stokes equations that describe the spatially filtered mass, momentum and energy $(\rho, \rho\mathbf{U}, \rho E)$ conservations, can be written in the following conservative form:

$$\frac{\partial \mathbf{W}}{\partial t} + \nabla \cdot \mathcal{F} = 0, \tag{1}$$

where $\mathbf{W}$ is the vector containing the conservative variables $(\rho, \rho\mathbf{U}, \rho E)^T$ and $\mathcal{F} = (\mathbf{F}, \mathbf{G}, \mathbf{H})^T$ is the flux tensor. For convenience, this flux is usually divided into two components:

$$\mathcal{F} = \mathcal{F}^C(\mathbf{W}) + \mathcal{F}^V(\mathbf{W}, \nabla\mathbf{W}), \tag{2}$$

where $\mathcal{F}^C$ is the convective flux depending on $\mathbf{W}$ and $\mathcal{F}^V$ is the viscous flux depending on both $\mathbf{W}$ and its gradients $\nabla\mathbf{W}$. The contributions of Sub-Grid Scale (SGS) turbulence models are included in the viscous flux through the addition of the so called turbulent viscosity ν_t [18,24]. For simplicity, the present work relies on the standard Smagorinsky SGS model for which the turbulent viscosity is modeled by

$$\nu_t = (C_S \Delta_g)^2 \sqrt{2\tilde{S}_{ij}\tilde{S}_{ij}}, \tag{3}$$

where $\tilde{S}_{ij}$ denotes the resolved rate-of-strain tensor, C_S denotes model constant and Δ_g denotes the characteristic filter length, usually corresponding to the local mesh cell size [68].

2.2. Numerical schemes

The governing equations are solved by the unstructured compressible LES solver, AVBP in which several numerical schemes are available [27,69]. Only two of those are presently considered. First, the Lax–Wendroff scheme (LW) is a 2nd-order finite volume scheme in time and space, which corresponds to the accuracy of most commercial codes as well as most of the turbomachinery CFD tools available today [70]. Secondly, the two-step Taylor–Galerkin finite element scheme TTG4A (4th-order in time and 3rd-order in space) provides improved LES quality on unstructured grids [71]. All schemes are expressed in the cell-vertex numerical discretization approach, for its compactness and effectiveness on parallel HPC. The cell-based residuals, *i.e.* the spatially dependent terms of the equations on each control volume Ω_j, are then calculated by integrating the fluxes over the cell as:

$$\mathbb{R}_{\Omega_j} = \frac{1}{V_{\Omega_j}} \int_{\partial\Omega_j} \mathcal{F} \cdot n \, dS, \tag{4}$$

where V_{Ω_j} is the cell volume and $\partial\Omega_j$ its boundary with normal vector n. Since the integration is obtained around a vertex, a distributed version of these cell-based residuals $\mathbb{R}_k$ is constructed via distribution matrices. One can hence express Eq. (1) into the semi-discrete scheme

$$\frac{d\mathbf{W}_k}{dt} = \mathbb{R}_k = -\frac{1}{V_k} \sum_{j|k\in\Omega_j} D^k_{\Omega_j} V_{\Omega_j} \mathbb{R}_{\Omega_j}, \tag{5}$$

where V_k is a control volume associated with a node k and $D^k_{\Omega_j}$ is the distribution matrix that weights the cell residual from the cell center Ω_j to node k [72,73].

In static (with stationary mesh element) parallel computations, the computational domain is divided into several individual vertices-shared partitioned domains each of which is attributed to one processor using Domain Decomposition Methods

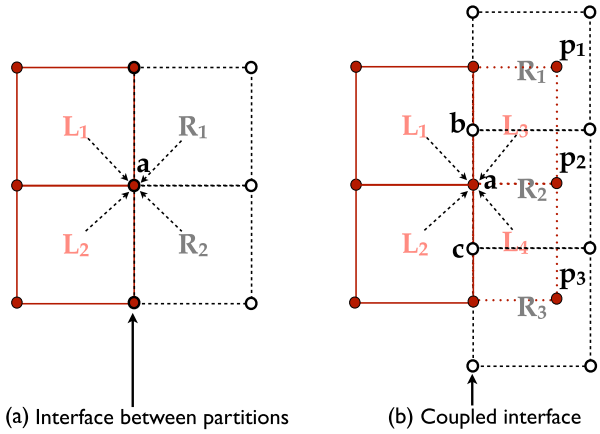

Fig. 1. (a) DDM for cell-vertex schemes used in parallel computations and (b) the proposed method for rotor/stator interface. $\mathbf{L_{1,2,3,4}}$ (composed of: solid lines – edges and filled symbols for the vertices) and $\mathbf{R_{1,2,3}}$ (composed of: dashed lines – edges and open symbols for vertices) denote the cells on the left and right sides of a partitioned domain, respectively. In the case of a moving fluid boundary, points **a** of domain **L** and points **b**, **c** of domain **R** are the vertices to be coupled at the interface. Points $\mathbf{p_{1,2,3}}$ and $\mathbf{L_{3,4}}$ are additional vertices involved in the coupling when the overlapping method is introduced.

(DDM) [66]. Fig. 1(a) illustrates the conventional DDM static coupling process for a cell-vertex scheme. The cells ($\mathbf{L_{1,2}}, \mathbf{R_{1,2}}$) are grouped into two domains respectively denoted by **L** and **R** and contribute to the common node **a** cell residual. Indeed in cell-vertex schemes, the cell-based residuals are computed locally (*i.e.* for all individual cells, $\mathbf{L_{1,2}}, \mathbf{R_{1,2}}$) and scattered to the belonging vertices. Vertex **a** that is located at the interface therefore needs all the contributions from the neighboring partitions for the nodal residual to be evaluated following Eq. (5). In conventional approaches of static massively parallel codes, this is simply done through network communications.

2.3. Overset method for rotor/stator computations

The problem for the rotor/stator coupling is similar to the DDM problem described above except that the two domains **L** and **R** are moving (translating or rotating) relatively to each other. Non-conformal vertices (shown in Fig. 1b) are hence present at a given instant and along the interface. Additional evaluations at every iteration are therefore needed if compared with static DDM. Numerically, several coupling methods are possible for such problems, all of which introduce the notion of interpolation for information reconstruction around or on the interface. In the implementation, Lagrange interpolators can be used for exchanging variables following:

$$\mathfrak{L}f = \sum_{i=1}^{n_{sh}} f(q_i)\,\phi_i, \tag{6}$$

where f is a function approximated by Lagrange polynomial elements and $f(q_i)$ are the function values at the vertices q_i; n_{sh} is the number of degrees of freedom of the element and ϕ_i are its shape functions. For nodes in an element or on a surface, the interpolation coefficients are calculated based on the shape functions using the local coordinates of the elements. In the current study, simple linear shape functions, *i.e.* barycentric interpolation or bilinear interpolations are used in agreement with $\mathbb{P}_1$ (triangular in $2D$ and tetrahedral in $3D$) and $\mathbb{Q}_1$ (quad in $2D$ and hexahedral in $3D$) elements, implying an order 2 for these operations.

Rotor/stator interface treatment may be introduced at various steps of the numerical scheme. Coupling fluxes before computing the cell-based residuals of Eq. (4) has the benefit of involving only the interface nodes limiting the number of unknowns and potential manipulations. Within such a context, the computed fluxes should be interpolated on the $2D$ coupled interface for a $3D$ computation as performed in the traditional sliding mesh approach for example [54]. An alternative is to couple nodal residuals. In this approach, each nodal residual $\mathbb{R}_a^L$, $\mathbb{R}_b^R$ and $\mathbb{R}_c^R$ are calculated by counting the contributions of all sub-domain local cells using Eq. (5) first. The contributions of each missing domain (*i.e.*: $\mathbf{R}_2$ residual contribution to node **a** for example) are then estimated by introducing an additive interpolation $\mathfrak{L}$ to obtain the vertex **a** residual at the interface for example,

$$\mathbb{R}_a = \mathbb{R}_a^L + \mathfrak{L}\left(\mathbb{R}_b^R, \mathbb{R}_c^R\right). \tag{7}$$

With this approach, the difficulty comes from the rotation terms added in the transport equations of the moving domain that are not compliant with the static part of the configuration. As a result such a scheme was found to be unstable in the case of a rotating domain coupled to a static domain if using simple linear interpolation schemes. The last solution, retained in the following, consists in reconstructing the residuals using an overset grid method that directly exchanges the multi-domain conservative variables by interpolation. As shown in Fig. 1(b), overset grids is introduced relying on extended domains **L** by two $\mathbf{L_{3,4}}$ or more ghost cells in the normal direction of the interface so that the nodal residual of vertex **a** can be computed from available sub-domain cell-based residuals of $\mathbf{L_{1,2,3,4}}$. Note that $\mathbf{L_{1,2,3,4}}$ is obtained using the interpolated

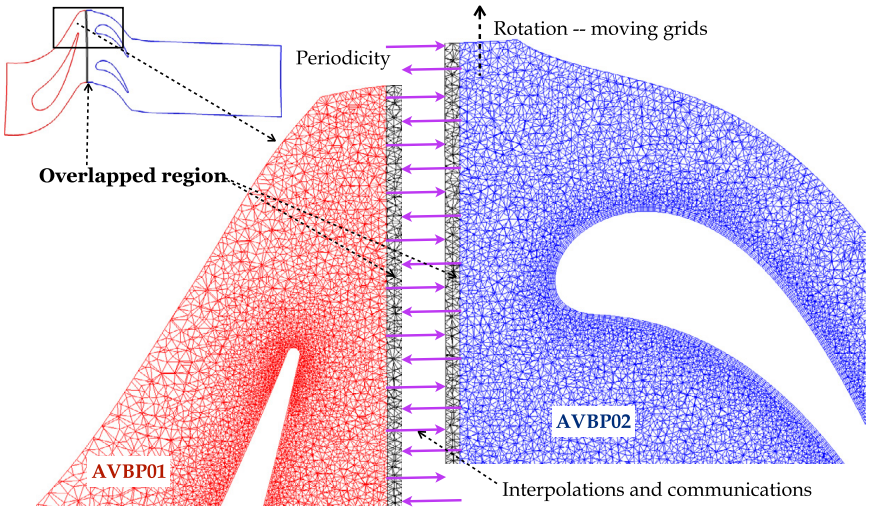

Fig. 2. Communication framework of coupling rotor/stator interface.

conservative variables within the overlap region to evaluate the right-hand side of Eq. (4). Note finally that cells $\mathbf{L_{3,4}}$ are geometrically overlapped with the domain **R** with points located in cells $\mathbf{R_{1,2,3}}$. In the more generic cases, the extent and topology of the duplicated cells will not coincide. The unknown conservative variables of the overset vertices $\mathbf{p_{1,2,3}}$ are hence approximated through an interpolation from the information of cells $\mathbf{R_{1,2,3}}$. The same procedure is used to compute the nodal residuals of $\mathbf{b}, \mathbf{c}$ in domain **R** that is also extended onto mesh **L** by two or more cells, since it is a two-way coupling. This third approach is selected here as it is easily implemented externally from any base CFD code and yields high-order accuracy if used in conjunction with high order interpolation [41,43,51,52,58,74].

In terms of methodology and overall strategy, the external code coupling is preferred over an internal implementation to extend the available LES solver so that it can deal with rotor/stator simulations. Hence two or more copies of the same LES solver (namely AVBP) each with its own computational domain and static DDM algorithm executing a given partitioning with a given target number of processes, are coupled through the parallel coupler OpenPALM [75]. The detailed implementation of such coupling includes: (1) find the enclosed cell; (2) calculate the local coordinates in the cell; (3) calculate the interpolation coefficients using a shape function; (4) calculate the interpolated value using Eq. (6). The current implementation [75] is compatible with the CGNS interpolation tool [76] and is external to the CFD code. Finally, note that a high order interpolation is viable for unstructured meshes by introducing high order shape functions [77], but with some significant additional efforts in implementing the proper stencils efficiently.

Fig. 2 shows a typical communication framework for a rotor/stator coupling approach using the MISCOG method described above. For this case, the whole flow domain should initially be divided into static (AVBP01) and rotating parts (AVBP02). For rotating parts, the code uses the moving-mesh approach in the absolute frame of reference while the remaining unit simulates the flow in the stationary part in the same coordinate system [78]. The interfaces between the two units involving rotating and non-rotating parts are coupled with the overset grids by interpolating and then exchanging the conservative variables wherever needed and as described above. To do so, an efficient distributed search algorithm is implemented in the coupler OpenPALM to locate the points in parallel partitioned mesh blocks. This coupling algorithm will then update at each time step the information and carry the interpolation from one sub-MPI world to the next and vice-versa. Issues of numerical stability of the coupled solution and the convergence of this coupled problem are directly linked to the size of the overlapped region and the stencil of the numerical schemes selected [79].

3. Numerical analysis of the coupling approach

Prior to the application of the proposed solution to a high fidelity LES of rotor/stator problem, three validation cases are conducted focusing on acoustical wave propagation ($1D$), convection of an inviscid or viscous vortex ($2D$), and rotating boundaries ($2D$). Each case is computed twice: the first evaluation is used to yield the benchmark solution using one standard AVBP procedure running on one mesh while the second computation uses two non-conformal overlapping meshes to evaluate the MISCOG strategy. The primary objective is to qualify and quantify errors introduced by the coupling approach.

3.1. Acoustics wave traveling in a static coupled simulation

An accurate compressible LES should first transport acoustic waves properly. The first validation case is therefore the simple problem of a $1D$ propagating acoustic wave (Euler equation) in a domain whose boundary conditions are non-reflective and the acoustic signal covers the entire computational domain. Fig. 3 illustrates the configuration for the reference and coupled simulations. In the latter, two overlapping $1D$ meshes are computationally communicating using MISCOG. In the

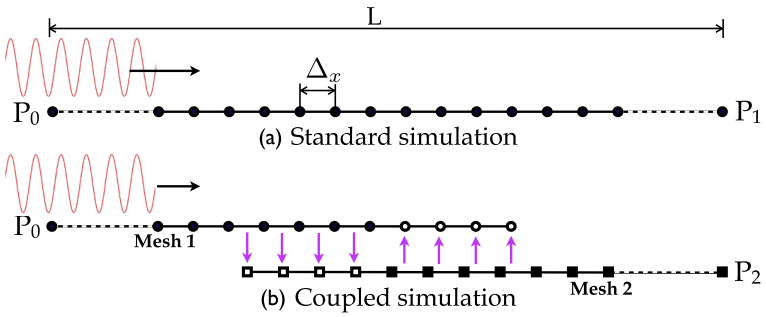

Fig. 3. 1*D* acoustic wave propagation simulated by two approaches: (a) the stand-alone solver and (b) the equivalent coupled approach. The total length of the computational domain is L and the cell size is Δ_x.

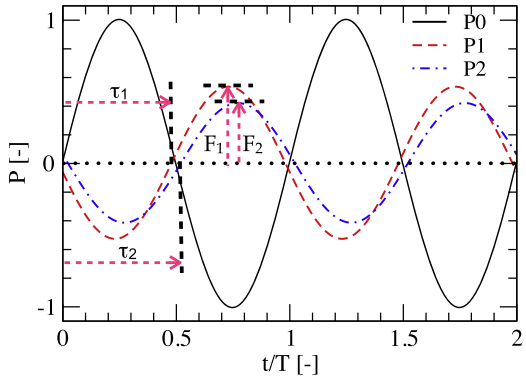

Fig. 4. Inlet wave signal (P_0) and signals at the downstream probe for the standard simulation (P_1) and the coupled simulation (P_2) as a function of time t normalized by the period T (mesh resolution of $\Delta x/\lambda = 0.125$ and LW scheme). Definitions of the gain factor F and phase-shift τ.

overlapped region, the meshes are non-coincident and the vertices from one mesh are located at the center of the corresponding cell in the other mesh. The conservative variables over several layers of nodes on each side are coupled and will be updated based on the interpolated values of the other mesh at each time step.

The incoming acoustic wave is imposed at the left side boundary of the domain (Fig. 3) using the Inlet Wave Modulation (IWM) approach [80], which is equivalent to modulating the target velocity at the inlet as:

$$u_{inlet} = U_0 + \frac{P^A}{\rho_0 c_0} \sin(2\pi f t). \tag{8}$$

The amplitude of the pressure perturbation is $P^A = 100$ Pa. The temporal frequency is $f = 1000$ Hz. A zero mean flow velocity is set ($U_0 = 0$), and the density $\rho_0 = 1.172$ kg/m^3 and sound speed $c_0 = 347.469$ m/s of the mean flow correspond to atmospheric conditions. Navier–Stokes Characteristic Boundary Conditions (NSCBC) are used at both inlet and outlet boundaries to prevent wave reflections [81]. The total length L of the computational domain is chosen to be 10 times the selected wave length, $\lambda = c_0/f$, which is then discretized by different mesh resolutions, $\Delta_x \in [\lambda/40, \lambda/4]$. To focus on the spatial discretization error, the time steps of all cases are set to a very small physical value $\Delta t = 6$ ms, which corresponds to a Courant–Friedrichs–Lewy (CFL) number of 0.2 for the finest mesh ($\Delta_x = \lambda/40$) and 0.02 for the coarsest mesh ($\Delta_x = \lambda/4$). The two numerical schemes (LW and TTG4A) presented above are tested here.

Fig. 4 shows the temporal evolutions of this flow solution obtained with LW. The inlet wave signal (P_0) is compared with the outlet probed signal for the two different approaches (P_1 for the standalone computation and P_2 for the coupled one). Only two wave periods of the input signals are taken for a mesh resolution $\Delta_x = \lambda/8$. In the exact solution to such a problem the sine wave should be preserved and only a delay of $\tau_{ex} = L/c$, where c stands for the speed of sound, should be present at all frequencies. A gain factor F and a phase-difference τ between inlet and outlet signals are introduced for all simulations to assess the differences with this exact solution. The results of the standalone simulations then provide the dissipative and dispersive properties of the selected scheme. When comparing with the results of the coupled simulations, the additional contribution of the coupling scheme and particularly the effect of the interpolation can be assessed. Fig. 5 quantifies both errors illustrated in Fig. 4. In Fig. 5(a), for large numbers of points per wave-length, all schemes show a small level of dissipation: the gain factor approaches unity in all cases as $\Delta x/\lambda$ decreases confirming the convergence of the discretized system (with or without interpolation). It shows that dissipation increases as the number of points per wave-length decreases, making F almost vanishing when the mesh resolution is poor: $\Delta x/\lambda = 0.16$ for LW and $\Delta x/\lambda = 0.25$ for TTG4A stressing the superiority of the Taylor–Galerkin schemes for compressible LES [30,72]. Several coupled computations with varying numbers of overlapping points N_o are also shown in Fig. 5(a) ($N_o = 1, 4, 5$), to find its optimal value for both numerical schemes. Only one overlapped node on each side is required for LW as confirmed by

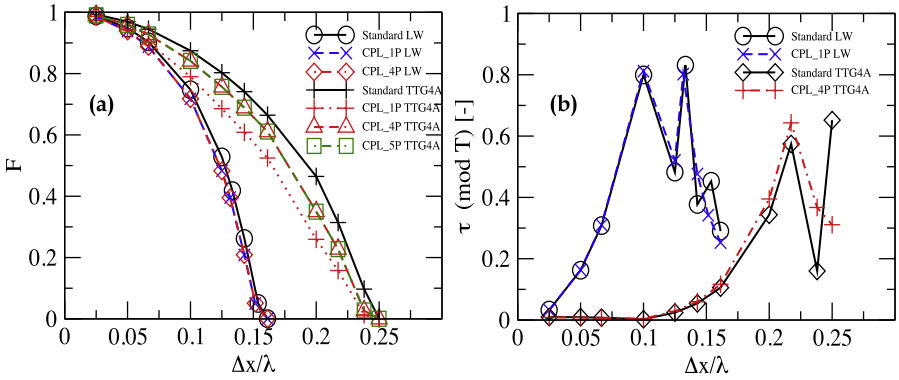

Fig. 5. The gain factor F (a) and phase-shift τ (b) errors for both standard and coupled simulations.

theoretical and numerical analyses [79]. Using one or four overlapped nodes also yields very similar results. For TTG4A, four overlapping nodes are needed to cover the full stencil at the interface. As shown in Fig. 5(a) adding a fifth point on either side of the overlapped interface does not improve the gain factor curve, since it does not appear in the stencil. Fig. 5(b) shows the phase errors for standard and coupled simulations. The curves indicate that interpolation does impact the results mainly at very poorly resolved scales. All these results are consistent with conventional analysis of numerical schemes designed for LES and confirm that the proposed rotor/stator interface treatment meets LES requirements provided that the uncoupled discretization scheme is of high order to minimize numerical dispersion and dissipation. This desired result is however obtained only if used with a sufficient number of overlapping points. Results also confirm that the interface treatment comes with an increased dissipation at all resolutions. Increased dispersion appears mainly for poorly resolved wave lengths.

3.2. Inviscid vortex traveling in a static and moving coupled simulation

Accurate compressible LES also relies on the model and solver ability to resolve and transport vortices within a complex geometry. The second validation case is specifically chosen to address the ability of the proposed solution to resolve a $2D$ vortex traveling through the overlapped interface using Euler equations. The numerical setups are given in Fig. 6. The standard and reference case (Fig. 6(a)) has a single mesh composed of $2N_x \times N_x$ quad cells of size $\Delta_x = 20R_c/N_x$, where R_c is the radius of the vortex, covering a rectangular (x,y) domain of dimensions $[-20R_c, +20R_c] \times [-10R_c, +10R_c]$. For the coupled cases, two computational domains are provided in Figs. 6(b) and (c), and consist of two rectangular boxes with an overlapped region for which N_o points are present on each side of the interface. The first box covers a domain of $[-20R_c, N_o\Delta_x] \times [-10R_c, +10R_c]$ and is meshed with $(N_x + N_o) \times N_x$ quad cells (indicated as **Mesh A** in Fig. 6). The second box covers $[-N_o\Delta_x + \Delta_x/2, +20R_c] \times [-10R_c, +10R_c]$ and has $(N_x + N_o) \times (N_x + 1)$ quad cells (indicated as **Mesh B** in Fig. 6). Similarly to the first test case, the overlapped vertices are located at the center of the quad cells of the other mesh. Two types of coupled simulations are conducted: (1) a static coupling; (2) a coupling with a translating interface in which the second coupled mesh is periodically translating in the vertical direction in Fig. 6, at a constant speed of 100, 200 and 300 m/s (typical rotating speeds of relevant turbomachinery applications). NSCBC are used again at both inlet at outlet boundaries to avoid wave reflections. To prevent spurious effects from the domain boundaries, all lateral surfaces are also set to be periodic.

An initial isotropic vortex [30,81,82] is imposed on a uniform mean flow going from left to right. It is based on the stream function

$$\Psi(x, y) = \Gamma e^{-r^2/2R_c^2}, \tag{9}$$

where Γ is the vortex strength and $r = \sqrt{(x - x_c)^2 + (y - y_c)^2}$ the geometric distance to the vortex center (x_c, y_c), initially located at $x_c = -10R_c$ and $y_c = 0$. R_c controls the size of the vortex. The resulting velocity and pressure fields simply read

$$u = U_0 + \frac{\partial \Psi}{\partial y} = U_0 - \frac{\Gamma}{R_c^2}(y - y_c)e^{-r^2/2R_c^2}, \qquad v = -\frac{\partial \Psi}{\partial x} = \frac{\Gamma}{R_c^2}(x - x_c)e^{-r^2/2R_c^2}, \qquad P = P_0 - \frac{\rho\Gamma^2}{2R_c^2}e^{-r^2/R_c^2}, \tag{10}$$

where P_0 and U_0 stand for the reference background pressure field and flow velocity respectively. For the present simulations the different parameters are $R_c = 0.01556$ m, $P_0 = 101{,}300$ Pa, $\rho = 1.172$ kg/m^3 and a constant uniform flow $U_0 = 100$ m/s. Three levels of vortex strength $\Gamma = 0.036, 0.1$ and 0.5 m^2/s are chosen leading to velocity fluctuations $u'_{max} = v'_{max} = 1.4, 3.9$ and 19.4 m/s and pressure fluctuations $P'_{max} = 3.1, 24.1$ and 601.8 Pa respectively. The time steps are chosen to yield CFL $= 0.07$ to minimize temporal effects. Additional simulations are obtained for CFL $= 0.7$ as recommended for TTG4A [73].

Only predictions for CFL $= 0.07$ are shown in Fig. 6 for the three simulation setups. In Fig. 6(a), the initial vortex evidenced by isolines of the transverse velocity component is convected with time by the main flow from left to right in the

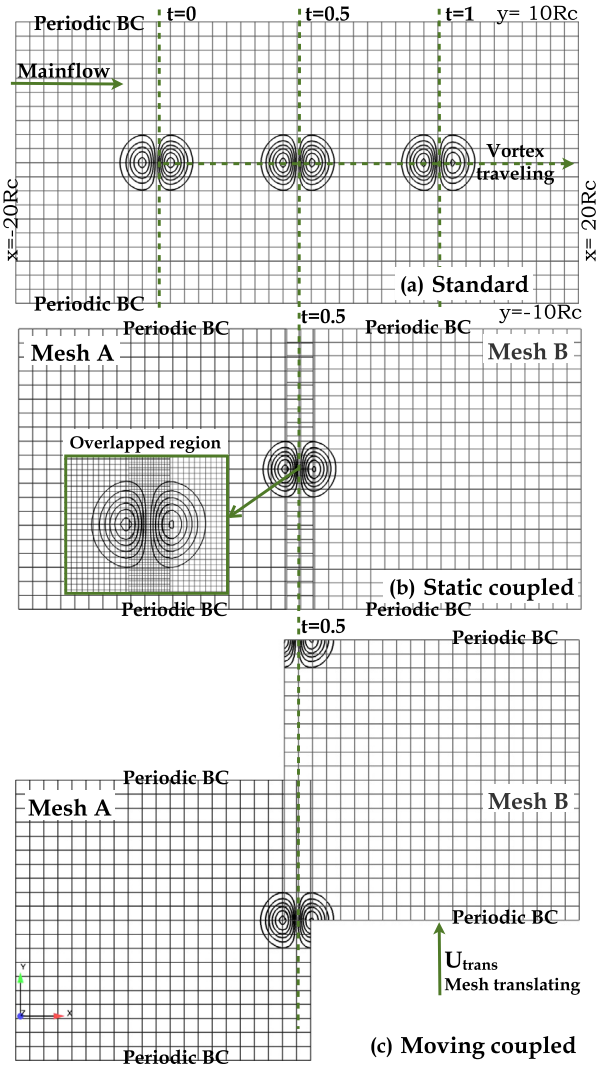

Fig. 6. Schematic of standard and coupled simulations of vortex traveling: (a) Standard case; (b) Static coupled case; (c) Moving coupled case: similar mesh sizes as the previous coupled case, except that mesh B is translating at speed of $u_{trans} = 100, 200$ or 300 m/s. The mesh size is $\Delta_x = R_c/4$ with $N_x = 80$ and $N_o = 4$ (only one-fourth of grid points are shown). The inviscid vortex (with radius R_c), shown by isolines of lateral velocity, is initialized at time $t = 0$ and is traveling from left to right and passing through the interface ($t = 0.5$). Time t is normalized by the vortex convection time over travel distance, $20R_c/U_0$.

standalone setup. In Figs. 6(b) and (c) for the static and moving mesh respectively, the vortex has reached the center of the coupling interface. As evidenced by the isolines, the vortex is well preserved in the coupled cases even when it crosses the coupling interfaces.

Numerical convergence of the proposed coupled strategy is then addressed on different mesh resolutions (N_x from 20 to 200), using both the LW and TTG4A schemes, with the quadratic mean errors of the instantaneous pressure field P (most sensitive variable)

$$L_2(P) = \|\epsilon_P\|_2 = \left[\sum V_i(\epsilon_{P,i})^2\right]^{1/2} \tag{11}$$

and the maximum error

$$L_\infty(P) = \|\epsilon_P\|_\infty = \max\left[|\epsilon_{P,i}|\right], \tag{12}$$

where $\epsilon_{P,i}$ is the difference between the nodal value of the analytical pressure field and the scheme value, and V_i is the area of the cell. The analytical fields are given by Eq. (10) with the vortex center advected to the anticipated positions. Figs. 7 and 8 show $L_2(P)$ and $L_\infty(P)$ curves as a function of the grid resolution at three dimensionless instants $t = 0.25, 0.5$ and 1, when the vortex is convected from the initial position $x = -10\,R_c$ at $t = 0$, to the positions $x = -5\,R_c$ (upstream of the interface) at $t = 0.25$, $x = 0$ (crossing the interface) at $t = 0.5$, and $x = 10\,R_c$ (downstream of the interface) at $t = 1$.

In Fig. 7(a), convergence at $t = 0.25$ is first checked for the small CFL number of 0.07. There are two sets of convergence plots with two different slopes, only depending on the numerical schemes. The coupled cases have the same errors as

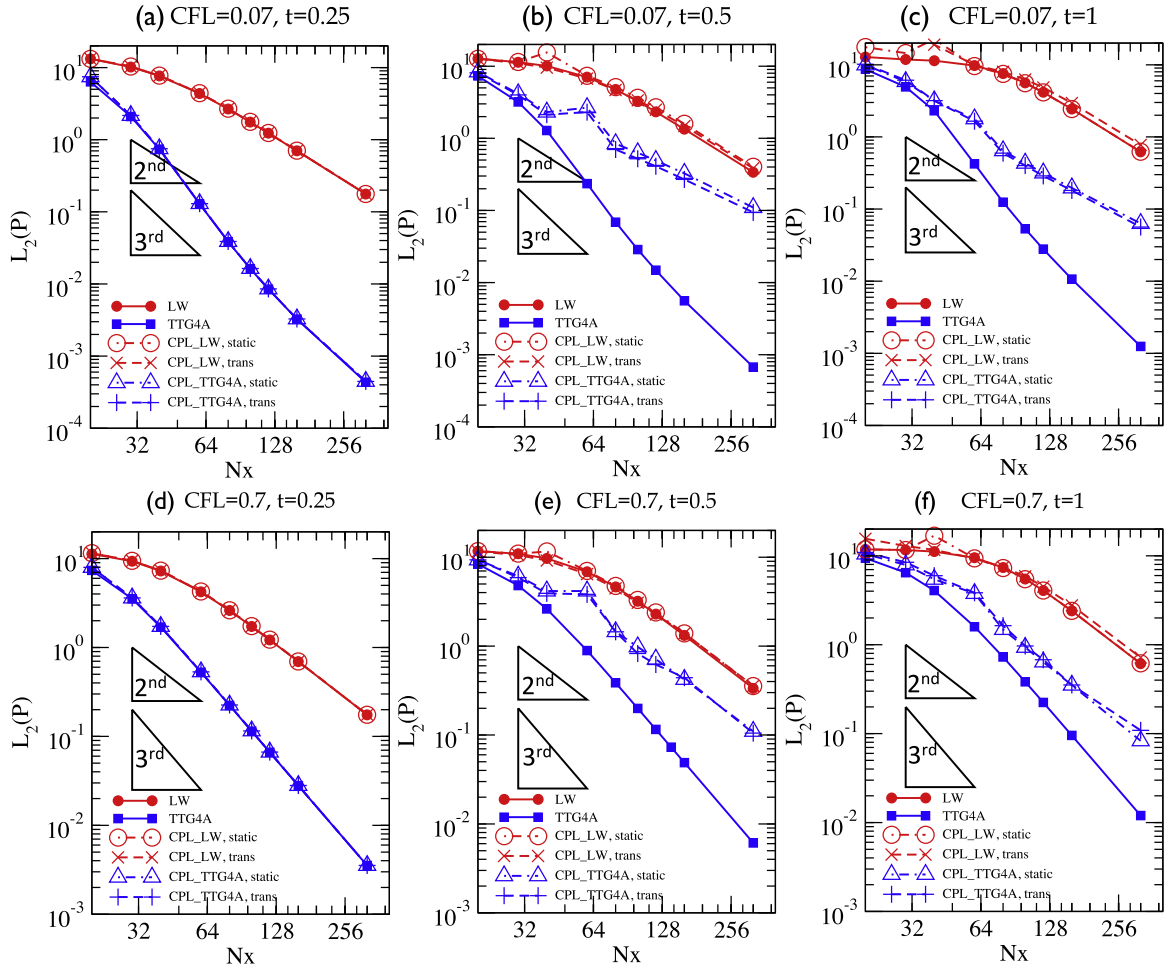

Fig. 7. The quadratic mean errors of instantaneous pressure fields $L_2(P)$ versus mesh resolution N_x for different cases using the LW or TTG4A schemes. The pressure profiles are compared with the analytic profiles when the vortex reaches upstream of the interface ($t = 0.25$), the interface ($t = 0.5$) and the downstream of the interface ($t = 1$). The computations are using two sets of time steps with CFL = 0.07 (top) and CFL = 0.7 (bottom). The translation speeds for the translating coupled cases is $U_{trans} = 200$ m/s.

the standard one. As expected, simulations using LW recover the scheme 2nd-order spatial accuracy, while simulations using TTG4A reaches a 3rd-order accuracy or slightly above. In Fig. 7(b), convergence results are given at $t = 0.5$. In the coupled cases, all static and translating ($U_{trans} = 200$ m/s) have similar error levels and slopes. Since the two domains are presently coupled by a 2nd-order linear interpolation scheme, only 2nd-order spatial accuracies are ensured for both LW and TTG4A simulations. Higher-order interpolation would be required to achieve higher spatial accuracy. Yet, coupled simulations with TTG4A contain almost a decade less errors than the coupled LW for any given grid resolution, as already evidenced in the above $1D$ test case. In Fig. 7(c), at $t = 1$, all the coupled simulations keep their 2nd-order spatial accuracy, even though the vortex has traveled $10R_c$ downstream the interface. Again, the mesh-translating coupled cases have similar error levels as the static ones. Figs. 7(d)–(f) show the same converged results for CFL = 0.7. All coupled cases again exhibit 2nd-order accuracy because of the 2nd-order interpolation (Figs. 7(e) and (f)). The translating coupled cases also have similar convergence rates as the static ones.

Temporal evolution of the above simulations is now considered to assess the spurious errors introduced at every time step by the moving coupled domains. The following mesh resolution is chosen: $N_x = 80$ ($\Delta_x = R_c/4 = 3.89$ mm). Fig. 9 shows the time traces of the pressure signals monitored at the middle point of the overall computational domain for different vortex strengths. Fig. 9(a) stresses that all temporal signals agree well with the standard simulation for a CFL of 0.07. Only high-frequency pressure fluctuations are introduced by the translating interface as evidenced in the zoom of the plot. When a standard FFT of the signal is performed in Figs. 9(b) and (c), these spurious oscillations are identified by a tone around 51.9 kHz independent of the vortex strengths and the coupling only introduces this additional high-frequency noise. When the CFL is increased to 0.7 in Fig. 9(d), the same conclusions can be drawn for all vortex strengths, except that additional humps appear around the tone.

The vortex strength is then set to $\Gamma = 0.5$ m^2/s. The pressure spectra are presented for different translating speeds $U_{trans} = 100, 200$ and 300 m/s in Fig. 10(a) and for different mesh sizes Δ_x in Fig. 10(b), all cases being summarized in Table 1. The frequencies of the spurious oscillations are clearly proportional to the translating speed and inversely propor-

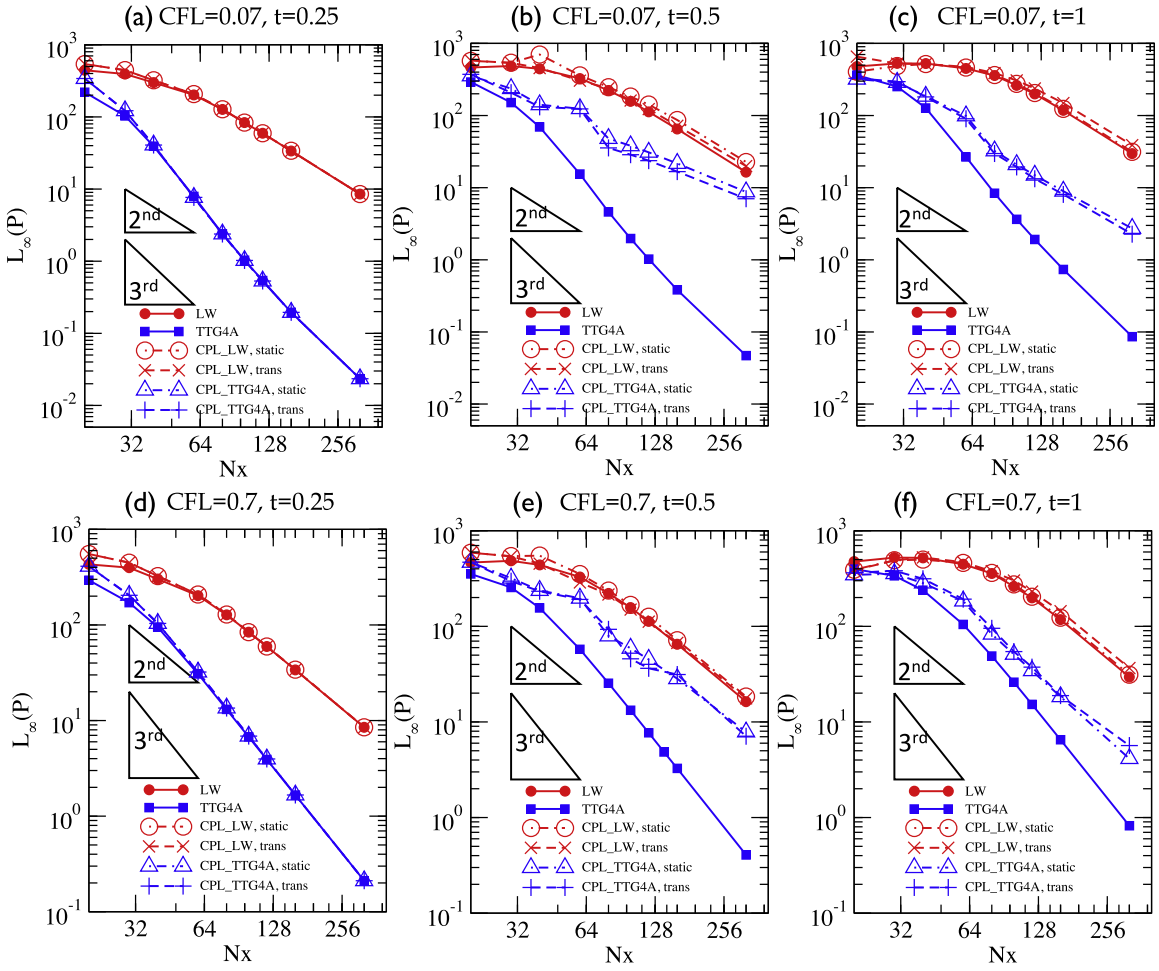

Fig. 8. The maximum errors of instantaneous pressure fields $L_\infty(P)$ versus mesh resolution N_x for different cases using the LW or TTG4A schemes. The pressure profiles are compared with the analytic profiles when the vortex reaches upstream of the interface ($t = 0.25$), the interface ($t = 0.5$) and the downstream of the interface ($t = 1$). The computations are using two sets of time steps with CFL = 0.07 (top) and CFL = 0.7 (bottom). The translation speeds for the translating coupled cases is $U_{trans} = 200$ m/s.

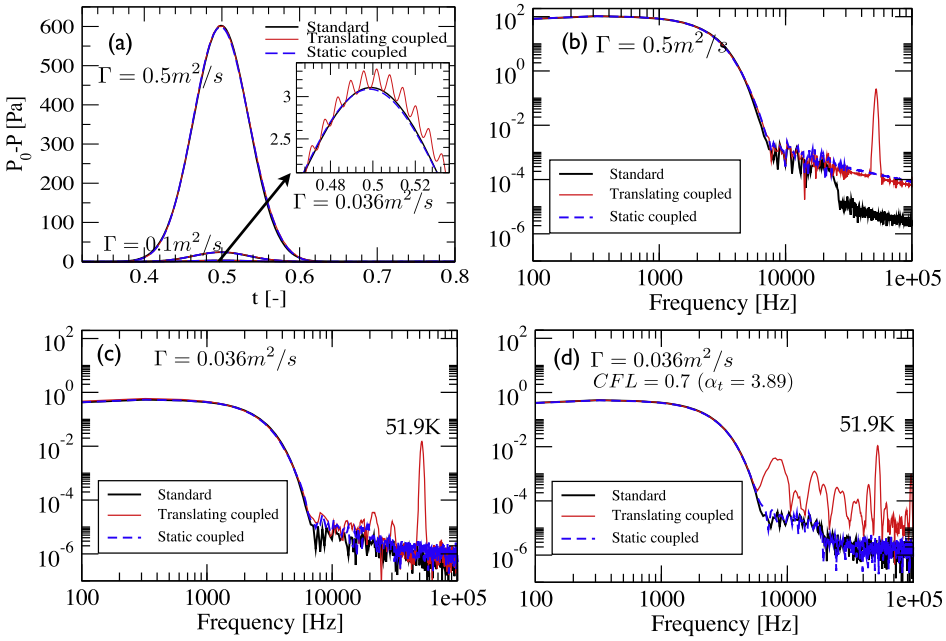

Fig. 9. Temporal evolutions of pressure signals at the central position $(0, 0)$ of interface for different vortex intensities (top: $\Gamma = 0.5$ m^2/s; bottom: $\Gamma = 0.036$ m^2/s) in standard, static coupled and translating ($U_{trans} = 200$ m/s) coupled cases. Time traces (a) and spectra (b)–(c) for CFL = 0.07. (d) Spectra for CFL = 0.7.

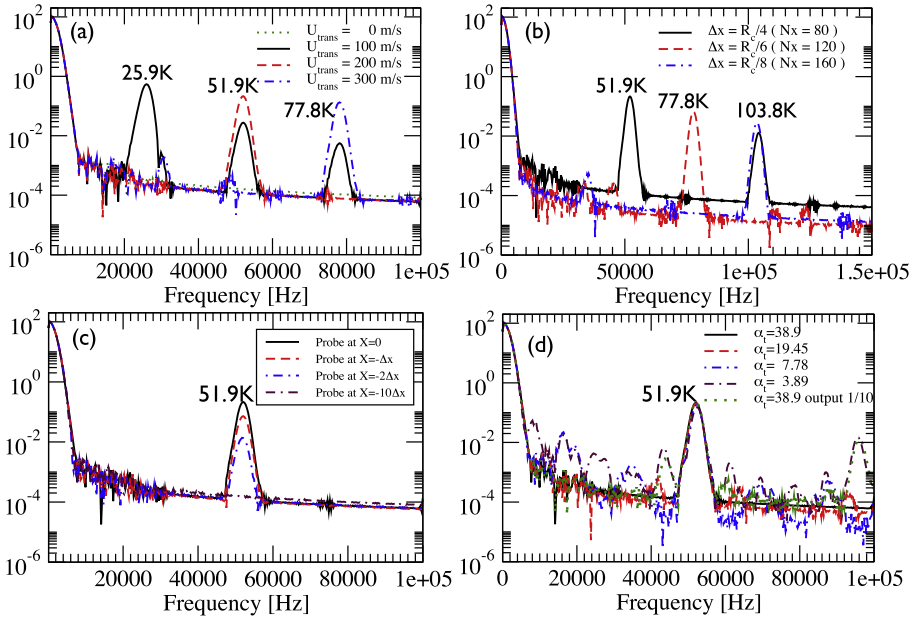

Fig. 10. Spectra of pressure signals at the central position $(0, 0)$ of interface in translating coupled cases (CFL $= 0.07$; vortex intensity $\Gamma = 0.5$): (a) with different translating speeds, $U_{trans} = 100$, 200 and 300 m/s and mesh size $\Delta x = R_c/4$; (b) with different mesh sizes, $\Delta x = R_c/4$, $R_c/6$ and $R_c/8$ for a translating speed $U_{trans} = 200$ m/s; (c) at different monitoring positions for a translating speed $U_{trans} = 200$ m/s; (d) using different time ratios $\alpha_t = 38.9$, 19.45, 7.78 and 3.89.

Table 1
Frequency f_{trans} of pressure signal spectra in translating coupled cases with different mesh sizes Δx and translating speeds U_{trans}.

Δx [mm]	U_{trans} [m/s]	f_{trans} [kHz]	$S_{trans} = \frac{f_{trans}\Delta x}{U_{trans}}$
3.8900	100	25.9	1.0075
3.8900	200	51.9	1.0095
3.8900	300	77.8	1.0088
2.5933	200	77.8	1.0088
1.9450	200	103.8	1.0094

tional to the mesh size, as confirmed by the non-dimensional ratio or equivalent Strouhal number obtained as the ratio between these three parameters

$$S_{trans} = \frac{f_{trans} U_{trans}}{\Delta_x} = 1.0. \tag{13}$$

Interpolation error is indeed fluctuating in time as the position of donor cells evolves with time. The level of this numerical noise is however two orders of magnitude smaller than the main vortex signal and can be considered negligible as long as it does not interfere with LES resolved large-scale motions. Moreover, this high frequency noise decreases rapidly away from the middle point as shown in Fig. 10(c) and is higher than the typical frequencies of combustion and turbomachinery noise of interest. Finally, Fig. 10(d) clearly shows that the additional humps observed in Fig. 9(d) are related to the ratio of the translation period T_{trans} to the timestep Δt

$$\alpha_t = \frac{T_{trans}}{\Delta t} = \frac{\Delta_x / U_{trans}}{CFL \cdot \Delta_x / (U_0 + c_0)}. \tag{14}$$

On the one hand, bigger α_t lead to less spurious frequency bands in the pressure spectra, and when T_{trans} is well resolved by the time step, only the peak translating frequency at 51.9 kHz can be seen. On the other hand, poor sampling of T_{trans} leads to aliasing frequencies [79,83].

3.3. Viscous vortex traveling in a static and moving coupled simulation

The viscous vortex [84] validation case is chosen to qualify the momentum diffusion using full 2D Navier–Stokes equations. The same setups as in the previous inviscid vortex problem is used here: the static test cases shown in Figs. 6(a) and (b), and the moving coupled case consisting of two computational domains coupled with MISCOG as in Fig. 6(c). An initial vortex with a core radius $R_c = 0.01556$ m is imposed using Eq. (10) on a viscous flow with uniform mean convecting velocity $U_0 = 100$ m/s. Two Reynolds numbers ($Re = U_0 R_c/\nu$) are chosen $Re = 102$ and $Re = 1020$. The CFL number is set to 0.7 and the two numerical schemes LW and TTG4A are tested for different mesh resolutions. The diffusion operator is discretized in AVBP with a second-order centered scheme on a compact stencil.

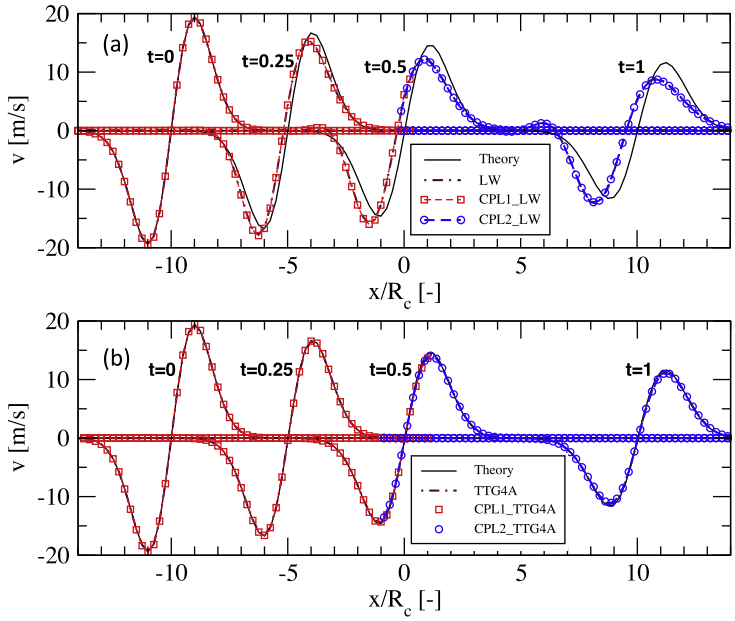

Fig. 11. Viscous vortex traveling case: the transverse velocity v convected and diffused with time t in simulations using LW (a) and TTG4A (b) schemes. Time t is normalized by $20R_c/U_0$. Mesh size $\Delta x = R_c/4$ and $Re = 102$.

The analytical solution for this temporally evolving velocity field can be obtained through a perturbation analysis of the governing equations detailed in [85], and reads:

$$u(x, y, t) = U_0 - \frac{\Gamma}{R_c^2}\frac{(y - y_c)}{\alpha^2} e^{-r^2/2\alpha R_c^2} \tag{15}$$

$$v(x, y, t) = \frac{\Gamma}{R_c^2}\frac{(x - x_c)}{\alpha^2} e^{-r^2/2\alpha R_c^2} \tag{16}$$

where the parameter α is defined as

$$\alpha = 1 + 2\nu t/R_c^2 \tag{17}$$

where the vortex strength is $\Gamma = 0.5$ m^2/s and the distance r is measured relative to the vortex center (x_c, y_c) traveling at U_0. The kinematic viscosity ν equals 1.52×10^{-3} or 1.52×10^{-2} m^2/s for the two Reynolds-number cases respectively.

Fig. 11 shows the temporal evolution of the transverse velocity component v along the x-axis. The vortex is initially located at $x = -10R_c$ at $t = 0$, traveling from left to right with the mean convecting flow while decaying due to diffusion. The coupled simulation has two computational domains (indicated by two different symbols) coupled at the interface $x = 0$. The vortex core travels through the interface at $t = 0.5$ and reaches $x = 10R_c$ at $t = 1$. The results predicted by the coupled simulations fit very well with those of the standard reference simulations. The TTG4A scheme agrees better with the analytical solution than the LW scheme, as it has less numerical diffusion and dispersion.

The velocity and its gradient profiles across or along the interface are further checked in Fig. 12 for the two schemes. The transverse velocity v is continuous across the interface in Figs. 12(a) and (b). All simulations in all domains yield the same results. The same conclusion can be drawn for the longitudinal velocity u along the interface ($x = 0$) in Figs. 12(c) and (d). Figs. 12(e) to (h) show the magnitudes of the gradients of the transverse velocity v. Very similar results are obtained for both the coupled and standard cases. However, the coupling interface seems to cause a slight damping of the magnitude of the gradients, and the continuity of the derivatives is no longer fulfilled because of the linear interpolation.

In Fig. 13 the numerical convergence is again checked by the L_2-error and L_∞-error on the transverse velocity field versus mesh resolution N_x by comparing with the exact analytical solution (Eq. (16)). For both Reynolds numbers $Re = 1020$ and 102 (Figs. 13(b) and (c) respectively), the TTG4A scheme exhibits 3rd-order spatial accuracy and the LW scheme 2nd-order accuracy in a very similar manner as the inviscid case (Fig. 13(a)). Similarly, the order of the coupled TTG4A scheme is reduced to 2nd-order because of the 2nd-order interpolation.

3.4. Flow past a rotating cylinder

A compressible LES of a rotor/stator configuration involves wakes crossing rotating boundaries. The final validation case therefore involves an overlapping rotating interface, and the flow past a rotating cylinder. It is a well-investigated test-case targeting wake dynamics and flow control [86]. Two critical parameters are relevant to this problem: (1) the Reynolds number $Re = U_0\ D/\nu$, based on the free-stream velocity U_0 and the cylinder diameter D as well as (2) the dimensionless

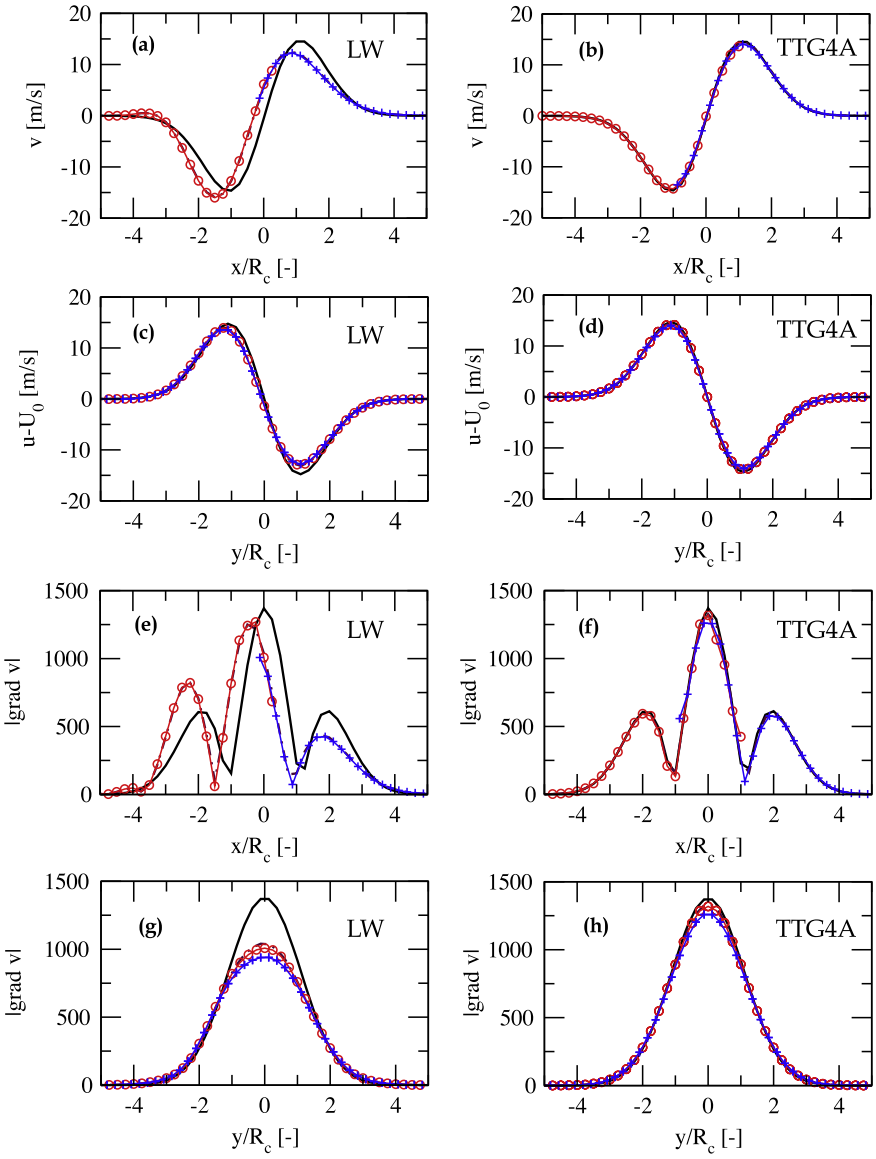

Fig. 12. The velocity and its gradient profiles when the viscous vortex travels through the interface at $t = 0.5$; analytical solution (hard lines), standard reference simulation (dashed lines) and coupled simulation (lines with symbols). The simulations are using the LW (left) or TTG4A (right) schemes. Mesh size $\Delta x = R_c/4$ and $Re = 102$.

peripheral velocity ratio $\alpha = 0.5D\omega/U_0$, defined as the ratio of the velocity magnitude at the surface of the cylinder $\omega D/2$ to the free-stream velocity. The case retained in the following simulation uses $Re = 200$ and $\alpha = 3.5$. For this operating condition, a stationary solution is expected with transient effects induced by the initial motion of the cylinder [86].

As shown in Fig. 14, two numerical configurations are again used for the simulation. In Fig. 14(a), a standard standalone simulation uses a single rectangular domain of dimensions $[-50D, 50D] \times [50D, 200D]$ with a cylinder centered at $(0, 0)$. The cylinder boundary condition is a rotating isothermal wall with a prescribed rotating wall velocity in the counter clockwise direction at a speed of $\omega = 2\alpha U_0/D$. The main flow value, U_0, is assigned at the upstream boundary while the downstream outlet uses a reference static pressure. Inlet and outlet boundaries also use NSCBC. The top and bottom boundaries are set to be adiabatic slip wall conditions. A close-up view of the unstructured mesh (made of triangular cells) is given in Fig. 14(a), with the smallest cell size equal to $D/400$ located on the cylinder surface. The coupled simulation has the same mesh topology, but consists of two meshes: one rotating mesh around the cylinder and extending radially up to $r \leq 2.25D$. Its rotation speed is fixed at $\omega = 2\alpha U_0/D$ and the cylinder wall condition is in this case an isothermal no-slip condition. A static mesh represents the outer domain for $r \geq 1.75D$. The two meshes overlap on an annulus located at $r = 2D$ with an overlapping thickness of $0.5D$. The characteristic mesh size is $0.05D$ in this region in both meshes. The numerical scheme of both simulations is TTG4A. As mentioned above, the two computations are impulsively started from a uniform free stream field covering the whole domain. The transient is computed for a total dimensionless time of 200 (time normalized by the convective time D/U_0), until the flow has reached a steady state. The results of the coupled configuration are in excellent agreement with the standard method as evidenced by the instantaneous vorticity fields in Fig. 14 or the axial velocity U profiles near the coupled region and at different instants in Fig. 15. Transient induced effects are further

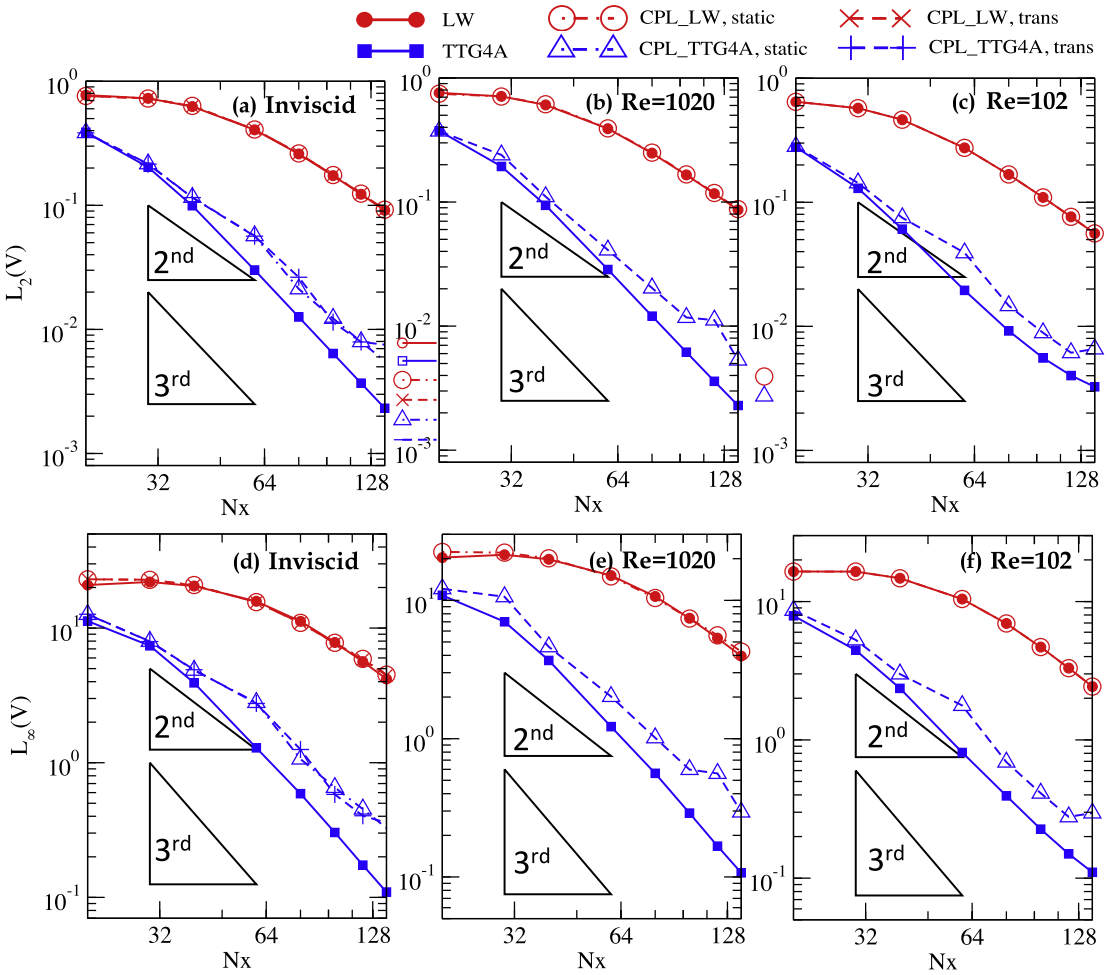

Fig. 13. Quadratic mean and maximum errors of instantaneous fields of transverse velocity $L_2(v)$ (a)–(c) and $L_\infty(v)$ (d)–(f) versus mesh resolution N_x for different cases using the LW or TTG4A schemes. The transverse profiles are compared with the analytic profiles when the vortex reaches the interface ($t = 0.5$) for three different Reynolds numbers: (a), (d) inviscid vortex; (b), (e) $Re = 1020$; (c), (f) $Re = 102$.

illustrated in Fig. 16 where the recorded lift and drag coefficients temporal evolutions are shown to fully agree whatever the CFD approach retained. At convergence, the lift and drag coefficients are $C_L = -13.41$ and $C_D = -0.03$ which is very closed to results obtained by Mittal and Kumar [86] for the same conditions, $C_L = -13.54$ and $C_D = -0.02$.

4. LES applications

As discussed in the introduction, the motivation for accurate and efficient coupling strategies is to provide a controlled numerical formalism allowing full LES in rotating machines. The latter should be able to account for all wave mechanisms in stages including wave generation and propagation. As evidenced in the previous sections, MISCOG implemented within OpenPalm provides an easy to implement extension for existing LES massively parallel solvers as the one developed at CERFACS for both translating and rotating interfaces. To illustrate the feasibility of LES in such a context, two applications are considered, one dealing with wave propagation in a linear cascade (translating interface), the other coping with wave interaction and generation in a realistic turbine stage (rotating interface).

4.1. LES of a rotor linear cascade for indirect noise predictions

The first application is the simulation of the propagation of acoustic and entropy waves in a linear rotor cascade shown in Fig. 17. This simpler set-up is preferred here as very long simulation times are required to statistically converge the reflected and transmitted waves at low frequencies of interest in combustion noise. The cascade geometry is taken from the mid-span profile of the MT1 rotor blade described in the next section [67,87]. The selected inlet and outlet relative Mach numbers are 0.653 and 0.366 respectively. The inlet and outlet flow angles are $-75.76°$ and $-60°$ respectively. The inlet and outlet total pressures are 18.464 and 14.239 bars respectively. A translating speed of 500 m/s is imposed to the rotor blade. The mean flow is subject to a modulated inflow or outflow condition with either acoustic or entropy plane waves in the stationary frame as detailed by Duran and Moreau [88]. As before, these pulsated waves are imposed using NSCBC boundary conditions. Periodic boundary conditions are used on the side edges of the computational domain.

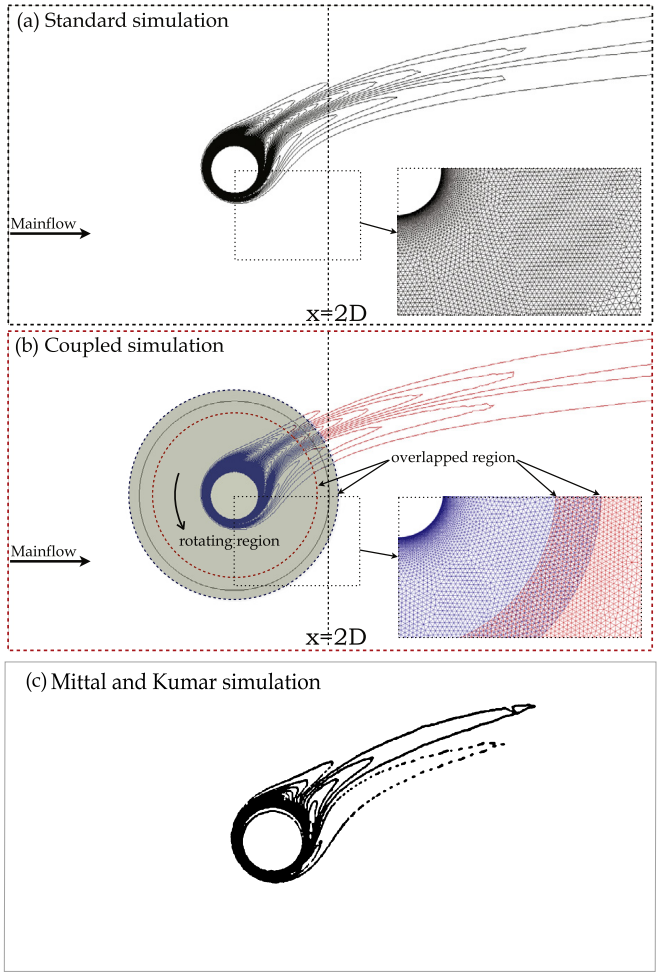

Fig. 14. Simulations of a $Re = 200$ flow past a rotating cylinder: iso-contours of vorticity are predicted by (a) single domain simulation (b) two domain coupled simulation and (c) Mittal and Kumar [86] simulation. The ratio of the rotating surface speed and free stream speed α is 3.5. The presented zoom near the cylinder $[-3.5D, 3.5D] \times [-5D, 9D]$ is extracted from the entire computational domain $[-50D, 50D] \times [50D, 200D]$.

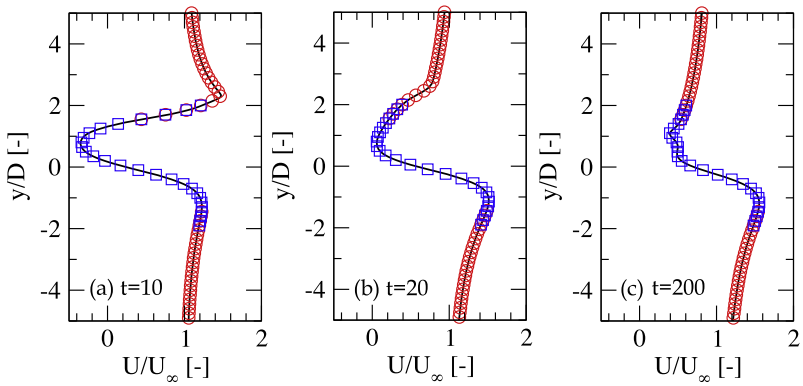

Fig. 15. Velocity profiles along a vertical line positioned at $x = 2D$ (shown in Fig. 14) at different instants $t = 10, 20$ and 200 of the simulations. Continuous lines denote the standard stand-alone simulation approach. Symbols refer to the coupled simulation results: static part (○) and rotating part (□).

Three different simulations are performed with AVBP using the TTG4A scheme. First a fixed mesh serves as a reference calculation as in the above test cases. A second method involves continuously deforming the mesh in the moving region around the blade. More details on the application of this Arbitrary Lagrangian–Eulerian (ALE) method can be found in Duran and Moreau [88]. Finally the MISCOG method is applied with translating interfaces. As shown in Fig. 17 an entropy wave or equivalently the temperature fluctuation is applied at the fixed inlet location. These waves are then traveling from left to right because of the mean inflow velocity field and create two acoustic waves (one reflected and the other transmitted) when going through the rotor blade passage. This is the source of indirect combustion noise in the first stage of an actual turbine [89,90]. Similar results have been obtained with acoustic waves imposed either at the inlet or the

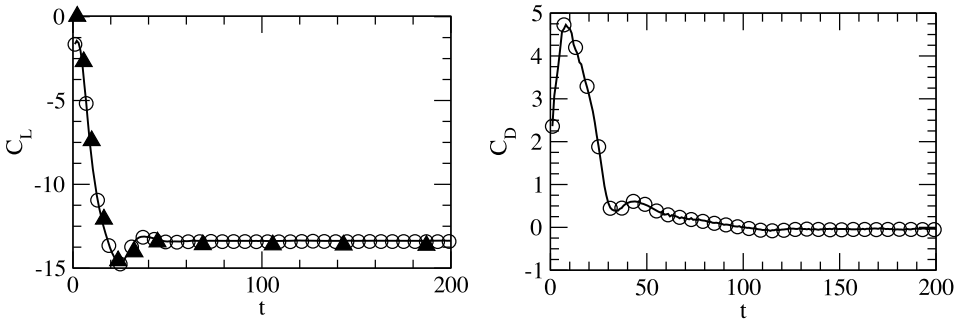

Fig. 16. Time histories of the lift (C_L) and the drag (C_D) coefficients for the two simulations: continuous lines denote the standard stand-alone simulation, open circles denote the coupled one and dark triangles refer to the numerical simulation of Mittal and Kumar [86].

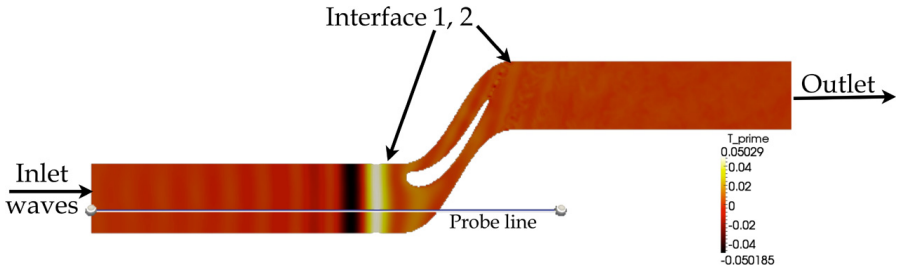

Fig. 17. Contours of instantaneous temperature fluctuations with an entropy wave train at the inlet of the MT1 rotor linear cascade.

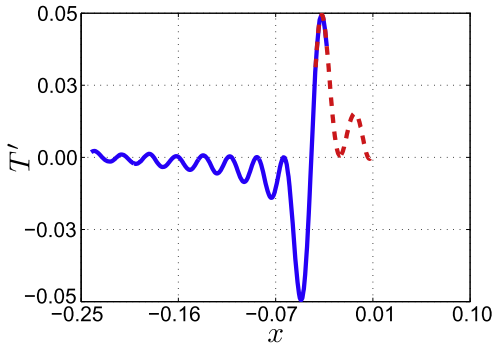

Fig. 18. Instantaneous profiles of temperature fluctuations along the line in Fig. 17 crossing the coupled interface, during the propagation of entropy wave. Solid and dashed lines denote two coupled domains with the interface respectively.

outlet of the cascade [88]. They mimic either direct combustion noise at low frequencies or noise created in the stages by wake interaction for instance. Once a steady state is reached for all simulations, the post-processing of the flow field shown in Fig. 17 is similarly performed in four steps. All the waves are first computed at each grid point as a function of time. Secondly, these waves are averaged in the transverse direction by integration. Thirdly, a Fourier transform of these transversally-averaged waves is performed for the discrete frequencies imposed at the inlet. Finally at the outlet some averaging along the propagation direction is performed to remove the random components from the rotor wakes. This procedure yields the final reflected and transmitted coefficients that can be compared to the analytical compact theory of Cumpsty and Marble [91].

As the overlapping method is not fully conservative by construction, the mass flow conservation has been first verified throughout the cascade in the third simulation. The mass flow rates are 365.04 kg/s and 365.07 kg/s in the static and rotating domains respectively, which yields an inconsistency of less than 0.08‰. The proper continuity of the flow properties with time is then checked in Fig. 18 by an instantaneous profile of temperature fluctuations taken along the line identified in Fig. 17. As indicated by the overlapped solid and dashed line, the profiles in the fixed and rotating domains are fully coincident. Both AVBP solvers compute the same information at the coupling interfaces, which in turn insures a correct transmission of the entropy waves through the interfaces. Finally the reflected and transmitted waves (due to an incident acoustic wave) are computed with the three different methods in Fig. 19. The MISCOG-based simulation yields very similar results as the reference case, much closer than the ALE simulation. Moreover and contrarily to the ALE method, no spurious spike is observed around 2250 Hz in agreement with the standalone predictions. At low frequencies, the simulation results fit well the theoretical value given by the compact theory which is strictly valid at zero frequency. Similar results have been obtained for the case where entropy waves are forced at the inlet [88]. Based on these initial results, the method has been

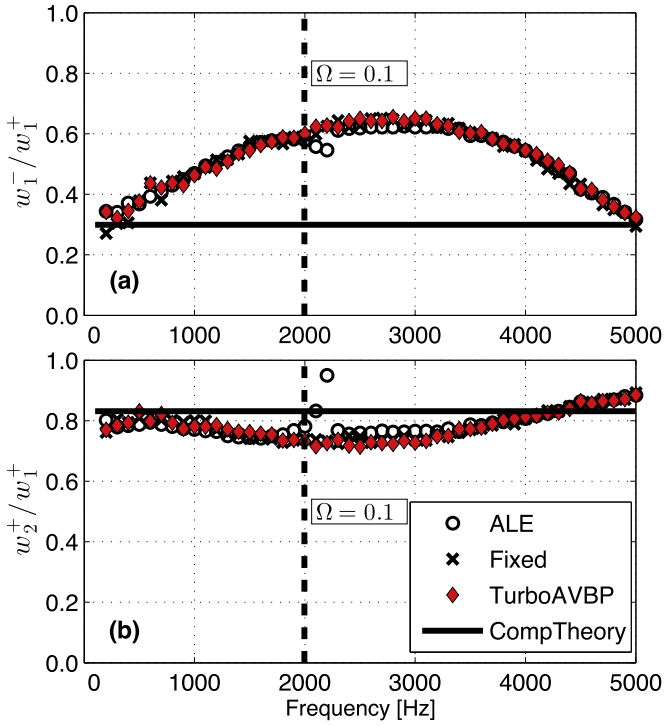

Fig. 19. Response of a rotor blade to an acoustic perturbation: (a) at the inlet and (b) the outlet. Compact theory (—), numerical simulation with stationary mesh (×), with ALE deforming mesh (○) and with MISCOG method (♦).

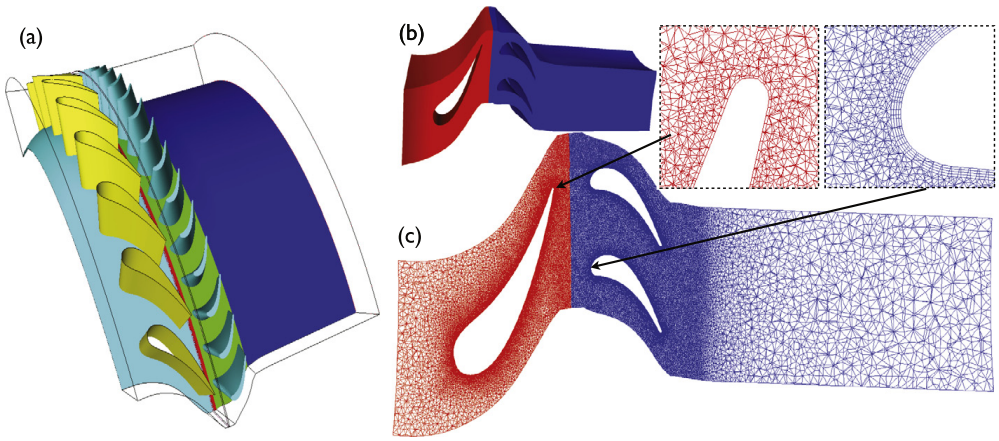

Fig. 20. The simulation configurations for the QinetiQ MT1 turbine: (a) the geometry of one quarter of turbine containing 8 stator vanes and 15 rotor blades; (b) the simulation domain of 12° with 1 scaled stator and 2 rotors; (c) the associated mesh.

recently extended to a complete turbine stage with the same good conservation properties at the stator–rotor interface, and the first numerical reflection and transmission coefficients for both acoustic and entropy waves [92].

4.2. 3D LES of a transonic turbine stage

The second application case involves the transonic MT1 turbine stage in the QinetiQ test facility [67,87] and rotating interfaces. A geometrically scaled configuration of 1 stator vane and 2 rotor blades (Fig. 20(b)) is actually computed. Indeed, to alleviate computational costs, the stator vane is geometrically scaled by a small factor of 32/30 to establish spatial periodicity in a 12° sector. The scaled blade count ratio is therefore 30 : 60, which maintains the initial solidity [93]. This scaling technique has been proposed and validated by Mayorca et al. [94] and has also recently been used for U-RANS simulations of the same configuration [93]. Such scaling techniques are commonly used in unsteady rotor–stator simulations using both RANS [93–96] or LES [14] approaches.

The computational domain consists of two overlapped meshes covering the stator and the rotor respectively. The unstructured hybrid meshes are generated using CENTAUR and include prismatic boundary layer cells around the vane and blade surfaces while using tetrahedral cells away from walls. Fig. 20(c) shows some details of the mesh for this 12° configuration. The height of the prismatic layer is chosen based on a normalized wall distance $y^+ = 50 \sim 90$ around the blades, with an

Table 2
Typical parameters used for the two configurations simulated by LES. Note that computational costs are here obtained for one full machine revolution (360°) of the turbine.

Periodicity	Stator + Rotor	No. cells	min y^+	Timestep	Iterations	CPU hours (BULL B510)
12°	1 + 2	5M + 8M	50	50 ns	126 K	4 K

Table 3
Setups for the current LES study and two RANS investigations, together with the experimental operating parameters.

Parameters (unit)	EXP	LES	RANS [98]	URANS [93]
Rotational speed (rpm)	$9500 \pm 1\%$	9500	9500	9500
Inlet: total pressure (bar)	$4.6 \pm 1\%$	4.5	4.6	4.615
Inlet: total temperature (K)	$444 \pm 1\%$	444	444	444.4
Outlet: static pressure (bar)	$1.428 \pm 1\%$	1.428	1.453	1.425
Pressure ratio	3.2	3.15	3.17	3.24
Blade: wall temperature (K)	–	288.5	288.5	–
Blade: min y^+	–	50	1–2	20
CFD solver	–	TurboAVBP	elsA	VolSol

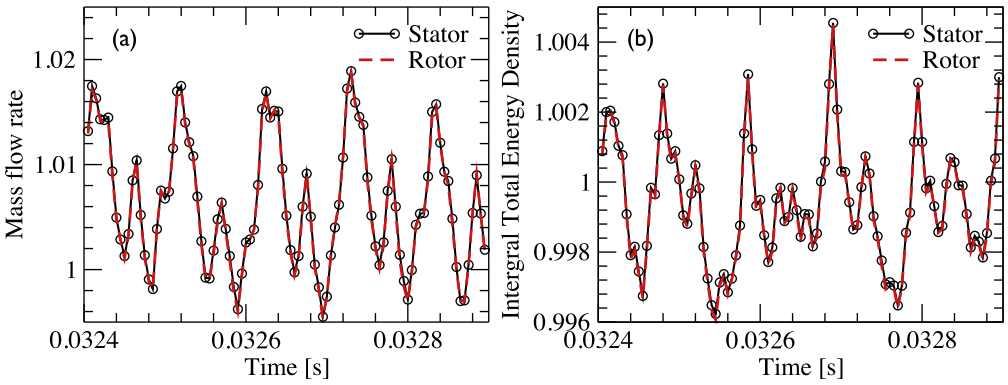

Fig. 21. The evolutions of integrated mass flow rate (ρu) and total energy (ρE) over the coupled middle planes on both stator and rotor sides.

aspect ratio $\Delta x^+ = \Delta z^+ = 4\Delta y^+$ and a wall-normal stretching ratio of 1.09. A classical logarithmic wall-law boundary condition is imposed on velocity to predict friction on solid walls since the current grid resolution is not adequate for a proper integration in the near-wall regions [97]. The resulting mesh then consists of 13 millions hybrid prismatic/tetrahedral cells (Table 2). The mesh size in the overlap region shown in Fig. 2 is 0.5 mm. Based on this setup, the characteristic frequency of the interpolation noise caused by the rotating domain is evaluated to be greater than 500 kHz and well above any expected flow unsteadiness or instability of such a problem.

A total pressure, total temperature and the velocity vector angles are prescribed at the inlet. A mean static pressure is targeted at the outlet of the flow passage. Both inlet and outlet NSCBC are again used to prevent waves reflections at these boundaries. The rotor mesh is rotated by a conventional moving grid method [78]; the rotor blades as well as the hub of this section are hence moving walls that follow the rotating motion. The two lateral surfaces delimiting the sector in the azimuthal direction are axi-periodic boundaries. Details of the boundary conditions are given in Table 3. Only LW is used here to limit the computational cost. It provides a reference simulation with an accuracy typically achieved in current turbomachinery applications. The LES solver being fully explicit in time, the time-step is controlled by the acoustic CFL number. According to the mesh refinement strategies for this configuration, the time step is fixed to $\Delta t = 0.5 \cdot 10^{-7}$ s, which results into 126,000 iterations for the simulation to fulfill one full revolution of the machine (Table 2). The resulting computational cost is about 4 K CPU hours, which is well within the range of todays HPC computational resources.

The first check has again been the conservative properties of the rotating interfaces. Fig. 21(a) shows the temporal evolution of the integrated mass flow rates through the middle plane of the coupled interface located in the stator and rotor meshes. Similarly, Fig. 21(b) provides the temporal evolution of the surface integral values of total energy ρE on these coupled interfaces. In both cases, the variations in the fixed and rotating grid interfaces are perfectly matching, indicating good mass and energy conservation of the coupled simulation. These quantities are evolving with time around their mean operating values stressing the unsteady nature of the flow and the strong stator–rotor interaction.

Two flow variables are considered to illustrate the flow topology obtained with the coupled strategy. On the one hand, Fig. 22 shows the instantaneous resolved Mach number at three different radii. These profiles on the rotor or stator sides fit well at the coupled interfaces, again stressing the reliability of the proposed approach. On the other hand, Fig. 23 shows the instantaneous subgrid-scale viscosity ν_t that is modeled by Eq. (3) with the Smagorinsky model [68] using the resolved scalars in the simulation at the same three spanwise locations. The profiles have a good overall match at the interface with some local discontinuities mainly in the wake region. This can be traced to the previous discontinuities observed on

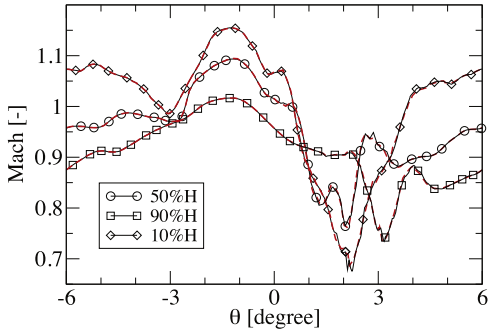

Fig. 22. Instantaneous profiles of Mach number at different span heights (10% H, 50% H and 90% H) in the coupled middle planes of stator (hard lines) and rotor (dashed lines).

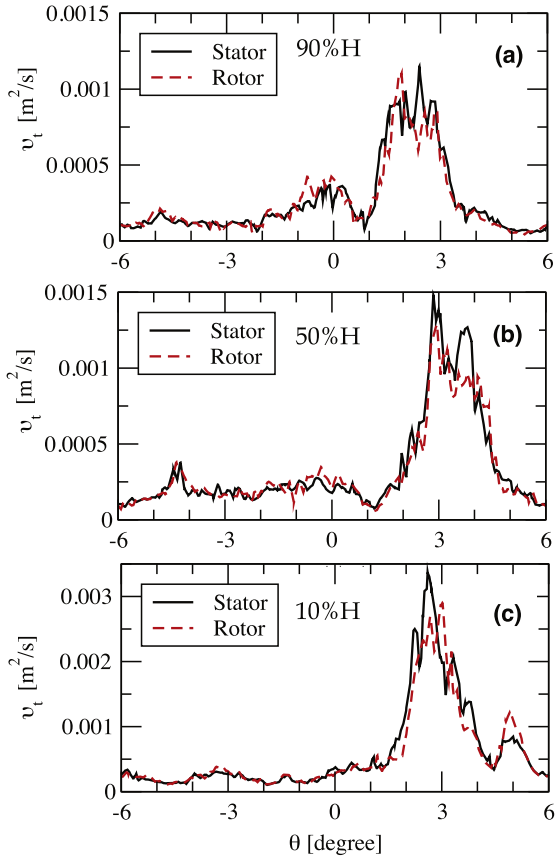

Fig. 23. Instantaneous profiles of turbulent viscosity ν_t at different spanwise heights (90% H, 50% H and 10% H) in the coupled middle plane of stator (hard lines) and rotor (dashed lines).

the derivatives of the flow variables present in the subgrid-scale modeling: the interface transfers the primitive variables correctly, but not exactly their derivatives. However, the differences remain acceptable with a maximum 20% variation on the turbulent viscosity. This error could be further reduced by either increasing the mesh resolution at the interface or by developing an interpolation including gradient information. Finally, Fig. 24 features an instantaneous field of vorticity magnitude in a radial plane located at mid span. Vortex shedding is generated at the blunt trailing edge of the stator where the boundary layers separate from the wall. The resulting von Kármán street is then convected downstream into the rotor passage through the interface without significant damping.

To assess the accuracy of the present LES, its predictions are compared with available experimental data and previous RANS/U-RANS results [93,98]. The wall-resolved RANS prediction uses a structured mesh with 2.6 M points ($y^+ \sim 1$–2) for one stator passage and one rotor passage using the elsA code [98]. The wall-modeled URANS results are obtained on a structured mesh with y^+ ranging from 20 to 200, based on the geometrically scaled setup of one stator passage and two rotor passages using the VolSol code [93]. All numerical setups are detailed in Table 3. LES data is obtained by simulating the flow over two full revolution times. Only part of the second revolution, out of the transient regime, is time-averaged to retrieve flow statistics, *i.e.* 50,000 iterations corresponding to a rotation of about 140°. Fig. 25 first shows the mean static pressure profiles at mid-span of the rotor blade. LES predictions are clearly better than RANS on the blade pressure side

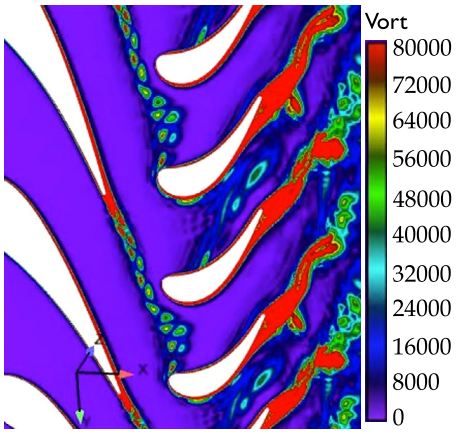

Fig. 24. Instantaneous vorticity magnitude field in the MT1 the rotor/stator stage.

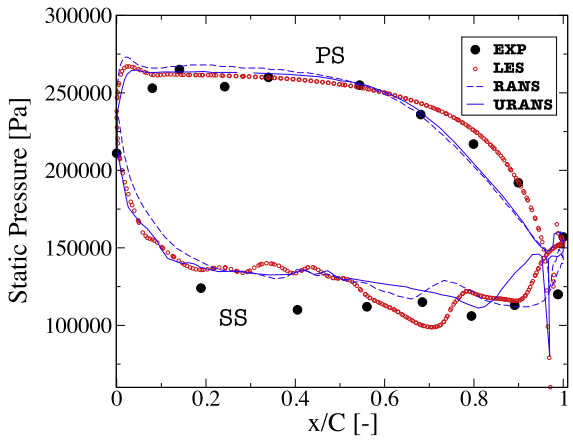

Fig. 25. Mean static pressure profiles at 50% span of the rotor blade: the LES predictions are compared with experimental data [67,87], RANS [98] and URANS [93] computations. **PS** and **SS** denote pressure and suction sides respectively.

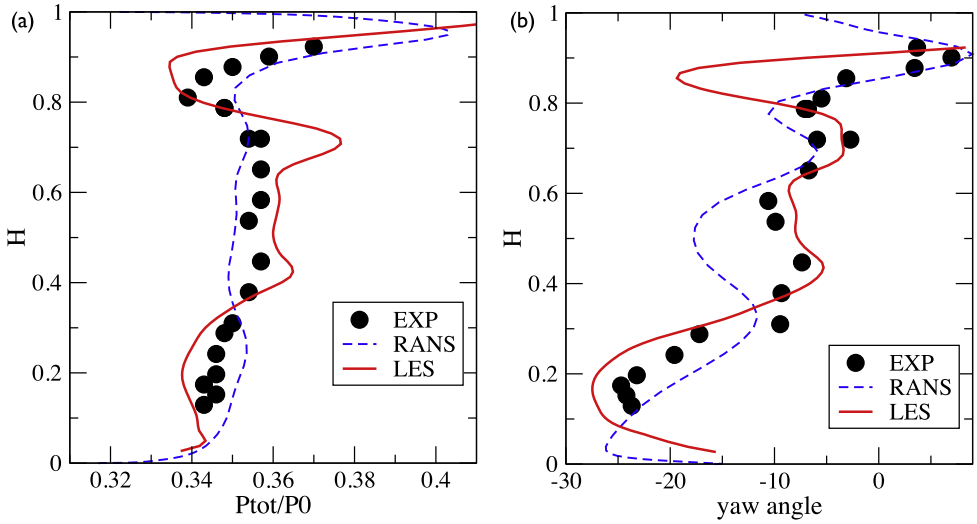

Fig. 26. Azimuthal mean profiles of total pressure (left) and yaw angle (right) near the rotor exit-plane. Total pressure is normalized by $P_0 = 4.6 \cdot 10^6$ Pa.

(denoted as **PS** in Fig. 25). On the suction side (denoted as **SS**), LES and RANS results have similar levels of discrepancy if compared with the experimental data. Some important flow structures may still not be well-captured in the LES predictions with the present mesh resolution on the suction side walls as evidenced by on-going simulations with finer grid resolution. Azimuthally-averaged profiles of total pressure and yaw angle are shown in Fig. 26 near the rotor-exit plane. All simulations are qualitatively in good agreement with experimental measurements. Yet the present LES better follows the radial variations of these flow parameters with closer values except beyond 90% span. Indeed, the fine RANS simulations are only doing better in the tip region where the current LES is clearly under-resolved with only 6∼7 layers of cells across the gap for an

effective height of 0.6 mm. The latter should be refined according to the recommendations of You et al. [7] for instance, to yield thinner tip vortex structures. Finally it should be stressed that the present LES allows capturing all the typical unsteady flow features that develop in a turbine stage as was shown by Wang et al. [15,29]: tip vortex, tip-separation vortex, tip-induced vortex, horse-shoe vortex, corner vortex, passage vortex and several shocks at the trailing edges of both the stator vane and the rotor blade.

5. Conclusions

LES is often recognized as a promising CFD tool that can improve our understanding while giving access to high quality fluid flow predictions in complex, high Reynolds industrial configurations. Improvement with such methods not only arises through the mean flow fields but also through the fully unsteady description of the large flow scales that evolve in such configurations. Limitations with LES essentially stem from its cost and the ability of the codes to efficiently use massively parallel super computers. In the context of turbomachinery, additional complexity is introduced which prevents full development and application of LES. Indeed, besides the wall physics that still needs to be improved by the LES modeling community, the numerical treatment of the moving interface between stationary and rotating components needs to be consistent with LES requirements.

Traditional LES numerical schemes are high order and centered to minimize artificial dissipation as well as dispersion of turbulent structures fundamental for proper LES predictions. Yet, they are hard to apply for such complex, confined, rotating internal flows. To address this specific difficulty, an in-house code (called TurboAVBP) has been successfully developed for LES of turbomachinery by coupling multi-copies of a massively parallel unstructured compressible LES solver AVBP with the parallel coupler OpenPALM. In the proposed strategy termed MISCOG, the rotor/stator interface is dealt with a coupling method based on the overset grid approach. Several numerical test cases with increasing degrees of complexity have been proposed to evaluate this solution for both translating and rotating interfaces. The coupling method is proven to handle acoustic and vortical wave propagation for both interfaces with an acceptable degree of accuracy for LES, provided that the overlapping region contains a sufficiently large number of points dependent on the selected numerical scheme. It almost recovers the dispersive and dissipative properties of the schemes in the stand-alone LES code. For the traveling vortex, the present implementation is currently limited close to the interface by the interpolation schemes but with a limited error for the high-order TTG4A scheme. It shows similar properties as the static cases except a high-frequency tone provided a proper sampling of the translation period is used. This tone is however weak (low level) and spatially localized close to the interface. Finally for the rotating cylinder, the wakes are properly convected without significant dissipation and distortion through the overlapping rotating interface.

Based on these satisfactory results, two turbomachinery cases have been run to illustrate the typical wave generation and propagation encountered in such machines and which cannot be captured by stationary RANS simulations. First the propagation of entropy and acoustic waves has been considered in a linear rotor cascade extracted from the QinetiQ MT1 high-pressure transonic experimental turbine. Excellent conservation properties and negligible wave distortion is found at the interface of the coupling cases. These yield similar results as the reference static cases. The reflection and transmission coefficients from this forced rotor-cascade problem, and more recently in a full cascade stage for both impinging acoustic and entropy waves (hot spots) are then correctly predicted. The novel approach is then applied to the full MT1 turbine to illustrate the potential of rotor/stator LES. Again good conservation properties of global properties and relevant physical parameters such as Mach numbers and vorticity are found at the overlapping interfaces along the whole blade span. Mean LES statistics prove to be in good agreement with experimental data. The LES predictions also appear to bring some improvement over the previous RANS or URANS results, except in the tip region where the current coarse grid resolution yields too large tip vortices. Moreover, the fully unsteady LES allows capturing many flow features otherwise difficult to anticipate. Of course computational costs are much larger than conventional steady RANS approaches but algorithmic improvements are possible to further take advantage of the ever increasing massively parallel computers. Such tools finally underline the need for high-order interpolation algorithms for unstructured meshes; more advanced wall models [99,100] as well as an increased mesh resolution should be tested for future turbomachinery simulations.

Acknowledgements

The authors would like to thank the foundation of Sciences et Technologies pour l'Aéronautique et l'Espace RTRA Project COEFFCI and EU FP7 COPA-GT Project for its financial support and special thanks for using the data of MT1 turbine stage achieved by European project TATEF2 team.

References

[1] J.U. Schluter, X. Wu, S. Kim, S. Shankaran, J.J. Alonso, H. Pitsch, A framework for coupling Reynolds-averaged with large eddy simulations for gas turbine applications, J. Fluids Eng. 127 (4) (2005) 608–615.
[2] S. Ghosal, P. Moin, The basic equations for the large eddy simulation of turbulent flows in complex geometry, J. Comput. Phys. 118 (1995) 24–37.
[3] M. Boileau, G. Staffelbach, B. Cuenot, T. Poinsot, C. Bérat, LES of an ignition sequence in a gas turbine engine, Combust. Flame 154 (1–2) (2008) 2–22.
[4] L. Gicquel, G. Staffelbach, T. Poinsot, Large eddy simulations of gaseous flames in gas turbine combustion chambers, Prog. Energy Combust. Sci. 38 (6) (2012) 782–817.

[5] B. Raverdy, I. Mary, P. Sagaut, High-resolution large-eddy simulation of flow around low-pressure turbine blade, AIAA J. 41 (3) (2003) 390–397.
[6] V. Michelassi, J.G. Wissink, J. Frohlich, W. Rodi, Large-eddy simulation of flow around low-pressure turbine blade with incoming wakes, AIAA J. 41 (11) (2003) 2143–2156.
[7] D. You, M. Wang, P. Moin, R. Mittal, Large-eddy simulation analysis of mechanisms for viscous losses in a turbomachinery tip-clearance flow, J. Fluid Mech. 586 (2007) 177–204.
[8] R. Bhaskaran, S.K. Lele, Large eddy simulation of free-stream turbulence effects on heat transfer to a high-pressure turbine cascade, J. Turbul. 11 (6) (2010) 1–15.
[9] T. Léonard, F. Duchaine, N. Gourdain, L.Y.M. Gicquel, Steady/unsteady Reynolds averaged Navier–Stokes and large eddy simulations of a turbine blade at high subsonic outlet Mach number, in: ASME Turbo Expo 2010, ASME, Glasgow, Scotland, GT2010-22469, June 14–18, 2010.
[10] E. Collado-Morata, N. Gourdain, F. Duchaine, L. Gicquel, Effects of free-stream turbulence on high pressure turbine blade heat transfer predicted by structured and unstructured LES, Int. J. Heat Mass Transf. 55 (21–22) (2012) 5754–5768.
[11] G. Medic, O. Sharma, Large eddy simulation of flow in a low-pressure turbine cascade, in: ASME Turbo Expo 2012, Copenhagen, Denmark, GT2012-68878, 11–15 June, 2012.
[12] F. Duchaine, N. Maheu, V. Moureau, G. Balarac, S. Moreau, Large eddy simulation and conjugate heat transfer around a low-Mach turbine blade, J. Turbomach. 136 (5) (2013) 051015, http://dx.doi.org/10.1115/1.4025165.
[13] V.N. Rao, P.G. Tucker, R.J. Jefferson-Loveday, J. Coull, Investigation of wake induced transition in low-pressure turbines using large eddy simulation, in: ASME Turbo Expo 2013, San Antonio, Texas, USA, GT2013-94418, June 3–7, 2013.
[14] W. McMullan, G. Page, Towards large eddy simulation of gas turbine compressors, in: Prog. in Astronautics and Aeronautics, vol. 52, 2012, pp. 30–47.
[15] G. Wang, S. Moreau, F. Duchaine, N. Gourdain, L. Gicquel, Large eddy simulations of the MT1 high-pressure turbine using TurboAVBP, in: Proceeding of 21st Annual Conference of the CFD Society of Canada, Sherbrooke, Quebec, Canada, May 6–9, 2013.
[16] J. de Laborderie, S. Moreau, A. Berry, Compressor stage broadband noise prediction using a large-eddy simulation and comparisons with a cascade response model, in: 19th AIAA/CEAS Aeroacoustics Conference, Berlin, Germany, AIAA-2013-2042, May 27–29, 2013.
[17] N. Gourdain, Validation of large-eddy simulation for the prediction of compressible flow in an axial compressor stage, in: ASME Turbo Expo 2013, San Antonio, Texas, USA, GT2013-94550, June 3–7, 2013.
[18] S. Pope, Turbulence Flows, Cambridge University Press, 2000.
[19] D.C. Wilcox, Turbulence Modeling for CFD, 3rd edn., DCW Industries, CA, USA, 2006.
[20] K. Menzies, Large eddy simulation applications in gas turbines, Philos. Trans. R. Soc. A, Math. Phys. Eng. Sci. 367 (1899) (2009) 2827–2838.
[21] L. Gicquel, N. Gourdain, J.-F. Boussuge, H. Deniau, G. Staffelbach, P. Wolf, T. Poinsot, High performance computing of flows in complex geometries, C. R., Méc. 339 (2–3) (2011) 104–124.
[22] P. Tucker, Computation of unsteady turbomachinery flows: Part 2 LES and hybrids, Prog. Aerosp. Sci. 47 (7) (2011) 546–569.
[23] T. Poinsot, D. Veynante, Theoretical and Numerical Combustion, 3rd edn., 2011, www.cerfacs.fr/elearning.
[24] P. Sagaut, Large Eddy Simulation for Incompressible Flows, Springer, 2002.
[25] V. Moureau, Design of a massively parallel CFD code for complex geometries, C. R., Méc. 339 (2011) 141–148.
[26] J.W. Nichols, S.K. Lele, F.E. Ham, J.E. Bridges, Prediction of supersonic jet noise using unstructured LES: effects of chevrons, Tech. rep., Center for Turbulence Research, Stanford University, 2013.
[27] AVBP, AVBP code, www.cerfacs.fr/cfd/avbp_code.php and www.cerfacs.fr/cfd/CFDPublications.html, 2013.
[28] P. Tucker, Computation of unsteady turbomachinery flows: Part 1 Progress and challenges, Prog. Aerosp. Sci. 47 (7) (2011) 522–545.
[29] G. Wang, D. Papadogiannis, F. Duchaine, N. Gourdain, L.Y.M. Gicquel, Towards massively parallel large eddy simulation of turbine stages, in: ASME Turbo Expo 2013, San Antonio, Texas, USA, GT2013-94852, June 3–7, 2013.
[30] O. Colin, M. Rudgyard, Development of high-order Taylor–Galerkin schemes for LES, J. Comput. Phys. 162 (2) (2000) 338–371.
[31] E.A. Volkov, The method of composite meshes for finite and infinite regions with piecewise smooth boundaries, Proc. Steklov Inst. Math. 96 (1968) 145–185.
[32] R. Magnus, H. Yoshihara, Inviscid transonic flow over airfoils, AIAA J. 8 (12) (1970) 2157–2162.
[33] G. Starius, Composite mesh difference methods for elliptic and boundary value problems, Numer. Math. 28 (1977) 243–258.
[34] E.H. Atta, J. Vadyak, A grid overlapping scheme for flowfield computations about multicomponent configurations, AIAA J. 21 (1983) 1271–1277.
[35] J. Steger, F. Dougherty, J. Beneck, A Chimera grid scheme, in: Advances in Grid Generation, in: ASME FED, vol. 5, 1983, pp. 59–69.
[36] J. Benek, J. Steger, F. Dougherty, A flexible grid embedding technique with application to the Euler equations, AIAA Paper 83-1944, 1983.
[37] M.J. Berger, On conservation at grid interfaces, SIAM J. Appl. Math. 24 (1987) 967–984.
[38] W.D. Henshaw, G.S. Chesshire, Multigrid on composite meshes, SIAM J. Sci. Stat. Comput. 8 (6) (1987) 914–923.
[39] G.S. Chesshire, W.D. Henshaw, Composite overlapping meshes for the solution of partial differential equations, J. Comput. Phys. 90 (1) (1990) 1–64.
[40] T. Emmert, P. Lafon, C. Bailly, Numerical study of self-induced transonic flow oscillations behind a sudden duct enlargement, Phys. Fluids 21 (2009), 15 pp.
[41] D.J. Bodony, G. Zagaris, A. Reichert, Q. Zhang, Provably stable overset grid methods for computational aeroacoustics, J. Sound Vib. 330 (17) (2011) 4161–4179.
[42] X.X. Chen, X. Zhang, High-order interface for aeroacoustic computation using overset grid, AIAA J. 51 (2013) 519–523.
[43] G. Desquesnes, M. Terracol, E. Manoha, P. Sagaut, On the use of a high order overlapping grid method for coupling in CFD/CAA, J. Comput. Phys. 220 (1) (2006) 355–382.
[44] W. Henshaw, K.A. Chand, A composite grid solver for conjugate heat transfer in fluid-structure systems, J. Comput. Phys. 228 (10) (2009) 3708–3741.
[45] P. Fast, M.J. Shelley, A moving overset grid method for interface dynamics applied to non-Newtonian Hele–Shaw flow, J. Comput. Phys. 195 (2004) 117–142.
[46] R.H. Nichols, R.W. Tramel, P.G. Buning, Solver and turbulence model upgrades to OVERFLOW 2 for unsteady and high-speed applications, in: 25th Applied Aerodynamics Conference, AIAA, San Francisco, California, AIAA-2006-2824, June 5–8, 2006.
[47] D.W.S. William, D. Henshaw, Moving overlapping grids with adaptive mesh refinement for high-speed reactive and non-reactive flow, J. Comput. Phys. 216 (2) (2006) 744–779.
[48] R.W. Noack, D.A. Boger, Improvements to SUGGAR and DiRTlib for OversetStore separation simulations, in: 47th AIAA Aerospace Sciences Meeting, Orlando, FL, USA, AIAA Paper 2009-340, Jan. 5–9, 2009.
[49] V.K. Lakshminarayan, J.D. Baeder, Computational investigation of microscale shrouded rotor aerodynamics in hover, J. Am. Helicopter Soc. 56 (2011) 042002.
[50] G. Billonnet, L. Castillon, J. Riou, G. Leroy, A. Paillassa, A technological effect modeling on complex turbomachinery applications with an overset grid numerical method, in: ASME Turbo Expo 2013, San Antonio, Texas, USA, GT2013-94181, June 3–7, 2013.
[51] T.K. Sengupta, V. Suman, N. Singh, Solving Navier–Stokes equation for flow past cylinders using single-block structured and overset grids, J. Comput. Phys. 229 (1) (2010) 178–199.
[52] S.E. Sherer, J.N. Scott, High-order compact finite-difference methods on general overset grids, J. Comput. Phys. 210 (2) (2005) 459–496.
[53] B. Francois, M. Costes, G. Dufour, Comparison of chimera and sliding mesh techniques for unsteady simulations of counter rotating open-rotors, in: 20th International Society for Airbreathing Engines Conference, Gothenburg, Sweden, ISABE-2011-1231, September 12–16, 2011.

[54] M.M. Rai, Navier–Stokes simulations of rotor/stator interaction using patched and overlaid grids, J. Propuls. Power 3 (5) (1987) 387–396.
[55] G. Browning, A comparison of three numerical methods for solving differential equations on the sphere, Mon. Weather Rev. 117 (1989) 1058–1075.
[56] W.D. Henshaw, A fourth-order accurate method for the incompressible Navier–Stokes equations on overlapping grids, J. Comput. Phys. 113 (1) (1994) 13–25.
[57] W.D. Henshaw, A high-order accurate parallel solver for Maxwell's equations on overlapping grids, SIAM J. Sci. Comput. 28 (5) (2006) 1730–1765.
[58] F. Daude, J. Berland, T. Emmert, P. Lafon, F. Crouzet, C. Bailly, A high-order finite-difference algorithm for direct computation of aerodynamic sound, Comput. Fluids 61 (2012) 46–63.
[59] J. Gao, A block interface flux reconstruction method for numerical simulation with high order finite difference scheme, J. Comput. Phys. 241 (15) (2013) 1–17.
[60] K. Nakahashi, F. Togashi, D. Sharov, Intergrid-boundary definition method for overset unstructured grid approach, AIAA J. 38 (2000) 2077–2084.
[61] H. Luo, D. Sharov, J.D. Baum, R. Lohner, An overlapping unstructured grid method for viscous flows, in: 15th AIAA Computational Fluid Dynamics Conference, Anaheim, CA, USA, AIAA Paper 2001-2603, June 11–14, 2001.
[62] R.W. Noack, Resolution appropriate overset grid assembly for structured and unstructured grids, in: 16th AIAA Computational Fluid Dynamics Conference, Orlando, Florida, USA, AIAA Paper 2003-4123, June 23–26, 2003.
[63] F. Togashi, Y. Ito, K. Nakahashi, S. Obayashi, Overset unstructured grids method for viscous flow computations, AIAA J. 44 (2006) 1617–1623.
[64] R. Shenoy, M.J. Smith, M.A. Park, Unstructured overset mesh adaptation with turbulence modeling for unsteady aerodynamic interactions, J. Aircr. 51 (2014) 161–174.
[65] S. Hahn, G. Iaccarino, S. Ananthan, J.D. Baeder, Extension of CHIMPS for unstructured overset simulation and higher-order interpolation, in: Annual Research Briefs 2009, Stanford University, 2009, No. 299-311.
[66] A. Toselli, O. Widluhd, Domain Decomposition Methods – Algorithms and Theory, Springer Series in Computational Mathematics, vol. 34, 2004.
[67] L. Hilgenfeld, M. Pfitzner, Unsteady boundary layer development due to wake passing effects on a highly loaded linear compressor cascade, J. Turbomach. 126 (2004) 493–500.
[68] J. Smagorinsky, General circulation experiments with the primitive equations: 1. The basic experiment, Mon. Weather Rev. 91 (1963) 99–164.
[69] T. Schonfeld, M. Rudgyardt, Steady and unsteady flow simulations using the hybrid flow solver AVBP, AIAA J. 37 (1999) 1378–1385.
[70] P.D. Lax, B. Wendroff, Difference schemes for hyperbolic equations with high order of accuracy, Commun. Pure Appl. Math. 17 (1964) 381–398.
[71] V. Selmin, Third order finite element schemes for the solution of hyperbolic problems, Tech. rep., INRIA, 1987.
[72] J. Donea, Taylor–Galerkin method for convective transport problems, Int. J. Numer. Methods Fluids 20 (1) (1984) 101–119.
[73] N. Lamarque, Schémas numériques et conditions limites pour la simulation aux grandes échelles de la combustion diphasique dans les foyers d'hélicoptère, PhD thesis, INP, Toulouse, 2007.
[74] F. Lekien, J. Marsden, Tricubic interpolation in three dimensions, Int. J. Numer. Methods Eng. 63 (3) (2005) 455–471.
[75] A. Piacentini, T. Morel, A. Thevenin, F. Duchaine, O-PALM an open source dynamic parallel coupler, in: Coupled Problems 2011 – IV International Conference on Computational Methods for Coupled Problems in Science and Engineering, Kos Island, Greece, 20–22 June, 2011.
[76] CNGS-Steering-Committee, The CFD general notation system standard interface data structures, Tech. rep., http://cgns.org, 2007.
[77] A. Ern, J.-L. Guermond, Theory and Practice of Finite Elements, Springer, 2003.
[78] V. Moureau, G. Lartigue, Y. Sommerer, C. Angelberger, O. Colin, T. Poinsot, Numerical methods for unsteady compressible multi-component reacting flows on fixed and moving grids, J. Comput. Phys. 202 (2) (2005) 710–736.
[79] E. Collado-Morata, Aerothermal environment effects on the temperature of a high pressure turbine blade, Ph.D. thesis, INP, Toulouse, 2013.
[80] A. Kaufmann, F. Nicoud, T. Poinsot, Flow forcing techniques for numerical simulation of combustion instabilities, Combust. Flame 131 (4) (2002) 371–385.
[81] T. Poinsot, S. Lele, Boundary conditions for direct simulations of compressible viscous flows, J. Comput. Phys. 101 (1) (1992) 104–129.
[82] M.R. Visbal, D.V. Gaitonde, High-order-accurate methods for complex unsteady subsonic flows, AIAA J. 37 (10) (1999) 1231–1239.
[83] J.U. Schluter, H. Pitsch, Antialiasing filters for coupled Reynolds-averaged/large-eddy simulations, AIAA J. 43 (3) (2005) 608–615.
[84] T. Colonius, S. Lele, P. Moin, The free compressible vortex, J. Fluid Mech. 230 (1991) 45–73.
[85] F. Nicoud, Etude de faisabilité d'une Simulation Numérique Directe d'un écoulement avec forte injection pariétale, Tech. rep. TR/CFD/94/10, CERFACS, 1994.
[86] S. Mittal, B. Kumar, Flow past a rotating cylinder, J. Fluid Mech. 476 (2003) 303–334.
[87] I. Qureshi, T. Povey, A.D. Smith, K.S. Chana, Effect of temperature nonuniformity on heat transfer in an unshrouded transonic HP turbine – an experimental and computational investigation, J. Turbomach. 134 (1) (2014).
[88] I. Duran, S. Moreau, Study of the attenuation of waves propagating through fixed and rotating turbine blades, in: 18th AIAA/CEAS Aeroacoustics Conference, Colorado, USA, AIAA 2012-2133, 2012.
[89] F.E. Marble, S. Candel, Acoustic disturbances from gas nonuniformities convected through a nozzle, J. Sound Vib. 55 (2) (1977) 225–243.
[90] N. Cumpsty, F. Marble, Core noise from gas turbine exhausts, J. Sound Vib. 54 (2) (1977) 297–309.
[91] N. Cumpsty, F. Marble, The interaction of entropy fluctuations with turbine blade rows: a mechanism of turbojet engine noise, Proc. R. Soc. Lond. 357 (1690) (1977) 323–344.
[92] I. Duran, S. Moreau, Numerical simulation of acoustic and entropy waves propagating through turbine blades, in: 19th AIAA/CEAS Aeroacoustics Conference, Berlin, Germany, AIAA 2013-2102, May 27–29, 2013.
[93] S.M. Hosseini, F. Fruth, D.M. Vogt, T.H. Fransson, Effect of scaling of blade row sectors on the prediction of aerodynamic forcing in a highly-loaded transonic turbine stage, in: ASME Turbo Expo 2011, Vancouver, Canada, GT2011-45813, June 6–10, 2011.
[94] M.A. Mayorca, J.A.D. Andrade, D.M. Vogt, H. Martensson, T.H. Fransson, Effect of scaling of blade row sectors on the prediction of aerodynamic forcing in a highly-loaded transonic compressor stage, in: ASME Turbo Expo 2009, Orlando, USA, GT2009-59601, June 8–12, 2009.
[95] J.P. Clark, G.M. Stetson, S.S. Magge, R.H. Ni, C.W. Haldeman, M.G. Dunn, The effect of airfoil scaling on the predicted unsteady loading on the blade of a 1 and 1/2 stage transonic turbine and a comparison with experimental results, in: ASME Turbo Expo 2000, Munich, Germany, 2000-GT-0446, May 8–11, 2000.
[96] M.M. Rai, Multi-airfoil Navier–Stokes simulations of turbine rotor–stator interaction, J. Turbomach. 112 (1990) 377–396.
[97] P. Schmitt, T. Poinsot, B. Schuermans, K.P. Geigle, Large-eddy simulation and experimental study of heat transfer, nitric oxide emissions and combustion instability in a swirled turbulent high-pressure burner, J. Fluid Mech. 570 (2007) 17–46.
[98] T.L. Pichon, Modélisation aérodynamique et aérothermique externe des aubages de turbines axiales avec le code elsA, Tech. rep., TurboMeca, 2008.
[99] S. Bocquet, P. Sagaut, J. Jouhaud, A compressible wall model for large-eddy simulation with application to prediction of aerothermal quantities, Phys. Fluids 24 (2014) 065103.
[100] N. Maheu, V. Moureau, P. Domingo, F. Duchaine, G. Balarac, Large-eddy simulations of flow and heat transfer around a low-Mach number turbine blade, in: Proceeding of the Summer Program Center for Turbulence Research, NASA AMES – Stanford University, USA, 2012.

Bibliography

[1] E. Motheau, L. Selle, T. Poinsot, and F. Nicoud. A mixed acoustic-entropy combustion instability in a realistic gas turbine. In *Proc. of the Summer Program* , 2012. IX, 3, 7, 93

[2] P. F. Beard, A. D. Smith, and T. Povey. Experimental and computational fluid dynamics investigation of the efficiency of an unshrouded transonic high pressure turbine. *J. of Power and Energy*, 225:1166–1179, 2011. IX, XI, 4, 22, 49, 50, 58, 99

[3] C. M. Cha, S. Hong, P. T. Ireland, P. Denman, and V. Savarianandam. Experimental and numerical investigation of combustor-turbine interaction using an isothermal, nonreacting tracer. *J. Eng. Gas Turb. and Power* , 134(8):081501, 2012. IX, 6

[4] I. Qureshi, A. Smith, and T. Povey. HP vane aerodynamics and heat transfer in the presence of aggressive inlet swirl. *J. Turbomach.* , 135(2):021040, 2012. IX, 6, 57, 128

[5] F. Wlassow. *Analyse instationnaire aérothermique d'un etage de turbine avec transport de points chauds; application a la maitrise des performances des aubages.* PhD thesis, Ecole Centrale Lyon, 2010. IX, 16, 21, 69, 130, 136, 139

[6] U. Piomelli and E. Balaras. Wall-layer models for large eddy simulations. *Ann. Rev. Fluid Mech.* , 34:349–374, 2002. IX, 16, 17, 18

[7] H. Choi and P. Moin. Grid-point requirements for large eddy simulation: Chapman's estimates revisited. *Phys. Fluids* , 24(1):011702, 2012. IX, 18, 19

[8] J. Tyacke and P. G. Tucker. Future use of large eddy simulation in aeroengines. In *Proc. of the ASME Turbo Expo 2014*, number GT2014-25434, 2014. XI, 51

[9] R. E. Mayle. The role of laminar-turbulent transition in gas turbine engines. *J. Turbomach.* , 113:509–537, 1991. XI, 50, 54, 85, 128

[10] O. P. Sharma and T. L. Butler. Predictions of endwall losses and secondary flows in axial flow turbine cascades. *J. Turbomach.* , 109(2):229–236, 1987. XI, 53, 55, 56

[11] H. P. Wang, S. J. Olson, R. J. Goldstein, and E. R. G. Eckert. Flow visualization in a linear turbine cascade of high performance turbine blades. *J. Turbomach.* , 119:1–8, 1997. XI, 55, 56

[12] J. P. Bindon. The measurement and formation of tip clearance loss. *J. Turbomach.* , 111:257–263, 1989. XI, 57

[13] D. You, M. Wang, P. Moin, and R. Mittal. Large-eddy simulation analysis of mechanisms for viscous losses in a turbomachery tip-clearance flow. *J. Fluid Mech.* , 586:177–204, 2007. XI, XII, 51, 57, 68, 69

[14] P. G. Tucker. Computation of unsteady turbomachinery flows: Part 2-LES and hybrids. *Prog. Aerospace Sci.* , 47:546–569, 2011. XII, 8, 50, 51, 52, 63, 85

[15] T. Povey, K. S. Chana, T. V. Jones, and J. Hurrion. The effect of hot-streaks on hp vane surface and endwall heat transfer: An experimental and numerical study. *J. Turbomach.* , 129:32–43, 2007. XII, XIV, 5, 68, 127

[16] A. McCarter, X. Xiao, and B. Lakshminarayana. Tip clearance effects in a turbine rotor: Part ii-velocity field and flow physics. *J. Turbomach.* , 123:305–313, 2001. XII, 57, 68, 69

[17] *The Jet Engine - 6th Edition*. Rolls Royce Publications, 2005. XIII, 93

[18] M. Leyko. *Mise en oeuvre et analyse de calculs aéroacoustiques de type SGE pour la prévision du bruit de chambres de combustion aéronautiques*. PhD thesis, Institut National Polytechnique de Toulouse, 2010. XIII, 7, 93, 94, 95, 112, 113

[19] M. G. Turner, A. Norris, and J. P. Veres. High-fidelity three-dimensional simulation of the ge90. In *16th Computational Fluid Dynamics Conference*, number AIAA-2003-3996, 2003. XIV, 122, 123

[20] G. Medic, G. Kalitzin, D. You, M. Herrmann, F. Ham, E. van der Weide, H. Pitsch, and J. Alonso. Integrated RANS/LES computations of turbulent flow through a turbofan jet engine. In *Annual Research Briefs* , pages 275–285. 2006. XIV, 123, 124

[21] G. Medic, G. Kalitzin, D. You, E. van der Weide, H. Pitsch, and J.J. Alonso. Integrated rans/les computations of an entire gas turbine jet engine. In *45th AIAA Aerospace Sciences Meeting and Exhibit*, number AIAA-2007-1117, Reno, USA, January 2007. XIV, 123, 124

[22] T. Povey and I. Qureshi. Developments in hot-streak simulators for turbine testing. *J. Turbomach.* , 131(3):1–15, 2006. XIV, 125

[23] E. Collado-Morata, N. Gourdain, F. Duchaine, and L. Y. M Gicquel. Structured vs unstructured LES for the prediction of free-stream turbulence effects on the heat transfer of a high pressure turbine profile. *Int. J. Heat and Mass Transfer* , 55(21-222):5754–5768, 2012. XIV, 6, 17, 31, 34, 40, 50, 51, 85, 128, 129

[24] C. Angelberger, D. Veynante, F. Egolfopoulos, and T. Poinsot. Large eddy simulations of combustion instabilities in premixed flames. In *Proc. of the Summer Program*, pages 61–82, 1998. XV, 169

[25] T. Poinsot and D. Veynante. *Theoretical and Numerical Combustion*. Third Edition (www.cerfacs.fr/elearning), 2011. XV, 7, 101, 143, 144, 162, 163, 164, 169

[26] L. He, V. Menshikova, and B. R. Haller. Effect of hot-streak counts on a turbine blade heat load and forcing. *J. Prop. Power* , 23(6):1235–1241, 2007. 5, 127, 139

[27] D. Dorney and K. Gundy-Barlet. Hot-streak clocking effects in a 1-1/2 stage turbine. *J. Prop. Power* , 12(3):619–620, 1996. 5

[28] R. J. Roback and R. P. Dring. Hot streaks and phantom cooling in a turbine rotor passage: Part 1 - separate effects. *J. Turbomach.* , 115:657–666, 1993. 5, 127

[29] D. Dorney and K.L. Gundy-Burlet. Effects of hot streak shape on rotor heating in a high-subsonic single-stage turbine. Technical report, NASA, 1999. 5, 127

[30] D. Prassad and G. J. Hendricks. A numerical study of secondary flow in axial turbines with application to radial transport of hot streaks. *J. Turbomach.* , 122:667–673, 2000. 5, 55, 128

[31] T. Arts and M. Lambert de Rouvroit. Aero-thermal performance of a two-dimensional highly loaded transonic turbine nozzle guide vane: A test case for inviscid and viscous flow computations. *J. Turbomach.* , 114(1):147–154, 1992. 6, 128

[32] S. C. Jenkins and D. G. Bogard. The effects of the vane and mainstream turbulence level on hot streak attenuation. *J. Turbomach.* , 127:215–221, 2005. 6, 50, 128

[33] I. Qureshi, A. Beretta, K. S. Chana, and T. Povey. Effect of aggresive inlet swirl on heat transfer and aerodynamic in an unshrouded transonic hp turbin. In *Proc. of the ASME Turbo Expo 2011*, number GT2011-46038, 2011. 6, 58, 128

[34] I. Duran and S. Moreau. Solution of the quasi one-dimensional linearized euler equations using flow invariants and the magnus expansion. *J. Fluid Mech.* , 723:190–231, 2013. 7, 93, 94, 117

[35] E. Motheau, F. Nicoud, and T. Poinsot. Mixed acoustic-entropy combustion instabilities in gas turbines. *J. Fluid Mech.* , 749(542–576), 2014. 7, 93

[36] M. S. Howe. Indirect combustion noise. *J. Fluid Mech.* , 659:267–288, 2010. 7, 94

[37] F. E. Marble and S. Candel. Acoustic disturbances from gas nonuniformities convected through a nozzle. *J. Sound Vib.* , 55:225–243, 1977. 7, 93

[38] N. A. Cumpsty and F. E. Marble. The interaction of entropy fluctuations with turbine blade rows; a mechanism of turbojet engine noise. *Proc. R. Soc. Lond. A* , 357:323–344, 1977. 7, 94, 99, 117, 119

[39] V. L. Doyle and R. K. Matta. Attenuation of upstream-generated low frequency noise by gas turbines. Technical Report CR-135219, NASA, 1977. 7, 94

[40] F. Bake, C. Richter, B. Muhlbauer, N. Kings, I.Rohle, F.Thiele, and B.Noll. The Entropy Wave Generator (EWG): a reference case on entropy noise. *J. Sound Vib.* , 326(5):574–598, 2009. 7, 93

[41] M. Leyko, S. Moreau, F. Nicoud, and T. Poinsot. Numerical and analytical modelling of entropy noise in a supersonic nozzle with a shock. *J. Sound Vib.* , 330(16):3944–3958, 2011. 7

[42] I. Duran, S. Moreau, and T. Poinsot. Analytical and numerical study of direct and indirect combustion noise through a subsonic nozzle. *AIAA Journal* , 51:42–52, 2013. 7, 93

[43] Top 500 supercomputer sites. 8, 51

[44] J. Tyacke, P. G. Tucker, R. Jefferson-Loveday, N. Vadlamani, R. Watson, I. Naqavi, and X. Yang. Large eddy simulation for turbines: Methodologies, cost and future outlooks. *J. Turbomach.* , 136(061009), 2014. 8, 51

[45] N. Gourdain. High-performance computing of gas turbine flows: current and fiture trends - habilitation á diriger des recherches, November 2011. 8, 22

[46] L. Y. M. Gicquel, G. Staffelbach, and T. Poinsot. Large eddy simulations of gaseous flames in gas turbine combustion chambers. *Prog. Energy Comb. Sci.* , 38(6):782–817, 2012. 8

[47] S. B. Pope. *Turbulent flows*. Cambridge University Press, 2000. 15, 16, 17, 50, 87

[48] A. Kolmogorov. The local structure of turbulence in incompressible viscous fluid for very large reynolds numbers. *Proc. R. Soc. Lond. A* , 434:9–13, 1991. 15

[49] H. Kawamura, K. Ohsaka, H. Abe, and K. Yamamoto. DNS of turbulent heat transfer in channel flow with low to medium-high prandtl number fluid. *Int. J. Heat Fluid Flow* , 19(5):482–491, 1998. 16

[50] X. Wu and P. A. Durbin. Evidence of longitudinal vortices evolved from distorted wakes in a turbine passage. *J. Fluid Mech.* , 446:199–228, 2001. 16, 51

[51] J. G. Wissink. DNS of separating, low reynolds number flow in a turbine cascade with incoming wakes. *Int. J. Heat Fluid Flow* , 24(4):626–635, 2003. 16

[52] B. Vreman, B. Geurts, and H. Kuerten. Subgrid-modelling in les of compressible flow. *Applied scientific research*, 54(3):191–203, 1995. 17

[53] G. Kalitzin, G. Medic, G. Iaccarino, and P. A. Durbin. Near-wall behavior of RANS turbulence models and implications for wall functions. *J. Comput. Phys.* , 204(1):265–291, 2005. 18

[54] D. R. Chapman. Computational aerodynamics development and outlook. *AIAA Journal* , 17(12):1293–1313, 1979. 18, 164

[55] S. Kawai and J. Larsson. Wall-modeling in large eddy simulation: Length scales, grid resolution, and accuracy. *Phys. Fluids* , 24(1):015105, 2012. 18

[56] N. Georgiadis, D. Rizzata, and C. Fureby. Large-eddy simulation: current capabilities, recommended practices, and future research. *AIAA Journal* , 48(8):1772–1784, 2010. 18, 60

[57] F. Nicoud and F. Ducros. Subgrid-scale modelling based on the square of the velocity gradient tensor. *Flow, Turb. and Combustion* , 62:183–200, 1999. 18, 64, 165

[58] G. I. Park and P. Moin. An improved dynamic non-equilibrium wall-model for large eddy simulation. *Phys. Fluids* , 26(1):015108, 2014. 19

[59] S. Bocquet, P. Sagaut, and J. C. Jouhaud. A compressible wall model for large eddy simulation with application to prediction of aerothermal quantities. *Phys. Fluids* , 24(065-103), 2012. 19, 64, 71

[60] M. Mayorca, J. De Andrade, D. Vogt, H. Martensson, and T. Fransson. Effect of scaling of a blade row sectors on the prediction of aerodynamic forcing in a highly-loaded transonic turbine stage. *J. Turbomach.* , 133(2), 2010. 20, 22, 23, 129

[61] D. Van Zante, J. Chen, M. Hathaway, and R. Chriss. The influence of compressor blade row interaction modeling on performance estimates from time-accurate, multistage, navier–stokes simulations. *J. Turbomach.* , 130(1):011009, 2008. 20

[62] J. D. Denton and Singh. Time marching methods for turbomachinery flow calculation. *VKI Lecture Series*, 1, 1979. 20

[63] W. N. Dawes. Toward improved throughflow capability: The use of three-dimensional viscous flow solvers in a multistage environment. *J. Turbomach.* , 114(1):8–17, 1992. 20

[64] S. R. Ray and M. Zangeneh. A robust mixing plane and its application in three-dimensional inverse design of transonic turbine stages. *J. Turbomach.* , 137(1):011004, 2014. 20

[65] E. van der Weide, G. Kalitzin, J. Schluter, G. Medic, and J. J. Alonso. On large scale turbo machinery computations. In *Annual Research Briefs* , pages 139–150. 2005. 20, 22, 62

[66] J. I. Erdos, E. Alzner, and W. McNally. Numerical solution of a periodic transonic flow through a fan stage. *AIAA Journal* , 15(11):1559–1568, 1977. 21, 156

[67] L. He. An euler solution for unsteady flows around oscillating blades. *J. Turbomach.* , 112(4):714–722, 1990. 22

[68] L. Castillon. Evaluation of a multiple frequency phase lagged method for unsteady numerical simulations of multistage turbomachinery. In *Proc. of the 28th ICAS*, 2012. 22

[69] M. Burnazzi. Assessment of advanced time integration approaches for contra-rotationg open rotor simulations. Master's thesis, Politecnico di Milano, 2010. 22

[70] S. Salvadori, F. Montomoli, F. Martelli, P. Adami, K. S. Chana, and L. Castillon. Aerothermal study of the unsteady flow field in a transonic gas turbine with inlet temperature distortions. *J. Turbomach.* , 133(031030), 2011. 22

[71] N. Gourdain, S. Burguburu, F. Leboeuf, and G. Michon. Simulation of rotating stall in a whole stage of an axial compressor. *Comput. Fluids* , 39(9):1644–1655, 2010. 22

[72] N. Gourdain. Validation of large-eddy simulation for the prediction of compressible flow in an axial compressible stage. In *Proc. of the ASME Turbo Expo 2013*, number GT2013-94550, 2013. 22, 23, 52

[73] S. M. Hosseini, F. Fruth, D. M. Vogt, and T. H. Fransson. Effect of scaling of a blade row sectors on the prediction of aerodynamic forcing in a highly-loaded transonic turbine stage. In *Proc. of the ASME Turbo Expo 2011*, number GT2011-45813, 2011. 23, 59

[74] F. Fruth, D. Vogt, and T. Fransson. Influence of the blade count ratio on aerodynamic forcing: Part II-high pressure transonic turbine. In *Proc. of the ASME Turbo Expo 2011*, number GT2011-46071, pages 1343–1354, 2011. 23

[75] W. A. McMullan and G. J. Page. Towards large eddy simulation of gas turbine compressors. *Prog. Aerospace Sci.* , 52:30–47, 2012. 23, 52

[76] T. Schoenfeld and M. Rudgyard. Steady and unsteady flow simulations using the hybrid flow solver avbp. *AIAA Journal* , 37:1378–1385, 1999. 25, 27

[77] G. Wang, F. Duchaine, D. Papadogiannis, I. Duran, S. Moreau, and L. Y. M. Gicquel. An overset grid method for large eddy simulation of turbomachinery stages. *J. Comput. Phys.* , 274:333–355, 2014. 25, 31

[78] E. A. Volkov. The method of composite meshes for finite and infinite regions with piecewise smooth boundaries. *Proc. Steklov Inst. Math.*, 96:145–185, 1968. 25

[79] R. Magnus and H. Yoshihara. Inviscid transonic flow over airfoils. *AIAA Journal* , 8(12):2157–2162, 1970. 25

[80] G. Starius. Composite mesh difference methods for elliptic and boundary value problems. *Numer. Math.*, 28:243–258, 1977. 25

[81] H. A. Essam and J. Vadyak. A grid overlapping scheme for flowfield computations about multicomponent configurations. *AIAA Journal* , 21:1271–1277, 1983. 25

[82] J. L. Steger, F. C. Dougherty, and J. A. Beneck. A chimera grid scheme. *Advances in Grid Generation, ASME FED*, 5:59–69, 1983. 25

[83] J. A. Benek, J. L. Steger, and F. C. Dougherty. A flexible grid embedding technique with application to the Euler equations. *AIAA Paper 83-1944*, 1983. 25

[84] M. J. Berger. On conservation at grid interfaces. *SIAM J. Appl. Math.* , 24:967–984, 1987. 25

[85] W. D. Henshaw and G. S. Chesshire. Multigrid on composite meshes. *SIAM J. Sci. Stat. Comput.* , 8(6):914–923, 1987. 25

[86] G. S. Chesshire and W. D. Henshaw. Composite overlapping meshes for the solution of partial differential equations. *J. Comput. Phys.* , 90(1):1–64, 1990. 25

[87] T. Emmert, P. Lafon, and C. Bailly. Numerical study of self-induced transonic flow oscillations behind a sudden duct enlargement. *Phys. Fluids* , 21:106105, 2009. 25, 26

[88] D. Bodony, G. Zagaris, A. Reichert, and Q. Zhang. Provably stable overset grid methods for computational aeroacoustics. *J. Sound Vib.* , 330(17):4161 – 4179, 2011. 25, 26, 30

[89] X. X. Chen and X. Zhang. High-order interface for aeroacoustic computation using overset grid. *AIAA Journal* , 51:519–523, 2013. 25

[90] G. Desquesnes, M. Terracol, E. Manoha, and P. Sagaut. On the use of a high order overlapping grid method for coupling in CFD/CAA. *J. Comput. Phys.* , 220(1):355–382, 2006. 25, 26, 30

[91] W. D. Henshaw and K. K. Chand. A composite grid solver for conjugate heat transfer in fluid-structure systems. *J. Comput. Phys.* , 228(10):3708–3741, 2009. 25

[92] P. Fast and M. J. Shelley. A moving overset grid method for interface dynamics applied to non-newtonian hele-shaw flow. *J. Comput. Phys.* , 195:117–142, 2004. 25

[93] R. H. Nichols, R. W. Tramel, and P. G. Buning. Solver and turbulence model upgrades to overflow 2 for unsteady and high-speed applications. In *25th Applied Aerodynamics Conference*, pages AIAA–2006–2824, 2006. 25

[94] D. W. Schwendeman W. D. Henshaw. Moving overlapping grids with adaptive mesh refinement for high-speed reactive and non-reactive flow. *J. Comput. Phys.* , 216(2):744–779, 2006. 25

[95] R. W. Noack and D. A. Boger. Improvements to SUGGAR and DiRTlib for oversetstore separation simulations. In *47th AIAA Aerospace Sciences Meeting*, pages AIAA Paper 2009–340, 2009. 25

[96] V.K. Lakshminarayan and J.D. Baeder. Computational investigation of microscale shrouded rotor aerodynamics in hover. *J. American Helicopter Society*, 56, 2011. 25

[97] T. K. Sengupta, V. K. Suman, and N. Singh. Solving Navier-Stokes equation for flow past cylinders using single-block structured and overset grids. *J. Comput. Phys.* , 229(1):178 – 199, 2010. 25, 26, 30

[98] S. E. Sherer and J. N. Scott. High-order compact finite-difference methods on general overset grids. *J. Comput. Phys.* , 210(2):459 – 496, 2005. 25, 26, 30

[99] R. Bhaskaran and S. K. Lele. Heat transfer prediction in high pressure turbine cascade with free-stream turbulence using les. In *Proc. of the 41st AIAA Fluid Dunamics Conference and Exhibit*, number AIAA2011-3266, 2011. 25, 26, 51, 54, 128

[100] G. Billonnet, L. l. Castillon, J. Riou, G. Leroy, and A. Paillassa. A technological effect modeling on complex turbomachinery applications with an overset grid numerical method. In *Proc. of the ASME Turbo Expo 2013*, pages GT2013–94181, June 3-7, 2013. 25

[101] B. Francois, M. Costes, and G. Dufour. Comparison of chimera and sliding mesh techniques for unsteady simulations of counter rotating open-rotors. In *20th International Society for Airbreathing Engines Conference*, number ISABE-2011-1231, 2011. 25

[102] M. Rai. Navier-Stokes simulations of rotor/stator interaction using patched and overlaid grids. *J. Prop. Power* , 3(5):387–396, 1987. 26, 29

[103] G. Browning. A comparison of three numerical methods for solving differential equations on the sphere. *Mon. Weather Rev.* , 117:1058–1075, 1989. 26

[104] W. D. Henshaw. A fourth-order accurate method for the incompressible Navier-Stokes equations on overlapping grids. *J. Comput. Phys.* , 113(1):13–25, July 1994. 26

[105] W. D. Henshaw. A high-order accurate parallel solver for Maxwell's equations on overlapping grids. *SIAM Journal of Scientific Computing*, 28(5):1730–1765, 2006. 26

[106] F. Daude, J. Berland, T. Emmert, P. Lafon, F. Crouzet, and C. Bailly. A high-order finite-difference algorithm for direct computation of aerodynamic sound. *Comput. Fluids* , 61:46–63, 2012. 26, 30

[107] J. Gao. A block interface flux reconstruction method for numerical simulation with high order finite difference scheme. *J. Comput. Phys.* , 241(15):1–17, 2013. 26

[108] A. Toselli and O. Widluhd. *Domain Decomposition Methods - Algorithms and Theory*, volume 34. Springer Series in Computational Mathematics, 2004. 26, 27

[109] J. Donea. Taylor-galerkin method for convective transport problems. *Int. J. Numer. Meth. Fluids* , 20(1):101–119, 1984. 27, 34

[110] N. Lamarque. *Schémas numériques et conditions limites pour la simulation aux grandes échelles de la combustion diphasique dans les foyers d'hélicoptère.* Phd thesis, INP Toulouse, 2007. 27, 36

[111] P. D. Lax and B. Wendroff. Difference schemes for hyperbolic equations with high order of accuracy. *Communications on pure and applied mathematics*, 17:381–398, 1964. 27, 62, 133, 144

[112] V. Selmin. Third order finite element schemes for the solution of hyperbolic problems. Technical report, INRIA, 1987. 27

[113] F. Lekien and J. Marsden. Tricubic interpolation in three dimensions. *Int. J. Numer. Meth. Eng.* , 63(3):455–471, 2005. 30

[114] A. Piacentini, T. Morel, A. Thevenin, and F. Duchaine. O-PALM an open source dynamic parallel coupler. In *Coupled Problems 2011 - IV International Conference on Computational Methods for Coupled Problems in Science and Engineering*, Kos Island, Greece, 20-22 June, 2011. 30

[115] CNGS-Steering-Committee. The cfd general notation system standard interface data structures. Technical report, http://cgns.org, 2007. 30

[116] V. Moureau, G. Lartigue, Y. Sommerer, C. Angelberger, O. Colin, and T. Poinsot. Numerical methods for unsteady compressible multi-component reacting flows on fixed and moving grids. *J. Comput. Phys.* , 202(2):710 – 736, 2005. 31

[117] A. Kaufmann, F. Nicoud, and T. Poinsot. Flow forcing techniques for numerical simulation of combustion instabilities. *Combust. Flame* , 131(4):371–385, 2002. 32

[118] T. Poinsot and S. K. Lele. Boundary conditions for direct simulations of compressible viscous flows. *J. Comput. Phys.* , 101:104–129, 1992. 33, 34, 43, 60, 101

[119] O. Colin and M. Rudgyard. Development of high-order taylor-galerkin schemes for unsteady calculations. *J. Comput. Phys.* , 162(2):338–371, 2000. 34, 100

[120] M. R. Visbal and D. V. Gaitonde. High-order-accurate methods for complex unsteady subsonic flows. *AIAA Journal* , 37(10):1231–1239, 1999. 34

[121] J. Schlüter and H. Pitsch. Anti-aliasing filters for coupled reynolds-averaged/large-eddy simulations. *AIAA Journal* , 43(3):608–616, 2005. 40

[122] R. H. Kraichnan. Diffusion by a random velocity field. *Phys. Fluids* , 13(1):22–31, 1970. 43

[123] T. Passot and A. Pouquet. Numerical simulation of compressible homogeneous flows in the turbulent regime. *J. Fluid Mech.* , 181:441–466, 1987. 43

[124] N. Guézennec and T. Poinsot. Acoustically nonreflecting and reflecting boundary conditions for vortcity injection in compressible solvers. *AIAA Journal* , 47(7):1709–1722, 2009. 43

[125] J. M. Tournier. Turbulence et lois de parois. Master's thesis, Institut National Polytechnique de Toulouse, 1993. 44

[126] H. Boughanem. *Evaluation des termes de transport et de dissipation de surface de flamme par simulation numerique directe de la combustion turbulente*. PhD thesis, Institut Francais du Petrol, 1998. 45

[127] D. Papadogiannis, G. Wang, S. Moreau, F. Duchaine, F. Sicot, and L.Y.M Gicquel. Large eddy simulation of a high-pressure turbine stage: Effects of sub-grid scale modeling and mesh resolution. In *Proc. of the ASME Turbo Expo 2014*, number GT2014-25876, 2014. 49

[128] K. Menzies. Large eddy simulation applications in gas turbines. *Phil. Trans. R. Soc. A* , 367:2827–2838, 2009. 50

[129] V. Michelassi, J. G. Wissink, J. Froehlich, and W. Rodi. Large eddy simulation of flow around low-pressure turbine blade with incoming wakes. *AIAA Journal* , 41(11):2143–2156, 2003. 50

[130] V. Michelassi, J. Wissink, and W. Rodi. Analysis of DNS and LES of flow in a low pressure turbine cascade with incoming wakes and comparison with experiments. *Flow, Turb. and Combustion* , 69(3-4):295–329, 2002. 50

[131] B. Raverdy, I. Mary, P. Sagaut, and N. Liamis. High-resolution large-eddy simulation of flow around low-pressure turbine blade. *AIAA Journal* , 41(3):390–397, 2004. 50

[132] C. Hah. Large eddy simulation of transonic flow field in NASA rotor 37. In *47th AIAA Aerospace Sciences Meeting*, Orlando, USA, 2009. 51

[133] A. Gomar, N. Gourdain, and G. Dufour. High fidelity simulation of the turbulent flow in a transonic axial compressor. In *European Turbomachinery Conference*, Istanbul, 2011. 51

[134] J. Joo, G. Medic, D. A. Philips, and S. T. Bose. Large-eddy simulation of a compressor rotor. In *Proc. of the Summer Program* , 2014. 51

[135] S. Lardeau, M. Leschziner, and T. Zaki. Large eddy simulation of transitional separated flow over a flat plate and a compressor blade. *Flow, Turb. and Combustion* , 88:19–44, 2012. 51

[136] J. G. Wissink, T. Zaki, W. Rodi, and P. A. Durbin. The effect of wake turbulence intensity on transition in a compressor cascade. *Flow, Turb. and Combustion* , pages 1–22, 2014. 51

[137] T. Jimbo, D. Biswas, and Y. Niizeki. Studies on unsteady flow characteristics in a high pressure turbine cascade based on a high-order large eddy simulation turbulence model. *J. Turbomach.* , 134(5):051018, 2012. 51

[138] F. Duchaine, A. Copron, L. Pons, V. Moureau, F. Nicoud, and T. Poinsot. Development and assessment of a coupled strategy for conjugate heat transfer with Large Eddy Simulation. application to a cooled turbine blade. *Int. J. Heat Fluid Flow* , 30(6):1129–1141, 2009. 51

[139] F. Duchaine, N. Maheu, V. Moureau, G. Balarac, and S. Moreau. Large-eddy simulation and conjugate heat transfer around a low-mach turbine blade. *J. Turbomach.* , 136(5), 2013. 51

[140] D. You, R. Mittal, M. Wang, and P. Moin. Computational methododology for large eddy simulation of tip-clearance flows. *AIAA Journal* , 42(2):271–279, 2004. 51, 57, 80

[141] P. Lampart. Investigation of endwall flows and losses in axial turbines. part 1: Formation of endwall flows and losses. *J. of Theoretical and Applied Mechanics*, 47(2):321–342, 2009. 51, 55

[142] A. Cahuzac, J. Boudet, M. C. Jacob, and P. Kausche. Large-eddy simulation of a rotor tip-clearance flow. In *17th AIAA/CEAS Aeroacoustics Conference*, 2011. 52

[143] N. Gourdain, F. Sicot, F. Duchaine, and L. Y. M. Gicquel. Large eddy simulation of flows in industrial compressors: a path from 2015 to 2035. *Phil. Trans. R. Soc. A* , 372, 2014. 52

[144] M. Tyagi and S. Acharya. Large eddy simulations of complex turbulent flows using immersed boundary method. In *Proc. of the Third AFOSR International Conference on DNS/LES*, number ADP013659, 2001. 52

[145] M. Rai. A direct numerical simulation of stator-rotor interaction in an axial compressor. (AIAA-2010-6533):25–28, 2010. 52

[146] M. Rai. A direct numerical simulation of flow through a low pressure turbine stage. pages AIAA–2011–3092, 2011. 52

[147] J. de Laborderie, S. Moreau, and A. Berry. Compressor stage broadband noise prediction using a large-eddy simulation and comparisons with a cascade response model. In *19th AIAA/CEAS Aeroacoustics Conference*, pages AIAA–2013–2042, 2013. 52

[148] N. Gourdain. Prediction of the unsteady turbulent flow in an axial compressor stage. part 1: comparison of unsteady rans and les with experiments. *Comput. Fluids* , 106(119-129), 2014. 52, 66, 82

[149] N. Gourdain. Prediction of the unsteady turbulent flow in an axial compressor stage. part 2: analysis of unsteady rans and les data. *Comput. Fluids* , 106:67–78, 2014. 52, 82

[150] J. H. Horlock and J. D. Denton. A review of some early design practice using computational fluid dynamics and a current perspective. *J. Turbomach.* , 127:5–13, 2005. 52

[151] B. Lakshminarayana. *Fluid Dynamics and Heat Transfer of Turbomachinery*. John Wiley & Sons, Ltd., 1996. 52

[152] K. D. Papailiou, K. M. Mathioudakis, and K. X. Giannakoglou. *Introduction to Thermal Turbomachinery*. 2000. 53

[153] J. D. Denton. Loss mechanisms in turbomachines. *J. Turbomach.* , 115:621–656, 1993. 53, 54, 57

[154] T. Cebeci and A. M. Smith. Cs method for turbulent boundary layers. *Analysis of Turbulent Boundary Layers*, 1974. 54

[155] C. Sieverding. Recent progress in the understanding of basic aspects of secondary flows in turbine blade passages. *J. Turbomach.* , 107:248–257, 1985. 55

[156] L. S. Langston. Secondary flows in axial turbines - a review. *Annals of the New York Academy of Sciences*, 934:11–26, 2001. 55

[157] P. Marchal and C. Sieverding. Secondary flows within turbomachinery bladings. In *Proc. of AGARD-CP-24 Secondary Flows in Turbomachines*, 1977. 55

[158] B. Lakshminarayana and J. H. Horlock. Generalised expressions for secondary vorticity using intrinsic co-ordinates. *J. Fluid Mech.* , 59:97–115, 1973. 55

[159] M. D. Barringer, K. A. Thole, and M. D. Polanka. An experimental study of combustor exit profile shapes on endwall heat transfer in high pressure turbine vanes. *J. Turbomach.* , 131, 2009. 55

[160] W. F. Colban, A. T. Lethander, and K. A. Thole. Combustor turbine interface studies - part 2: flow and thermal field measurements. *J. Turbomach.* , 125(2), 2003. 55, 128, 148

[161] J. W. Bae, K. S. Breuer, and C. S. Tan. Active control of tip clearance flow in axial compressors. *J. Turbomach.* , 127:353–362, 2005. 57

[162] F. J. Heyes, H. P. Hodson, and G. M. Dailey. The effect of blade tip geometry on the tip leakage flow in axial turbine cascades. *J. Turbomach.* , 114(3), 1992. 57

[163] B. Lakshminarayana, M. Zaccaria, and B. Marathe. The structure of tip clearance flow in axial flow compressors. *J. Turbomach.* , 117:336–347, 1995. 57

[164] M. A. Hilditch, A. Fowler, T. V. Jones, K. S. Chana, M. L. Oldfield, R. W. Ainsworth, S. I. Hogg, S. J. Anderson, and G. C. Smith. Installation of a turbine stage in the pyestock isentropic light piston facolity. In *Proc. of the ASME Turbo Expo 1994*, number ASME-94-GT-277, 1994. 58

[165] H. Schlichting and K. Gersten. *Boundary-layer theory*. Springer, 2000. 60

[166] P. G. Tucker, S. Eastwood, C. Klostermeier, R. Jefferson-Loveday, J. Tyacke, and Y. Liu. Hybrid les approach for practical turbomachinery flows:part 1-hierarchy and example simulations. In *Proc. of the ASME Turbo Expo 2010*, number GT2010-23431, 2010. 63

[167] D. R. Chapman and G. D. Kuhn. The limiting behaviour of turbulence near a wall. *J. Fluid Mech.* , 170:265–292, 1986. 63, 166

[168] F. Nicoud, H. Baya-Toda, O. Cabrit, S. Bose, and J. Lee. Using singular values to build a subgrid-scale model for large eddy simulations. *Phys. Fluids* , 23(8), 2011. 63, 64, 166

[169] E. R. Van Driest. On turbulent flow near a wall. *J. Aeronaut. Sci.* , 23:1007–1011, 1956. 64, 88

[170] E. Leveque, F. Toschi, L. Shao, and J-P. Bertoglio. Shear-improved smagorinsky model for large-eddy simulation of wall-bounded turbulent flows. *J. Fluid Mech.* , 570:491–502, 2007. 64, 88

[171] J. Smagorinsky. General circulation experiments with the primitive equations, i. the basic experiment. *Mon. Weather Rev.*, 91:99–164, 1963. 64, 163, 165

[172] S. Kawai and J. Larsson. Wall-modeling in large eddy simulation: Length scales, grid resolution, and accuracy. *Phys. Fluids* , 24(1):015105, 2012. 64, 84

[173] G. Haller. An objective definition of a vortex. *J. Fluid Mech.* , 525:1–26, 2005. 67

[174] A. Hussain and W. C. Reynolds. The mechanics of an organized wave in turbulent shear flow. *J. Fluid Mech.* , 41(2):241–258, 1970. 75

[175] R Dénos, T Arts, G Paniagua, V Michelassi, and F Martelli. Investigation of the unsteady rotor aerodynamics in a transonic turbine stage. *J. Turbomach.* , 123(1):81–89, 2001. 82

[176] J. Bodart and J. Larsson. Sensor-based computation of transitional flows using wall-modeled large eddy simulation. *Annual Research Briefs* , pages 229–240, 2012. 83, 84

[177] D. Papadogiannis, G. Wang, S. Moreau, F. Duchaine, L.Y.M Gicquel, and F. Nicoud. Assessment of the indirect combustion noise generated across a high-pressure turbine. In *Proc. of the Summer Program* , 2014. 92

[178] D. Papadogiannis, G. Wang, S. Moreau, F. Duchaine, L.Y.M Gicquel, and F. Nicoud. Assessment of the indirect combustion noise generated across a high-pressure turbine. In *Proc. of the ASME Turbo Expo 2015 - accepted also in Journal of Turbomachinery*, number GT2015-42399, 2015. 92

[179] European Parliament. Proposal for a regulation of the european parliament and of the council on the establishment of rules and procedures with regard to the introduction of noise-related operating restrictions at union airports within a balanced approach. 92

[180] M. J. Lighthill. On sound generated aerodynamically. i. general theory. *Proc. R. Soc. Lond. A* , 211(1107):564–587, 1952. 92

[181] W. C. Strahle. On combustion generated noise. *J. Fluid Mech.* , 49(2):399–414, 1971. 92

[182] R. Rajaram and T. Lieuwen. Parametric studies of acoustic radiation from premixed flames. *Combust. Sci. Tech.* , 175(12):2269–2298, 2003. 92

[183] Silva C., Leyko M., Nicoud F., and Moreau S. Assessment of combustion noise in a premixed swirled combustor via Large-Eddy Simulation. *Comput. Fluids* , 78:1–9, 2013. jx. 92

[184] *Modern Methods in Analytical Acoustics*. Springer Verlag, 1996. 92

[185] A. Mishra and D. Bodony. Evaluation of actuator disk theory for predicting indirect combustion noise. *J. Sound Vib.* , 332:821–838, 2012. 94, 104

[186] M. Leyko, I. Duran, S. Moreau, F. Nicoud, and T. Poinsot. Simulation and modelling of the waves transmission and generation in a stator blade row in a combustion-noise framework. *J. Sound Vib.* , 333(23):6090–6106, 2014. 94

[187] I. Duran and S. Moreau. Study of the attenuation of waves propagating through fixed and rotating turbine blades. In *18th AIAA/CEAS Aeroacoustics Conference*, pages AIAA2012–2133, 2012. 94

[188] P. Schmid. Dynamic mode decomposition of numerical and experimental data. *J. Fluid Mech.* , 656:5–28, 2010. 95, 113, 172

[189] I. Duran. *Prediction of combustion noise in modern aero-engines combining Large Eddy SImulations and analytical methods*. PhD thesis, Institut National Polytechnique de Toulouse, 2013. 99, 104, 112, 117

[190] L. Selle, F. Nicoud, and T. Poinsot. The actual impedance of non-reflecting boundary conditions: implications for the computation of resonators. *AIAA Journal* , 42(5):958–964, 2004. 103

[191] V. Granet, O. Vermorel, T. Leonard, L. Y. M. Gicquel, and T. Poinsot. Comparison of nonreflecting outlet boundary conditions for compressible solvers on unstructured grids. *AIAA Journal* , 48(10):2348–2364, 2010. 103

[192] M. Sanjose and A. Fosso-Pouangue. Total pressure, total temperature nscbc. Technical report, Université de Sherbrooke, 2013. 103

[193] G. Bennett and J. Fitzpatrick. Noise source identification for ducted fan systems. *AIAA Journal* , 46(7):1663–1674, 2008. 112

[194] P. Schmid. Dynamic mode decomposition. In *VKI Lecture Series*. 2013. 113

[195] M. R. Jovanovic, P. Schmid, and J. Nichols. Sparsity-promoting dynamic mode decomposition. *Phys. Fluids* , 26(2):024103, 2014. 116

[196] J. Kopitz, E. Bröcker, and W. Polifke. Characteristics-based filter for identification of planar acoustic waves in numerical simulation of turbulent compressible flow. In *Proc. of the 12th ICSV*, 2005. 118

[197] E. J. Hall, S. R. Lynn, N. J. Heidegger, and R. A. Delaney. Preview of the national combustion codes. In *33rd AIAA/ASME/SAE/ASEE Joint Propulsion Conference and Exhibit*, number AIAA-98-3119, Seattle, USA, July 1997. 122

[198] W. P. Jones and B. E. Launder. The prediction of laminarization with a two-equation model of turbulence. *Int. J. Heat and Mass Transfer* , 15:301–314, 1972. 122

[199] M. G. Turner, R. Ryder, A. Norris, M. Celestina, J. Moder, N.S. Liu, J. Adamczyk, and J. Veres. High-fidelity three-dimensional turbofan engine simulation with emphasis on turbomachinery-combustor coupling. In *38th AIAA/ASME/SAE/ASEE Joint Propulsion Conference and Exhibit*, number AIAA-2002-37696, Indianapolis, USA, July 2002. 122

[200] M. G. Turner. Full 3D analysis of the GE90 turbofan primary flowpath. Technical Report CR-2000-209951, NASA, 2000. 122

[201] M. G. Turner, R. Ryder, A. Norris, M. Celestina, J. Moder, N.S. Liu, J. Adamczyk, and J. Veres. Lessons learned from the ge90 3d full engine simulations. In *48th AIAA Aerospace Sciences Meeting including the New Horizons Forum and Aerospace exposition*, number AIAA-2010-1606, Orlando, USA, July 2010. 123

[202] G. Boudier, L.Y.M Gicquel, T. Poinsot, D. Bissieres, and C. Berat. Comparison of les, rans and experiments in an aeronautical gas turbine combustion chamber. *Proc. Combust. Inst.* , 31(2):3075–3082, 2007. 123, 144

[203] G. Medic, D. You, and G. Kalitzin. An approach for coupling rans and les in integrated computations of jet engines. In *Annual Research Briefs* , pages 287–298. 2006. 124

[204] G. Medic, D. You, and G. Kalitzin. On coupling of RANS and LES for integrated computations of jet engines. In *Proc. of the ASME Turbo Expo 2007*, number GT2007-27096, 2007. 124

[205] J. Schlüter. Consistent boundary conditions for integrated les/rans simulations: Les outflow conditions. In *Annual Research Briefs* , pages 19–29. 2001. 124

[206] J. Schlüter and X. Wu. On les outflow conditions for integrated les-rans computations. In *Annual Research Briefs* , pages 107–116. 2004. 124

[207] J. L. Kerrebrock and A. A. Mikolajczak. Intra stator transport of rotor wakes and its effect on compressor performance. *J. Eng. Gas Turb. and Power* , 92:359–378, 1970. 125

[208] T. L. Butler, O. P. Sharma, H. D. Joslyn, and R. P. Dring. Redistribution of an inlet temperature distortion in an axial flow turbine stage. *J. Prop. Power* , 5(1):64–71, 1989. 126

[209] M. D. Barringer, K. A. Thole, and M. D. Polanka. Experimental evaluation of an inlet profile generator for high-pressure turbine tests. *J. Turbomach.* , 129(2):382–394, 2004. 128

[210] R. W. Radomsky and K. A. Thole. Flowfield measurements for a highly turbulent flow in a stator vane passage. *J. Turbomach.* , 122:255–262, 2000. 128

[211] A. A. Ameri, E. Steinthorsson, and D. L. Rigby. Effect of squealer tip on rotor heat transfer and efficiency. *J. Turbomach.* , 120(4):753–759, 1998. 130

[212] L. Cambier and J-P. Veuillot. Status of the elsa cfd software for flow simulation and multidisciplinary applications. In *46th AIAA Aerospace Sciences Meeting and Exhibit*, number AIAA-2008-664, 2008. 133

[213] B. R. Smith. The k-l turbulence model and wall layer model for compressible flows. In *AIAA, 21st Fluid Dynamics, Plasma Dynamics and Lasers Conference*, 1990. 133

[214] J. D. Mattingly. *Elements of gas turbine propulsion.* American Institute of Aeronautics and Astronautics, 2005. 134

[215] P. Wolf, R. Balakrishnan, G. Staffelbach, L. Y. M Gicquel, and T. Poinsot. Using LES to study reacting flows and instabilities in annular combustion chambers. *to be published in Flow, Turbulence and Combustion*, 2012. 141, 144

[216] S. Mendez and F. Nicoud. Adiabatic homogeneous model for flow around a multi-perforated plate. *AIAA Journal* , 46(10):2623–2633, 2008. 142

[217] B. Franzelli, E. Riber, M. Sanjosé, and T. Poinsot. A two-step chemical scheme for large-eddy simulation of kerosene-air flames. *Combust. Flame* , 157(7):1364–1373, 2010. 143

[218] B. Franzelli. *Impact of the chemical description on direct numerical simulations and large eddy simulations of turbulent combustion in industrial aero-engines.* PhD thesis, Institut National Polytechnique de Toulouse, 2011. 143

[219] O. Colin, F. Ducros, D. Veynante, and T. Poinsot. A thickened flame model for large eddy simulations of turbulent premixed combustion. *Phys. Fluids* , 12(7):1843–1863, 2000. 143, 144, 170

[220] P. Wolf, L. Y. M. Gicquel, G. Staffelbach, and T. Poinsot. Grid effects on les thermo-acoustic limit-cycle of a full annular aeronautical engine. In *Quality and Reliability of Large-Eddy Simulations II*, volume 16, pages 231–240, 2011. 144

[221] M. Giles. Stator/rotor interaction in a transonic turbine. *J. Prop. Power* , 6(5):621–627, 1990. 156

[222] M. Germano, U. Piomelli, P. Moin, and W. H. Cabot. A dynamic sub-grid scale eddy viscosity model. *Phys. Fluids* , A(3):1760–1765, 1991. 165

[223] P. J. Schmid, L. Li, M. P. Juniper, and O. Pust. Applications of the dynamic mode decomposition. *Theoretical and Computational Fluid Dynamics*, 25(1-4):249–259, 2011. 172

[224] K. Chen, J. Tu, and C. Rowley. Variants of dynamic mode decomposition: boundary condition, koopman and fourier analyses. *J. of Nonlinear Science*, 22(6):887–915, 2012. 172

[225] R. Penrose. A generalized inverse for matrices. *Proc. of the Cambridge Phil. Soc.*, 51:406–413, 1955. 172